TABLE OF CONTENTS

2. SITE CHARACTERISTICS 2.1-1

2.1 GEOGRAPHY AND DEMOGRAPHY OF SITE SELECTED 2.1-1
2.1.1 Site Location 2.1-1
2.1.2 Site Description 2.1-2
2.1.3 Population Distribution and Trends 2.1-4
2.1.4 Uses of Nearby Land and Waters 2.1-5
2.2 NEARBY INDUSTRIAL, TRANSPORTATION, AND MILITARY FACILITIES 2.2-1
2.3 METEOROLOGY 2.3-1
2.3.1 Regional Climatology 2.3-1
2.3.2 Local Meteorology 2.3-10
2.3.3 Onsite Meteorological Monitoring Program 2.3-10
2.3.4 Diffusion Estimates 2.3-11
2.4 SUFACE HYDROLOGY 2.4-1
2.4.1 Hydrologic Description 2.4-1
2.4.2 Floods 2.4-4
2.4.3 Probable Maximum Flood (PMF) on Streams and Rivers 2.4-5
2.4.4 Potential Dam Failures (Seismically Induced) 2.4-8
2.4.5 Probable Maximum Surge and Seiche Flooding 2.4-9
2.4.6 Probable Maximum Tsunami 2.4-9
2.4.7 Ice Flooding 2.4-10
2.4.8 Flooding Protection Requirements 2.4-10
2.4.9 Environmental Acceptance of Effluents 2.4-10
2.5 SUBSURFACE HYDROLOGY 2.5-1
2.5.1 Regional Characteristics. 2.5-1
2.5.2 Site Characteristics. 2.5-2
2.5.3 Contaminant Transport Analysis 2.5-3
2.6 GEOLOGY AND SEISMOLOGY 2.6-1
2.6.1 Basic Geological and Seismological Infromation 2.6-1
2.6.2 Vibratory Ground Motion 2.6-13
2.6.3 Surface Faulting 2.6-44
2.6.4 Stability of Subsurface Materials and Foundations 2.6-47
2.6.5 Slope Stability 2.6-55
2.6.6 Volcanism 2.6-55
2.7 SUMMARY OF SITE CONDITIONS AFFECTING CONSTRUCTION AND OPERATING REQUIREMENTS 2.7-1
2.8 REFERENCES 2.8-1
2.9 TABLES 2.9-1
2.10 FIGURES 2.10-1
2.11 REFERENCES FOR TABLES AND FIGURES 2.11-1

2. SITE CHARACTERISTICS

This chapter discusses meteorology, hydrology, seismology, geology, and volcanism as they relate to the Idaho National Engineering and Environmental Laboratory (INEEL), the Idaho Nuclear Technology and Engineering Center (INTEC), and the Three Mile Island - 2 Independent Spent Fuel Storage Installation (INEEL TMI-2 ISFSI). The geographical location of the INEEL, INTEC, and INEEL TMI-2 ISFSI, the population distribution within and around the INEEL, land and water use, and associated site activities are also discussed. The information presented also provides an evaluation of the site with respect to plant safety. The INEEL is not considered a candidate site for the High Level Waste repository.

Throughout this chapter the units of measure are reported in SI units and/or English units consistent with the source documents.

2.1 Geography and Demography of Site Selected

The following contains information concerning the site geography, population, access transportation routes, and land usage.

2.1.1 Site Location

The INEEL TMI-2 ISFSI will be located at the INTEC within the INEEL. The INEEL is one of nine multiprogram laboratories within the Department of Energy (DOE) complex. The INEEL area measures approximately 60.3 km (37.5 mi) north to south and about 56.0 km (34.8 mi) east to west and encompasses 2300 km^2 (890 mi^2) It is located in Idaho on the Upper Snake River Plain at the southeast foot of the Lost River, Lemhi, and Beaverhead Mountain ranges of the northwest edge of the Upper Snake River Plain, Idaho. Figure 2.1-1 depicts the location of the INEEL in relation to Idaho and adjacent states, and Figure 2.1-2 shows the location of the INEEL relative to surrounding counties. Most of the INEEL is located within Butte County, but portions are also within Bingham, Bonneville, Jefferson, and Clark counties. The INEEL TMI-2 ISFSI and INTEC are located on the INEEL, totally within Butte County.

The geographic location of the INEEL TMI-2 ISFSI is east 43°–34'-13” latitude, north 112°–56'-56" longitude. The Universal Transverse Mercator (UTM) coordinates of the ISFSI location within INTEC will be 343,867 m east by 4,825,583 m north.

Four major all-weather highways service the INEEL. The Union Pacific Railroad crosses the southwest corner of the INEEL, and a spur line provides interchange for facilities on the INEEL. Transmission lines owned by Idaho Power Company and Utah Power and Light Company supply electrical power to the INEEL. The locations of the highways, railroad tracks, and facilities are shown in Figure 2.1-3. There are no oil or gas pipelines passing through the INEEL or the INTEC.

The INEEL TMI-2 ISFSI will be constructed within the INTEC exculsion area. An aerial photograph of the INTEC and the INEEL TMI-2 ISFSI site is included as Figure 2.1-4 and a site plan showing the proposed location of the INEEL TMI-2 ISFSI is provided in Figure 2.1-6. A topographical map of the INTEC is shown in Figure 2.6-39.

2.1.2 Site Description

The INEEL, where the INEEL TMI-2 ISFSI will be constructed, was designated as an exclusion area to build, test, and operate various nuclear reactors and associated facilities. The isolated location was chosen to assure maximum public safety. The INEEL has no residents, and ingress and egress of site personnel for performance of their duties and visiting personnel on official business is strictly controlled. No casual visitations are permitted, except for persons driving through the INEEL on the public highways (see Figure 2.1-8) and visitors to the Experimental Breeder Reactor Number 1 (EBR-I), National Historical Monument, which is open to the public during the summer months. The only recreational activity allowed within the INEEL is limited hunting, and limited grazing is allowed subject to special requirements (see Section 2.1.4).

The INEEL is located in a broad, mostly flat plain averaging 1482.8 m (4865 ft) above mean sea level (msl). The Big Lost River runs through the INEEL, close to the northwest corner of the INTEC area, approximately 850 m (2,800 ft) from the INEEL TMI-2 ISFSI site. This section of the river is a runoff channel from the mountains to the northwest. Water flows intermittently during the spring and winter, sinking through the basaltic lava rock underlying the INEEL into a huge natural underground reservoir of water known as the Snake River Plain Aquifer, which lies about 137.3 m (450 ft) below grade. The subsurface hydrology conditions for the INEEL TMI-2 ISFSI location and the Snake River Plain are discussed in section 2.5. All surface water entering the INEEL sinks below the ground surface within the INEEL boundary (see Figure 2.4-1).

Figure 2.1-5 indicates the distance from the proposed location of the INEEL TMI-2 ISFSI to the INEEL boundary. The shortest distance from the INEEL TMI-2 ISFSI to the INEEL boundary will be 13.7 km (8.5 mi) to the south. The INEEL TMI-2 ISFSI will be located on the INEEL and is remote from major population centers, waterways, and interstate transportation routes. The INEEL TMI-2 ISFSI will be located 67.6 km (42 mi) west of Idaho Falls, Idaho. The INTEC, where the INEEL TMI-2 ISFSI is located, is a restricted area occupying 0.49 km^2 (120 acres). Figure 2.1-6 shows the orientation of

various buildings at the INTEC on the site and the proposed location of the INEEL TMI-2 ISFSI site [2.1].

The typical work force at INEEL facilities is shown in Table 2.1-1. As of March 1996, there were approximately 4860 employees at the INEEL. These employees live in more than 30 communities adjacent to the INEEL; the largest percentage lives in Idaho Falls. The U.S. DOE-operated bus service for INEEL employees is provided from the major communities to the INEEL. The portions of INEEL boundary nearest to adjacent communities are 46.7 km (29 mi) west of Idaho Falls, 51.4 km (32 mi) northwest of Blackfoot, 80 km (50 mi) northwest of Pocatello, and 11.3 km (7 mi) east of Arco.

Public access to the INEEL TMI-2 ISFSI, INTEC, and the INEEL is controlled by DOE security forces that may stop traffic and conduct vehicle searches on the INEEL. The Federal Aviation Administration discourages all air traffic below approximately 1829 m (6000 ft) msl. Five commercial airports are situated within approximately 161 km (100 mi) of the site: 1) 96.6 km (60 mi) southeast, in Pocatello; 2) 67.6 km (42 mi) east, in Idaho Falls; 3) approximately 144.8 km (90 mi) southwest, in Twin Falls; 4) 96.6 km (60 mi) west, near Hailey; and 5) 168.5 km (105 mi) east-northeast, near Jackson, Wyoming. Several smaller gravel-surface landing strips near the INEEL are used primarily for charter flights and crop dusting aircraft. The closest of these is located at Atomic City, which is 17.7 km (11 mi) southeast of the INEEL TMI-2 ISFSI.

The principal surface materials at the INEEL are basalt, alluvium, lake bed or lacustrine sediments, slope wash sediments and talus, silicic volcanic rocks, and sedimentary rocks. A complete review of surface soils and vegetation types is found in Dahl, et al., 1978. The natural plant life consists mainly of sagebrush and various grasses (see Figure 2.1-7). The vegetation of the INEEL is limited by soil type, meager rainfall, and extended drought periods. Only a few deciduous trees, located principally along the Big Lost River, exist on the INEEL. The most prominent ground cover is a mixture of vegetation consisting of sagebrush (Artemisia tridentata) and a variety of grasses. Lanceleaf rabbitbrush (Crysothamnus viscidiflorus) covers about 80% of the INEEL and can be found in any given area. (see Figure 1.2-7)

The soil at the INEEL TMI-2 ISFSI site is previously disturbed sandy gravel and the flat terrain precludes erosion. The entire INTEC area is kept free from vegetation so there is no fuel for a fire near the INEEL TMI-2 ISFSI.

2.1.2.1 Other Activities Within the Site Boundary

The controled area boundary for the INEEL TMI-2 ISFSI is the boundary of the INEEL site. Inside of the INEEL boundary is the INTEC boundary. The INEEL TMI-2 ISFSI facility is also surrounded by a security fence. Many activities occur within the INEEL, but only those activities within 100 meters of the INEEL TMI-2 ISFSI could have an impact on the INEEL TMI-2 ISFSI. These activities are described below. See Figure 2.1-8 and Figure 2.2-2.

Figure 2.1-6 shows the area inside of the INTEC boundary. Nuclear fuels are stored and waste from previous fuel processing activities is managed and treated within this restricted area. The high-level radioactive waste managed at the INTEC is retained on-site for processing and is not released to any water system, above or below ground. The only interactions between the ISFSI and other activities within the INTEC boundary would be for routine operation and maintenance by site operators.

Within 100 meters of the ISFSI the only activities that occur are spent nuclear fuel storage at building CPP-666 and dry spent nuclear fuel storage in the below-grade areas of CPP-749. An office building also lies within 100 meters of the ISFSI. Occasional security and maintence vehicle traffic may pass within 100 meters of the INEEL TMI-2 ISFSI.

The security fence for the INEEL TMI-2 ISFSI defines the ISFSI boundary. There are no activities within this boundary except those related to the operation of the ISFSI.

2.1.2.2 Boundaries for Establishing Effluent Release Limits

The INEEL boundary (property boundary lines), shown in Figure 2.1-5, establishes the exclusion area, defined in 10 CFR Part 100, for protection of the public from exposure to airborne radioactivity. Figures 2.1-3 and 2.1-4 show the relative position of the restricted INTEC area, which includes the INEEL TMI-2 ISFSI within the larger exclusion area of the INEEL. For more information on radioactivity see Section 2.2.

Access to the central portion of the INEEL, INTEC, and in turn to the INEEL TMI-2 ISFSI, is controlled by DOE-contracted security forces, who may, during emergency situations, interrupt traffic on the public highways that cross the INEEL.

2.1.3 Population Distribution and Trends

Population in the region is projected to reach 276,395 persons by 2004 based on population and employment trends. Over the period 1990 to 2004, the average annual growth rate is projected to be 1.6 percent compared to a projected State-wide annual growth rate of 1.7 percent. Figures 2.1-9, 2.1-10, 2.1-11, and 2.1-12 show population densities, based on the 1990 Census, for the years 1990 through 2020 at 10-year intervals for the 80 km (50 mile) radius around INTEC/ INEEL

TMI-2 ISFSI. These 50-mile radius figures are provided instead of 5-mile radius because there are no residents within 5 miles. Also shown are the relative locations of the major towns. The nearest populated area to the INEEL is Atomic City, population about 30, located approximately 1.6 km (1 mile) from the southern INEEL boundary and about 18 km (11 miles) from the INEEL TMI-2 ISFSI.

No permanent residents live within a 16-km (10-mile) circle centered at the INTEC on the INEEL. No cities or towns are within 16 km (10 miles) of the INEEL TMI-2 ISFSI (Figure 2.1-2). However, several INEEL facilities, such as the CFA, TRA, and RWMC are within 10 miles of the INEEL TMI-2 ISFSI. Also, the Experimental Breeder Reactor I (EBR-I), a National Historic Landmark, is located southwest and within 10 miles of the INEEL TMI-2 ISFSI. Institutional control would continue to restrict access to INEEL lands for the next 100 years [2.201], thus population within 16 km (10 miles) of the INEEL TMI-2 ISFSI is unlikely to change through 2035.

Variations in populations are caused by the daily influx of the INEEL workforce. About 4,110 workers are employed within 16 km (10 miles) of the INEEL TMI-2 ISFSI. U. S. Highways 20 and 26 pass through the site and are within 16 km (10 miles) of INEEL TMI-2 ISFSI. Traffic on these highways, other than the daily site traffic, is related to travel between cities surrounding the site and the many recreational opportunities in the area. The projected INEEL workforce for the year 2004 is 7,250 [2.2]

Construction, operation, and decommissioning of the INEEL TMI-2 ISFSI will have a negligible impact on the population of the region.

2.1.4 Uses of Nearby Land and Waters

Categories of land use at the INEEL site include facility operations, grazing, general open space, and infrastructure, such as roads. Facility operations include industrial and support operations associated with energy research and waste management activities. Land is also used for recreation and environmental research associated with the designation of the INEEL as a National Environmental Research Park. Much of the INEEL site is open space that has not been designated for specific uses. Some of this space serves as a buffer zone between INEEL facilities and other land uses. About 2 percent of the total INEEL site area (11,400 ac or 4,600 ha) is used for facilities and operations, thus designation as “rural” for dispersion purposes is appropriate. Public access to most facility areas is restricted. Approximately 6 percent of the INEEL site, or 34,260 acres (13,870 ha), is devoted to public roads and utility rights-of-way that cross the site. Recreational uses include public tours of general facility areas and EBR-I and controlled hunting, which is generally restricted to 0.8 km (0.5 mi)

within the INEEL boundary. Between 300,000 and 350,000 acres (121,000 and 142,000 ha) are used for cattle and sheep grazing. A 900-acre (400-ha) portion of this land, located at the junction of Idaho State Highways 28 and 33, is used by the U.S. Sheep Experiment Station as a winter feed lot for approximately 6,500 sheep. Grazing is not allowed within 3 km (2 miles) of any nuclear facility, and, to avoid the possibility of milk contamination by long-lived radionuclides, dairy cattle are not permitted. Rights-of-way and grazing permits are granted and administered by the U. S. Department of the Interior's Bureau of Land Management. Selected land uses at the INEEL and in the surrounding region are presented in Figure 2.1-13.

Small communities and towns located near the INEEL boundaries include Mud Lake to the east; Arco, Butte City, and Howe to the west; and Atomic City to the south. The larger communities of Idaho Falls/Ammon, Rexburg, Blackfoot, and Pocatello/Chubbuck are located to the east and southeast of the INEEL site. The Fort Hall Indian Reservation is located southeast of the INEEL site. Recreation and tourist attractions in the region surrounding the INEEL site include Craters of the Moon National Monument, Hell's Half Acre Wilderness Study Area, Black Canyon Wilderness Study Area, Camas National Wildlife Refuge, Market Lake State Wildlife Management Area, North Lake State Wildlife Management Area, Yellowstone National Park, Targhee and Challis National Forests, Sawtooth National Recreation Area, Sawtooth Wilderness Area, Sawtooth National Forest, Grand Teton National Park, Jackson Hole recreation complex, and the Snake River (see Figure 2.1-8).

All county plans and policies encourage development adjacent to previously developed areas in order to minimize the need to extend infrastructure improvements and to avoid urban sprawl. Because the INEEL is remotely located from most developed areas, INEEL lands and adjacent areas are not likely to experience residential and commercial development, and no new development is planned near the INEEL site. However, recreational and agricultural uses are expected to increase in the surrounding area in response to greater demand for recreational areas and the conversion of range land to crop land [2.3].

The four most prominent tourist/recreation areas or attractions in the INEEL area include Yellowstone National Park, which is approximately 117 km (72.5 mi) northeast of the INEEL, and 160 km (99.5 mi) from the INTEC; EBR-I, which is situated on the INEEL; Craters of the Moon National Monument, which is located approximately 30 km (19 mi) southeast of the INEEL; and the resort areas of Ketchum and Sun Valley, which are approximately 95.8 km (59.5 mi) west of the INEEL [115.9 km (72 mi) from the INEEL TMI-2 ISFSI.

2.2 Nearby Industrial, Transportation, and Military Facilities

Since the INEEL site is so large and remote, no ordinary industrial or military facilities are located closer to the INEEL boundary than Idaho Falls, which is approximately 46.7 km (29 mi) away. However, all three branches of the military have conducted nuclear experimental work at the INEEL. Currently, the only operating military facility on the INEEL is the former U.S. Navy reactor training program site, which is located over 8 km (5 mi) away from the INEEL TMI-2 ISFSI at the Naval Reactor Facilities (NRF) area (see Figure 2.2-1].

Facilities within 8 km (5 mi) of the INEEL TMI-2 ISFSI have been evaluated per Nuclear Regulatory Commission Guidelines; Central Facilities Area (CFA), Test Reactor Area (TRA), and Power Burst Facility/Waste Experimantal Reduction Facility (PBF/WERF) are within 8 km (5 mi). Activities at these facilities are subjected to periodic reviews to ensure the safety of the workers and the public. Potential accidents at these facilities are considered in the development of the INEEL emergency management plans.

The CFA poses no radiological, toxic, or hazardous chemical concern to the INEEL TMI-2 ISFSI, since it provides only centralized support services for INEEL operations (e.g., medical services, vehicle maintenance, machine shops, and environmental sample analysis). Radiological consequences at the canceled Special Isotope Separation (SIS) site from accidents at PBF and TRA have been calculated. Location differences between the proposed SIS site project and the INEEL TMI-2 ISFSI have negligible effects on the consequences of PBF/WERF and TRA accidents. Therefore, the calculated consequences for the SIS site may be used for the INEEL TMI-2 ISFSI. The limiting potential release accident at PBF is the flow blockage of a single PBF/Boron Neutron Capture Therapy (BNCT) fuel canister. This could result in a calculated effective dose equivalent (EDE) of 0.1 rem at the INTEC. At TRA, a maximum hypothetical loss of coolant accident at the Advanced Testing Reactor (ATR) would result in an EDE of 3.23 rem at the INTEC. The ICRP-30 dose calculation methodology as incorporated into the 3S version of the RSAC computer code was used to calculate the doses. These doses assume the receptor remains outside in the plume at the INTEC for eight hours for the PBF/BNCT accident and two hours for the TRA accident [2.1].

Because of the distance between the INEEL TMI-2 ISFSI and other INEEL facilities, airborne contamination is the primary potential consequence of an emergency condition at one of the nearby nuclear facilities. The Warning Communications Center (WCC) at Department of Energy, Idaho Operations Office (DOE-ID) headquarters maintains a continuous sitewide surveillance of all INEEL facilities and transmits warning signals for any existing unsafe conditions. On receipt of a warning signal, the INEEL Emergency Plan/RCRA Contingency Plan goes into effect, and the appropriate emergency procedures are activated.

Accidents in all of the nearby nuclear facilities have been evaluated in the facility specific Safety Analysis Reports. The facilities are built to withstand their design accidents, so the only impact on the INEEL TMI-2 ISFSI from an accident in a nearby facility could be airborne contamination. The ISFSI would be decontaminated as part of the general recovery from the accident.

The nearby facilities are nuclear facilities or associated support facilities. Support operations include maintenance, laboratory operations, security, medical, and others. Materials near the INEEL TMI-2 ISFSI associated with these support operations include:

- Small amounts of hazardous materials,
- Temporary waste storage,
- Satellite fuel storage (propane, gasoline, diesel, etc.) and
- Small amounts of maintenance materials (solvents, paints, etc.).

None of these materials present a hazard to the INEEL TMI-2 ISFSI.

There are no natural gas pipelines, mines or stone quarries, oil or gasoline plants, or other activities in which a fire or explosion could cause damage to the ISFSI. The nearest road, which is in the access controlled area, is approximately 1 km (0.6 mi) away. The area within 200 meters (600 ft) of the ISFSI is cleared of vegetation, therefore range or brush fires are not a threat.

The only expected airborne pollutant at the INEEL TMI-2 ISFSI site may be NOX released from the INTEC main stack when the NWCF is in operation. The levels of NOX are closely monitored. The very low levels expected at the INEEL TMI-2 ISFSI which is approximately 400 meters from the stack would have no effect on the facility.

Aircraft crashes at the INTEC have been analyzed [2.4]. The analysis included both commercial flights and helicopter operations for security. These various aircraft crashes were shown to have a frequency of occurrence very near the incredible range. Crashes into individual INTEC facilities are incredible (<9.6E-7 per year). INEEL security has discontinued the routine use of helicopters.

There are no structures tall enough that, if they collapsed, could damage the ISFSI.

<u>Transportation Routes and Facilities</u>. Public transportation routes nearest the INEEL TMI-2 ISFSI site include U.S. Highway 20/26, which passes approximately 6 km (4 mi) south of the ISFSI, and the Mackay Branch of the Union Pacific Railroad, which passes 11 km (7 mi) south of the ISFSI (see Figures 2.1-3 and 2.1-8).

Other roads in proximity to the ISFSI are the controlled access roads between various INEEL facilities. The road nearest to the ISFSI is Lincoln Boulevard, the main north-south road at the INEEL. It passes within 0.8 km (0.5 mi) to the west of the ISFSI. A

railroad spur from the Mackay Branch (which also services only the INEEL) passes within about the same distance to the east of the ISFSI. Hazardous materials, including spent nuclear fuels, radioactive waste, and various chemicals are transported on these routes. Accidents along these transportation routes would not impact the INEEL TMI-2 ISFSI.

2.3 Meteorology

2.3.1 Regional Climatology

2.3.1.1 Data Sources

The climatology of the INEEL TMI-2 ISFSI site is well characterized. Research grade meteorological observations have been continuously taken by the National Oceanic and Atmospheric Administration and its predecessor agencies since 1949. These data have been summarized in:

> Climatography of the Idaho National Engineering Laboratory, 2nd Edition., DOE/ID-12118, 1989; and the
>
> Climates of the States, Western States Water Information Center, Inc., 1974.

The meteorological observation station at Central Facilities Area (CFA), 2 miles south of the INEEL TMI-2 ISFSI site, is labeled "Idaho Falls 46W" in the national climatological summaries. A well-equipped 200-foot research tower ("Grid 3") is located approximately 1/2 mile northwest of the INEEL TMI-2 ISFSI site, and is the preferred site for representative wind observations.

2.3.1.2 General Climate

Terrain Influences on INEEL Climate

The INEEL is situated on a mile high area of the Snake River Plain in southeastern Idaho. All air masses entering the Snake River Plain must first cross a mountain barrier, precipitating a large percentage of their moisture. Annual rainfall at the INEEL is light, and the region has semiarid characteristics.

The local northeast - southwest orientation of the Eastern Snake River Plain and bordering mountain ranges tend to channel the prevailing west winds so that a southwest wind predominates over the INEEL; the second most frequent winds come from the northeast. The relatively dry air and infrequent low clouds permit intense solar heating of the surface during the day and rapid radiational cooling at night. These factors combine to give a large diurnal range of temperature near the ground.

Because of the moderating influence of the Pacific Ocean, most of the air masses flowing over this area are usually warmer during winter and cooler during summer than air masses flowing at a similar latitude in the more continental climate east of the Continental Divide. The Centennial and Bitterroot Mountain Ranges keep most of the shallow, but intensely cold winter air masses from entering the Eastern Snake River Plain (ESRP)

when they move southward from Canada. Occasionally, however, the cold air can spill over the mountains. When this happens, the cold air is held in the ESRP by the surrounding mountains, and the INEEL experiences low temperatures for periods lasting a week or longer.

A simplified topographic map of the INEEL area is presented in Figure 2.3-1 [2.5]. The height values of the contour lines given are in hundreds of feet above mean sea level. The stippled area indicates the area of the plain which lies below 5000 ft. The large dots indicate the location of tower mounted wind sensors. Winds at the INEEL are influenced by:

- Northwesterly, down-canyon winds which develop in the Little Lost River and Birch Creek Valleys and spill out onto the ESRP to the southeast.

- Southwesterly winds which result from redirection of the westerly winds aloft by the mountains bordering the ESRP.

- Northerly or northeasterly winds which result from air cooling and descending from the elevated terrain north of INEEL.

- Reversals in wind direction which occur when shallow surface winds, resulting from surface cooling and density differences, are overcome by winds aloft moving in an opposite direction. This is caused by surface heating. The opposite transition can also occur.

- Stagnations which occur in areas where light winds converge.

- Large horizontal eddies which form as a result of convergence, mountain lee effects, or passing pressure systems associated with larger thermal and moisture fields.

These influences combine to result in regional scale wind trajectories which rarely, if ever, maintain their initial direction to long distances or persist for more than a few hours. The impact of this variability on atmospheric transport and dispersion at INEEL is discussed in more detail in Section 2.3.4

Regional Temperature

Monthly and annual average temperatures for the INEEL TMI-2 ISFSI (taken from CFA data) are given in Table 2.3-1 [2.5]. Average monthly maximum temperatures range from 87°F in July to 27°F in January. Average monthly minimum temperatures range from 49°F in July to 4°F in January. Through 1982 the warmest temperature recorded was 101°F and the coldest was -40°F.

Regional Precipitation

Table 2.3-2 [2.6] summarizes the average monthly and annual precipitation. The average annual precipitation is 8.71 inches, and the yearly totals range from 4.50 to 14.40 inches. Maximum observed 24-hour precipitation amounts are less than 2.0 inches, and the maximum 1-hour amounts are just over 1.0 inch.

About 26.0 inches of snow falls each year. The maximum yearly total was 40.9 inches, and the smallest total was 11.3 inches. The greatest 24-hour total snowfall was 8.6 inches. The greatest snow depth observed on the ground was 27.0 inches. January and February average about 7 inches for a monthly maximum snow depth. The ground is usually free of snow from mid-April to mid-November. Table 2.3-3 [2.5], presents snowfall amounts expected at the INEEL TMI-2 ISFSI site.

Regional Atmospheric Moisture

The moisture content of the air is described by the wet bulb and dew point temperatures. During January (the coldest month) the temperature averages 16.5°F, and the dew point averages 7.4°F. During July, the temperature averages 69.0°F and the dew point averages 33.5°F. The air over the INEEL is typically very dry, and relative humidities during summer afternoons may often range from 5 to 15%. The lowest absolute moisture content of the air occurs during the coldest part of the year. Table 2.3-4 [2.5] presents monthly and annual dew point temperatures expected at the INEEL TMI-2 ISFSI site.

Regional Winds

Wind directions at INTEC, the INEEL TMI-2 ISFSI site, are mostly from the northeast or southwest quadrants, due to airflow channeling by the bordering mountains. Monthly annual average hourly wind speeds are provided in Table 2.3-5 [2.5] for both the 20 ft and 250 ft heights above ground level; these speeds are 7.5 and 12.6 miles per hour (mph), respectively. The greatest hourly average wind speeds of 51 (20 ft tower level) and 67 mph (250 ft tower level) have occurred during winter or early spring, when large scale weather patterns are most intense. Peak gusts of 78 and 87 mph, respectively, have been observed.

2.3.1.3 Severe Weather

Maximum and Minimum Temperatures

Extremes of daily maximum, minimum, and average temperatures are listed in Table 2.3-6 [2.5]. The maximum difference between the highest and lowest temperatures recorded during a given month was in March with a difference of 98°F. The largest differences between extremes of monthly daily average temperatures occur in the winter, and the smallest differences are between the averages for the summer months. The differences between the highest and lowest daily average temperatures within a given month are large. The maximum difference (67°F) between the highest and lowest daily average temperatures occurred during December.

The INEEL TMI-2 ISFSI design temperatures are for a high of 103°F and a low of -50°F.

Temperature Ranges

Although the values above are extremes taken over the total period of record, the maximum ranges between the highest and lowest daily temperatures are also large. Table 2.3-7 [2.5] lists the daily ranges expected, based on the mean temperatures for each month and the maximum daily range during that month. The maximum daily range experienced was 58°F at CFA.

Freeze Thaw Cycles

An indication of the amount of weathering to certain materials is the frequency of occurrence of daily freeze-thaw cycles. These data are based on the air temperature at 5 ft in an instrument shelter, which, because of its distance from the ground, may underestimate the actual number of freeze thaw cycles. Despite this limitation, the data presented in Table 2.3-8 [2.5] are indicative of the general frequency and seasonal variation.

Degree Days

A degree day is defined as the number of degrees that the mean temperature is less than 65°F for that day. This unit is used as a basis for design considerations and heating energy requirements. Table 2.3-9 [2.5] lists the daily average degree days expected at the INEEL TMI-2 ISFSI site. The highest and lowest daily degree day values are listed for each month.

Design Temperatures

Heating and cooling load calculations are based on the frequency of occurrence of hourly temperatures. The design temperature for heating load calculations is the temperature at which 2.5% of the hourly temperatures are equal to or below during the months of December through March. The design temperature for cooling load calculations is the temperature equaled or exceeded 2.5% of the time from June through September. Design temperatures at the 2.5% level have been computed for the INEEL. For cooling it is 90°F and for heating it is - 9°F [2.5].

Subsoil Temperatures

During a seven-year study, soil temperatures were recorded from thermometer probes placed at one-foot intervals from depths of two through seven feet beneath a sandy surface, representing the natural terrain with the overlying vegetation removed. Similar measurements were also made under an asphalt road surface. The temperatures at all six levels have been averaged for each month, and isotherms with depth are presented in Figures 2.3-2 and 2.3-3 [2.5] for both types of surfaces. These two figures show a significant difference between the two locations. Under the asphalt, temperatures average approximately 10°F higher in the summer near the surface while, in the winter, colder temperatures occur over a longer period and to a greater depth.

Extreme Winds

High wind speed episodes occur during all months of the year, with the highest hourly average winds occurring during winter and spring. At INEEL, the passage of synoptic frontal systems involves higher and more sustained hourly wind speed events than those of thunderstorm gust fronts.

Downslope winds are occasionally responsible for wind damage at canyon-mouth locations in the eastern Rocky Mountains. These winds are very rare on the Eastern Snake River Plain, because the terrain is unfavorable for their occurrence.

The peak wind speed gusts anticipated at the INEEL TMI-2 ISFSI site at both upper and lower levels are listed by month in Table 2.3-10 [2.5]. Values Presented in Table 2.3-10 are based on the highest period of record values occurring at either Test Area North (TAN) or CFA, regardless of location. These values will be relevant to maximums occurring over the flat terrain anywhere on the INEEL. While strong gusts may be a result of pressure gradients from large-scale systems, they may also be a result of a thunderstorm. Since thunderstorms may form at any location and move in any direction, very strong gusts can be expected from any direction of the compass. Experience has shown, however, that most of these strongest gusts are likely to be from the south, or southwest to west.

The INEEL TMI-2 ISFSI load for winds is bounded by the tornado.

Tornadoes

A tornado is defined as a violent local vortex in the atmosphere. It is usually accompanied by a funnel shaped cloud with spiraling winds of very high velocity (may be greater than 300 mph). Tornadoes usually occur in association with thunderstorms, especially those which produce hail. When a vortex cloud reaches the land surface, it is classified as a tornado. If the vortex cloud does not reach the ground surface it is classified as a funnel cloud.

Most of the tornado activity in the U.S. occurs east of the Rocky Mountains. In Idaho, tornadoes have been reported only in the spring and summer seasons (April through August). In the 42-year period 1916 through 1957, 19 tornadoes were reported in Idaho. With expanding population and better surveillance methods, the average number of tornadoes per year will probably continue to increase slowly in Idaho, but compared to areas in the Midwest, the frequency will remain very small. With very few tornadoes occurring in the state per year, the chances of any one location being struck are remote.

National tornado statistics have been compiled which, when taken in context with maximum atmospheric moisture content, surrounding geography, and other statistics, allow a realistic assessment of tornado risk and establish a value for the maximum credible tornado which may be expected at the INEEL. For the years 1950 to present the

NOAA record indicates there have been a total of five funnel clouds sighted within the boundaries of the INEEL. The calculated return period for a tornado on the INEEL with wind speeds exceeding 120 mph, according to Coats and Murray [2.7], is 1.0E6 years.[2.6]

The characteristics of the INEEL design basis tornado are extracted from the INEEL architectural engineering standards for the U.S. Department of Energy, Idaho Operations Office (original issue December 1978, Revision 3, June 15, 1982). These characteristics are shown in Table 2.3-11.

The design basis for the INEEL TMI-2 ISFSI tornado is taken from SECY-93-087 for Region III which is bounding for any tornado expected on the INEEL. The INEEL TMI-2 ISFSI design basis tornado is also shown on Table 2.3-11.

Dust Devils

Although tornadoes are rare at INEEL, the whirling winds of the less violent "dust devils" are common. These dust devils pick up dust and pebbles and can overturn, blow down, or carry off insecure objects. They usually occur on warm sunny days with little or no wind. The dust cloud may be several hundred yards in diameter and extend several hundreds of feet into the air.

Hurricanes and Tropical Storms

Because of the moderating influence of the Pacific Ocean and the isolating influence of surrounding mountains, neither hurricanes nor tropical storms occur at INEEL.

Precipitation Extremes - Recorded Hourly and Daily Precipitation Events

For precipitation extremes, the highest INEEL value (regardless of location) is cited. The greatest amounts recorded during l-h and 24-h periods are listed monthly and annually in Table 2.3-12 [2.5]. The high hourly amounts during May and June were the result of heavy thunderstorms passing over the rain gauge. The maximum for one hour was 1.15 in. at TAN. Precipitation amounts greater than one inch per day have occurred during 10 of the calendar months within the period of record. Some months have had multiple occurrences.

Precipitation Extremes - Predicted Maximum Storm Events

Hershfield [2.9] used the long term precipitation records of more than 1600 stations to develop return periods for 24-hour storms (Table 2.3-12). He also used short term records from about 5000 stations to define short return period storms. From these results he constructed isopluval maps for the continental United States for storms with return periods of 2 and 100 years. He then interpolated isopleth maps for other storm durations and return periods. Sagendorf [2.8] has recently analyzed data for all available Upper Snake River stations (including INEEL) and independently validated the Hershfield data,

as well as tested a function to adjust 24 hour Hershfield totals to INEEL storms of shorter duration.

Precipitation Extremes - Precipitation Occurrence

In addition to amounts, the frequency of occurrence, and duration of precipitation periods are frequently used for planning purposes. Table 2.3-14 [2.5] lists the average number of days (from midnight to midnight) per month and annually during which specified amounts of precipitation fell at CFA. These frequencies of occurrence apply to the INEEL TMI-2 ISFSI site.

Thunderstorms and Lightning

A thunderstorm day is defined by the National Weather Service as a day on which thunder is heard at the observing station. Lightning may or may not be seen; rain and/or hail may or may not occur. By this definition, the INEEL TMI-2 ISFSI site may experience, on the average, two or three thunderstorm days during each of the months from June through August. Several individual thunderstorms may occur on each of these thunderstorm days. Thunderstorms have occurred during all of the year but very rarely occur during the November through February period.

The surface effects from thunderstorms over the ESRP are usually much less severe than are experienced east of the Rocky Mountains or even in the mountains surrounding the ESRP. At times, the precipitation from the thunderstorm evaporates before reaching the ground so that little or none may be recorded with the storm's passage. Even so, the storm may be accompanied by strong, gusty winds which may produce local dust storms. Cloud-to-ground lightning may occur. Occasionally, rain in excess of the long-period average monthly total may result from a single thunderstorm passing over a station.

The U.S. Bureau of Land Management Interagency Fire Center (Boise) currently operates a lightning detection system by which the location and number of lightning strikes may be documented, in real time if necessary [2.5]. Although the INEEL is surveyed by the system, no historical statistics for the area have been compiled. While the number of lightning strikes occurring over the INEEL is not high, the lack of natural targets and the poor conductivity of the lava rock and desert soil allow man-made structures to be susceptible to lightning strikes.

The security fence and lighting system will contain grounded lightning protection for the INEEL TMI-2 ISFSI.

Snow Storms and Snow Accumulation

Snowfall and snow depth records are available only from CFA, since it is the only manned weather station at the INEEL. CFA values are representative of snow conditions at the INEEL TMI-2 ISFSI site. Snowfall is the amount of snow that falls within a given period regardless of the amount that accumulates on the ground. Since snow may melt as it falls, the snowfall amount must occasionally be estimated from the water equivalent of

snow. The average monthly and annual snowfall amounts are listed in Table 2.3-3, cited previously. Considerable variation is noted between the maximum and minimum totals for the period of record, particularly December with a difference of nearly 22.3 in. The maximum snowfalls in 24-h periods were 8.5 in. in January and 8.6 in. in March.

The average number of days (from midnight to midnight) in a given month during which a specified amount of snowfall has been recorded is listed in Table 2.3-15 [2.5]. The difference between maximums and minimums are quite large for small amounts of snowfall.

The averages and ranges of the maximum monthly snow depths are listed in Table 2.3-16 [2.5]. The maximum depth ever recorded was 27 in. During periods when several inches of loose snow are present along with moderate to strong surface winds, considerable blowing and drifting will occur with drifts accumulating to several feet high.

The INEEL TMI-2 ISFSI snow load is 30 psf and the design is for greater than 30 psf.

Hail and Ice Storms

Although small hail frequently occurs with thunderstorms (see statistics noted above), damage from this cause has not yet been experienced at the INEEL. Crop damage from hail is not unusual in nearby areas. Hail-caused property damage in the City of Idaho Falls has occurred, so INEEL damage from this source is possible.

Severe glaze icing resulting from freezing rain rarely occurs at the INEEL. Brief periods of glazing conditions occasionally accompany a transition from rain to snow and bring about slippery sidewalks and roads, but produce insufficient accumulation to damage power or communication lines.

Rime icing, which occurs when fog droplets impinge upon objects at temperatures below freezing, is a more likely phenomenon. The period of record has shown that accumulation on power lines and air intakes has not constrained operations at the INEEL.

Supercooled fog or low stratus clouds occur occasionally in winter. With a snow cover and a persistent high pressure system these conditions may last for several consecutive days.

Other Phenomena

In historical INEEL on-site measurement programs, dust concentrations varied from a low of 14.1 ug/m^3 over a total snow cover to a high of 772 ug/m^3 during the summer. In an undisturbed area, even with dust devils present, a concentration of only 151 ug/m^3 was recorded. Annual geometric means of 24-hour particulate samples were approximately 30 ug/m^3 [2.6].

In relatively undisturbed areas, median dust particle sizes ranged from 0.330 to 0.425 microns. Less than 1% of the ambient particulate is larger than 10 microns; a few particles reach several hundred microns. Petrographic examinations of dust particles indicate the dust would be classified as moderately abrasive. During the daytime, with strong winds present, there is a sharp decrease of dust concentration with height to approximately 70 ft. indicating air intakes should be located as high off the ground surface as possible. Vehicular traffic and activities in construction areas (disturbed areas) contribute more to locally elevated high dust concentrations than do strong winds over undisturbed areas.(see Table 2.3-17)

The Idaho Division of Environmental Quality (DEQ) has analyzed typical dust concentrations in various airsheds within the state, and has established estimated background values for pollutants having National Ambient Air Quality Standards. EPA has determined that INEEL air quality is in attainment of all applicable National Ambient Air Quality Standards by a wide margin [2.10]. Existing INEEL air quality poses no potential constraints to INEEL TMI-2 ISFSI development.

Station Pressure

Measurements of atmospheric pressure are important to many phases of design and operations at the INEEL. Station pressure, the actual measured pressure without reduction to sea level, has been recorded continuously at CFA since February, 1950. The station pressure record from February 1950 to August 1964 is summarized in Table 2.3-18 [2.5]. Later data were not made available for the current analysis because they are believed to vary insignificantly from the existing data. The CFA station mercurial barometer standard is at 4937.57 ft. ASL. The INEEL TMI-2 ISFSI site is about 4940 ft ASL. CFA data may be used directly for the INEEL TMI-2 ISFSI site.

The average station pressure of 25.06 in. and the highest and lowest recorded pressures of 25.69 in. and 24.26 in., respectively, over the period of record, would indicate that the extreme limits of station pressure would be 24.00 and 26.00 in. The difference between the highest and lowest pressures recorded in any month over the period of record reflects the development of more intense pressure systems in the winter compared to the weaker systems prevalent in the summer months. The annual mean daily pressure range is 0.15 in. varying from near 0.10 in. in the summer to 0.20 in. in the winter. The largest pressure change recorded in one day was 0.680 in. Although specific records of the maximum pressure change in a l-h and a 24-h period have not been recorded at the INEEL, evaluation of synoptic and climatological records indicate maximum changes would be bounded by 0.1 in. per hour and 1.0 in. per day.

Air Density

The average density of air at the INEEL is a value of some interest and is related to pressure. It is computed from the Equation of State using average values of temperature, pressure, and moisture. For sea level, using a standard pressure of 29.92 in. of mercury and 32°F, a standard density of 1.29 x 10-3 g/cm^3 can be computed [2.5].

A normal average temperature of 42.4°F and an average station pressure of 25.06 in. of mercury gives an average density of 1.06 x 10-3 g/cm^3 for the INEEL [2.6].

2.3.2 Local Meteorology

2.3.2.1 Local Meteorology Data Sources

A site-specific climatology prepared in 1984 for a proposed reactor to be located just one mile east of the INTEC site contains the most applicable site-specific data for INEEL TMI-2 ISFSI climatological conditions:

> Climatography of the Idaho National Engineering Laboratory --Site Specific Summary NPR Primary and Alternate Site, Draft, November, 1984, IDO-12048B

2.3.2.2 Topography

Regional topography in the INEEL TMI-2 ISFSI site area is presented in Figure 2.6-39. A detailed topography survey at 2-foot contour intervals for the 5-mile radius of INTEC has been compiled from Dwgs. B50-001-ASC, plates 16,17,21,22. 50-mile and 5-mile radii about the INEEL TMI-2 ISFSI site are depicted in Figures 2.3-4 and 2.3-5, respectively [2.5]. Topographic cross-sections have been produced for each of 16 radii corresponding to the 16-point compass directions, from the INEEL TMI-2 ISFSI site to the 50-mile limit. These cross sections are presented in Figures, 2.3-6 through 2.3-13.

The terrain features shown on the figures cause a subtle channeling of the diurnal, low wind speed flows, even over the valley floor even where relative topographic relief is very small. This influence can be seen under both daytime surface heating and nocturnal surface cooling conditions. Terrain surrounding the INEEL also is known to channel and redirect the upper level (global scale) winds and determine the character of their interaction with the valley surface. Down-valley winds formed in the surrounding valleys and interaction of the mountains with nearby frontal systems are also significant causes of valley winds.

2.3.3 Onsite Meteorological Monitoring Program

Wind Roses

The wind station closest to the INEEL TMI-2 ISFSI site is Grid 3 (with a 200-ft tower with two levels of wind and three levels of temperature instrumentation), and represents the wind flows at the ISFSI site. Stability wind roses for the Grid 3 10m and 61m levels are presented in Figures 2.3-14 through 2.3-17 [2.5].

Adequacy of Existing Monitoring Program

Except for local-scale surface drainage winds near INTEC, the climatological data obtained from the ongoing observations at CFA ("Idaho Falls 46W") provide a fully representative characterization of the atmosphere at the INEEL TMI-2 ISFSI site.

Grid 3, a 64 meter (200-foot) research-grade meteorological tower sited approximately 1.6 miles north of INTEC, provides wind and temperature data for ongoing use in INEEL TMI-2 ISFSI climatology, and is integrated into the INEEL emergency dose prediction system maintained by NOAA. The Grid 3 site can sense phenomena resulting from local terrain considerations (e.g., boundary layer wind shear resulting from channeling near the Lost River near INTEC) which make use of lower level CFA winds data less appropriate.

Grid 3 wind instrumentation spans the full height of the tower, with continuous 10m and 61m wind data reduced for climatological use. These sensor heights mirror atmospheric heights in which transport and dispersion from surface and elevated (stack) releases, respectively, may occur. Because they are above much of the friction layer, the 61m winds are representative of release heights above that level. Table 2.3-21 shows an example of the Grid 3 data output.

Observations for Off-site Concentration Assessments

Wind data have been collected continuously at a large number of stations in the vicinity of the INEEL since the 1950s. The data are currently available in real time by radiotelemetry. During the INEEL TMI-2 ISFSI operations phase, weather data will continue to be obtained from the Grid 3 tower. Data may also be used from the 26 additional telemetered towers which are maintained by NOAA for use in near real-time off-site concentration assessments.

Current instrument locations relative to the INEEL TMI-2 ISFSI site are depicted in Figure 2.3-18 [2.5]. At each location, wind sensors are sited at the National Weather Service standard height of 10m. Equipment Specifications, maintenance standards, and data analysis procedures conform with requirements of NRC Regulatory Guide 1.23, National Weather Service protocols, and quality requirements of EPA QAMS 005/80. Details on these requirements are available in consultation with NOAA.

2.3.4 Diffusion Estimates

This section presents the preliminary dispersion modeling performed by NOAA ARLFRD for the proposed INEEL TMI-2 ISFSI project sources. Total integrated concentrations for two different spatial scales were calculated using normalized emission rates and up to four different sets of meteorological data to simulate the release and dispersion of pollutants from the proposed INEEL TMI-2 ISFSI facility. Regional scale modeling using a variable-trajectory Gaussian puff model (MESIDIF) was performed to determine the spatial and temporal variations in the normalized concentration patterns. A

single sector-averaged Gaussian plume model (XOQDOQ) was used to compare regional and local impacts [2.11].

Single Station Modeling - XOQDOQ

The computer program XOQDOQ is used by the Nuclear Regulatory Commission (NRC) in its independent meteorological evaluations of continuous and anticipated intermittent releases from commercial nuclear power reactors. The program implements the assumptions outlined in Section C (excluding Cla and Clb) of NRC Reg. Guide 1.111. Annual relative effluent concentrations, X/Q, and annual average relative deposition, D/Q, are calculated at user specified locations, and at various standard radial distances and segments for downwind sectors. Evaluations of possible intermittent (e.g., containment or purge) releases which occur during routine operation may also be evaluated using the program. Evaluation of intermittent releases provides both X/Q and D/Q values at various standard locations, as well as user-specified points of interest.

Model Operational Theory

XOQDOQ is based on the theory that material released to the atmosphere will have a normal (Gaussian) distribution about the plume centerline. In predicting concentrations for longer time periods, the Gaussian distribution is assumed to be evenly distributed within the directional sector. A straight-line trajectory is assumed between the point of release and all receptors.

The plume rise equations used in XOQDOQ are taken from Briggs, [2.12], and [2.13]. Plume rise is calculated as a function of stability. Effective plume height is then given as the sum of plume rise and the physical stack height.

For a specific receptor and source configuration, a long-term estimate of X is obtained by solving the dispersion equation for each meteorological condition assigned by the user, then summing all such concentrations after weighting each by its frequency of occurrence.

The sum of the frequencies for each long-term analysis (e.g., seasonal or annual) should be very near unity. A one-hour occurrence of a particular meteorological condition will be included in an annual joint frequency distribution as (1 h/yr)/(8760 h/yr) = 0.00011, and in a seasonal (quarter annual) array as 0.00045.

The representative speeds usually assigned to the six climatological wind speed categories (0-3, 4-6, 7-10, 11-16, 17-21 and 21 knots), are 0.67, 2.45, 4.47, 6.93, 9.61, and 12.52 m/s. These ranges are user-specified.

The horizontal and vertical dispersion parameters (sigma y and sigma z) used in XOQDOQ are in the form of continuous functions of downwind distance and stability.

XOQDOQ allow specifications of sigma y and sigma z from measured curves obtained from actual field studies at INEEL. The main advantages of using this approach are (a) the stability classification scheme may be used on easily obtained parameters and (b) the relationships of sigma y and sigma z under low windspeed, inversion conditions are

allowed to depart from a power law function, and thus make the results more realistic. This option was exercised in the computer analyses presented in this section. The curves are presented in Figures 2.3-19 and 2.3-20. Model operational theory is described at length in Sagendorf, et al,[2.11].

The six stability categories (S = 1 through 6 in order of increasing atmospheric stability, 4 being neutral) of the joint frequency distribution are defined on the basis of the criteria stated by Turner, 1961 and 1970. The classification is based upon ground-level meteorological observations only (surface wind speed, cloud cover, ceiling), supplemented by solar elevation data (latitude, time of day, and the time of year). Thus the stability estimates can be obtained for any site at which suitable observations have been made.

Modeling Assumptions and Input Data

Four XOQDOQ runs were made to examine the relationship between local and regional concentration patterns. Two spatial scales were used: zero to five miles from the source and zero to fifty miles from the source. The INEEL TMI-2 ISFSI site was examined for each scale. Meteorological conditions the INEEL TMI-2 ISFSI site were represented by the joint frequency distribution of 1982 wind and stability data from the telemetry station at the Power Burst Facility (PBF) as a worst likely situation.

XOQDOQ has several options which may be exercised when executing the program. Table 2.3-19 [2.5]. summarizes the options used in previous modeling for the site.

Results

Annual normalized concentrations calculated by XOQDOQ are presented in Figures 2.3-21 and 2.3-22 [2.5]. Overall concentration patterns consist of bimodal distributions extending along the annual prevailing wind directions (approximately southwest and northeast).

Figure 2.3-21 presents the concentration isopleths out to a 50-mi radius due to normalized emissions from the INEEL TMI-2 ISFSI site. The concentration pattern exhibits a strong southwest to northeast distribution with very little buildup in the northwest-southeast direction, except for a small tertiary lobe toward the south-southeast.

Figure 2.3-22 presents the concentration isopleths out to a radius of five miles from the normalized emission source at the INEEL TMI-2 ISFSI site. Again, there is a bimodal distribution with major axis along the direction from southwest to northeast. The case exhibits a slightly wider concentration distribution at the northern lobe. The tertiary lobe extending toward the southeast is much less developed on this spatial scale. Note the maximum concentration area centered about one-half mile northeast of the source. This feature was not evident on the regional scale (50-mi radius).

Gridded Windfield Modeling - MESODIF

MESODIF Model Description

MESODIF is a regional-scale variable-trajectory Gaussian puff model developed at NOAA's Air Resources Laboratory at the INEEL [2.14]. It is designed to take into account the spatial and temporal variations in the advection, diffusion, transformation, and removal mechanisms governing plume dispersion. It differs from the conventional Gaussian plume approach in that MESODIF simulates the deformation of a continuous plume by a time varying, vertically-uniform horizontal wind field. MESODIF simulates a continuous point source by super positioning discrete puffs of a circular, horizontal cross-section. Each puff is advected as a element with its time history independent of preceding or succeeding puffs. The dimensions of an individual puff are proportional to its travel distance (or travel time). The representation of a continuous plume is by the serial releasing of sufficient numbers of discrete puffs (finite plume segments). With suitable choices of input parameters, MESODIF can reproduce the results of a conventional Gaussian plume model in the near field from a source. Since its initial formulation, MESODIF has been modified by others and offered by EPA as one of the Users Network of Applied Models for Air Pollution (UNAMAP) Version IV Series under the name MESOPUFF.

A continuous point source (CPS) is often used to examine the effects of spatial and temporal variations of the low-altitude wind flows upon time-integrated concentration estimates. Because the transporting regional wind surrounding the INEEL TMI-2 ISFSI site exhibits curving, recirculating, and at times stagnating flows, a Gaussian simple CPS type of equation could not be used in MESODIF (because the resulting plume geometry would be inapplicable). Because the CPS equation is an integration of the more general Gaussian instantaneous point-source (IPS), this IPS equation is the beginning point for MESODIF.

The sigma values used in MESODIF are the Pasquill A through F stratifications of values which were measured from continuous plume releases of 1/2- to l-h duration. The application of these rates to puff diffusion tends to slightly overestimate the dilution (and to underestimate the concentration) of puffs within the first few kilometers. It should be noted that the specifications of sigma values versus stability categories and trajectory distances primarily apply to distances of a few kilometers. Extrapolation of these curves to regional scale distances has been accomplished in several INEEL field studies.

In application, the MESODIF model disperses plume effluent through the advective transport of puff centers and through the diffusion of effluent puffs about their individual centers. The transport of puffs is determined from a horizontal field of spatially and temporally varying winds.

For vertical dispersion, a capping stable layer or restricting lid to upward diffusion is considered. The height of the base of the capping lid or stable layer is denoted as "L". In

MESODIF, L is specified each hour to account for known diurnal variability of the depth of mixing. An hourly value of L is applied uniformly throughout the computation area.

The source emission strength Q may be specified each hour if desired. For the INEEL TMI-2 ISFSI site analysis, it has been held constant at one unit per hour; each puff then contains one unit divided among the number of puffs released per hour. Removal mechanisms, such as dry deposition, precipitation scavenging, and chemical and photochemical changes, are not incorporated.

The two essential parts of the computation are the determination of the locations of the puffs as they are carried by the wind, and the calculation of the growth and subsequent dilution of each puff. A third portion of the computation involves the determination of the contribution of the puffs to the time-integrated dosage on any array of grid points. The concentration is computed and accumulated for each grid point which lies within the radius of influence of each puff.

MESODIF Modeling Assumptions and Input Data

A series of MESODIF runs were made to examine the spatial and temporal variations that would occur in the normalized concentration patterns for various source locations and for different periods of meteorological data. INTEC was modeled using MESODIF, normalized emission rates, surface releases, and a gridded meteorological data set for 1980. 1981, and 1982 [2.5]. Also, a long-term average of ten years of gridded data has been used to produce annual long-term mean concentrations for the period (1974 - 1983). For the INTEC source location the 1974-1983, 1980, 1981, and 1982 data sets were used. Key input parameters for the MESODIF modeling are summarized in Table 2.3-20 [2.5].

MESODIF Results

Figures 2.3-23 through 2.3-26 [2.5] present isopleths of annual normalized total integrated concentration calculated by MESODIF. Concentration patterns overall are quite similar for all meteorological years and emission source locations. They show a bimodal distribution with lobes extending along the annual prevailing wind directions for this area (southwest and northeast) and a rapid decrease in concentration with distance.

Figure 2.3-23 presents concentration isopleths for normalized emissions from the INEEL TMI-2 ISFSI site with 1980 meteorological data. The concentration pattern exhibits all of the general characteristics identified above. In addition, there is evidence of a minor tertiary concentration lobe extending toward the southeast. Figure 2.3-24 presents concentration isopleths for normalized emissions from the INEEL TMI-2 ISFSI site with 1981 meteorological data. Again, concentration patterns are similar to 1980 with slightly less development in the tertiary lobe. Concentration isopleths due to normalized emissions from the INEEL TMI-2 ISFSI site, calculated using 1982 meteorological data, are presented in Figure 2.3-25. Concentration patterns are similar to the other two years but the magnitude of the concentrations appears somewhat lower in 1982. This is evident in the area enclosed by the isopleths. For 1982, the area enclosed by a line of given

magnitude is generally smaller in 1982 than in 1980 or 1981, indicating that low concentrations occur closer to the source in 1982 than in either 1980 or 1981.

Figure 2.3-26 presents the ten-year mean concentration isopleths for normalized INEEL TMI-2 ISFSI emissions calculated using the 1974-1983 meteorological data set. These long-term mean isopleths exhibit all of the general characteristics shown by the isopleths for each individual year. The long-term mean isopleths are most like the isopleths calculated using 1982 meteorology in spatial distribution -- the southwest-northeast extensions dominate, there is little tertiary lobe development, and the maximum concentration areas near the source are more confined and localized than in the other study years. Thus, it appears that the 1982 meteorological data set used in the INEEL TMI-2 ISFSI site modeling is most representative of long term meteorological patterns.

Conclusions

Several general conclusions pertaining to regional modeling exercises are indicated by comparing the XOQDOQ and MESODIF analyses:

- For short-term (accidental) releases, the greatest shortcoming of XOQDOQ is its failure to accurately describe the effluent trajectory, and the subregion which would be affected within the spatially variable winds at INEEL. MESODIF's annual average or multiyear total integrated concentration patterns are significantly broader than XOQDOQ's. This is a result of XOQDOQ's inability to incorporate short term wind variabilities in the long term average.

- Beyond 15-30 mi, XOQDOQ overestimates annual total integrated concentrations by about an order of magnitude. The inability of XOQDOQ to accommodate time changes in stability category during effluent transport is the single most influential factor in this bias.

- Because MESODIF more realistically simulates recirculations and stagnation which occur at INEEL, pockets of elevated concentration about 4.5 times the XOQDOQ value are indicated during short term MESODIF modeling.

- The bimodal distribution for annual concentrations is stable from year to year, and for multiyear averages. Therefore, the meteorological data for 1982 is deemed representative of the long-term mean weather patterns.

- Normalized concentration magnitudes for sources at different locations are very similar; some differences in annual isopleth pattern forms are evident. These differences increase when shorter (episode) time periods are considered.

- MESODIF is based on a wind and concentration calculation grid of finite size such that resolution at subgrid scales (about five miles as configured for this analysis) is not possible. XOQDOQ can economically simulate dispersion at that distance scale.

2.4 Suface Hydrology

The following sections discuss the hydrology of the region, area, and site as it pertains to the safe design and operation of the INEEL TMI-2 ISFSI.

2.4.1 Hydrologic Description

Most of the INEEL and all of Idaho Nuclear Technology and Engineering Center (INTEC), where the INEEL TMI-2 ISFSI will be located, is in the Pioneer Basin. The Pioneer Basin is a closed topographic depression on the Snake River Plain that receives intermittent runoff from the Big Lost River, Little Lost River, and Birch Creek drainage basins (Figure 2.4-1). The Pioneer Basin is not crossed by any perennial streams because of the permeability of alluvium and underlying rock of the basin, which causes the water to infiltrate into the ground. In addition, much of the water from the tributary drainage basins is diverted for irrigation upstream of the INEEL. The largest stream, the Big Lost River, enters the INEEL near the southern end from the west and, during exceptionally wet years, flows in a large arc north to the foot of the Lemhi Mountain Range, where it ends in a series of playas (sinks). The only other naturally occurring stream on-site is Birch Creek, which enters from the north. This stream is usually dry, except during heavy spring runoff when water may flow onto the INEEL. The Little Lost River approaches the INEEL from the northwest through Howe and ends in a playa just off the INEEL site.

The Big Lost River is the most important element affecting the surface water hydrology of the INEEL and INTEC (Figure 2.4-2). The Big Lost River discharges an average of 260.2 E+06 m^3/y (211,000 acre<ft/y) below Mackay Dam, 48 km (30 mi.) northwest of Arco [2.15]. The largest recorded annual flow of the Big Lost River for the entire period of record occurred in 1984 and amounted to 587.1 E+06 m^3/y (476,000 acre<ft/y), which was measured below Mackay Dam. The second largest annual flow occurred in 1965 and amounted to roughly three quarters of the 1984 record [2.16].

Other than these intermittent streams, playas, and manmade percolation, infiltration, and evaporation ponds, there is little surface water at the INEEL site. Surface water that reaches the INEEL is not used for consumptive purposes (e.g., irrigation, manufacturing, or drinking). In addition, there are no future uses of surface water that reaches the INEEL that have been identified.

2.4.1.1 Site and Structures

The location and description of the INEEL TMI-2 ISFSI (presented in Chapters 1 and 2 of this SAR) include figures showing the general arrangement, layout and relevant elevations. (Note: see Figure 2.6-9 for regional topographic map, Figure 2.6-39 for area topographic map). The INEEL TMI-2 ISFSI will be located within the INTEC on the

INEEL. The northwest boundary of INTEC is closest to the Big Lost River channel, approximately 16 m (200 ft). This is near the point where the channel intersects with Lincoln Boulevard on the INEEL. The INEEL TMI-2 ISFSI will be located in the southern portion of INTEC, about 850 m (2,800 ft) from the channel. The INEEL TMI-2 ISFSI pad surface elevation will be 1,498.7 m. (4,917 ft.) or approximately .3 to .45 m. (12-18 in.) above the existing ground surface. Fill material will be placed around the elevated pad to provide for positive drainage of runoff away from the pad and ISFSI. This fill material will be placed so as to transition back to the existing contours within approximately 10 m (32.8 feet) of the pad. Runoff will be diverted to the existing INTEC storm drain system that is designed to accommodate peak runoff rates from the 25-year/24-hour storm. Due to the limited area where this fill material will be placed (Figure 2.4-3) and the distance to the existing INTEC drainage structures [further than 30 m. (98.4 ft.)], the fill material will not modify this existing INTEC stormdrainage system.

2.4.1.2 Hydrosphere

Streamflows from the Little Lost River and Birch Creek very seldom reach the INEEL and would have no effect on the INEEL TMI-2 ISFSI as they are far to the north (Figure 2.4-1). The Little Lost River drains the slopes of the Lemhi and Lost River ranges. Water in the Little Lost River is diverted seasonally for irrigation north of Howe, Idaho, and does not flow onto the INEEL. Birch Creek originates from springs below Gilmore Summit in the Beaverhead Mountains and flows in a southeasterly direction onto the Snake River Plain. The water in the creek is diverted north of the INEEL for irrigation and hydropower purposes. In the winter months when the water is not being used for irrigation, flows are returned via a man-made channel to the main Birch Creek channel within the INEEL boundary. The channel leads to a gravel pit near Playa 4, approximately 6.4 km (4 mi.) north of Test Area North (TAN), where it infiltrates the channel and gravel pit bottom recharging the Snake River Plain Aquifer.

The Big Lost River is the principle natural surface water feature on the INEEL and the only stream with potential impacts to the INEEL TMI-2 ISFSI as described in Section 2.4.2 “Floods.” The Big Lost River flows southeast from Mackay Dam, through the Big Lost River Basin past Arco, Idaho, and onto the Snake River Plain. Stream flows are often depleted before reaching the INEEL by irrigation diversions and infiltration losses along the river. When flow in the Big Lost River reaches the INEEL, it is either diverted to the flood diversion facilities (FDF) or flows northward across the INEEL in a shallow, gravel-filled channel to its terminus in the Big Lost River playas where its flow is lost to evaporation and infiltration recharging the Snake River Plain Aquifer. For monthly discharge of the Big Lost River at Lincoln Boulevard near the INTEC see Table 2.4.1.

Major control on the Big Lost River upstream of the INEEL TMI-2 ISFSI site include the mackay Dam and the INEEL FDF each of which is discussed in greater detail below.

MACKAY DAM

Mackay Dam, located about 45-mi (48-km) upstream from the INEEL, impounds water from the Big Lost River for irrigation purposes downstream. Mackay Dam is a 1,430 ft (433 m) long, 79 ft (24 m) high earthfill dam built for the Big Lost River Irrigation District. The dam was completed in 1917 and has a storage capacity of 44,500 acre-ft (5.0E+07 m^3) and surface area of 1,241 acres (502 hectares) at a water surface elevation of 6,066.5 ft (1,849 m) (Table 2). An ungated overflow spillway with a weir length of 75 ft (23 m) at elevation 6,066.5 ft (1,849 m) msl is located near the west abutment of the dam. The spillway is designed for a discharge of 3,250 cfs (92 m^3/s) with 4 ft (1.2 m) of freeboard on the dam. The outlet works are also located near the west abutment and extend through the embankment and under the spillway to form an outlet channel. The outlet works consist of five motor-operated slide gates measuring 4 by 8 ft (1.2 by 1.4 m), mounted in an upstream control tower. The arched-roof outlet tunnel measures 10 by 10 ft (3 by 3 m), and reaches 500 ft (152 m) downstream into a 10-ft (3 m) diameter steel pipe, which extends to the outlet. At the outlet, the pipe branches into six 4-ft (1.2 m) diameter pipes emptying into a stilling basin at the toe of the dam. The total discharge capacity of Mackay Dam is less than 10,000 cfs (283 m^3/s). Water from the Big Lost River is impounded for the irrigation of about 57,500 acres of land downstream from the reservoir and for recreational opportunities. Another 10,200 acres of land upstream from the reservoir are also irrigated with Big Lost River water.

INEEL FLOOD DIVERSION FACILITIES (FDF)

The INEEL FDF include a diversion dam, dikes, and spreading areas located about 16 km (10 mi.) upstream from INTEC. The FDF was constructed in 1958 and enlarged in 1984 to reduce the threat of flood on the INEEL from the Big Lost River. The FDF controls or divides the flow in the Big Lost River between the spreading areas to the south and the playas to the north where the water can be temporarily stored until it infiltrates into the ground and, thus, avoid flows of flood size past the INTEC and other INEEL facilities. The spreading areas (A, B, C, and D) and the playas (1, 2, 3, and 4) are shown in Figure 2.4-1. The FDF has an elevation between 1533.1 and 1543.7 m (5030 and 5064.7 ft) msl; the INTEC lies at about 1498.7 m (4917 ft) msl, and the playas located about 28.9 km (18 mi.) downstream from INTEC, lie between about 1456.9 and 1460.0 m (4780 and 4790 ft) msl.

The FDF's diversion dam consists of a small earthen diversion dam and headgate that diverts water from the main channel, through a connecting channel, and into a series of four natural depressions, called spreading areas. Flow in the diversion channel is uncontrolled at discharges that exceed the capacity of the culverts. The diversion channel is capable of carrying 204 m^3/s (7,200 cfs) from the Big Lost River channel into the spreading areas. Two low swales located southwest of the main channel will carry an additional 59 m^3/s (2,100 cfs) for a combined diversion capacity of 263 m^3/s (9,300

cfs)[2.17]. The capacity of the spreading areas is about 7.2E+07 m^3 (58000 acre-ft) at an elevation of 1,530 m (5,050 ft) msl [2.18]. An overflow weir in spreading area D allows water to drain southwest, off the INEEL. Runoff from the Big Lost River has never been sufficient to exceed the capacity of the spreading areas and overflow the weir [2.19]. Gates placed on two 1.8 m (6 ft) diameter corrugated steel culverts control flow downstream onto the INEEL. At full capacity the culverts are capable of handling up to 25.5 m^3/s (900 cfs) of flow through the diversion dam downstream onto the INEEL [2.20]. See Table 2.4-2 for Mackay Dam and INEEL Diversion Dam reservoir characteristics.

As stated above, there are no users of the surface water which reaches the INEEL.

2.4.2 Floods

Since this site is not a flood-dry site, as defined in ANSI/ANS-2.8-1984, the following analysis is presented

2.4.2.1 Flood History

A study of recorded discharge data from several U.S. Geological Survey streamflow stations along the Big Lost River upstream of the INEEL suggests a history of low-magnitude floods [2.21]. Flooding in the basin is associated with peak flows during the snowmelt season and occasional flooding caused by ice jams in the stream channel. Big Lost River flows seem to be attenuated due to the gravels, deep alluvium and permeable basalt found in the channel bed. These streamflow losses, combined with controlled streamflow, diversion canals, and irrigation use, impact the natural flood peaks significantly. Downstream on the INEEL, the local semi-arid climate, relief and geology combine to regulate local runoff. Local flooding in the past has been associated with unseasonably warm temperatures and rain on frozen ground as the following local flood history describes.

Flooding in 1965**.** A record snowpack occurred in the Big Lost River basin in the winter of 1964-65. The maximum runoff occurred in late June. The Mackay Reservoir was full, and most of the runoff was passed on down to the basin and through the FDF on the INEEL. During the flood peak, June 29, 1965, approximately 51 m^3/s (1,800 cfs) were diverted to the spreading areas from a peak flow of 62 m^3/s (2215 cfs) [2.22]. The Big Lost River overflowed its banks above Arco through most of June. On the INEEL, the flood was controlled by the FDF and by the storage and infiltration in the river channels, playas, and sinks [2.23]. The water did not reach the end of the Big Lost River channel at the Birch Creek playa during this flood. This flood is significant because it exhibited the largest crest and largest water volume to be discharged onto the INEEL in 65 years of record, yet caused no damage to INEEL facilities.

Flooding in 1984**.** High streamflows in the Big Lost River and a severe cold spell during the winter of 1983 to 1984 caused ice jams that imposed a danger of localized flooding. Ice buildup in Spreading Area A (Figure 2.4-2) resulted in waters backing up in the diversion channel and ultimately threatening to overtop Dike 1. The high streamflows in the Big Lost River in 1983 and 1984 were largely the result of the Borah Peak earthquake of October 28, 1983. The earthquake created new springs upstream of Mackay Reservoir which increased the inflows to the reservoir significantly. Outflows from the reservoir were also increased to reduce the storage behind the dam. In response to this flood threat, upgrades to the Diversion Area were made to provide additional flood control, increasing the diversion channel flow capacity of 71 m^3/s (2,500 cfs) to over 255 m^3/s (9,000 cfs) Downstream INEEL facilities were not threatened or damaged by this accumulation of ice in the diversion channel.

Generally during the winter months there is no flow in the Big Lost River downstream on the INEEL, however if there is nearly all flow is diverted to the FDF to avoid the accumulation of ice in the main channel, reducing the possibility of flooding downstream. In review of the historical information, no flooding or inundation from storms or runoff has caused flooding of the INEEL TMI-2 ISFSI site.

2.4.2.2 Flood Design Considerations

As identified in Section 3.2.2 of this SAR, the top of the INEEL TMI-2 ISFSI pad is designed to be at or above the PMF flood elevation to ensure that the HSMs are not subjected to any flood loading throughout their lifetime.

2.4.2.3 Effects of Local Intense Precipitation

As discussed in Section 2.4.3, a bounding flood scenario to determine the adequacy of flood protection for the INEEL TMI-2 ISFSI is the overtopping failure of the Mackay Dam due to a general storm PMP. A detailed discussion of this general storm PMP may be found in Section 2.4.3.1. The INEEL TMI-2 ISFSI site is at or above the extent of floodwaters (4917' msl) predicted for this hypothetical dam failure scenario.

Normal rainfall is generally higher in the mountains to the west than it is in the Pioneer basin. For average, highest, and lowest total monthly and annual precipitaion at CFA from January 1950 to December 1988, see Table 2.4-3. The frequency of occurrence of thunderstorms is low on the INEEL and the total amount of rain generated during a thunderstorm is usually relatively small due to the arid climate of the Snake River Plain.

2.4.3 Probable Maximum Flood (PMF) on Streams and Rivers

The PMF represents the hypothetical flood that is considered to be the most severe flood event reasonably possible, based on hydrometeorlogical application of maximum precipitation and other hydrologic factors. The PMF may be caused by either an unusually severe storm or some catastrophic event, such as a dam failure. For conservatism in safety and design, a PMF induced overtopping failure of the Mackay Dam caused by an extreme precipitation event, the general storm PMP, is the bounding scenario used for INEEL facilities. Figure 2.4-4 represents the PMF hydrograph and Figure 2.4-5 is the inundation map for the PMF-induced failure of the Mackay Dam. Table 2.4-4 provides information on the peak water surface elevation, peak flow, water velocity, and time of arrival at several downstream locations for this dam failure scenario.

2.4.3.1 Probable Maximum Precipitation

The general storm PMP for the drainage basin above Mackay Dam resulted from a 48 hour general storm in June, preceded three days in time by an antecedent storm with a magnitude of 40% of the 48 hour storm [2.24]. This scenario provides for no flow losses to the ground in order to be conservative and represent situations in which the ground may be frozen or fully saturated. The peak flow for the PMF is 82,100 cfs, occurring 154 hr after the beginning of the storm. The PMF estimate falls within the 50,000-200,000 cfs Myers envelope curve used by the U.S. Army Corps of Engineers. The PMF peak flow is almost 20 times higher than the highest flow of 4,420 cfs recorded at Howell Ranch, a USGS station located approximately 17 mi. northwest of the dam. The PMF is based on the maximum potential for critical hydrometeorlogical conditions to occur, not on probabilities or historical flood frequencies.

2.4.3.2 Precipitation Losses

The Big Lost River leaves the mountains at Arco. Below this point, the topography and drainage characteristics change along the river. The area is a low, flat plain with basalt bedrock. The drainage from most of the area in Pioneer Basin is integrated with the Big Lost River. Locally, some depressions in the basalt receive intermittent runoff. There is seldom enough precipitation in this area to exceed the infiltration capacity of the soil to create intermittent streams to the Big Lost River.

2.4.3.3 Runoff Model

The combined Big Lost River Basin and Pioneer Basin range in elevation from 1454.1 m (4784 ft) to over 3829.8 m (12,600 ft) msl. Thus, this area has over 2130 m (7000 ft) of relief, resulting in large differences in temperature and climate at any given time. The low land in the Pioneer Basin is subjected to periods of warm wind, rain, and snowmelt during the winter months. These conditions cause runoff and minor flooding in the lower basins during regional storms and substantially increase the snowpack in the uplands. The largest documented runoff periods in the lower parts of the basins have occurred in January, February, or March; the maximum runoff from the highlands is usually in May or June. Generally, frost leaves the ground in the Pioneer Basin and the valley floors of the

mountains basins in March or April; the permeable soils and gravels can then accept surface water by infiltration before the bulk of the snow pack starts to melt. Most surface water reaching the Pioneer Basin from the tributary drainage basins eventually infiltrates beneath the soil and rock to the groundwater reservoir. The remainder is lost through evaporation.

2.4.3.4 Probable Maximum Flood Flow

The spillway of Mackay Dam is not adequate to pass the PMP safely, therefore overtopping and subsequent breaching of the dam due to this PMP storm were analyzed. During this overtopping failure, the inflow is sufficient to raise the water surface above 6,077 ft (1,852 m) msl, 1 ft (0.3m) above the crest of the dam. A trapezoidal breach was assumed to develop over a 1-hr period and extend to the base of the dam. The computer code DAMBRK, developed by the National Weather Service, was used in the flood-routing analysis [2.24].

The peak flow resulting from the PMP-induced overtopping failure is 306,700 cfs in the reach immediately downstream of the Mackay Dam (Table 2.4-4). This peak flow attenuates to 71,850 cfs at the INEEL Diversion Dam and to 66,830 cfs at INTEC. The flood wave reaches the INEEL Diversion Dam in 10 hr. Water velocities are approximately 1 to 3 ft/s downstream on the INEEL.

2.4.3.5 Water Level Determinations

The computer program DAMBRK identified the water levels at specified locations for the PMF-induced overtopping failure [2.24]. Peak water surface elevations, flow, velocity, and time of arrival are identified in Table 2.4-4.

2.4.3.6 Coincident Wave Activity

The wind activity at the INEEL coincident with the largest projected flood crest could not produce waves that would exceed 0.2 m (0.5 ft) due primarily to the shallow depth of water surrounding most INTEC buildings [2.25]. Thus, the static and dynamic effects of wave activity would be negligible.

2.4.4 Potential Dam Failures (Seismically Induced)

Mackay Dam is classified as a "high hazard" dam by the State of Idaho [2.25a) with reference to the U.S. Army Corps of Engineers guidelines for safety inspection of dams [2.26]. This high hazard classification is based on the concentration of people and property downstream, the size of the dam, and its storage capacity, not on any aspect of the dam's current condition or operation.

Mackay Dam is located in a region of historical seismicity as evidenced by the 1983 Borah peak earthquake. The performance of the dam during this earthquake demonstrated the stability of the embankment during moderate ground motion. However, Mackay dam was built without any seismic design criteria therefore, a seismically-induced dam failure has been analyzed to determine potential impacts at the INEEL [2.24]. This analysis assumed a postulated seismic failure of Mackay Dam during an inflow to the reservoir equal to the 25-yr recurrence interval flood (peak flow 4,030 cfs). Because a seismic event may potentially disrupt a significant part of the dam's structure, the breech was assumed trapezoidal, extending to the bottom of the structure at 5,997 ft msl, and developing over 1-hr period. The peak flow from the seismic dam failure in the reach immediately downstream of the dam is 107,480 cfs (Table 2.4-5). This peak flow attenuates to 45,410 cfs at the INEEL Diversion Dam and to 39,080 cfs at the INTEC. The leading edge of the wave reaches the INEEL diversion dam in about 12 hours. Average water velocities on the INEEL are 1 to 3 ft/sec.

2.4.4.1 Reservoir Description

Mackay Dam, built in 1917, is a 433 m (1,430 ft) long, 24 m (79 ft) high earthfill dam built for the Big Lost River Irrigation District. Characteristics of the dam and reservoir are identified in Table 2.4-2. Water from the Big Lost River is impounded for the irrigation of about 23,270 hectares (57,500 acres) of land downstream from the reservoir and for recreational opportunities. Another 4,128 hectares (10,200 acres) of land upstream from the reservoir are also irrigated with Big Lost River water.

The INEEL flood diversion dam, located approximately 10.5 km (6.5 mi) downstream from the western INEEL boundary, was built in 1958 to divert flows from the Big Lost River to protect downstream facilities. Characteristics of the dam and reservoir are also identified in Table 2.4-2. Water from the Big Lost River is impounded for flood control.

2.4.4.2 Dam Failure Permutations

See discussion and results in Sections 2.4.3 and 2.4.4 for overtopping dam failure due to the PMP and a seismically induced dam failure, respectively. Other dam failure permutations examined include two hydraulic (piping) failures concurrent with a 100-year and 500-year inflow floods to the reservoir. The INEEL diversion dam would be overtopped by the floodwaters released from the failure of Mackay Dam. This overtopping of the INEEL diversion dam will contribute to the flooding downstream on the INEEL. The DAMBRK analysis assumes that the INEEL diversion dam begins to fail when flood waters reach 5,065 ft msl, an overtopping depth of 0.3 ft. Because of the small size of this dam, the breach is assumed to be fully developed after 0.1 hr, an essentially instantaneous failure. Characteristics of the four hypothetical dam failures analyzed are provided in Table 2.4-6.

2.4.4.3 Unsteady Flow Analysis of Potential Dam Failures

The flood from dam failure would initially travel down a valley between basalt flows. The initial velocity would be high near the failure, but the average velocity would decrease to approximately 1 ft/s near the FDF. Water entering the FDF from this flood is much less than the actual capacity of the spreading areas [2.24]. Water that bypasses the FDF would continue to spread out across the floodplain and have a peak water velocity of 2.7 ft/s at INTEC.

2.4.4.4 Water Level at the Installation Site

The worst evaluated flooding condition at the INTEC results from the failure of Mackay Dam due to the PMP storm. This would result in flood water within the INTEC controlled area up to 1,498.7 m. (4,917 ft). The existing undisturbed ground elevation of the INEEL TMI-2 ISFSI site is 1498.0 m (4914.7 ft) msl. Fill will be provided to elevate the ISFSI pad foundation to a level of 1,498.7 m. (4,917 ft) msl.

2.4.5 Probable Maximum Surge and Seiche Flooding

The INEEL, located on the Eastern Idaho Snake River Plain, is remote from major bodies of water. Therefore, effects from surge and seiche flooding are not potential natural phenomena.

2.4.6 Probable Maximum Tsunami

The Eastern Idaho Snake River Plain, on which the INEEL is located, is remote from major bodies of water. Tsunami flooding at the INEEL is not a potential natural phenomenon.

2.4.7 Ice Flooding

Ice flooding is not a threat at the INEEL because, during the winter months, flow of the Big Lost River is diverted to the FDF to avoid ice accumulation in the main channel downstream of the diversion dam. Possible ice jams upstream of the diversion dam are of no concern because overflowing of the banks at that location can cause no damage to the INTEC.

2.4.8 Flooding Protection Requirements

As identified in Section 2.4 of this SAR, to avoid all flood related loads on the HSM, the ISFSI base slab will be constructed at or above the MPF elevation. This will ensure that the HSMs are not subjected to any flood loading throughout their lifetime.

2.4.9 Environmental Acceptance of Effluents

There are no liquid effluents associated with the operation of the INEEL TMI-2 ISFSI.

2.5 Subsurface Hydrology

The Snake River Plain Aquifer serves as the water supply source for the region. A description and discussion of this aquifer provide the essence of the INEEL subsurface hydrology. The INEEL geohydrology and the INEEL TMI-2 ISFSI site geohydrology have very similar characteristics and are interrelated; therefore, the INEEL geohydrology is presented in this section to provide a broader picture.

2.5.1 Regional Characteristics.

The Snake River Plain Aquifer is a continuous body of groundwater underlying the INEEL and nearly all the eastern Snake River Plain (Figure 2.5-1). The aquifer is about 321.9 km (200 mi) long by 48.3 to 96.6 km (30 to 60 mi) wide and is composed of a series of basalt flows 3.1 to 22.9 m (10 to 75 ft) thick with interbedded layers of fluvial, lacustrian, windblown, and pyroclastic sediments. Most of its permeability occurs along the upper and lower contacts of successive basaltic flows, which have large and irregular fractures, fissures, and other voids. These discontinuities lead to a large degree of heterogeneity and anisotropy in the hydraulic properties of the aquifer.

Most of the INEEL lies within a topographic depression on the Snake River Plain. The Big Lost River, entering the depression from the southwest, is the only significant natural recharge to the aquifer on the INEEL (see section 2.4). All Big Lost River water entering the INEEL (minus evaporation losses) is recharged to the Snake River Plain Aquifer. A small amount of recharge occurs from infiltration of precipitation directly on the INEEL. In some years of high runoff, Birch Creek water flows onto the INEEL and seeps underground.

Groundwater in the aquifer generally flows from the northeastern recharge areas to the southwestern discharge areas (Figure 2.5-1). Nearly 8017.7 E+06 m^3 (6.5 E+06 acre-ft) of water is discharged by the aquifer annually. Most of the discharge occurs as spring flow between Hagerman and Twin Falls (Figure 2.5-1). About 2590.3 E+06 m^3 (2.1 E+06 acre-ft) of irrigation water are pumped from the Snake River Plain Aquifer in a typical year. About half of this water reenters the ground as return flow to the aquifer.

The altitude of the regional groundwater surface underlying the INEEL ranges from about 1402.1 m (4600 ft) in the north to about 1341.1 m (4400 ft) near the southwest boundary of the INEEL. The average hydraulic gradient slopes to the south and southwest on the INEEL at about 1.9 m per km (10 ft per mi) (Figure 2.5-2). Due to the large volume of water and the hydraulic gradient reversing of the aquifer flow is highly unlikely. Within the INEEL boundaries, the depth below the land surface to the

regional groundwater table ranges from 61 m (200 ft) in the northeast to 274.3 m (900 ft) in the west-southwest.

The Snake River Plain Aquifer is the only source of water used at the INEEL. Figure 2.5-3 shows all wells where water withdrawal is occurring within 8 km (5 miles) of the TMI-2 ISFSI. The combined groundwater withdrawal averages approximately 9.7 E+06 m^3/y (7 E+06 gal/day) or 8,000 acre-ft/y.

Table 2.5-(x) lists the INEEL production wells, the depth of the well, the depth to water at the well, and the annual volume of water withdrawn from each well. All wells withdraw water from the main body of the Snake River Plain Aquifer. The water withdrawn from each well is used for potable water on the Site, for ground maintenance, and necessary facility operations.

The underflow (i.e., that amount of water passing directly under the INEEL boundaries) of the INEEL is approximately 1.8 E+09 m^3/y (4.7 E+11 gal/y); the consumption is less than 1% of the INEEL underflow and less than 0.1% of the total annual aquifer discharge.

The Snake River Plain Aquifer, one of the largest and most productive groundwater resources in the United States, underlies the INEEL. The aquifer is listed as a Class I aquifer and was designated by the EPA as a sole source aquifer in 1991. Groundwater from this aquifer supplies essentially all drinking water consumed within the Eastern Snake River Plain.

Irrigated agriculture provides a significant portion of the economic base for the people of southern Idaho, and the Snake River Plain Aquifer plays a major role in meeting irrigation requirements. The aquifer provides ground water for irrigation of over one third of the three million irrigated acres of the Snake River Plain. It is estimated that over 127,000 people depend on the aquifer for domestic and municipal water needs. Total domestic water consumption is approximately 46,000 ac-ft/yr and ground water discharge from well pumpage equals approximately 1.92 million ac-ft. [Ref. 2.203]

The
INEEL TMI-2 ISFSI will not use any groundwater.

2.5.2 Site Characteristics.

The depth to water in the INEEL TMI-2 ISFSI area is about 137.2 m (450 ft). Figure 2.5-3 shows the contours of the INEEL depth to the water table.

The transmissivity of the aquifer generally ranges from 1.3 E+04 to 1.2 E+08 m^3 per day per m (1 E+06 to 100 E+06 gal per day per ft (gpd/ft)). The average value for

transmissivity is 6.2 E+04 m^3/day per m (5 E+06 gpd/ft). Measured storage coefficients of the aquifer are highly variable both spatially and temporally, ranging from 0.001 to 0.2 and averaging 0.15. The effective porosity ranges from 5 to 10%.

Groundwater from the Snake River Plain Aquifer is very low in dissolved solids and is satisfactory for most purposes without treatment. The low dissolved-solids content reflects the abundant rain and snowfall in the surrounding mountains. The groundwater contains calcium and magnesium carbonate as the major dissolved solids. The groundwater has a pH range of 7.7 to 9.6 with a median of 8.01. [2.27]

Low levels of radioactive contamination are present in the groundwater near the INEEL TMI-2 ISFSI site. This contamination is due to past disposal of waste water using an injection well at INTEC. Since the use of the well was discontinued and the well was sealed, the contaminant levels have been dropping steadily. The major radionuclides in the contamination are tritium, strontium 90, and cesium 137.

The INEEL TMI-2 ISFSI will not have any monitoring wells. There are no groundwater recharge areas within the influence of the installation. Construction activities will be covered by the National Pollutant Discharge Elimination System (NPDES) Storm Water Pollution Prevention Plan for Construction Activities under the Clean Water Act.

The INEEL TMI-2 ISFSI will have no groundwater sources and so will not use any groundwater in operation. Small amounts of groundwater may be used in construction and these would come from existing wells.

2.5.3 Contaminant Transport Analysis

The INEEL TMI-2 ISFSI will be loaded with canisters which are not externally contaminated. The design precludes leaking, so no contamination to the outside of the facility is expected. To reach the groundwater any contamination would have to travel through 450 feet of soil column. No contamination will reach the groundwater.

Although many contaminant analyses have been performed following the movement of the existing contamination a transport analysis is not included due to the very low probability that any contamination would be released.

2.6 Geology and Seismology

2.6.1 Basic Geological and Seismological Infromation

2.6.1.1 Regional Geology.

2.6.1.1.1 Physiographic Provinces and Geomorphology

INEEL is located on the eastern Snake River Plain (ESRP). The ESRP is the eastern part of the Snake River Plain physiographic province (Figure 2.6-1), a broad low-relief basin floored with basaltic lava flows and terrigenous sediments [2.28; 2.29; 2.30; 2.31; 2.32; 2.33]. It is about 80 to 100 km wide and over 560 km long. It extends in a broad arc from the Idaho-Oregon border on the west to the Yellowstone Plateau on the east. It transects and sharply contrasts with the mountainous country of the Northern Basin and Range province and the Idaho batholith (Figure 2.6-2). Surface elevations on the Snake River Plain decrease continually and gradually from about 2000 meters near Yellowstone to about 650 meters near the Idaho-Oregon border [2.34]. Summits of mountains surrounding the Plain range up to 3700 meters in elevation, producing a maximum elevation contrast of about 2300 meters.

The northern Basin & Range province, which bounds the ESRP on the north, is comprised of north- to NW-trending mountain ranges (with peaks up to 3700 meters high) separated by intervening basins (1400 to 1600 meters in elevation) filled with terrestrial sediments and volcanic rocks. Individual mountain ranges in the vicinity of the Snake River Plain are up to 200 km long and 30 km wide. They are sharply separated from the intervening basins by late Tertiary to Quaternary normal faults [2.32]. The basins are 5 to 20 km wide and grade onto the ESRP.

The Yellowstone Plateau, which occurs at the northeastern end of the ESRP, is a high volcanic plateau underlain by Pleistocene rhyolitic volcanic rocks (Figures 2.6-1 and 2.6-2). Its elevation of about 2100 to 2600 meters is significantly higher than that of the ESRP but not as high as the mountain summits of the northern Basin-and-Range province. The Plateau is characterized by extremely high heat flow from the surface [2.35], very high temperatures at shallow depths [2.36], abundant hot spring, fumerolic, and geyser activity, and landforms controlled by thick rhyolitic lava flows [2.37]. These characteristics reflect the recency of volcanic activity in the area, 2 million years ago to several tens of thousands of years ago [2.37].

The Idaho Batholith, which adjoins the northern margin of the central Snake River Plain, is characterized by a large area of irregular mountainous terrain [2.38] with peaks ranging in elevation from 2400 m to 3700 m. Streams dissecting the area usually have dendritic

drainage patterns reflecting the homogeneous nature of the underlying granitic rocks that comprise the batholith (Figures 2.6-1 and 2.6-2).

The four physiographic provinces described here (the ESRP, the northern Basin-and-Range province, the Yellowstone Plateau, and the Idaho Batholith) also correspond to tectonic or seismo-tectonic provinces. Each province has a different seismogenic potential that is determined by the nature of its intrinsic tectonic processes. The nature and seismogenic potential of these tectonic processes is discussed in Section 2.6.2.2 - Vibratory Ground Motion.

2.6.1.1.2 Geologic History

2.6.1.1.2.1 Paleozoic, Mesozoic, and early Cenozoic History

The mountains northwest of the ESRP near INEEL are composed of thick sequences of late Precambrian through Pennsylvanian sedimentary strata (Figure 2.6-3). The Precambrian through lower Ordovician rocks are mostly clastic (shales, quartzites), whereas the upper Ordovician through Pennsylvanian rocks are mostly carbonates (dolomites, limestones). They occur within westward-dipping thrust sheets that formed during east-directed Mesozoic compressional tectonism [2.39; 2.40].

During the Paleozoic and Mesozoic eras, deposition of continental shelf carbonates (limestones and dolomites) occurred in a north-trending belt, which included southeastern Idaho, along western margin of the North American continent [2.41]. Thrust faulting accompanied the deposition of these sediments in Paleozoic time (Antler orogeny), at the Paleozoic/Mesozoic boundary (Sonoma orogeny), and again in Mesozoic/Cenozoic time (Sevier/Laramide orogenies). This thrust faulting produced the Idaho/Wyoming thrust belt (the Overthrust Belt) that extends through eastern Idaho (Figure 2.6-4). In early Cenozoic time, eastward-directed thrust faults and belts of deformation may have continued uninterrupted through southeast Idaho.

Large volumes of granitic rock were emplaced by igneous intrusion into the upper crust during Mesozoic and early Cenozoic thrusting to produce the Idaho Batholith in central Idaho (Figure 2.6-4). Subduction of the Pacific plate beneath the North American plate caused large-scale melting of lithospheric rocks all through the western Cordillera. In addition to the Idaho batholith, the Sierra Nevada batholith and other large granitic intrusive bodies were formed during this time.

In the early Cenozoic, northwest-southeast-directed extension produced the northeast-trending Trans-Challis fault zone and the associated Custer and Panther Creek grabens (Figure 2.6-5). Accompanying volcanism caused caldera subsidence along the trend of the grabens. Volcanic rocks of the Challis volcanic field, which covers much of south-central Idaho adjacent to the northwestern margin of the ESRP, were erupted from sources along the Trans-Challis zone and elsewhere in south-central Idaho.

2.6.1.1.2.2 Late Cenozoic and Quaternary History of the Yellowstone-ESRP Volcano-tectonic Province

The Yellowstone hotspot

The processes that caused development of the ESRP began about 17 million years ago. A rising plume of anomalously hot rocks in the earth's mantle (the Yellowstone hotspot) first impinged on the base of the lithosphere at that time. Since the mantle plume is rooted deep in the earth, probably at the mantle-core boundary, it has remained relatively stationary while the lithosphere and crust (North American plate) have shifted across it due to plate tectonic processes. At 17 million years ago the North American plate was positioned so that the area now located in north-central Nevada was directly above the hotspot. As plate tectonic activity has moved the plate southwestward at about 3.5 cm/year the hotspot has left its distinctive effects as evidenced by a braod crescent-shaped plain extending from its present position at Yellowstone National Park to north-central Nevada.

The effects of the hotspot on the lithosphere and crust have been profound. Two types of large-scale melting have occurred. 1. Melting of the hot mantle material in the rising plume itself generated basaltic melts (magmas) that migrated to mid-crustal levels (about 20 km depth). This melting was due to decrease in pressure on high temperature mantle material as it moved from great depth. 2. Melting of mid-crustal rocks produced granitic melts that migrated upward to near-surface reservoirs and caused widespread explosive and effusive rhyolitic volcanism typical of that at Yellowstone National Park. This melting was due to heating of mid-crustal rocks by the much hotter basaltic magmas that rose from the mantle plume.

The effects of the hotspot that can be observed at the surface of the earth today include widespread, large-volume sheets of rhyolitic volcanic rocks emplaced by explosive processes, large-volume rhyolitic lava flows, calderas from which the rhyolitic volcanic rocks erupted, elevated topography in the area directly over the hotspot due to buoyant effects of the hotspot, and the basin of the ESRP caused by subsidence as plate motion moved volcanic highlands southwestward from the hotspot.

Calderas from which the rhyolitic volcanic rocks erupted are typically 30 to 70 km across and resulted from foundering of the roof of shallow magma chambers as voluminous explosive eruptions occurred. As the roofs foundered into the evacuated magma chamber, the resulting depressions were filled with thick sequences of rhyolitic volcanic rocks. As the North American plate has migrated to the southwest across the Yellowstone hotspot, a string of calderas and volcanic fields has been formed in the wake of the hotspot (Figure 2.6-6). The subsidence of the surface due to crustal cooling along this string of volcanic fields has lead to the formation of the ESRP.

Another way to view the progression of hotspot-related rhyolitic volcanism is in a plot of age of volcanic rocks vs. distance from Yellowstone along the ESRP (Figure 2.6-7). This diagram shows that the beginning of rhyolitic volcanism becomes younger towards Yellowstone and that basaltic volcanism has covered most of the rhyolitic volcanic fields in the ESRP.

Modifications to crustal structure resulting from hotspot processes

In addition to large scale melting and volcanism described in previous sections, the crust beneath the ESRP was modified significantly by the melting processes associated with the hotspot. The crystallization of large volumes of basaltic magma in the mid-crust produced a roughly 10 km thick lens of anomalously dense rock that transmits seismic waves faster than the material above or below (Figure 2.6-8). The added weight of this material to the crust, along with the contraction due to cooling after passing over the hotspot, has caused the ESRP to subside in elevation by about 2 km during the past 4 million years.

Basalt volcanism and sedimentation in the subsiding ESRP basin

The subsidence of the ESRP has produced an elongate northeast-trending basin in which two types of materials have accumulated to a total thickness of 1 to 2 km. These two types of materials are: 1. basalt lava flows that were generated by residual heat in the upper mantle beneath the ESRP and that rose to the surface to erupt into the subsiding basin; and 2. deposits of sedimentary material that have formed interbeds between lava flows. The sediments are composed of fine-grained silts that were deposited by wind action, silts, sand, and gravels deposited by streams such as the Big Lost River, and clays, silts, and sands deposited in lakes such as Mud Lake and its much larger ice-age predecessor, Lake Terreton.

The accumulation of these two types of rocks in the ESRP has resulted in the observed sequence of interlayered basalt lava flows and sedimentary interbeds. Volcanism is a sporadic process. During the long periods of quiescence between volcanic periods, sediments accumulated to thicknesses of <1 m to >60 m. During short periods of volcanic activity, several lava flows commonly accumulated to thicknesses reaching several tens of meters.

2.6.1.1.2.3 Basin-and-Range Tectonic Activity

The Basin and Range province of the western United States (Figures 2.6-1 and 2.6-2) is a region of extending crust, high elevations, high heat flow, and extensive Cenozoic volcanism [2.42]. The north to NNW trends of normal faults and mountain ranges in the Basin and Range province, as well as various types of in-situ stress determinations [2.43], show that the area is subjected to east-west to northeast-southwest directed tension. In the northern Basin and Range, which is transsected by the ESRP, the extension produces

north-trending normal faults and mountain ranges on the southern side of the ESRP and north-west trending ones on the northern side. The mountain ranges are caused by a process called block faulting. As extension stretches the area the brittle upper crust (upper 10-16 km) can respond only by breaking into blocks that rotate slightly along the faults between to produce long, narrow mountain ranges with intervening basins (valleys).

The rugged topography and high elevations characteristic of these mountain ranges die out at the margins of the ESRP (Figure 2.6-2) and give way to the relatively flat and low-lying topography characteristic of the Plain. The activity on the normal faults that bound the ranges must also die out at the Plain margins, else the mountain ranges would continue across.

2.6.1.2 ISFSI Site Geology

2.6.1.2.1 Topographic and Physiographic Description

INEEL Area

The topographic relief of the ESRP is subdued with respect to the surrounding Basin and Range province. Total relief of the floor of the Plain in the INEEL area is about 200 m, ranging from 1460 m at Big Lost River Sinks to about 1650 m on the northeast trending axial ridge of the plain (Figure 2.6-9). Four prominent "buttes" occur along the axial ridge of the ESRP and they stand noticeably higher than the Plain. Big Southern Butte (2308 m), Cedar Butte (1776 m), Middle Butte (1948 m), and East Butte (2003 m) offer additional relief of 120 to 650 m above the axial ridge.

The axial ridge, known as the Axial Volcanic Zone [2.33], constrains the Snake River to the southeastern edge of the Plain and causes rivers from the mountains to the north of the Plain to drain into closed basins (sinks). The most prominent example is the Big Lost River, which flows onto the Plain near Arco, turns northeastward in the southwestern part of INEEL, and flows north to the Big Lost River Sinks in the northern part of INEEL. The Little Lost River and Birch Creek also empty into sinks (playas) in the northern part of INEEL.

In detail, much of the ESRP exhibits very rough, uneven topography due to the character of the numerous basalt lava flows that make up the surface. The topography is characterized by lobate forms, numerous steep-walled closed depressions and mounds, and anastomosing fissures. Erosional processes have not established classic drainage patterns; streams tend to be intermittent, wandering, and blind as they follow lava flow contacts and lava channels, commonly ending in closed depressions.

In many areas the lava flow topography is softened by deposition of windblown silt into fissures and depressions. In some areas, the silt deposition has been so great that the

topography is dominated by dune forms and rolling terrain with little or no basalt at the surface. Development of intermittent lakes and ponds in many closed depressions in the lava flow surface has resulted in deposition of fine silts and clays, producing small flat-floored playas [2.44].

ISFSI Site

The ISFSI site is located in a flat-lying area near the Big Lost River in the south central part of the INEEL (Figure 2.6-9). The area is underlain by about 9-18 m (30 to 60 ft) of Big Lost River alluvial silts, sands, and gravels, which lie on an alternating sequence of basalt lava flows and interbedded sediments extending to a depth of about 600 to 700 m. Landforms in the vicinity of ISFSI consist of braided channels (some abandoned) of the Big Lost River to the west and north of the site, and irregular flow lobes of basalt lavas to the east of the site.

2.6.1.2.2 Stratigraphy and Areal Geology

2.6.1.2.2.1 INEEL Area

Stratigraphy. Table 2.6-1 summarizes the thickness, age, distribution, characteristics, and origin of stratigraphic units on and near INEEL. During the past 4 million years, the ESRP, including the INEEL area, has experienced volcanic activity, mostly in the form of mild outpourings of basaltic lava flows. Vents for the basaltic volcanism are concentrated in northwest trending volcanic rift zones and along the Axial Volcanic Zone [2.33; 2.45] (Figure 2.6-10). Sediments deposited by wind action, streams and lakes have also accumulated in the ESRP, concurrent with the basaltic lava flows. Lithologic logs of four INEEL deep holes (>2000 ft deep) (Figure 2.6-11) [2.46, 2.47; 2.48; 2.33] and hundreds of shallower drill holes [2.44] show that an interlayered sequence of basalt lava flows and poorly consolidated sedimentary interbeds, known as the Snake River Group [2.34], occur to depths of 1 to 2 km beneath INEEL. This sequence is underlain by a large, but unknown thickness of Late Tertiary rhyolitic volcanic rocks.

Sedimentary interbeds within the Snake River Group are of diverse origins. These include silts deposited by wind action, silts, sands, and gravels deposited by streams such as the Big Lost River, and clays, silts, and sands deposited in playas and lakes such as Mud Lake and its much larger Pleistocene predecessor, Lake Terreton. All of these sedimentary processes continue to operate today, producing surficial deposits of alluvial, eolian, and lacustrine/playa origin.

The interlayering of unconsolidated and poorly consolidated sediments within the basalts has several implications for facilities at INEEL.

1. The interbedded sediments are composed mostly of fine-grained materials (silts and clays) which have very low permeability and high absorption capabilities [2.44].

Therefore they retard the downward migration of water and contaminants to the water table.

2. The low permeability of the sedimentary interbeds commonly causes localized perched water zones beneath some INEEL infiltration ponds [2.50] and beneath natural infiltration/recharge zones such as the Big Lost River channel and sinks at flood stage [2.49].

3. They can represent confining or semi-confining layers in the aquifer, thereby affecting the manner in which water (and contaminants) move vertically and horizontally.

4. The alternating high and low seismic velocities associated with basalts and poorly-consolidated sedimentary interbeds, respectively, causes greater-than-normal attenuation of earthquake strong ground motions [2.51, 2.52, 2.53].

5. The unconsolidated sands and clays intercalated within the hard, brittle basalts contribute to difficult drilling and downhole geophysical logging conditions, increasing the expense and time necessary for development of exploratory drill holes and monitoring wells at the INEEL.

Areal Geology. Surface rocks on and near the INEEL are mostly Quaternary basalt lava flows, the upper part of the Snake River Group, ranging in age from <15,000 to >730,000 years (Figure 2.6-12) [2.54]. A wide band of Quaternary mainstream alluvium extends along the course of the Big Lost River from the southwestern corner of INEEL to the Lost River Sinks area in north-central INEEL. Lacustrine (lake) deposits of clays and sands deposited in Ice Age Lake Terreton occur in the northern part of INEEL. Beach sands deposited at the high stand of Lake Terreton were reworked by winds in late Pleistocene and Holocene time to form large dune fields (eolian deposits) in the northeastern part of INEEL [2.44; 2.55]. Several Quaternary rhyolite domes occur along the Axial Volcanic Zone near the south and southeast borders [2.33]. Paleozoic limestones, late-Tertiary rhyolitic volcanic rocks, and large alluvial fans occur in limited areas along the northwest margin of INEEL [2.54].

Vertical and horizontal facies of basalt lavas. An idealized section showing distribution of vertical and horizontal facies variation in ESRP basalt lava flows is shown in Figure 2.6-13. From bottom to top, basalt lava flows typically are composed of a basal rubble zone, a lower vesicular zone, a massive columnar jointed zone, an upper vesicular and fissured zone, and a cap of platy jointed crust.

The near vent facies of lava flows is typified by thin, vesicular, platy flows (shelly pahoehoe). Also pyroclastic ash and breccia layers are commonly interleaved within the thin flow layers. With distance from the vent, the shelly pahoehoe grades rapidly into the layered facies structure, described above, which typifies the medial and distal portions of the lava flow (Figure 2.6-13). Deflation pits, in which solidified crust has subsided over areas where lava has drained away, are common throughout the flow but more numerous near the terminus.

Sediment facies. Sediments of diverse origins occur covering and interbedded with basalts of the ESRP. Surface lava flows throughout INEEL and surrounding regions are covered by varying thicknesses of windblown silt (loess). Alluvial sands and gravels are common along the Big Lost River channel through the site and lacustrine clays deposited in Pleistocene Lake Terreton are common in the northern and northeastern part of the site (Figure 2.6-12). Since the sedimentary depositional processes operating in the geologic past are similar to those operating today, these same types of sediments make up the interbeds in the subsurface.

2.6.1.2.2.2 ISFSI Site.

Stratigraphy.

At the ISFSI site, the surficial sediments (Big Lost River alluvium) vary from 9 to 18 m (30 to 60 ft) and consist mostly of gravel, gravelly sands, and sands. In some locations, a thin (0-2 m thick) layer of clay and silt underlie the gravelly alluvium, forming a discontinuous low-permeability layer just above the basalt bedrock [2.56].

Sedimentary interbeds within the Snake River Group beneath the ISFSI site are composed mostly of silts, clayey silts, and sandy silts. Cross sections showing the positions and thickness of interbeds are presented in Figures 2.6-14, 2.6-15, and 2.6-16 [2.57]. These sections show that an "interbed" occurs at a depth of about 45-60 m below the surface. Several more interbeds are shown to occur between 60 and 180 m, and they presumably occur throughout the entire thickness of the basalt section (between 0.7 and 1.1 km in this area) because they are present in deep exploration wells INEEL-l (Figure 2.6-11), which is located about 5 km north of the ISFSI site, and WO-2, which is located about 5 km east of the site.

Based on analysis of geophysical logs of wells, examination of drill core from coreholes, chemical analyses of core samples, and radiometric age determinations, twenty-three basalt lava-flow groups have been identified in the first 700 feet beneath INTEC [2.57]. These flow groups have been “named” with the letter designations shown in Figures 2.6-14 through 2.6-16. Because the detailed stratigraphic work was initiated at the Radioactive Waste Management Complex, about 9 km south of the TMI-2 ISFSI site at INTEC, the “named” groups there have been extended to correlative units beneath the INTEC area. Additional groups have been identified beneath the INTEC area and thus letter designations such as DE-1, DE-2, etc. have been developed. In general, flow group B is the youngest at INTEC and flow group I is the oldest. The age of flow group B is between 100,000 and 200,000 years and the age of flow group I is about 640,000 years.

Correlations based on regional mapping and analysis of well and drill hole data throughout INEEL provide knowledge of the source areas for some of the flow groups. Many others, however, have unknown source areas and unknown areal distributions because their source vents have been buried by later flows or sediments and the current

distribution of drill-holes does not provide sufficient subsurface information to identify all vent locations.

Flow group I erupted from AEC Butte, which lies less than 2 km north of TRA, and covers a large portion of southern INEEL. It has a distinctive chemistry and petrography that allows for easy identification in geophysical logs (gamma logs) and drill core. Flow group F is easily recognized by its paleomagnetic properties because it was emplaced during a short period of reversed magnetic polarity about 565,000 years ago [2.235]. It probably flowed into the INTEC area from a vent to the southwest, somewhere in the Arco Volcanic Rift Zone.

Basalt lava flow groups make up about 85% of the upper 700 feet of stratigraphy beneath INTEC. The remaining 15% consist of sediment interbeds, which are not named in the cross sections. The surficial sediment ranges in thickness from a few feet to about 80 feet, with the thickest areas lying west of INTEC and south of TRA. Surficial sediment is mostly composed of sandy and silty gravels deposited by the Big Lost River during late Pleistocene time. Sediment interbeds from deeper in the section are composed of both eolian silts and sands, and alluvial sediments.

The thickness of surficial sediment at the TMI-2 ISFSI (25->50 feet) is greater than that of most interbeds in the vadose zone beneath the site. The interbeds in the vadose zone (down to about 400 feet) average about 8.6 ft (2.6 m) in thickness and range from 3 ft (1m) to 15 ft (4.7m). Greater interbed thicknesses occur at greater depth in the sequence (Figure 2.6-18**)**. At depths of about 500 m (1600 ft) and greater, several interbeds of thickness 30 to 100 ft (10 to 30 m) occur, and the average interbed thickness from 500 m to the base of the basalt-sediment sequence is about 28 ft (8.4m). On an INEEL-wide basis, sediment interbed thickness distributions with depth are similar to that beneath the TMI-2 ISFSI site. For all INEEL wells and drill holes, the thickness of interbeds tends to be smaller at depths less than 1000 feet (mean =17 ft; median = 9 ft) than at depths greater than 1000 feet (mean = 38 ft; median = 25 ft). In addition, the thickness of interbeds tends to be greater in the northern part of INEEL (median ~ 16 ft) than in the southern and southeastern parts (median ~ 7 ft).

Although the surficial sediment at the TMI-2 ISFSI site is composed of alluvial gravels, the composition of sediments in most interbeds directly beneath the TMI-2 ISFSI site ranges from silty sand to clayey silt, probably of mostly alluvial and eolian origin. Some of the deeper, thicker interbeds contain significant alluvial materials, including sands and gravels and, at the northern end of the INTEC near the course of the Big Lost river, some of the interbeds within the vadose zone contain sands and gravels.

A detailed stratigraphic column and shear-wave velocity profile are presented for the TMI-2 ISFSI site (Figure 2.6-18). Physical and engineering characteristics of surficial sediments are given in Table 2.6-13. Knowledge of the engineering characteristics of interbeds is very sketchy. They typically are overlain by a thick layer of competent basalt

and occur at depths much greater than the bottoms of facility foundations. They are unsaturated to depths of several hundred feet, and there is great difficulty in obtaining in-situ properties and in obtaining samples for laboratory analysis.

At the New Production Reactor (NPR) site, which lies about 2.5 miles to the east of the TMI-2 ISFSI site, geotechnical analyses of several interbeds in the depth range of 70 to 300 feet have been done [2.203]. In addition, cross hole seismic surveys have been done there to measure compression wave and shear wave velocities of basalts and interbeds to a depth of about 300 feet [2.204]. The NPR site is farther from the Big Lost River than the TMI-2 ISFSI site, and thus likely to have a greater proportion of eolian silty sedimentary interbeds than at the TMI-2 ISFSI site. Nevertheless, this is the only geotechnical information that exists for interbeds in the INTEC area and it is presented for completeness.

The NPR geotechnical data is summarized in Golder 1991 [2.203] and Weston 1991 [2.204], and shows that, in contrast to INTEC surficial sediments, the materials at the NPR Site are mostly sand and clay/silt instead of gravels. The cross-hole seismic surveys show interbed shear wave velocity at about 200 feet depth is about 300 m/sec, and compression-wave velocity is about 460 m/sec.

Areal Geology.

The INTEC lies just southeast of the channel of the Big Lost River in the south-central part of the INEEL (Figure 2.6-9). In this area, the Big Lost River has a broad low-relief floodplain about 6 km wide that is bounded on the southeast and northwest by outcrops of basalt lava flows (Figure 2.6-12). The current channel of the river and the INTEC lie near the middle of the floodplain. The INTEC is constructed on Late Pleistocene alluvial gravels above the Holocene floodplain, which lies to the northwest of the river channel between INTEC and TRA. The Holocene floodplain is characterized by numerous abandoned channels and perhaps braided channels of the Big Lost River. The presently active channel, which is dry most of the time, is incised into the Holocene floodplain deposits by about 1.5-2 meters, and is floored by sands and fine gravels of light tan color. The Pleistocene floodplain deposit on which the INTEC is located shows no evidence in air photographs of recent channels or braids of the river. A subdued meander-scroll topography is present over large areas of the Pleistocene surface, especially to the south and southwest of INTEC. The surface is covered by sagebrush and the meander-scrolls are recognizable mainly from tonal anomalies on air photographs. Based on degree of soil development, the deposits that make up this surface were laid down during periods of high runoff during retreat of the most recent (Pinedale) glaciers, probably in the range of 15,000 to 20,000 years ago [2.55].

The landforms outside the floodplain are dominated by lava flow surface morphology that has been subdued somewhat by deposition of loess and fine eolian sand in low areas and in the lee of ridges and hills. The lava flow surfaces are characterized by rugged but low-relief topography. Due to deflation of parts of the surface during waning stages of

volcanic activity, there are numerous closed basins separated by undeflated ridges. The largest of the basins (up to several 10s of meters across) commonly contain thin playa deposits which cover the basin floors. The ridges are riddled with anastomosing fissures that are roughly parallel to the margins of the collapse basins. Many of the outcrops show columnar jointing that produces a hexagonal or polygonal pattern of fractures on the outcrop surface.

The basalts at the surface just to the east of the ISFSI site (Figure 2.6-12) and perhaps lying beneath the surficial sediment layer, are about 230,000 years old and flowed from vents located about 14 km southeast of the site [2.54]. Basalt flows beneath those at the surface are older and range in age to as much as ~4.3 million years at the base of the basalt sequence [2.33]. These basalts have accumulated in the ESRP basin that has continuously subsided at a rate of about 0.5 mm/year since passage of the Yellowstone hotspot about 4.3 million years ago (see Section 2.6.1.1.2.2 - Late Ceonzoic and Quarternary History of the Yellowstone-ESRP Volcano-tectonic Province).

In contrast to vent locations for surface basalts, the source vents for basalts in the subsurface are poorly known. It is clear that some of the subsurface basalts (Figures 2.6-14, 2.6-15, and 2.6-16, the "I" flows of Anderson, [2.57]), were erupted from the volcanic vent at AEC Butte about 3 km northwest of the ISFSI site. Others came from vents in the Lava Ridge-Hells Half Acre volcanic rift zone, the Axial Volcanic Zone, and possibly the Arco volcanic rift zone (see Section 2.6.6 - Volcanism).

Basalts in the ISFSI site area, and throughout the ESRP, are olivine tholeiites. They are mostly prophyritic and contain up to 20% by volume phenocrysts of olivine and plagioclase. The groundmass is composed of olivine, plagioclase, clinopyroxene, magnetite, ilmenite, and minor amounts of apatite, glass, rutile, and oxidation products. An average of 78 chemical analyses [2.31] and ion exchange capacity on a fresh sample of basalt from the subsurface at INEEL [2.44] are presented in Table 2.6-2.

2.6.1.2.3 Structural Geologic Conditions

The cross sections through the ISFSI site area constructed by Anderson [2.57] suggest the possibility of folding (doming) and/or faulting of basalt lava flows in the subsurface. In the cross section shown in Figure 2.6-14, a domal structure is interpreted in rocks older than the DE4 flow and in an area about 0.6 km directly west of ISFSI. Since the structure does not show up in other sections through the area (Figures 2.6-15 and 2.6-16), its true configuration and significance is uncertain. In fact, the dome interpretation on the cross section shown in Figure 2.6-14 is necessitated by K/Ar age determinations [2.58] in one core hole (USGS-80). Those K/Ar age determinations suggest that the basalts in USGS-80 are >400,000 years old (about 200,000 years older than rocks interpreted to occur at similar levels in adjacent drill holes and wells). It is this conflicting data (K/Ar age vs gamma log correlation of rocks in boreholes) that lead Anderson [2.57] to hypothesize the

dome shown in Figure 2.6-14 [2.59]. Additional work since 1991 has lead Anderson to the conclude that the hypothesized dome does not exist [2.60].

Other conflicts between K/Ar ages and paleomagnetism on the one hand and gamma log and geochemical correlation on the other hand are apparent in boreholes and wells beneath the INTEC-TRA area [2.59]. The correlations based on gamma logs and geochemical analyses of core samples suggests that the stratigraphy is nearly horizontal beneath the INTEC-TRA area. K/Ar ages and paleomagnetic inclinations, however, suggest that discontinuities exist at depths of >300 feet in rocks older than about 300,000 years, and that faults or a fold exists there. Work is underway by USGS geologists and Idaho State University geology department personnel to develop additional data to help resolve these conflicting interpretations.

Individual basalt lava flows have well developed fissure sets that formed during emplacement of the lava. These fissures result from bending of the solidified lava crust as still-molten lava flows away, leaving deflated areas (Figure 2.6-13). In addition, post-solidification cooling joints develop in the lava flows, usually producing columnar joints with polygonal patterns. These emplacement- and cooling-related fissures and joints are ubiquitous in ESRP lava flows; they are not through-going tectonic structures; and they should not be viewed as indications of folding or faulting. They are separate and distinct from fissuring related to dike injection in volcanic rift zones (see Section 2.6.1.2.2.1), which is a seismogenic process and has significance for seismic hazards.

The slope of the bedrock surface from a “plateau” of about 25 ft depth in the southeastern part of the TMI-2 ISFSI Site to about 60 ft depth in the northwest part of the TMI-2 ISFSI Site (Figure 2.6-14) is typical of the rough topography on the upper surfaces of Snake River Plain lava flows. The typical shape of the upper surface of a lava flow is irregular and rugged. High “plateaus” correspond to inflated areas, where the lava beneath the solidified crust remained in place and solidified, freezing in the full thickness of the lava flow. Low areas correspond to basins and pits, where lava has escaped from beneath the solidified crust and allowed the crust to collapse to elevations as much as 30 to 40 feet below the inflated areas. The margins of the pits and craters are commonly marked by concentric fissures developed in the crust as it collapsed because of removal of support from below. None of the TMI-2 ISFSI site drill holes encountered such a fissure.

2.6.1.2.4 Geologic History Related to Regional Geologic History

The geologic history at the ISFSI site and its relationship to regional geologic history can be summarized as follows:

1. Eruption of voluminous, explosive silicic volcanic rocks during passage of the Yellowstone hotspot beneath the area at 6.5 to 4.3 million years ago.
2. Subsidence of the area as the hotspot passed with coeval eruption of basaltic lavas and accumulation of clastic sediments in the ESRP basin.

3. Accumulation of about 700 to 1000 m of interbedded basalts and sediments, the Snake River Group, from 4.3 million years ago to present.
4. Establishment of the Big Lost River's course through the central part of INEEL, probably within the last 0.5 to 1.0 million years. Upstream of the town of Arco the river's course is controlled by the positions of basin-and-range block fault mountain ranges, whereas downstream it is controlled by the positions of volcanic zones and the local slope of the surface of the ESRP.
5. The last volcanism at the ISFSI site occurred ~230,000 years ago. Since that time Big Lost River alluvium has accumulated to a depth of 9 to 18 m.

2.6.1.2.5 Engineering Geologic Conditions

The engineering geologic conditions of the site are presented in section 2.6.4, Stability of Subsurface Materials and Foundations.

2.6.1.2.6 Groundwater Conditions

The uppermost aquifer is located approximately 450 ft (140 m) below ground surface. The ISFSI will not use any groundwater and the depth to groundwater precludes groundwater affecting the ISFSI. For more information see section 2.5.

2.6.2 Vibratory Ground Motion

2.6.2.1 Engineering Properties of Materials for Seismic Wave Propagation and Soil Structure Interaction Analysis

See section 2.6.4 Stability of Subsurface Materials

2.6.2.2 Earthquake History

2.6.2.2.1 Regional Setting

The ESRP is defined as the eastern portion of the SRP extending from the Yellowstone Plateau to the Great Rift (Figure 2.6-19). The relatively aseismic ESRP is surrounded by the seismically active Intermountain seismic and Centennial Tectonic belts (Figure 2.6-19). The Intermountain seismic belt (ISB) is a zone of concentrated seismicity that extends from northwestern Montana through the Yellowstone Plateau, southeastern Idaho, central Utah, and into southern Nevada [2.61; 2.62; 2.63; 2.64; 2.65]. It is divided into three parts referred to as the northern (Montana), central (Idaho), and southern (Nevada and Utah) ISB [2.65]. North of the ESRP a branch of the ISB extends from Hebgen Lake, Montana westward into central Idaho (Figure 2.6-19) and has been characterized as an independent zone of earthquake activity referred to as the Centennial Tectonic belt (CTB) [2.66]. Smith and Arabasz [2.65] consider the CTB (formerly called

the Idaho Seismic Zone) as a part of the central ISB which "wraps around" the ESRP. In the following discussions, this zone of seismicity will be referred to as the CTB to distinguish it from the north-trending zone of seismicity within the central and northern ISB (Figure 2.6-19).

Figure 2.6-23 shows a compilation of the minimum principle stress directions for the ESRP region derived from focal mechanisms, geologic indicators, and borehole breakouts [2.67; 2.32; 2.68; 2.43]. The minimum principle stress directions indicate northeast-trending extension northwest of the ESRP and more east-trending direction south of the ESRP. Although a rotation in the stress field may occur somewhere within the ESRP, the ESRP appears to be subjected to the same extensional stress field as the surrounding region [2.67]. Strain rates have been compiled by Eddington et al. [2.69] for the ESRP region (Figure 2.6-24). Strain rates for the region around the ESRP range between 1.1 x 10^{-15} per sec for Yellowstone Plateau to 3.8 x 10^{-17} per sec for the ISB. Preliminary estimates for the ESRP are 1 x 10^{-16} per sec based on the amount of extension measured within the ESRP volcanic rift zones for the Holocene and is similar to strain rates outside the ESRP [2.70].

2.6.2.2.2 Earthquake Data

Earthquakes of magnitudes > 2.0 for the time period 1850-1995 (shown in Figure 2.6-20 and 2.6-21) were compiled, from the following sources:

Agency	**Dates**
INEEL	1986-1995
United States Geological Survey (USGS)	1986-1995
Montana Bureau of Mines and Geology (MBMG)	1986-1995
United States Bureau of Reclamation (USBR)	1986-1995
University of Utah Seismograph Stations (UUSS)	1986-1995
Engdahl and Rinehart, (1988; 1991)	1880-1985
State Seismicity Maps for Idaho, Wyoming, Montana, Utah and Nevada, USGS Denver, Colorado	1850-1985

The earthquake compilation was initially developed by Woodward-Clyde Consultants [2.52] for the time period 1884-1989. It was updated by Woodward-Clyde Federal Services [2.53] to include earthquakes occurring in 1991 and 1992, and again by Woodward-Clyde Federal Services (1997)[2.233] to include earthquakes occurring during 1993-1995.

For the central ISB, the earthquake record extends back to November 10, 1884, the date of the first documented earthquake (Richter magnitude (M_L) 6.3), which occurred near Paris, Idaho. Prior to the 1960's, seismographic coverage of the ESRP and surrounding Basin and Range was relatively poor, with only earthquakes larger than magnitude 5.0

recorded by seismographs worldwide. The detection of earthquakes prior to this time was based on felt and damage reports made by local residents. Such epicentral locations may be in error by 100 km or more [2.52]. Over 90 % of the earthquakes shown in Figure 2.6-17 have occurred during 1970-1995. The epicenters have been determined from localized seismic networks within the intermountain region. Epicentral errors for this time period could range from 1 to more than 20 km depending the number and spatial distribution of the seismic stations recording the event.

In the early 1960's, seismographs were installed in the intermountain area by the UUSS and, in 1971, on the ESRP by INEEL (Figure 2.6-22). The USGS installed and operated a seismic network at Yellowstone National Park, Wyoming from 1970-1981 and, the UUSS, from 1983 to present. Seismic stations were installed near Teton Dam, Idaho (currently operated by Ricks College) beginning in 1980, in southwestern Montana (MBMG) starting in 1981, and in western Wyoming near Jackson Lake (USBR) during 1986. With additional seismic stations, smaller magnitude earthquakes could be detected.

Based on the number of seismic stations operating over specific time intervals, periods of completeness can be established for various magnitudes. The periods of completeness are the time periods over which independent earthquakes (excluding aftershocks) can be considered to be completely detected [2.52]. Table 2.6-3 shows the periods of completeness for various magnitudes of the earthquake data shown in Figure 2.6-17 [based on 2.71; 2.72; 2.73; 2.52]. The completeness periods indicate that, for historic times, the data base for larger magnitude earthquakes is more complete than for smaller magnitude events.

2.6.2.2.3 Moderate to Large Earthquakes

Moderate to large earthquakes of magnitude $\geq$ 5.5 have occurred within a 200-mile radius of the ISFSI site and are shown on Figure 2.6-19.. For these events, Table 2.6-4 lists the largest magnitude computed, moment magnitude if computed, and Modified Mercalli intensities at the epicenter and documented in the vicinity of the ISFSI site. Since earthquakes ($M \geq 2.5$) occur at distances greater than 50 km from the ISFSI site, only events of $M \geq 5.5$ are listed in Table 2.6-4. Of the events listed in Table 2.6-4, six have documented effects at the ISFSI site.

1959 Hebgen Lake Earthquake. The largest earthquake in the region, surface-wave magnitude (M_s) 7.5, occurred within the ISB on August 17, 1959 at Hebgen Lake, Montana (Figure 2.6-19) [2.74]. It was located 190 km northeast of the ISFSI site. The ISFSI site is located in Modified Mercalli intensity zone VI (Figure 2.6-33). Although the earthquake was felt at the INEEL, it caused no damage to INEEL facilities [2.75].

The 1983 M_s 7.3, Borah Peak, Idaho earthquake occurred on October 28, 1983 in the CTB at a distance of 89 km from INTEC. The earthquake resulted from normal faulting

along the Lost River fault [2.76]. The epicenter for this event was located in the Thousand Springs valley near the western flank of Borah Peak [2.77]. Substantial damage occurred to masonry structures in the local communities of Mackay and Challis, Idaho near the epicentral area [2.78].

The ISFSI site was located in Modified Mercalli Intensity zone VI during the earthquake (see Figure 2.6-31; [2.78]). Inspections of existing facilities near the ISFSI site following the earthquake revealed no apparent structural or component damage that would compromise structural integrity at INTEC or at the nearby Advanced Test Reactor (ATR). The ATR automatically scrammed without incident when the Plant Protective System's trip was triggered by earthquake ground motions which exceeded the 0.01 g threshold level of the trip [2.75].

Currently, the INEEL operates 25 strong motion accelerographs (SMA's). They are located at various levels (i.e., basement, first floor, roof tops) within critical facilities and at free-field sites (not within buildings). There are five instruments located at the INTEC, two of which are at the FAST facility, only a few 10's of feet from the ISFSI site. Instruments within facilities record the response of the building to the earthquake ground shaking and, at free-field sites, the level of earthquake ground motions at the earth's surface. At the time of the Borah Peak earthquake, the INEEL had 15 SMA's in operation. Peak horizontal accelerations recorded at INEEL ranged from 0.022-0.078 g for basement and free-field sites [2.79].

Table 2.6-5 shows the corrected peak accelerations, velocities, and displacements measured by the three SMAs at INTEC facilities which were 89 km from the Borah Peak epicenter [2.80]. See Jackson et al., [2.80] for copies of the corrected acceleration, velocity, and displacement time-histories and response and Fourier spectra for the vertical and two horizontal components for these SMAs.

<u>The 1905 M_L 5.5 Shoshone, Idaho earthquake</u> was reported to have occurred in the south-central portion of the Snake River Plain (see details in section 2.6.2.3.4.1.2). This earthquake was felt in Idaho, Utah, Nevada, and Oregon. Although the INEEL did not start operations until 1949, the isoseismal map determined by Oaks [2.117] for the Shoshone earthquake suggests that the ISFSI site would have been located within a Modified Mercalli intensity zone IV (Figure 2.6-26).

<u>The 1975 M_b 6.1 Pocatello Valley, Utah earthquake</u> occurred near the Idaho-Utah border. An isoseismal map developed by Cook and Nye [2.152] show that the ISFSI site was located in a Modified Mercalli intensity zone III (Figure 2.6-29). They stated that the earthquake was felt out to a distance of 190 miles (305 km). No damage was reported at the INEEL for this earthquake.

The 1975 M_L 6.1 Yellowstone Park, Wyoming earthquake was located in the central portion of the Yellowstone National Park. This earthquake was reportedly not felt at the INEEL (Figure 2.6-31)[2.228].

The 1994 M_w 5.7 Draney Peak, Idaho earthquake occurred in Idaho, 18 km west of Afton, Wyoming. The earthquake was reported to be felt in parts of southeastern Idaho but was not reportedly felt at the INEEL (Figure 2.6-35)[2.210].

2.6.2.3 Procedures to Determine the Design Earthquake

2.6.2.3.1 Identification and Description of Earthquake Sources: Tectonic Provinces

The tectonic provinces of most concern for seismic and volcanic hazards at INEEL are the eastern Snake River Plain and the northern Basin and Range province (Figures 2.6-1 and 2.6-23). Other provinces that are sufficiently close to INEEL that consideration may be required, especially for probabilistic seismic hazards assessments, are the Yellowstone Plateau and the Idaho Batholith.

Eastern Snake River Plain is distinguished from the surrounding provinces by subdued topography, lower elevations, absence of Basin and Range faults and mountain ranges (Figure 2.6-2), and historic aseismicity (Figure 2.6-21)[2.81]. In addition, it is associated with a regional gravity high [2.82], positive aeromagnetic anomaly [2.83], and high seismic velocity [2.84] reflecting zones of dense, magnetic mafic rocks near the surface and in the mid-crust beneath the Plain. The zone of mafic material in the mid-crust is believed to represent the zone of accumulation and solidification of mafic magmas that were generated by the Yellowstone hotspot as it passed beneath the ESRP.

The northern Basin and Range province is distinguished by north-northwest trending block fault mountain ranges that formed in response to east-northeast directed extension. North-northwest-trending normal faults bounding these ranges have accumulated 1 to 2 km of vertical displacement during Late Tertiary and Quaternary time [2.32]. Seismicity and Holocene paleoseismicity in the northern Basin and Range Province are concentrated on those parts of the faults that lie in a parabolic zone that passes through the Yellowstone Plateau and flanks both sides of the ESRP (Figures 2.6-19 and 2.6-21) [2.81; 2.32]. The limbs of the parabolic zone are closest to the ESRP near the Yellowstone Plateau and diverge outward from the ESRP margin with distance to the southwest. In the vicinity of INEEL, the limbs lie about 40 to 50 km from the margins of the ESRP. Historic moderate to large earthquakes that have occurred in the parabolic zone include the 1983 Borah Peak, the 1959 Hebgen Lake, the 1975 Pocatello Valley, the 1975 Yellowstone, the 1934 Hansel Valley, and the 1994 Draney Peak earthquakes.

The Yellowstone Plateau is distinguished by exceptionally high heat flow [2.35; 2.36], low seismic velocities at shallow crustal levels [2.85; 2.36], abundant hot spring and geyser activity [2.86; 2.87], persistent swarms of seismic activity [2.85], and rapid rise and fall (centimeter-scale inflation and deflation within months to years) of land surface elevations [2.85]. The area has experienced rapid and continuing uplift during the late Quaternary over the Yellowstone hotspot, in close proximity to areas (northeastern ESRP) that are rapidly subsiding. This results in development of large faults with high slip rates [2.32] and with trends inconsistent with the direction of regional extension (for example: the Centennial, Teton, and Hebgen/Red Canyon faults, Figure 2.6-19; [2.74; 2.69; 2.68]. In addition, the Yellowstone Plateau has much greater levels of seismicity than either the ESRP or the northeastern Basin and Range province [2.65], a situation possibly resulting from interaction of regional extension with rapid local vertical crustal movements, from hydrothermal activity, and from magma movements in shallow chambers. Occurrence of voluminous Quaternary explosive silicic volcanism [2.37], significant delays in teleseismic P-waves beneath the caldera area [2.88; 2.89], and the 5 km depth limit of seismicity within the caldera [2.85] all suggest extremely high temperatures and presence of magma in the crust and upper mantle.

The Idaho Batholith is distinguished by high, rugged topography, sparsity of Basin-and-Range faults, and absence of late Tertiary and Quaternary volcanism (Figures 2.6-1 and 2.6-2). Seismicity is much less intense than that observed in the Basin and Range [2.65], with maximum magnitudes of about 5. The batholith appears to have been relatively unaffected by regional extension, perhaps because the granitic rocks are stronger or more coherent than rocks in the basin and range province to the east and southwest.

2.6.2.3.2 Identification and Description of Earthquake Sources: Faults

Faults of several ages and origins occur in the INEEL region. Some of them are old and inactive, presenting no earthquake threat, whereas others are capable of generating earthquakes that could affect INEEL facilities. Detailed correlation of faults with earthquakes is presented in Section 2.6.2.3.4 - Correlation of Earthquake Activity with Geologic Structures or Tectonic Provinces.

Mesozoic thrust faults occur in the mountain ranges bordering the ESRP (Figure 2.6-4; [2.40; 2.39]). They formed during a period of east-directed thrusting related to the Sevier orogeny. They are gently westward-dipping structures that separate major Paleozoic thrust sheets. These faults are mostly inactive at the present time because the compressional forces that created them at about 60 Ma are no longer in existence. However, it is possible that steeply dipping parts (ramps) of some of the thrust faults have been reactivated by basin-and-range normal faults in Late Tertiary to Recent times [2.90].

Eocene to Oligocene normal faults trend northward across the Lost River, Lemhi, and Beaverhead ranges north of the ESRP [2.91]. Although these faults have several kilometers of accumulated displacement, their orientation with respect to the present

stress field is such that they have little tendency for movement. Therefore they are not active today and pose no threat for earthquake hazards.

Basin-and-Range normal faults (Figure 2.6-19) of Miocene to Holocene age bound the present northwest trending mountain ranges north and south of the ESRP [2.92]. These faults have accumulated 1 to 3 km of displacement in the past 4-7 Ma and are still active today as evidenced by fault scarps cutting latest Quaternary and Holocene alluvial fan deposits and by the occurrence of the 1983 Borah Peak earthquake. Table 2.6-6 summarizes the important characteristics of most Basin-and-Range normal faults around the ESRP.

The closest of these faults to INEEL facilities, the Lost River, Lemhi, and Beaverhead faults (Figure 2.6-19), each bound the southwest side of a mountain range, producing typical Basin-and-Range half graben. These are large normal faults that extend from the northern margin of the ESRP northwards to the Salmon River. Based on seismic and paleoseismic investigations, they are capable of generating earthquakes of magnitude 7 or larger [2.93; 2.94]. Because of their size, activity, and proximity to many INEEL facilities, they control much of the INEEL seismic hazard.

Lemhi fault. Detailed paleoseismic and structural investigations have been performed on the southern Lemhi fault [2.94 and 2.95]. Results are:

1. Segmentation of the southern Lemhi fault is redefined based on timing of paleoseismic events and on detailed mapping of the structure of the fault in bedrock and surficial deposits (Figure 2.6-24).
2. The most recent earthquake events on the various segments ranges from 15 to 24 ka. (Figure 2.6-25).
3. There is evidence for temporal clustering of earthquake events (i.e., clusters of several events over a few thousand years separated by long intervals (10's of thousands of years) of quiescence.
4. Maximum magnitude of earthquakes in the southern part of the fault is estimated to be M_w7.15 [2.52, 2.53].
5. Bedrock structural features of the southern part of the fault suggest that Quaternary displacement dies out at the south end of the Lemhi Range and that significant seismogenic fault movements do not extend onto the ESRP (Figure 2.6-26). Seismic reflection lines along the extended trace of the fault onto the ESRP also show that recognizable offset of rock layers does not extend for more than 1 km from the end of the range [2.96]
6. The horizontal distance from the inferred southern termination of the fault to the TMI-2 ISFSI is approximately 26.5 km.
7. The best estimate of slip rate for the southern segment of the fault is 0.15 mm/year. In the 1996 probabilistic seismic hazard investigation the slip rate is allowed to range up to 1 mm/yr to account for uncertainties in temporal clustering characteristics [2.53].

Lost River fault. The Lost River fault is slightly farther from the ISFSI site than the Lemhi fault, but poses similar seismic hazard because potential maximum magnitudes are slightly larger. Detailed paleoseismic and structural investigations of the segments closest the INEEL, the Arco and Pass Creek segments [2.95; 2.97; 2.98], produced the following results:

1. Activity on both segments is younger than previously believed. The ages of the two most recent events on the Arco segment are between 21±4 and 20±4 Ka (±2σ), and the ages of the three most recent events on the Pass Creek segment are between 18±3 and 17±4 Ka. Because of the overlap in age estimates (within 2σ), the two most recent events on both segments may have been contemporaneous.
2. Ages of individual earthquake events indicate temporal clustering (i.e., clusters of several events over a few thousand years separated by long intervals [tens of thousands of years] of quiescence). Recurrence intervals vary from around 1000 years or less to 40,000 years or more on both segments.
3. Paleomagnitude estimates based on vertical displacements yield a range of moment magnitudes (M_W) from 6.6 to 7.3 for the Arco segment and 6.7 to 7.5 for the Pass Creek segment. The range of values results from assumptions as to whether measured displacements represent average or maximum values of displacement. Maximum magnitude estimates based on segment length for the Arco segment are M_W 6.6-6.8 and for the Pass Creek segment M_W 6.7.
4. The Arco segment may extend south of the terminus of the Lost River range for several kilometers onto the ESRP and into the northwestern end of the Arco volcanic rift zone.
5. The horizontal distance from the southern exposed trace of the fault to the TMI-2 ISFSI is 29 km.
6. The best estimate of slip rate for the southern segment of the fault is 0.12 mm/year. In the 1996 probabilistic seismic hazard assessment slip rate was allowed to range from 0.05 mm/year to 1.0 mm/year to account for uncertainties in temporal clustering characteristics.

Beaverhead fault. Although considerably farther from the TMI-2 ISFSI (~52 km horizontal distance) than the Lemhi and Lost River faults, earthquakes on this fault will contribute to the probabilistic hazard assessment. No trenching investigations have been done for the fault, but surface mapping and studies of scarp characteristics [2.99; 2.100] furnish general information about its paleoseismology. The southernmost two segments of the Beaverhead fault (the Blue Dome and Nicholia segments), those closest to the INEEL, seem to have quite different faulting histories. The Blue Dome segment (the southernmost segment) has no scarps in alluvium, even though the range front is steep and straight, suggesting geologically recent faulting. Both the range front morphology and the lack of scarps in alluvium suggest that the most recent surface faulting predated about 100,000 years BP. In addition, the exposure of bedrock on both sides of the fault scarp at the southern end of the range suggests that total vertical displacement is much smaller here than in segments farther north. Slip rate estimates for the Blue Dome

segment range from 0.02 mm/year to 0.3 mm/year. In contrast, the Nicholia segment (the next segment to the north of the Blue Dome segment) is characterized by scarps that cut all alluvium except Holocene alluvium. In fact, scarps in Pinedale-age alluvium suggests that the most recent earthquake event was about 15,000 years ago and slip rate estimates range up to 1.0 mm/year.

Grand Valley-Star Valley fault. The active portions of the Grand Valley-Star Valley fault system are located more than 160 km from the proposed ISFSI site and contribute significantly less to the seismic hazard than the Lost River, Lemhi, and Beaverhead faults northwest of the ESRP. The northern termination of the Grand Valley-Star Valley fault may extend as far as the town of Rexburg [2.103]. This termination position is located about 90 km from the proposed TMI-2 ISFSI site. Field investigations by Anders and others [2.81], Piety and others [2.101], and McCalpin and others [2.102] have shown that the northern part of this fault system was very active from about 4 to 2 million years ago, but since then has been inactive. The southern end of the fault, in the Alpine and Star Valley area, however, has experienced late Pleistocene and Holocene earthquake activity (Table 2.6-6). Piety and others [2.101] estimated a maximum credible earthquake of M_L 7 ½ for the Grand Valley-Star Valley fault based on comparison of scarp heights and fault displacements with those of historic earthquakes in the Intermountain Seismic Belt.

The northwest boundary of the ESRP has been investigated as a possible source of earthquakes that could contribute to the seismic hazards of INEEL facilities [2.104]. There is no evidence to support active faulting of postulated northeast-trending normal or strike-slip faults [2.105; 2.84] along the northwest boundary of the ESRP. The abrupt termination of the northwest-trending mountain ranges at the margins of the ESRP (Figure 2.6-2), the discontinuity observed in some geophysical surveys (refraction seismic, gravity, and magnetotelluic) at the northwest boundary of the ESRP [2.105; 2.84; 2.217, 2.227], and the aseismic nature of the ESRP relative to the surrounding seismically active region, have been interpreted by some investigators [2.106; 2.207, 2.217, 2.213] to suggest the presence of active boundary faults along the margins of the ESRP.

Formation of the ESRP related to migration of the crust over the Yellowstone hotspot [2.29; 2.32], the lack of geologic evidence (i.e., northeast-trending fault scarps) for large normal faults along the margins of the ESRP [2.110; 2.111; 2.112], and seismologic and volcanic evidence indicating that the ESRP and surrounding basin-and-range regions are subjected to northeast-directed extension [2.33; 2.43; 2.67; 2.127] do not support the possibility that any such faults in the subsurface are active. The strain-rate (or extension-rate) estimates for the ESRP [2.70; Parson et al., 1998] are consistent with those estimated for areas outside the ESRP [2.69] (see section 2.6.2.2.1 for additional discussion). The ESRP is a broad volcanic basin and does not resemble continental rift systems, such as the Rio Grande rift or the East African Rift, which are large graben structures bounded by active normal faults.

In further efforts to look for possible recent fault activity along the margins of the ESRP, a small northeast-trending topographic scarp [2.55] on an alluvial fan on the southeast side of the Arco Hills was trenched in 1989. The results of the logging by the Idaho Geological Survey, under subcontract to EG&G Idaho, showed no evidence for faulting. The scarp was formed from some surficial processes, perhaps eolian modifications to a fire scar [2.112].

Other investigations have been conducted on northeast-trending faults at the southern terminations of the Lemhi Range and Beaverhead Mountains near the margins of the ESRP [2.110; 2.111; 2.95]. Results indicate that these faults were active more than 2 million years ago (Ma) because they do not displace sediments and volcanic rocks younger than 2 Ma and they have small lengths, generally less than 10 km, and small total displacements.

Non-tectonic lineaments on and near INEEL can be observed from the air, on aerial photographs, and on satellite images. One of the most pronounced of these lineaments, the Principal Lineament, has been studied extensively and shown to be caused by eolian modifications to a large fire scar [2.113]. This process produces many lineaments and perhaps even small topographic scarps on the ESRP. Other lineaments are caused by unmodified fire scars, linear stream drainages, alignments of vegetative or soil contrast with unknown causes, fluvial (stream, river) deposits, paleoflood deposits, and eolian deposits (dunes) [2.114; 2.112]. A discussion of lineaments near the TMI-2 ISFSI site is presented in Section 2.6.3.2 - Evidence of site fault offset.

Late Tertiary caldera boundary faults are postulated to exist in the silicic volcanic rocks beneath the Snake River Group. There are several bases for this postulation:

1. Calderas like those that exist on the Yellowstone Plateau today must have been associated with the late-Tertiary silicic volcanic fields occurring along the margins of the ESRP.
2. In some areas (southern ends of the Lemhi and Beaverhead Ranges near INEEL, and northern ends of the Caribou and Snake River Ranges near Rexburg) structures interpreted to be caldera boundary structures have been recognized [2.107].
3. The great thicknesses of silicic volcanic rocks observed in INEEL deep exploration holes, INEEL-1 and WO-2 (Figure 2.6-11), suggest that they were emplaced into an intra-caldera setting.

The exact sizes, shapes, and locations of the buried calderas is uncertain, but interpretations have been made (Figures 2.6-6 and 2.6-19) on the basis of geophysical anomalies, positions of volcanic fields, flow-direction indicators in ash flow sheets, and paleomagnetic data [2.107; 2.115]. Several general observations are possible, however. Caldera size is such that some of them are likely to span the entire width of the ESRP. Caldera shape, and thus the configuration of associated caldera boundary faults, are generally circular to oval. Given the tendency for calderas to overlap each other (Figures

2.6-6 and 2.6-19], it is likely that most of the ESRP boundary is characterized by caldera boundary faults buried beneath the edges of the Snake River Group. Caldera boundary faults can explain, in a manner consistent with data and concepts, Pankratz and Ackermann's [2.105] interpreted buried fault along the northwest margin of the ESRP.

Several lines of evidence, summarized in section 2.6.6.2.1, show that the calderas are no longer active because the causative heat source has moved to a new position beneath Yellowstone. The possibility of reactivation of the faults due to contemporary tectonism should be considered, but does not seem to be a cause for concern for two reasons. 1. Since the faults have a circular to oval configuration, they are not likely have long sections oriented properly for movement in contemporary stress fields. 2. No late-Pleistocene or Holocene faulting that could be related to reactivation of these faults is observed on the ESRP [2.114].

2.6.2.3.3 Identification and Description of Earthquake Sources: Volcanic Rift Zones and Axial Volcanic Zone

Volcanic vents on the ESRP are concentrated in NW-trending and NE-trending linear belts (Figure 2.6-10). The NW-trending belts have associated ground deformation features and are referred to as volcanic rift zones (VRZ's). The ground deformation features are fissures, faults, grabens, and monoclines that form due to dilational stresses above the tops of basalt dikes as magma moves from depth to the surface. Three well defined volcanic rift zones occur in the INEEL region of the ESRP, the Great Rift VRZ (which extends southeastward from Craters of the Moon National Monument), the Arco VRZ (which extends SE from Arco across the southwestern corner of the INEEL), and the Lava Ridge-Hells Half Acre VRZ (which extends from the south end of the Lemhi Range to the Hells Half Acre lava field) (Figure 2.6-10). In addition, a fourth volcanic rift zone, the Howe-East Butte VRZ, has been postulated, but it is an ill-defined zone consisting only of a few vents that are several hundred thousand years old [2.45].

By analogy with active volcanic rift zones in other parts of the world (for example, Iceland and Hawaii), it can be inferred that volcanic rift zones are sources of earthquakes during periods of volcanic activity (see section 2.6.6 - Volcanism). The magnitudes of volcanic rift zone earthquakes are small (M<5.5), but because of their proximity to INEEL facilities their contributions to both deterministic and probabilistic seismic hazards have been assessed [2.52; 2.53].

Some volcanic vents on the ESRP are concentrated in a northeast-trending zone along the axis of the ESRP (Figure 2.6-10). This is called the Axial Volcanic Zone (AVZ) to distinguish it from volcanic rift zones. It is important to make this distinction because the AVZ does not contain northeast-trending ground deformation features that would qualify it to be a volcanic rift zone. The few ground deformation features that do occur in the AVZ are NW-trending fissures. This indicates that the volcanic vents in the AVZ are fed by NW trending dikes and that, even though it is not a volcanic rift zone, seismicity can

be associated with volcanism there. Thus it also has been evaluated in deterministic and probabilistic seismic hazards assessment [2.52; 2.53].

2.6.2.3.4 Correlation of Earthquake Activity with Geologic Structures or Tectonic Provinces

Table 2.6-7 lists earthquakes M $\geq$ 5.5 that have occurred within a 200-mile region around the ISFSI site and which can be correlated with tectonic structures. Table 2.6-7 includes the seismic moments, focal mechanisms, focal depths, rupture lengths, and horizontal and vertical displacements computed by various seismological methods for these earthquakes (see references in Table 2.6-7 for more details). The following discussion of earthquakes and their relationships to geologic structures or provinces is separated into areas based on tectonic provinces.

2.6.2.3.4.1 ESRP Province

2.6.2.3.4.1.1 Seismicity

Stover and others [2.202] noted 14 historic earthquakes that may have possible locations within the SRP. Figure 2.6-19 shows their locations and Table 2.6-8 lists their dates of occurrence, intensities, magnitudes (if reported), and location uncertainties. Earthquakes listed in Table 2.6-8 occurring between 1905 and 1937 have locations based on felt reports and large location errors. The earthquakes listed for 1954, 1964, and 1969 have instrumentally determined locations, but due to the lack of local seismic networks prior to 1970, they also have large location errors.

In compiling earthquake data (pre-1970) into the Decade of North American Geology (DNAG) catalog for the western U. S., Engdahl and Rinehart [2.73; 2.116] selected only large magnitude earthquakes to represent earthquake source zones. Source zones were defined by using instrumentally located epicenters (post 1970) to determine seismically active areas. Within these areas, only large magnitude earthquakes (pre-1970) would be retained in the catalog. Thus, Figure 2.6-19 excludes the epicenters for eight of the possible SRP events due to their low intensities (hence, low magnitudes) and large location errors, and only includes the epicenters for the 1905 (M_L 5.5) Shoshone, 1928 (M_L 5.2) and 1937 (M_L 5.4) events. Although, the epicenters for the 1928 and 1937 events are outside of the SRP boundaries as shown in Figure 2.6-17 (located near the Idaho-Nevada border), Woodward-Clyde Consultants [2.52] included them within the SRP since Smith and Arabasz [2.65] extend the SRP boundary to Idaho-Nevada border based on distribution of rhyolitic volcanic rocks. More commonly, as shown in Figure 2.6-19, the SRP boundaries are defined by topographic features which separate the flat, low-lying SRP region from the surrounding mountainous region (Basin and Range province).

Figure 2.6-21 shows that from 1850 through 1995, the 1905 earthquake near Shoshone, Idaho is the only event located within the SRP. The November 11, 1905 Shoshone earthquake occurred before there was instrumental monitoring in Idaho and, since its location was based on felt reports, it may have an error of 100 km or more. This earthquake is significant to assessing seismic hazards at INEEL, since it may have originated within the SRP.

2.6.2.3.4.1.2 1905 Shoshone Earthquake

Recently, Oaks [2.117] conducted a comprehensive investigation of historical records throughout an eight-state region to determine the magnitude and epicenter of the Shoshone earthquake. For the investigation, historical documents were sought from Nevada, Oregon, Idaho, Utah, Wyoming, Montana, California, Colorado, and Washington, D.C. Primary sources included original field notes of the Department of Agriculture weather observers reports, daily and monthly journal notations by U.S. Army Surgeons and other scientific and military personnel at U.S. Army Command posts, personal diaries, and church records. Secondary sources, those transcribed from primary sources for use in another document, included newspapers, journal articles, books, maps, reports, and earthquake catalogs.

From a compilation of damage reports, Oaks [2.117] determined the Modified Mercalli intensity (MMI) for towns in Idaho, Utah, Nevada, and Oregon. Figure 2.6-30 shows the contours for intensities IV and V, and the possible location of the epicenter near the Idaho-Utah border. Both Shoshone, Idaho and Elko, Nevada reported damage which correspond to intensity VI. It is noted that for other earthquakes (see Figures 2.6-31 and 2.6-32) these towns report higher intensities than surrounding towns [2.78]. A magnitude of M_L 5.5 $\pm$ 0.5 was estimated for the Shoshone earthquake based on notes of seismic-wave amplitudes observed on a seismogram recorded by a station in Canada and measurements of the area within of the intensity V contour. Comparison of the intensity contours for the 1905 earthquake with earthquakes occurring near the Idaho-Utah border in 1934 (M_L 6.6), 1962 (M_L 5.7), and 1975 (M_L 6.0) also provides further support for an origin outside the SRP. Even though this study suggests the earthquake may be located outside the SRP, recent seismic hazards assessments at INEEL estimated the level of ground motions from an earthquake similar in size to Shoshone occurring within the ESRP near the INEEL.

2.6.2.3.4.1.3 INEEL Seismic Monitoring

Local seismic monitoring within the ESRP began in December 1971 when a seismic station was installed at INEEL [2.118]. By 1979, this network included five stations located within and near the boundaries of the ESRP. Additional seismic stations were added to the network beginning in 1986. Currently, the INEEL seismic network consists of 26 seismic stations (Figure 2.6-22).

Earthquake data have been compiled by the INEEL seismic network for a 23-year period from 1972-1995, primarily covering the ESRP (Figure 2.6-22). During this period, approximately 19 microearthquakes have been located within or near the boundary of the ESRP, indicating that infrequent, small-magnitude earthquakes ($M \leq 1.5$) may be characteristic of ESRP seismicity [2.119; 2.120; 2.67]. Although 13 of these microearthquakes have occurred near or within the INEEL boundary, Jackson and others [2.67] indicate that the INEEL area of the ESRP is not more microseismically active than other areas, but rather that the INEEL seismic network has an adequate detection threshold ($M = 0$) to record these small events.

Figure 2.6-21 shows that 1850-1995 earthquakes ($M_L \geq 2.5$) were located in the ISB and CTB, but not within the ESRP. Also, earthquakes are located closest to the margins of the ESRP near the Yellowstone Plateau and farthest (up to 70 km away) from the ESRP margins near the Great Rift and Pocatello. From similar compilations of earthquake data, several investigators have concluded that the ESRP is aseismic [2.63; 2.121; 2.122; 2.65]. Contemporary seismic monitoring of the ESRP (1972-1995) suggests that only infrequent small-magnitude earthquakes (19 events over 23 years of $M_L \leq 1.5$) occur within the ESRP as compared to the thousands of events of similar and larger size that occur within the surrounding region. Although it is recognized that historic earthquakes may have occurred within the ESRP, their large location uncertainties do not support origins within the ESRP, particularly when other geologic and geophysical data are considered.

2.6.2.3.4.1.4 Hypotheses for Aseismic Nature of ESRP

Earthquakes up to M_s 7.5 associated with basin-and-range faults have occurred within the ISB, but only small magnitude earthquakes ($M_L \leq 1.5$) have been detected instrumentally within the ESRP. In addition, the rate of seismicity (number of earthquakes per unit time) is much lower within the ESRP than that in the ISB and CTB [2.67]. Several investigators have attempted to explain the comparative aseismicity of the ESRP. Their analyses have considered the distribution of instrumental seismicity and active faults, topography (surficial geologic features), the geologic history of formation of the ESRP and Basin and Range province, tectonic stress patterns, crustal heat flow, and crustal- and upper-mantle compositions and properties. Earthquakes in the CTB and ISB indicate that the region around the ESRP is subjected to a tectonic extensional stress field that actively extends the crust by normal faulting which over millions of years produces mountains and valleys. The ESRP is also subjected to this same stress field and possibly similar strain rates (Figures 2.6-27 and 2.6-28), but Basin-and-Range-style normal faults are not present within the ESRP, leading investigators to propose alternative mechanisms for extensional deformation:

1. Aseismic Creep. Smith and Sbar [2.63] and Brott and others [2.123] suggest that deformation occurs by creep in response to high crustal temperatures beneath the ESRP. Comparisons of heat flow data in and outside the ESRP suggests that

temperatures are higher beneath the ESRP [2.123; 2.124; 2.125]. Unlike the Basin and Range, where brittle deformation (rock fracture) and associated earthquakes raise the mountains and lower the valleys, the ESRP experiences only ductile deformation (aseismic creep) because high temperatures in the crust preclude brittle deformation.

2. Crustal Strength. Anders and others [2.81] suggest that the ESRP and the adjacent region near its boundary (the so-called "collapse shadow") have increased integrated-lithospheric strength. They propose that the presence of a mid-crustal mafic intrusion (see Section 2.6.1.1.2.2) strengthens the crust so that it is too strong to fracture. Smith and Arabasz [2.65] also suggested that the mid-crustal mafic body beneath the ESRP may act to increase crustal strength and thereby, reduce the seismic capability of the ESRP.

3. Dike-Injection. Parsons and Thompson [2.126] proposed that magma overpressure through dike injection suppresses normal faulting and associated seismicity by altering the local stress field. In addition, the intrusion of numerous northwest-trending dikes during the long-term history of intermittent basaltic volcanism allows extension on the ESRP to keep pace with tectonic extension occurring in the surrounding Basin and Range province or ISB [2.127; 2.33]. Dike intrusion extends the crust because pressurized magma dilates the walls of the dike by a meter or more with each intrusion event.

4. Crustal Strain Rates. Anders and Sleep [2.128] suggest that the introduction of mantle-derived mafic magmas into the mid-crust increases the strain rate in the region directly over the hotspot (for example, the contemporary high seismicity rate within the Yellowstone Plateau). Cooling and crystallization of the mid-crustal mafic magmas as the crust moves away from the hotspot causes the strain rate to decrease to very low levels (the current situation within the ESRP). Several million years are required after that before strain rates climb to pre-hotspot levels.

2.6.2.3.4.1.5 Causes of ESRP Microearthquakes

Investigators have also suggested possible mechanisms for microearthquakes that occur within the ESRP. Because the ESRP is a volcanic province, magmatic processes are considered as a possible mechanism for the low-level microearthquakes. Brott an others [2.123] suggested that microearthquakes may be a result of subsidence due to cooling and contraction of the ESRP following the passage of the hotspot. Pelton and others. [2.120] suggested association with dike-injection or mass loading of the crust by the rhyolite domes located near the axis of the ESRP. Jackson and others [2.67] observed that the microearthquakes which have occurred in the ESRP from 1972-1995 do not have the distinct spatial or temporal patterns observed for contemporary dike-injection events at Kilauea, Hawaii or Krafla, Iceland [2.129; 2.130; 2.131] and therefore are not likely due to magmatic processes. Although no detailed analyses of mass loading and its role in

producing microearthquakes within the ESRP has been performed, Jackson and others [2.67] attribute the occurrence of microearthquakes ($M \leq 1.5$) to small-scale faulting in the shallow crust, in response to the regional extensional tectonic stress field.

2.6.2.3.4.1.6 Volcanic Seismicity

Several volcanic rift zones (see section 2.6.6 for complete description) occur on the ESRP in the vicinity of the INEEL. In addition to volcanic vents, the volcanic rift zones contain fissures, monoclinal flexures, normal faults, and graben, all of which are induced by shallow dike intrusion during periods of volcanic activity. Seismic studies at active volcanic rift zones, such as in Hawaii and Iceland, and theoretical and physical models of the resulting surficial deformation features indicate that dike-injection can produce small normal faults which extend to or slightly below the top of the dike (2-4 km) [2.132; 2.133; 2.134; 2.135; 2.136, 2.137].

Since a dike-injection event has not been observed within an ESRP rift zone, two methods are used to estimate maximum magnitudes of earthquakes that could be associated with future dike intrusion events. The first method uses analogy to active volcanic rift zones of the world to estimate the maximum magnitude of earthquakes that would accompany future ESRP volcanism (Table 2.6-9). In the active volcanic rift zones of Iceland, Hawaii, and east Africa, small magnitude earthquakes, commonly less than 4.5, accompany basalt dike injection, although magnitude 5.5 earthquakes have been observed [2.138; 2.139; 2.140; 2.52]. Rubin [2.137] suggests that some small normal faults form aseismically during multiple dike-injection events. Bjornsson and others [2.141] observed offsets of 1-2 m along normal faults during intrusion into the Krafla volcanic rift zone, Iceland, while the largest associated earthquake was magnitude 3.8.

The second method for estimation of the upper bound maximum magnitude of seismicity associated with potential future dike injection events on the ESRP uses the empirically based relationship of fault-area vs. moment magnitude (M_w) developed by Wells and Coppersmith [2.142]. Table 2.6-10 shows the range of magnitudes, $3.3 \leq M_w \leq 5.3$, derived from the fault area vs. moment magnitude relationship for normal fault lengths within the Arco and Lava Ridge-Hells Half Acre volcanic rift zones [2.96]. These values are somewhat similar to the observational values shown in Table 2.6-9. Using the fault-area vs. maximum magnitude relationship to estimate the maximum magnitude results in an upper bound for several reasons (1.139]: 1) deformation can occur aseismically and seismic moment release may be small compared to total moment released through inelastic deformation [2.143; 2.144; 2.137]; 2) faults rupture in small increments in tandem with dike propagation; 3) dike-induced normal faults have shallow downdip widths resulting in small areas for rupture [2.145]; 4) using magnitude-fault area relationships assumes rupture along the entire length, but observations indicate that the faults move in small increments or even aseismically; and 5) the relationship of moment magnitude to fault area assumes a crustal value for rigidity (3×10^{11} dyne/cm^2) which

may be lower for near-surface volcanic rocks to appropriately describe volume changes (~ 0.5-1.8 x 10^{11} dyne/cm^2) [2.143; 2.146; 2.144].

Recurrence intervals of the dike-induced seismicity within the ESRP volcanic rift zones are based on the volcanic rock record [2.33]. For the current INEEL probabilistic assessment, the maximum magnitude (M_w5.5) earthquake is assumed to occur during each dike-injection episode (see Table 2.6-15; section 2.6.6-Volcanism), even though observational seismicity during dike-injection events in Iceland and Hawaii show that most episodes of dike injection are accompanied by earthquakes of magnitude 3.5 or less.

2.6.2.3.4.2 Northern Basin and Range Province

2.6.2.3.4.2.1 Centennial Tectonic Belt (CTB)

The 1983 M_s 7.3 Borah Peak, Idaho earthquake is the largest event to occur in the CTB (Figures 2.6-19 and 2.6-21). Figure 2.6-31 shows a map of the Borah Peak earthquake intensity distribution [2.78]. The focus of the earthquake was at a depth of 16±4 km, near the base of the seismogenic crust, at the south end of the Thousand Springs segment of the Lost River fault [2.93]. It ruptured to the northwest producing 36 km of surface faulting along the Thousand Springs and a portion of the Warm Springs segments. It also produced a surface scarp with a maximum of 2.7 m vertical displacement [2.76]. The Borah Peak mainshock and aftershocks define a normal fault dipping 40-50° to the southwest which is consistent with dips determined from first motions, body-wave analysis, and geodetic observations (Table 2.6-7) [2.77]. The stress drop determined from seismic moment is 17 bars and from geologic data, 12 bars. Even considering the possible sources of error in the calculations, the stress drop probably did not exceed 75 bars suggesting that the Borah Peak earthquake was a low stress-drop event when compared to other normal faulting earthquakes in the same magnitude range [2.93].

2.6.2.3.4.2.2 Intermountain Seismic Belt (ISB)

Several moderate to large magnitude earthquakes can be correlated to tectonic structures within the central part of the ISB near the ESRP (Figure 2.6-19):

1. Hansel Valley. The March 12, 1934, M_L 6.6, Hansel Valley Utah earthquake was felt over an area of 440,000 km^2 and reached Modified Mercalli intensity VIII [2.65]. Shenon [2.147] mapped north-trending subparallel fractures displacing salt flats and unconsolidated late Quaternary sediments in the southwestern part of Hansel Valley over an area 6 km wide and 12 km long. Up to 50 cm of vertical displacement and 25 cm horizontal offset were reported by dePolo and others [2.148]. The focal mechanism from seismic wave-form modeling by Doser [2.149] indicates that the mainshock occurred along a strike-slip fault with left-lateral slip on a northeast-

trending structure. The event originated at focal depth of 8-10 km and had a subsurface rupture length of 11 km [2.149].

2. Cache Valley. Re-analysis of seismograms for the August 30, 1962, M_s 5.7, Cache Valley earthquake indicates that it may be associated with the Temple Ridge fault, a less prominent feature with only 500 m of Neogene throw located east of the East Cache fault [2.150]. Focal depth is estimated to be 10±2 km and focal mechanisms from first motions and body wave analysis suggest a dip of 49° and 58°, respectively, to the west (Table 2.6-7). Woodward-Clyde Consultants [2.52] estimated Brune and RMS stress drops of 25.2±5.2 bars and 45±4 bars, respectively.

3. Pocatello Valley. The March 28, 1975, M_b 6.1, Pocatello Valley earthquake occurred along a northeast-trending structure with a large left-lateral component of slip [2.151]. Figure 2.6-32 shows the Modified Mercalli intensity distribution [2.152]. Studies of the aftershock sequence were consistent with a fault dip of 39° to the northwest [2.153]. The event originated at a focal depth of about 9 km (Table 2.6-7) and has an inferred stress drop of about 50 bars for initial faulting [2.151].

2.6.2.3.4.3 Yellowstone Plateau

2.6.2.3.4.3.1 Hebgan Lake Earthquake

The August 18, 1959, M_s 7.5, Hebgen Lake earthquake is the largest event to occur in the ISB region. Figure 2.6-33 shows the Modified Mercalli intensity distribution from [2.154]. Seismic waveform analysis by Doser [2.74] indicates that the mainshock was a double event consisting of subevent one, an M_b 6.3 followed 5 sec later by subevent two, an M_b 7.0. Her analysis also suggests that the rupture occurred along one or more fault planes with east-west strike orientations (Table 2.6-7) slightly discordant with the trace of surface faulting along the Hebgen and Red Canyon faults. Maximum vertical displacements of 6.7 m over a surface scarp length of 23 km and 6.1 m over 14.5 km were observed along the Red Canyon and Hebgen faults [2.106; 2.155]. A 1-m scarp was observed along a 3-km segment of a fault adjacent to Madison Canyon, but it is difficult to determine whether it was related to coseismic movement associated with the Hebgen Lake earthquake [2.106].

Focal mechanisms derived from first motions and body-wave analysis for the subevents indicates fault dips ranging between $40\text{-}60^o$ to the southwest. Subevent 1 initiated at a focal depth of 10 km and subevent 2 at 15 km. The estimated stress drop for the mainshock is 115 bars [2.74].

2.6.2.3.4.3.2 Yellowstone Caldera

The June 30, 1975, M_L 6.1, Yellowstone Park earthquake occurred near the northern rim of the Yellowstone caldera. Figure 2.6-34 shows the Modified Mercalli intensity

distribution from [2.156]. The focal depth of this event was shallow, 6 km. Aftershock studies and first motions suggest normal faulting along a northwest-trending structure dipping about 70° to the northeast [2.156; 2.151].

2.6.2.3.4.4 Northern Rocky Mountains

2.6.2.3.4.4.1 Clarkston Valley

The July 10, 1925, M 6.8, Clarkston, Montana earthquake was felt over an 800,000 km^2 area and reached a Modified Mercalli intensity of VIII in the epicentral area [2.65]. Although this earthquake was large, it produced no surface scarp, but some ground cracks were observed [2.157]. Seismic wave analysis indicates a focal depth of 9 km, a rupture length of 25 km, and oblique normal slip on a northwesterly-dipping plane (Table 2.6-7) [2.158].

2.6.2.3.4.4.2 Virginia City

The November 23, 1947, M 6.3, Virginia City earthquake may be associated with rupture along a portion of the northwest-trending Madison Canyon fault based on first motions [2.159]. Reanalysis using seismic waveforms [2.158] suggests right-lateral slip along a fault striking east-west. Doser suggests that fault motion at depth in this part of the Hebgen Lake/Madison region occurs along structures striking nearly east-west and that the northwest-strike of surface faulting may reflect the trend of preexisting weaknesses that the earthquake ruptures exploited as they propagated to the surface. The event originated at a focal depth of about 8 km [2.158].

2.6.2.3.5 Maximum Earthquake Potential

Patterns of seismicity and locations of mapped faults have been used to assess potential sources of future earthquakes for estimating ground shaking at INEEL. The sources and maximum magnitudes of earthquakes which could produce the maximum levels of ground motions at the ISFSI include (Figure 2.6-23): 1) a magnitude 7.15 earthquake at the southern end of the Lemhi fault; 2) a magnitude 7.25 earthquake at the southern end of the Lost River fault; 3) a magnitude 5.5 earthquake associated with dike-injection in either the Arco or Lava Ridge-Hell's Half Acre volcanic rift zones and the axial volcanic zone; 4) a background magnitude 5.5 earthquake occurring within the ESRP; and 5) a background earthquake with magnitude up to 6.75 in the northern Basin and Range Province [2.53]. Ground motion contributions from other sources such as the postulated ESRP boundary fault, northern Basin and Range province, Yellowstone Plateau, and Idaho Batholith are significantly smaller due to their distant locations or lower maximum magnitudes.

2.6.2.3.5.1 Lemhi Fault - Howe Segment

The Howe segment, located at the southern end of the Lemhi fault, is the closest part of the Lemhi fault to INEEL (Figure 2.6-23). The ISFSI site is located a horizontal distance of about 26.5 km from the mapped southern termination of the Howe segment [2.53]. The most recent event (MRE) occurred between 15,000 and 24,000 years ago [2.94]. The lengths of the Howe and Fallert Springs (the segment just north of the Howe segment (Figure 2.6-25)) segments are approximately 15-20 km and 25-30 km, respectively [2.160; 2.161; 2.99]. Recent paleoseismic investigations (four trenches excavated across the segments) by Woodward-Clyde Consultants [2.52; 2.94] indicate that the MRE could have ruptured portions of both the Howe and Fallert Springs segments resulting in a total length of 35 km. For the MRE, maximum and average displacements are 2.5 m and 1.5 m, respectively [2.94]. The maximum magnitude estimated for the southern Lemhi fault is 7.15 based on empirical data from Wells and Coppersmith [2.143] using: 1) surface rupture length; 2) subsurface rupture length, 3) rupture area (length x downdip extent; 31 x 21 km; Figure 2.6-36); 4) maximum displacement; and 5) average displacement [2.52; 2.53]. The slip rate of 0.1 mm/yr for both the Howe and Fallert Springs segments is lower than the estimated 0.3 mm/yr for the Thousand Springs segment of the Lost River fault indicating that the Howe segment is less active [2.76].

2.6.2.3.5.2 Lost River Fault - Arco Segment

The Arco segment is located at the southern-most end of the Lost River fault and is the closest part of the fault to INEEL (Figure 2.6-23). The north and south ends of the Arco segment have been mapped at different locations by various investigators. The northern terminus was orginally mapped at King Mountain [2.55; 2.164], but has more recently been established at Ramshorn Canyon [2.76; 2.162; 2.91; 2.97]. Woodward Clyde Federal Services [2.53] use the Ramshorn Canyon terminus in their detailed analysis of fault behavior. The location of the southern terminus is less certain. Three scenarios are possible. Scenario 1: The fault ends about one kilometer south of Arco where scarps that are mapped along the main range front disappear under alluvium in the Arco Basin (21 km total length, 9 km west of the INEEL boundary). Scenario 2: The fault ends about 2 km south of the range-front scarps in an area west of Butte City [2.92] where scarps in basalt lava flows ocurr. Most evidence [2.163; 2.53] supports this interpretation (25 km total length, 7 km west of the INEEL boundary). Scenario 3: Wu and Bruhn [2.97] suggest that the terminus may lie 7 km southeast of Butte City at a set of monoclinal flexures in the northwestern end of the Arco volcanic rift zone (30 km total length, 1 km west of the INEEL boundary). Each of these scenarios are used in the 1996 probabilistic seismic hazards assessment for INEEL [2.53].

The most recent and penultimate events on the Arco segment occurred between 21±4 Ka and 20±4 Ka, possibly with contemporaneous rupture on the Pass Creek segment to the north. Maximum magnitude estimates for the Arco segment range from 6.6 to 7.3 [2.98]. The uncertainty in magnitude is due to uncertainty in rupture length, uncertainty in assumptions that the measured displacements represent average or maximum values, and the apparent discrepency between length-based and displacement-based magnitudes (See

section 2.6.2.3.2 and reference 2.98 for further details). The net vertical displacement at the Arco Peak site (on the Arco segment) averages 1.2 to 1.5 meters per event. The best estimate of slip rate between 58 and 20 Ka is 0.12 mm/year [2.76; 2.98].

2.6.2.3.5.3 Beaverhead Fault - Blue Dome Segment

The Blue Dome segment is located at the southern-most end of the Beaverhead fault (Figure 2.6-23). The ISFSI site is located 52 km horizontal distance from the Blue Dome segment. Stickney and Bartholomew [2.66] estimate the MRE at more than 30,000 years ago]. More recent mapping in the area suggests that it has not been active for several hundred thousand years because no scarps are present on Quaternary alluvial fans [2.99; 2.100]. The length of the segment is estimated to be about 25 km [2.99]. Woodward-Clyde Consultants [2.52] estimates a maximum magnitude of 7.0 for an earthquake on along the Blue Dome fault based on analogy to the Lemhi and Lost River faults further to the west. Several investigators suggest that this segment has a slip rate of 0.02 mm/year to 0.3 mm/year [2.76; 2.81].

2.6.2.3.5.4 ESRP Volcanic Zones

Volcanic vents are not randomly distributed on the ESRP, but occur in discrete zones. Most vents occur in northwest-trending volcanic rift zones and a concentration of vents also occurs along the axis of the ESRP (the Axial Volcanic Zone - see section 2.6.2.3.5.5.4, below). Volcanic rift zones on the ESRP contain a variety of structures, other than volcanic vents, that suggest an association with shallow northwest-trending dikes in the subsurface (see for example Figure 2.6-48 in section 2.6.6.2.3.1). These structures include fissures, fissure swarms, fault scarps, and monoclines, all of which have been observed in active volcanic rift zones of Iceland and Hawaii and demonstrated to be associated with shallow dike intrusion [2.135; 2.136]. The great age range of exposed volcanic rift zones on the ESRP (from over 1 million years to 2000 years; 2.33; 2.45] suggest that basaltic volcanism throughout the history of the ESRP has been fed by volcanic rift zone processes. The northwest trend of volcanic rift zones and the dikes that produce them is controlled by the regional northeast-directed extensional stress field [2.43]. The same stress field produces northwest-trending normal faults, northwest-trending fault-block mountain ranges, in the Basin-and-Range province to the north and south of the ESRP.

The long-term (~4My to present) intrusion of northwest-trending basalt dikes into the ESRP has accommodated northeast-directed extension that was elsewhere accommodated by normal faulting [2.127]. The supplanting of normal faulting and its associated earthquakes in the ESRP by dike intrusion is the mechanism that best explains the relatively aseismic nature of the ESRP with respect to the surrounding Basin-and-Range province and Yellowstone Plateau [2.126; 2.138].

2.6.2.3.5.4.1 Arco Volcanic Rift Zone

The Arco volcanic rift zone extends from the southern end of the Lost River Range across the southwestern corner of the INEEL (Figure 2.6-23). The ISFSI site is about 14 km away from the closest point on the boundary of the rift zone. The rift zone is about 8 km wide and 20 km long [2.165; 2.166, 2.54]. Small normal faults within the rift zone are 5-6 km in length, have maximum cumulative vertical offsets of about 12 m (multiple offsets) and are postulated to extend to a depth of 2 km below the surface [2.132; 2.165; 2.166; 2.52; 2.53]. A set of fissures in the Box Canyon graben area are colinear with the small normal faults (5 km length; Table 2.6-10) bounding the graben which results in a total length of 8 km. Based on the compilation of earthquake data for active rift zones (Table 2.6-9) a maximum magnitude of 5.5 is assumed possible for future dike-injection events within the rift zone. This is consistent with a magnitude of 5.2 based on the assumption that an earthquake associated with dike injection ruptures a fault area of 16 km^2 (length x depth; 8 x 2 km; Figure 2.6-36) [2.52; 2.53]. The most recent volcanic activity within the central part of the volcanic rift zone appears to have been about 95,000 years ago [2.167; 2.166; 2.165; 2.168]. The 10,000 to 13,000 year old Cerro Grande and North and South Robbers lava flows occur at the southern end of the VRZ at its intersection with the Axial Volcanic Zone [2.54].

2.6.2.3.5.4.2 Lava Ridge-Hell's Half Acre Volcanic Rift Zone

The Lava Ridge-Hell's Half Acre (LR-HHA) volcanic rift zone extends from the southern end of the Lemhi range across the INEEL to the southeastern corner (Figure 2.6-23). The ISFSI site is about 28 km away from the closest point on the boundary of the rift zone. The rift zone is 3-6 km wide and 50 km long. At the southern end of the rift zone, two sets of fissures, which may or may not be associated with small normal faults (Hell's Half-Acre fissures in Table 2.6-10), are about 4 km in length [2.114]. Since portions of the fissures are covered by younger lava flows, the fissure sets could extend 11 km farther south. A maximum magnitude of 5.5 was assumed possible for earthquakes associated with future dike-injection events within the LR-HHA rift zone based on the compilation of earthquake data shown in Table 2.6-9. This is consistent with a magnitude of 5.5 which was estimated using fault area (15 x 3 km = 30 km^2) and assuming rupture along the entire fissure lengths [2.52; 2.53]. The most recent volcanic activity within the LR-HHA rift zone occurred with the eruption of the Hell's Half Acre Volcanic Field at its intersection with the Axial Volcanic Zone about 5,200 years ago [2.167; 2.166].

2.6.2.3.5.4.3 Howe-East Butte Volcanic Rift Zone

The postulated Howe-East Butte (H-EB) volcanic rift zone extends across the central portion of the INEEL from the range-front south of Howe to East Butte (Figure 2.6-23). It is poorly expressed surficially and is mostly covered by fluvial and lacustrine sediment [2.169] (See section 2.6.6.2.3.1 - Volcanic Rift Zones). The ISFSI site is located within the postulated H-EB volcanic rift zone. Woodward-Clyde Consultants [2.52; 2.53] consider the maximum magnitude for the H-EB to be 5.5 similar to the Arco and LR-

HHA volcanic rift zones. Volcanic vents in the H-EB volcanic rift zone are dated at 580,000 to 641,000 years old [2.54], and a conservative minimum age for the H-EB volcanic rift zone is 230,000 years, based on the age of lava flows from the Axial Volcanic Zone that cover volcanic rift zone structures and vents [2.54].

2.6.2.3.5.4.4 Axial Volcanic Zone

The Axial Volcanic Zone (AVZ) is located along the ESRP axis and crosses portions of the INEEL's southern and eastern boundary. The ISFSI site is about 13 km from the closest point of the AVZ boundary. Dike-induced structures are located near the intersections of the Arco and LR-HHA volcanic rift zones with the AVZ. Thus, a maximum magnitude of 5.5 is assumed possible based on the interpretation that dike injection mechanisms in the AVZ are similar to those in other ESRP volcanic rift zones.. The most recent volcanic activity took place about 5,000 years ago at the Hells Half Acre lava field [2.167,2.54].

2.6.2.3.5.4.5 Great Rift Volcanic Rift Zone

The Great Rift volcanic rift zone crosses the ESRP in the northwest to southeast direction. It is about 45 miles (70 km) in total length, but is divided into three segments with slightly different trends. The three segments range in length from 15 to 30 km. The ISFSI site is located 45-km northwest from the closest approach of the Great Rift.

The dimensions of fissure sets along the Great Rift are similar to those in the Lava Ridge-Hells Half Acre volcanic rift zone and thus a magnitude 5.5 is possible for earthquakes associated with future dike intrusion events. The most recent volcanic activity in the Great Rift occurred about 2000 years ago [2.167]. Because of the great distance of the Great Rift from the ISFSI site, ground motions resulting from volcanic seismicity will be less than ground motions from ESRP background seismicity and seismicity associated with closer volcanic rift zones.

2.6.2.3.4.6 ESRP Background Province

Although instrumental seismicity indicates that the ESRP is relatively aseismic, an earthquake similar in size to the 1905 Shoshone event is considered possible within the ESRP. For estimating ground motions at INEEL, an earthquake of maximum magnitude 5.5 is postulated to occur anywhere within a 25 km radius of each facility. This is referred to as a "background earthquake" and is commonly used for design of commercial nuclear reactors to assess effects from earthquakes that may occur on unknown faults (those without surface exposures).

2.6.2.3.4.7 Northern Basin and Range Background Province

The northern Basin and Range background source region surrounds the ESRP. Excluding known normal faults which are capable of generating magnitude 7.0 events, a background earthquake with a maximum magnitude of 6.75 is possible within this source region on unknown or "blind" faults [2.52; 2.53]. Doser [2.170] suggests that earthquakes of magnitude 6.0-6.75 could occur in the ISB without producing surface rupture, and thus would leave no geologic record of their occurrence. An example of this phenomena is the 1975 M_L 6.0 Pocatello Valley earthquake near the Idaho-Utah border (See Section 2.6.2.3.4.2.2 - Intermountain Seismic Belt). This event occurred on a "blind" (not evident in surface geology) cross-fault which trended transverse to the trend of nearby Basin and Range normal faults [2.171].

2.6.2.3.4.8 Idaho Batholith Background Province

The Idaho Batholith is seismically quiet region and its boundaries are defined by the extent of granitic rocks associated with the batholith. No extensive or well-defined Quaternary faults are mapped within the Idaho Batholith [2.52; 2.53]. Although seismographic coverage is poor (a detection threshold of $M \geq 3$), it appears to have a low seismic potential [2.65]. Woodward-Clyde Consultants [2.52; 2.53] estimated the maximum magnitude to be M_w 5.5.

2.6.2.3.4.9 Yellowstone Plateau Background Province

The Yellowstone Plateau is the topographically high region of the Yellowstone volcanic field and surrounding areas. The elevation of the plateau averages ~2500 m and, in addition to the Yellowstone Caldera, it includes the Beartooth uplift to the east, the Hebgen Lake fault zone to the west, and the Teton Range to the south [2.85]. It is an area of extremely high heat flow, profuse seismicity, abundant geothermal activity, low seismic velocity, low gravity, and rapid vertical crustal movements, all of which suggest high temperatures and perhaps magma bodies at relatively shallow depths in the crust [2.85]. Since detailed recording began in 1973, the maximum magnitude of seismicity within the Yellowstone caldera has been about 4.5 and the focal depths have been less than 10km. Outside the caldera and along the caldera rim, Yellowstone Plateau seismicity attains a greater focal depth (~20km) and greater magnitude. It includes the 1959 Hebgen Lake (M_S 7.5) event, largest earthquake in the ISB and the 1975 Yellowstone Park (M_L 6.1) earthquake. Thus, the maximum magnitude of Yellowstone Plateau seismicity is assumed to be M_s 7.5 for the INEEL probabilistic seismic hazards assessment [2.52; 2.53].

2.6.2.3.6 Seismic Wave Transmission Characteristics

2.6.2.3.6.1 Regional Attenuation

For the ground motion modeling studies, regional attenuation was characterized by a frequency-dependent quality factor, Q(f). Singh and Herrman [2.172] determined a regional crustal coda Q_o of 450 and h of 0.2 for Q(f) in the Basin and Range northwest of the ESRP. Braile and others [2.173] observed high attenuation in the 1978 ESRP seismic refraction experiment within the ESRP for the P-wave quality factor Q_p. They attributed it to low Q values in the volcanic rocks (Q_p 20 to 200) and throughout the crust (Q_p 160 to 300). Woodward-Clyde Consultants [2.51, 2.52] used the model parameters of Q_o and h from Singh and Herrman [2.172] in their deterministic analyses. They also suggest that the relatively short source-to-site distance of 20 km does not significantly attenuate earthquake ground motions.

2.6.2.3.6.2 Near-surface Geological Attenuation

Woodward-Clyde Consultants [2.51] indicate that near-surface geology (0-5 km depth) has a significant influence on earthquake ground motions at a site. The INEEL resides upon the ESRP which is covered with basalt lava flows and sediments (see section 2.6.1 - Basic Geologic and Seismic Information). Boreholes located throughout the INEEL site indicate the basalt is interbedded with sedimentary layers; in some areas, the percentage of interbeds reaches 50%.

This unique stratigraphy has the affect of deamplifying or decreasing the level of earthquake ground motions because seismic waves travel through a sequence of alternating high (basalt) and low (sediments) velocity zones which tend to scatter the seismic energy. Also, seismic energy is intrinsically dampened by the sedimentary interbeds. The net effect of the interbedded basalt is to reduce the level of earthquake ground motions when compared to a homogeneous basalt (no interbeds) [2.51, 2.52; 2.53]. The amount of deamplification is dependent on the difference between the velocities for the basalt and sedimentary layers, but probably is in the range of 20 to 25%.

Figure 2.6-18 shows the shear-wave velocity (Vs) profile determined to estimate earthquake ground motions at the INTEC [2.52; 2.53]. The velocity model was derived from using well and borehole logs located at and near INTEC. Since the velocity model has large contrasts (basalt vs sediment), the velocity profiles were smoothed to taper the large effects of scattering which resulted in low-amplitude spectra. Regional earthquakes were digitally recorded near two boreholes at TRA (about 3 km to the northwest of the ISFSI site). These data were used to estimate the near-surface attenuation, k, and to determine the amount of smoothing in the velocity profiles.

2.6.2.3.7 Maximum Earthquake

2.6.2.3.7.1 INEEL Seismic Hazard Studies

Both deterministic and probabilistic seismic hazard assessments to evaluate potential earthquake ground motions have been conducted at the INEEL since the early1970's for establishing seismic design criteria. Since that time, ground motion seismology and

federal regulations (NRC and DOE) have continued to evolve, and geoscience investigations have continued at INEEL. To keep pace with these changes, site-specific deterministic and probabilistic ground motion studies were completed for all INEEL facility areas during the 1990's [2.51; 2.53]. These results formed the basis for Woodward-Clyde Federal Services [2.179] to evaluate site-specific probabilistic and deterministic ground motions at the ISFSI site. Recent changes in NRC requirements for independent fuel storage facilities allow for the use of probabilistic seismic design parameters. The ISFSI design earthquake parameters are based on the recent probabilistic results [2.179] and are discussed Section 2.6.2.3.7.2.

The following sections discuss the results of both probabilistic and deterministic studies that are applicable to the INTEC, the host site for the TMI 2 ISFSI. Both discussions are provided because DOE-ID is nearing completion on an update of the INEEL Architectural Engineering (AE) Standards [2.174] to include probabilistic seismic design parameters for the INTEC. In the initial license application submittal, the ISFSI is designed to the deterministic seismic criteria which were in the INEEL AE Standards [2.174] at that time.

The INEEL AE Standards incorporates the results of seismic hazard studies in the form of seismic design parameters, peak ground accelerations and response spectra. These seismic parameters are the criteria formally approved for use in design of INEEL facilities. The criteria provide technical direction and guidance in the development of designs for construction type work performed for DOE-ID at the INEEL. The peak horizontal accelerations for rock in the AE Standards [2.174] are based on deterministic studies conducted in the 1970's [2.175; 2.176; 2.177; 2.178] and are supported by the results of the 1990 site-wide deterministic study conducted by Woodward-Clyde Consultants [2.51].

2.6.2.3.7.1.1 Deterministic Seismic Hazard Studies Applicable to the TMI-2 ISFSI Site

The deterministic studies conducted in the 1970's were based on empirical attenuation relationships of maximum acceleration on rock as functions of magnitude and distance (Table 2.6-11). Limited paleoseismic studies at the southern ends of the Lost River and Lemhi faults and speculation that future earthquakes would be of similar size to earthquakes that had previously occurred in the basin and range (i.e., 1915 M 7.8 Pleasant Valley, Nevada earthquake), led some investigators to select a maximum credible earthquake of M_L 7.75 at a distance of 24 km from the INTEC. Using the empirical attenuation relationship developed by Seed et al. (1969) (which includes very few rock recordings), the evaluation resulted in a peak horizontal acceleration of 0.33 g for rock at the New Waste Calcining Facility (NWCF) at the INTEC (~320 m north of the ISFSI site) [2.175; 2.177]. The investigators also estimated a horizontal acceleration of 0.46 g for 50 ft of soil (sand and gravel) based on an amplification factor of 1.4 derived from the lumped-mass method which incorporated representative dynamic soil properties.

In 1977, Agbabian Associates [2.178] reviewed the previous deterministic evaluations conducted for INEEL facilities (this included NWCF) with respect to NRC requirements for a nuclear reactor. They recommended an alternative deterministic approach using an empirical attenuation relationship that incorporated worldwide earthquake recordings that had been developed by Woodward-Clyde Consultants [2.176]. They suggested a maximum credible earthquake of M_L 6.75 (taking into account fault surface lengths and the lack of historical earthquakes of M_L 7.75 in the Idaho region) at a distance of 24 km from the Lost River fault. This resulted in a peak horizontal acceleration of 0.30 g for rock (Table 2.6-11).

At about this same time, studies to develop seismic design criteria for other INEEL facilities near the INTEC were being conducted. Based on the results of these studies and those for INTEC, the DOE-ID issued the first draft of the INEEL AE Standards which contained peak accelerations to be used for design of INEEL facilities [2.211, 2.214]. This document directed that future designs at the INTEC for bedrock were to use a peak horizontal acceleration of 0.24 g and a vertical acceleration 2/3 that of the horizontal acceleration.

The 1990 deterministic study was conducted by Woodward-Clyde Consultants [2.51] at the request of DOE-ID to update the seismic design criteria contained within the INEEL AE Standards. This deterministic study estimated peak ground accelerations for INTEC based on the largest earthquake (M_w 6.9) that could occur along the Lemhi fault at a distance of 21 km. This evaluation incorporated all available results from geoscience investigations pertaining to the earthquake source and subsurface stratigraphy beneath the ESRP (crustal structure) and INTEC (near-surface stratigraphy).

Woodward-Clyde Consultants [2.51] developed a site-specific geologic profile beneath two facility areas at the INTEC to assess the nature of seismic-wave propagation. The geologic profiles were used with the stochastic numerical modeling technique known as the Band-Limited-White-Noise (BLWN) ground motion model combined with random vibration theory to determine site-specific accelerations. Sensitivity analyses indicated that the size of the earthquake (stress drop) and near-surface geology (kappa) had the most significant affects on the levels of earthquake ground motions.

Peak horizontal accelerations and response spectra were estimated for the 16th, 50th, and 84th percentiles. The peak horizontal acceleration at the 84th percentile for rock at a site (called FPR) within 200 m of the ISFSI is 0.20 g and for a soil site (called SIS) within 600 m of the ISFSI site, 0.30 g. This suggests an amplification factor of about 1.5 between these two sites at the INTEC (Table 2.6-11).

In this same study, the vertical to horizontal ratio was evaluated using regional recordings of earthquakes at the INEEL facility areas. The average was 0.72 for rock sites which is consistent with the standard value of 2/3. The results of the 1990 deterministic study

were incorporated into the INEEL AE Standards. These results suggested that the peak accelerations determined from the 1970's studies are conservative.

The 1996 site-specific deterministic evaluation conducted for the ISFSI site [2.179] was based in part on the stochastic numerical modeling methodology of the 1990 deterministic evaluation [2.51] and incorporated results of recent fault-trenching studies conducted along the Lemhi and Lost River faults [2.94; 2.98]. The Lemhi fault is the closest basin-and-range normal fault to the ISFSI site and controls the deterministic seismic hazard. The paleoseismic characteristics and geometry of this fault indicate that it has the potential for a M_w 7.1 earthquake at a distance of 22 km from the ISFSI site.

The same attenuation relationships (empirical and stochastic numerical models) from the 1996 probabilistic study were used in the deterministic analysis and were weighted the same as in the 1996 probabilistic evaluation (discussed in section 2.6.2.3.7.1.2). The deterministic evaluation resulted in a peak horizontal acceleration of 0.28 g for rock at the 84th percentile (Table 2.6-11). A soil acceleration of 0.56 g was estimated by using an amplification factor of 2 (based on the site-specific probabilistic results in section 2.6.2.3.7.1.3).

2.6.2.3.7.1.2 Probabilistic Seismic Studies Applicable to the TMI-2 ISFSI Site

In 1977, a probabilistic seismic hazard study was conducted by Agbabian Associates [2.178]for the NWCF site at the INTEC to calculate the probability of experiencing the design earthquake during the service life of the facility (Table 2.6-12). The procedure used the mathematical model of Der-Kiureghian and Ang [2.208]. The investigators used three source areas having magnitude range from 6.75-7.5 with corresponding intensities of IX-X and recurrence intervals based on a limited historical earthquake catalog. They developed intensity attenuation relationship using five regional earthquakes (1935 MMI VII Helena Montana; 1959 MMI X Hebgen Lake, Montana;1962 MMI VII Richmond, Utah; 1967 MMI VII Tushar-Sevier Central Utah; and 1975 MMI VII Pocatello Valley, Idaho). Their results suggested that for a peak horizontal acceleration of 0.40 g on rock, there is 0.01% chance of exceedance in 100 years.

In the 1984 probabilistic seismic hazard study, Terra Corporation calculated probabilities of peak horizontal accelerations for the Argonne National Laboratory West site on INEEL. They developed seismic hazard maps for all of the INEEL including the INTEC. Their methodology used the Tera [2.229] model developed from the work of Mortgat et al [2.219] and Mortgat and Shah [2.218]. They specified nine source regions, three of which included the major range-bounding faults (Lost River, Lemhi, and Beaverhead). The magnitudes for the source regions ranged from 6.5 to 7.75. The recurrence intervals for the sources regions were derived from a 17-year earthquake record of the local region. The attenuation relationship was based on Campbell [2.204] and Tera [2.230] incorporating values of crustal attenuation determined from regional earthquake

recordings [2.226] and the results of the ESRP refraction survey [2.84]. For the INTEC, the resulting seismic hazard maps show 0.18 g at a return period of 1,000 years and 0.30 g at a return period of 10,000 years (Table 2.6-12).

The 1996 probabilistic seismic hazards evaluation by Woodward-Clyde Federal Services [2.53] was conducted for all INEEL facility areas including the INTEC. This study has undergone extensive peer review and provides the basis for developing seismic design parameters to be used at INEEL.

The probabilistic methodology used in the study is based on Cornell [2.208] and Youngs and Coppersmith [2.232]. It provides for explicit inclusion of the range of scientifically defensible seismologic and tectonic interpretations including seismic source characterization and ground motion attenuation models (consistent with approaches contained in NRC Regulatory Guide 1.165, "Identification and Characterization of Seismic Sources and Determination of Safe Shutdown Earthquake Ground Motions," Sections C 1 through 3). Uncertainties in conceptual models and parameters were incorporated into the hazard through use of logic trees. Sensitivity analyses were performed to examine the important contributors to the total hazard and to the uncertainties in the hazard. This evaluation incorporated results of all geologic, seismologic, and geophysical investigations conducted for INEEL since the 1960's.

Earthquake magnitudes and recurrence rates were assessed for all earthquake sources which contribute to potential ground motions at the INTEC site. The four closest sources (Figure 2.6-23) that contribute to the hazard at INTEC include:

1. Basin and Range normal faults which are characterized by magnitudes ranging from M_w 6.5 to 7.75 based on fault dimensions (surface length, displacements, and area) and recurrence methods are based on slip rates or recurrence intervals.

2. Northern Basin and Range background seismicity which is characterized by magnitudes ranging from M_w 6.25 to 6.75 and recurrence models are based on the historical earthquake record (1884-1992).

3. ESRP background seismicity which is characterized by magnitudes ranging from M_w 5.0 to 6.0 based on the possible occurrence of the 1905 Shoshone earthquake within the Snake River Plain. Because the ESRP is aseismic, the recurrence is estimated by assuming that 1/3 of the time earthquakes of this magnitude range occur in the ESRP and 2/3 of the time earthquakes of this magnitude range occur outside the ESRP.

4. Volcanic rift zones of the ESRP which are characterized by magnitude ranging from M_w 4.5 to 5.5 based on analogy with other active volcanic rift zones and measurements of fault dimensions for small normal faults produced by dike injection within the volcanic rift zones. The recurrence intervals are based on the recurrence of volcanism (Table 2.6-15).

A site-specific attenuation relationship was developed for the INTEC site using the stochastic numerical ground motion modeling approach [2.51; 2.53] and results of shear-wave velocity measured in boreholes at the ISFSI site and INTEC (see Attachment 6). In addition, four empirical ground motion attenuation relationships, which represent the uncertainty in empirical modeling of earthquake ground motions, were used in the study. The site-specific stochastic attenuation relationship was weighted at 0.6 because it is representative of the ESRP geological conditions which are vastly different for typical California sites. The empirical attenuation relationships [2.215, 2.223, 2.216, 2.206] were weighted individually based on their relative applicability [2.212], but total to a combined weight of 0.4.

Results of the INEEL seismic hazard evaluation significant to the ISFSI include [2.53]:

- The ISFSI is located within the ESRP, which is characterized by a very low rate of seismicity and small magnitude earthquakes. Thus, the background earthquakes within the ESRP contribute very little to the hazard at the ISFSI.

- There is very little contribution from the volcanic rift zones because the volcanic episodes have long recurrence intervals (>15,000 yrs) and any associated seismicity is characterized by small magnitude (< 5.5) earthquakes.

- In general, the stochastic relationship results in lower motions at short periods than the empirical relationships because of the interbedded volcanic stratigraphy which has a lower velocity gradient in the upper 1 km than homogeneous rock and the alternating high and low velocities which tend to dampen out high frequency ground motions.

- At shorter return periods (<2000 yrs) the hazard is dominated by the northern Basin and Range background seismicity due in part to the extremely low level of seismicity in the ESRP and the long recurrence intervals of the Basin and Range faults.

- The Basin and Range faults contribute more to the hazard at 10,000 yrs because this return period approaches the average recurrence interval of the faults.

The results of the 1996 probabilistic seismic hazard evaluation are for rock in the form of mean peak horizontal accelerations and uniform equal hazard spectra for return periods of 500, 1,000, 2,000, and 10,000 years. For the INTEC, the peak horizontal acceleration is 0.13 g at a return period of 2,000 years (Table 2.6-12).

2.6.2.3.7.1.3 <u>Site-Specific Probabilistic Evaluation for ISFSI Seismic Design Parameters</u>

The results of the 1996 INEEL probabilistic study are being used to develop site-specific probabilistic design earthquake ground motion parameters, accelerations and response spectra, for the ISFSI. The response spectra for rock surface conditions are based on the mean uniform hazard spectra (UHS) computed for the site-specific probabilistic analysis at INTEC [2.53]. The UHS were deaggregated to determine the contributions from dominant earthquakes at low and intermediate frequencies. The UHS were supplemented by these results to derive the smoothed rock surface response spectra at damping values of 2, 5, 7, and 10% for 1,000, 2,000, and 10,000 years return periods. Figure 2.6-37 shows the 5% damping curves for the specified return periods [2.179].

The peak horizontal acceleration for rock at a 2,000 year return period is 0.13 g (Table 2.6-11). In addition to the horizontal accelerations, Woodward-Clyde Federal Services [2.179] also calculated vertical accelerations for rock (0.06 g for 1,000 yrs; 0.08 g for 2,000 yrs; 0.13 g for 10,000 yrs) and response spectra (see reference [2.179] for spectra).

Since the ISFSI basemat will be founded in surficial sediments, the design earthquake accelerations and response spectra will include the soil response. A soil velocity profile to a depth of 23 m was developed using shallow seismic and downhole shear-wave measurements obtained from boreholes at the ISFSI site (Table 2.6-15: Figures 2.6-15 , 2.6-43 and 2.6-46) supplemented by data obtained from other boreholes at the INTEC [2.56].

The soil response was incorporated by calculating power spectra that are spectrally matched to the horizontal rock spectra and propagating these spectra through the one-dimensional soil column using a frequency-domain equivalent-linear formulation similar to the program SHAKE [2.180]. This is accomplished by deconvolving the rock power spectra from the soil-rock interface down to a depth of 1 km and then propagating them back up through the rock and soil profiles. Thirty runs were made randomizing the layer thicknesses and velocities to incorporate uncertainties in sediment thickness and shear-wave velocities over the area of the ISFSI site. The total mean thickness of the soil 15.2 m was varied by $\pm$ 6.1 m.

The preliminary mean peak horizontal acceleration for soil surface conditions is 0.30 g at 2,000 years. The horizontal accelerations for the other return periods are shown in Table 2.6-12. The peak vertical acceleration is 0.21 g at 2,000 years (and the others: 0.16 g at 1,000 yrs; 0.33 g at 10,000 yrs). The soil response spectra for return periods of 1,000, 2,000, and 10,000 years at a damping of 5 % for the horizontal and vertical components are shown in Figures 2.6-38 and 2.6-39, respectively. The curves for damping values of 2, 7, and 10% are contained within Woodward-Clyde Federal Services [2.179].

Time histories were also calculated for the ISFSI site. They were developed by combining a Fourier amplitude spectrum with a phase spectrum from an observed strong ground motion record using the procedure of Silva and Lee [2.225]. The strong ground

motion records are from the 1989 M_w Loma Prieta, California and 1980 Irpinia M_w 6.9 earthquakes recorded on rock sites.

2.6.2.3.7.2 ISFSI Seismic Design Parameters

The design basis horizontal acceleration for the ISFSI, including effects for soil amplification is 0.30 g for a 2,000 year return period. The smoothed response spectra used for design is shown in Figures 2.6-38 and 2.6-39. These design values were chosen because they are consistent with NRC regulations for an independent fuel storage facility and the revisions to the INEEL AE Standards. The design basis parameters are site-specific probabilistic results which incorporate all that in known about the geology and seismology of the ESRP region and ISFSI site at this time [2.53; 2.179].

Under the initial license application submittal to the NRC the ISFSI seismic design is based on the deterministic 0.36 g peak horizontal acceleration used in conjunction with the NRC Regulatory Guide 1.60 spectra (consistent with the criteria in the INEEL AE Standards [2.174] at that time). A comparison between the probabilistic response spectra at 0.30 g with the NRC Regulatory Guide 1.60 spectra at 0.36 g shows that the design for the ISFSI site at the deterministic value of 0.36 g exceeds the probabilistic 0.30 g value at all frequencies and results in a more conservative design. Thus, the current ISFSI design will resist stresses induced by seismically transmitted peak horizontal accelerations up to 0.36 g.

Footnote
a - This value is preliminary and will likely change based on incorporation of recently acquired data from boreholes drilled at the ISFSI site.

2.6.3 Surface Faulting

Surface faulting, defined as the rupture of the earth's surface due to tectonic or magmatic activity, is of concern in some areas of INEEL, but not at the ISFSI site itself. The only place on the INEEL that could be affected by surface faulting related to tectonic activity is near the southern tip of the Lemhi fault (Figures 2.6-19 and 2.6-26). It is conceivable that surface faulting associated with an earthquake on the Howe and Fallert Springs segments could extend into the INEEL for a distance of several kilometers in the area just east of the Big Lost River Sinks. The age of most recent earthquake activity on the southern Lemhi fault is given in Section 2.6.2.3.2, Identification and Description of Earthquake Sources: Faults.

Other areas in which surface faulting is of concern are in volcanic rift zones. Areas in and near the Arco and the Lava Ridge-Hells Half Acre volcanic rift zones (Figures 2.6-10 and 2.6-19) have the greatest potential for such dike-induced surface faulting (see section 2.6.6.2.3.3). Also, the fissures north of NRF (Figure 2.6-40) appear to be dike-induced

fissures. The potential recurrence of such fissuring is tied closely to periods of volcanic activity in volcanic rift zones and is quantified in Section 2.6.6.2.3.4.

2.6.3.1 Geologic conditions of the site

See section 2.6.1.2.2.2, ISFSI Site.

2.6.3.2 Evidence of site fault offset

No evidence for fault offset at or near the surface exists in the immediate vicinity of INTEC. Several lineaments are visible on aerial photographs and Landsat images. These lineaments are mostly northeast trending alignments of contrasting density and distribution of vegetation whose origin is most likely due to eolian modifications of old range-fire scars (see for example, [2.113]).

A dense array of drill holes in the INTEC area (shallow geotechnical holes, deeper groundwater monitoring wells, production wells, and injection wells) and several 40- to 50-ft deep excavations to bedrock have revealed no evidence of surface ruptures or displacements in the near-surface basalt lava flows. Geologic cross sections based on lithologic and geophysical logs of many of these holes (Figures 2.6-15, 2.6-16, and 2.6-17) show no evidence of near surface faulting. However, one cross section (Figure 2.6-15) has been interpreted to show doming of some of the deeper basalt/sediment layers [2.57], and some interpretations of subsurface correlation of lava flow units based on paleomagnetism and K/Ar ages of core samples suggest that a graben or downwarp may be present in rocks deeper than about 400 feet and older than about 300,000 years [2.138]. See section 2.6.1.2.3 for a discussion of these interpretions.

Lithologic relationships in numerous drill holes and wells in the INTEC area show no evidence for folding or faulting in the subsurface. Although some basalt lava flows are present in parts of the area and absent in others, it has been demonstrated that they have not been structurally disrupted [2.236]. Their discontinuous distribution is due to pinching out of lavas that flowed into the Big Lost River valley from vents to the southeast and southwest. See section 2.6.1.2.3 for more discussion.

2.6.3.3 Earthquakes associated with capable faults

No capable faults have been identified in the INTEC area, and no significant earthquakes have been recorded or reported in the area. Several microearthquakes have been recorded in the INEEL area since 1972 but they were not felt and they do not define or correlate with faults (see Section 2.6.2.3.4.1.3, INEEL Seismic Monitoring).

2.6.3.4 Investigation of capable faults

See section 2.6.2.3.2, Identification and Description of Earthquake Sources: Faults.

2.6.3.5 Correlation of epicenters with capable faults

The only earthquake epicenters in the INTEC area are microearthquakes and they are not correlated with, nor do they define, capable faults. No capable faults have found in the INTEC area.

2.6.3.6 Description of capable faults

There are no capable faults within 5 miles of the INTEC facility. However, at a distance of 6 miles, just northwest of the NRF facility, is an east-trending, one-mile-long fissure that has a section about 1100 ft long with vertical displacement of about 2 m [2.114]. A little over a mile northwest of this fissure is a shorter northwest trending fissure (Figure 2.6-40). Although these fissures are outside the 5-mile radius stipulated by regulation, the small amount of information relating to their origin and age is presented here.

These fissures appear to be dike-induced fissures like those in ESRP volcanic rift zones but they occur outside of well-defined volcanic rift zones, and the east trend of the southernmost fissure is not consistent with the trend of fissures that would form under the present northeast directed extensional stress field. They occur within the postulated Howe-East Butte volcanic rift zone, the most poorly defined volcanic rift zone on the ESRP [2.45]. It has the lowest vent density, and, if the fissures northwest of NRF are part of it, only two fissures. The ages of lava fields within the postulated volcanic rift zone are 300 to 600 ka [2.45] and, if other rift zone features are present they are covered by sediments or younger lava flows flows from vents in the Axial Volcanic Zone.

The age of the fissures can be constrained only within very broad limits. They cut rocks that are 400,000 to 730,000 years old [2.54], so they must be younger than that. They are covered in places by very recent (<5000 years) alluvial sediments [2.55], so they must be older than that. Although some untried methods could be applied to try to further constrain their age, the chances of success are small.

Information available from geologic mapping of the fissures northwest of NRF and from mapping of volcanic rift zones elsewhere on the ESRP suggests that the NRF fissures do not pose a surface faulting threat to the ISFSI site. The evidence is:

1. The fissures possess many of the characteristics of volcanic rift zone fissures (dike-induced fissures), i.e. mostly dilational displacement, local zones of minor vertical displacement, west to northwest trend, magnitude of dilation and minor vertical offset consistent with injection of a single dike. They do not appear to be tectonic faults.
2. Since the age of basalt lavas and four volcanic vents in the area [2.54] are between 400,000 and 700,000 years old, it is likely, but not proven, that the fissures are close to that age also. This is because the fissures require dike intrusion for their formation and

the most likely time for dike intrusion to have happened was during or soon after the development of the volcanic vents in the area.

3. No recognized tectonic faults occur near the fissures.
4. The section of the southernmost fissure with vertical displacement is so short (~1100 ft) that any prehistoric seismicity associated with its formation would have been very low magnitude.

2.6.3.7 Zone requiring detailed faulting studies

No recorded earthquakes or structures are present within 5 miles of the ISFSI site. Also, the fissures north of NRF are more than 5 miles from the ISFSI site. Therefore, there is no zone requiring detailed faulting studies.

2.6.3.8 Results of faulting investigations

No detailed faulting investigations are necessary within the 5-mile radius, and none have been done for the fissures northwest of NRF.

2.6.4 Stability of Subsurface Materials and Foundations

2.6.4.1 Geologic features

2.6.4.1.1 Surface or subsurface subsidence

Due to the nature of geologic materials and the processes of their formation, several potential conditions can contribute to subsidence. As summarized below, it is demonstrated that none of these potential conditions exist at the ISFSI site.

Lava Tubes. Lava tubes are linear open cavities which allowed lava to flow from its source vent. Their observed dimensions in basalts of the ESRP range up to several tens of kilometers in length and 10 meters in diameter. No lava tubes are recognized in the lava flows at or near the ISFSI site, and the dense pattern of drill holes in the INTEC area has revealed none in the subsurface. The potential for subsidence due to lava tubes at the ISFSI site is extremely low.

Interflow Rubble Zones. In some areas of the ESRP and the INEEL, interflow rubble zones with large void volumes have been observed in outcrops and in drill holes. However, none have been revealed in the drilling that has been done in the INTEC area.

Fine-Grained Sediments. Surficial sediments at INTEC are alluvial deposits of the Big Lost River and consists mostly sandy gravels and gravelly sands. Their thickness ranges from 10 to 15 m, and they are underlain by basalt bedrock. In some places, a 1-2 meter-thick clay layer occurs just above the basalt bedrock [2.56]. Several sediment interbeds

ranging in thickness from 1m to 6m occur within the basalt bedrock between some of the lava flows. These interbeds occur at depths of about 100 ft, 150 ft, 200 ft, 275 ft, 400 ft, 580 ft, and 710 ft [2.56; 2.59]. The interbeds are composed mostly of fine-grained silty sands with some clay lenses. Due to infiltration of water from settling ponds, sewage lagoons, and pipe leaks within the facility some of the interbeds are saturated with perched water bodies. The surficial sediments however are not saturated except in the area directly beneath the settling ponds at the south end of INTEC, over 1000 ft from the ISFSI site. The surficial sediments beneath the ISFSI site, and most of the other facilities at INTEC are dry. Saturation of interbeds is not considered to be a problem for settling of structures or liquification during earthquakes because the shallowest interbed is at a depth of 100 ft, and is overlain by 55-60 ft of basalt bedrock. The surficial sediments are not considered to be a problem for settling or liquification because they are not saturated.

2.6.4.1.2 Previous loading history

Rocks at the surface of the ESRP have no previous loading history. The slow subsidence of the ESRP basin during the past 4 million years has resulted in the continuous accumulation of the basalts and sediments of the Snake River Group. Rocks and sediments at the surface have never been subjected to lithostatic or tectonic loading.

2.6.4.1.3 Rock jointing and weathering patterns, weak materials

This discussion of rock jointing and other zones of discontinuity in the rocks beneath INTEC focuses on two types of discontinuity. The first is discontinuity between lava flows, a result of the emplacement process of the lava flows. The zones between lava flows typically is characterized by a layer of rubble or breccia (Figure 2.6-13), which is composed of blocks of basalt that broke from the advancing front of the overlying lava flow and formed a layer of broken blocks over which the flow advanced. These interflow rubble zones range up to a meter thick and commonly possess a great amount of void space between blocks. That void space can remain open after burial and contribute to groundwater flow in the aquifer, or it can become infilled with silty sediments and become a barrier to water flow. In addition to basal rubble zones, development of fissures in the upper part of lava flows is common during emplacement. This is caused by bending and tilting of solidified crust (sometimes several meters thick) during flow of still-molten lava beneath. Fissures developed by the process can be up to 2 m wide and 3-5 meters deep. They form complex, irregular patterns on the lava flow surface and often are crudely parallel to the edge of the flow. They are sometimes filled by surficial sediments before burial by younger lava flows, and sometimes not.

The second type of structural discontinuity in lava flows is related to cooling and contraction of the lava flow after solidification. This process produces columnar jointing in the lava flow with columns being polygonal in cross section and perpendicular to the lava flow surfaces (Figure 2.6-13). The cooling process also causes development of platy joints parallel to and near the upper and lower surfaces of the lava flow. These two sets

of joints cause the basalt to break into columnar blocks and irregular plates when it is weathered and eroded or when it is broken by excavation or mining processes.

Weathering of basalts beneath INTEC is minor to non-existent because the lava flows are not exposed to surface weathering processes for sufficiently long periods of time before they are buried by younger flows and/or sediments. As basalts are buried to greater and greater depths, they become altered by hydrothermal waters, but that does not happen until depths of over 400 m, well below the effective base of the Snake River Plain aquifer, are reached. Therefore, no altered basalts are present near the surface beneath INTEC.

Fine-grained sedimentary interbeds between lava flows can cause structural weakness in some areas, but at INTEC the first interbed occurs at a depth over 30 m and would not affect foundation integrity. Surficial sediments, being composed of gravels and coarse sands, are not prone to structural weakness.

2.6.4.1.4 Unrelieved residual stresses

Geologic units at and near the surface at the ISFSI site, and throughout the ESRP, have never been buried to greater depths than they are at present, and thus they have not acquired residual stresses from great lithostatic or tectonic loads. The stresses that were generated during cooling and contraction of the basalt lavas were relieved by development of the columnar jointing and platy fracture patterns.

2.6.4.1.5 Hazardous soils

No hazardous soils occur beneath the ISFSI site.

2.6.4.2 Properties of Underlying materials

See section 2.6.4.4

2.6.4.3 Plot Plan

See figure 2.6-14.

2.6.4.4 Soil and Rock Characteristics

The parameters that affect the mechanical behavior of the soils and sediments are summarized below. Refer to Table 2.6-13 for values specific to the INTEC facility

> **Dry density** is the weight of solids per cubic foot of soil. It is determined by weighing the soil after drying in an oven to remove moisture. Also called unit weight, reported in lbs/square ft. It is used in development of many of the other

parameters of soil, including dynamic damping, and helps to evaluate the potential for liquefaction. Values for INTEC soils are typical of those for sandy gravels worldwide.

Relative density is a measure of the soil density at a particular site with respect to the possible range of densities for that particular soil type. It is a measure of how densely or compactly the particles are packed together. Relative density is calculated by a ratio of dry densities (density in densest state times density of sample minus density in loosest state divided by density of sample times difference between density in densest state and the density in loosest state) and usually reported in percent (meaning percent of density in densest state). The relative densities reported for soils at INTEC are mostly in the range of 40 to 100%, corresponding to dense to very dense sands, and thus have a low potential for further compaction and for liquefaction.

Moisture content is the weight of water per unit weight of solids. It is useful for establishing requirements for compaction, if compaction is required. It influences the potential for liquefaction. Since the moisture contents of gravels and sands from the TMI-2 ISFSI site is so low, generally less than 20%, reflecting the unsaturated condition of the soils, there is very little potential for either liquefaction or for consolidation (see description of consolidation characteristics below).

Porosity is the fraction or percentage of bulk volume that is not occupied by solids, or, in other words the fraction or percentage of bulk volume occupied by voids or pores. It is a general indicator of the potential of the soil for further compaction, and obviously closely related to density and relative density. Porosities reported for INTEC soils are 30 to 40% and are slightly lower than porosities for most graded gravels and sands composed of rounded grains (36-46%). Again, this suggests a relatively low potential for further reduction in pore volume by compaction or settling.

Strength characteristics are parameters that describe the resistance to shear. They are "C", which is cohesion or interparticle attraction, and ϕ, which is the angle of internal friction or the resistance to interparticle slip. The sandy gravels at INTEC have "C" values of 0, indicating that they are cohesionless. The angle of internal friction for INTEC sandy gravels ranges from 35° to 45° and corresponds to values for dense sands. This indicates a relatively high resistance to interparticle slip. Natural cohesionless materials (sand and gravels) range from $<30^o$ for very loose sands to $>45^o$ for very dense sands.

Vp is the velocity at which seismic compression waves travel through the material, often referred to as P-wave velocity. Used for seismic hazards

assessments. The values reported for INTEC and for the TMI-2 ISFSI site (400 to 1000 m/sec) are typical of values for gravels and sands worldwide.

Vs is the velocity at which seismic shear waves travel through the material, often referred to as S-wave velocity or shear velocity. It is an important input parameter for the stochastic ground motion model used for seismic hazards assessment at INTEC and the TMI-2 ISFSI site. Also, it is very important in estimation of the amplification of ground motion by the upper layer of soil at the site. It is also useful for evaluation of liquefaction potential (see Section 2.6.4.8). Reported Vs for INTEC and the TMI-2 ISFSI site range from about 230 to 600 m/sec and are typical of values for stiff soils and cohesionless sands and gravels worldwide.

Damping is a measure of the vibrational energy absorbing characteristic of the soil. It is used in seismic design of foundations and structures. Although some tests have been done on sieved and reconstituted samples from INTEC, little confidence is given to the results. Since it is not possible to obtain undisturbed samples at INTEC for lab tests, Dames and Moore [2.237] recommend using the average of measured damping values for sand [2.239].

Shear Modulus (G) is the ratio of shear stress to shear strain. It is used to estimate the foundation frequency and displacement amplitudes during seismic ground shaking. For earthquake ground motion estimations it is usually measured in the lab using undisturbed samples from the soils at the site. It can be measured in the lab using either cyclic loading or resonant column apparatii. Because undisturbed samples of the coarse sandy gravels at INTEC and the TMI-2 ISFSI site cannot be obtained, the values reported have been measured in the lab using sieved and reconstituted samples from INTEC soils or estimated using empirical equations. It can also be estimated by multiplying the soil density by the shear wave velocity squared.

Poisson's Ratio is the ratio of transverse to axial strain. It describes the amount of lateral bulging that accompanies axial compression in rock or soil samples. It is an input parameter for calculation of soil spring constant (i.e., modulus of subgrade reaction), of the dynamic shear modulus, and also allows estimation of Vs from measured Vp. Most natural soils and rocks have values between 0 and 0.5. Values measured at INTEC range from 0.27 to 0.45. Most sands worldwide have values from 0.3 to 0.35, so the alluvial soils at INTEC are fairly typical.

Static modulus of elasticity (E) is the ratio of stress increment to the strain that it produces. It is essentially the slope of the stress-strain curve for elastic or nearly elastic materials, and is often not constant throughout the range of possible stresses. It also varies with load, as seen in Table 2.6-13.

Bulk Modulus (K) describes the rate of density change with change in confining pressure. It is used in the determination of the amount of settlement that will occur beneath a structure. It is closely related to the static modulus of elasticity, and Table 2.6-13 reports similar values for these two parameters.

Consolidation characteristics consist of Cv, the coefficient of consolidation, and Cc, the compression index. They provide a measure of the time dependent volume change due to an applied load in saturated soils. In saturated conditions the applied load is commonly supported initially by pore pressure, and over time the pore fluid is forced from the voids and the load is gradually transferred to the soil framework (grains). Consolidation is defined as the time-dependent volume reduction accompanying this transfer of the load. For unsaturated, cohesionless, granular soils (as those at the TMI-2 ISFSI site) the transfer of load to the soil framework is immediate and there is very little time dependent behavior. This is illustrated by the very low Cv and Cc values reported for INTEC soils. The term consolidation may not be applicable to unsaturated granular soils, and some geotechnical engineers prefer to use the term settlement.

2.6.4.5 Excavations and backfill

The only excavation will be for the installation of the concrete pad. These excavations will be shallow and be backfilled with removed soil and compacted per engineering specifications.

2.6.4.6 Groundwater conditions

The INEEL TMI-2 ISFSI will not affect groundwater and the groundwater will not affect the INEEL TMI-2 ISFSI.

2.6.4.7 Response of soil and rock to dynamic loading

Dynamic test results, seismic wave velocities, etc for INTEC facilities summarized in Table 2.6-16.

2.6.4.8 Liquefaction potential

Alluvial sediments above the first basalt at the INTEC are mostly sandy gravels and gravelly sands with the gravel content ranging from 20% to 66% in 26 samples at the High Level Waste Tank Farm [2.56]. The coarseness of this material, and the fact that it is in the vadose zone far above the water table indicates that liquefaction is not a problem for structures in the INTEC area. Atterberg limits for silty, clayey, and fine sandy sediments that sometimes occur in a thin layer just above the first basalt have been determined for 3 samples by Golder Associates, 1992. They are summarized below:

Liquid Limit	Plastic Limit	Plasticity Index	Moisture Content	Liquidity Index
26	19	7	20.5	0.17
35	18	17	24.8	0.41
23	21	2	20.5	0

All of the geotechnical data for soils at the INTEC and TMI-2 ISFSI site show that the site will be stable with respect to landsliding, slumping, and liquefaction during earthquake ground shaking. Although most of the data provided in Table 2.6-13 represents samples from outside the TMI-2 ISFSI site, it is generally applicable to the TMI-2 ISFSI site because the soils encountered in the subsurface throughout the INTEC site are virtually identical. There are minor variations in relative percentages of gravel, sand, and silt, and most places exhibit crude stratification of sand-rich and sand-poor layers, but the stratigraphy is remarkably uniform throughout the INTEC area. Specific indicators of soil stability include very gentle surface gradient, unsaturated conditions, low water contents of the soils, high blow counts in standard penetration tests, high shear wave velocity, and large grain size. Following is a discussion of each of these factors.

There is no potential for landsliding or slumping because the topography of the site is essentially flat Figures 2.6-9 and 2.6-41. Maximum surface gradients are in the range of 10 feet per mile.

The surface soils are over 400 feet above the water table and have water contents of 20% or less. It is possible that saturated conditions could exist locally and temporarily due to flooding or to the proximity to percolation ponds. However, no saturation of surficial sediments has been observed at or near the TMI-2 ISFSI site during the history of operations at INTEC. The percolation ponds are located at the far south end of INTEC and do not have influence on the surficial sediment conditions at the TMI-2 ISFSI site. Temporary saturation of sediments has been observed in the vicinity of the Big Lost River at the far north end of the INTEC during times when the river flows through the area, but the TMI-2 ISFSI site is so far from the river's course that it has never been affected. Even if an exceptionally large flood caused temporary saturation of the soils at the TMI-2 ISFSI site, other factors (discussed below) would still prevent the occurrence of liquefaction or subsidence during potential seismic events.

During drilling of several boreholes in and around the TMI-2 ISFSI site in the fall of 1997, standard penetration tests (SPT) were performed at intervals during the drilling (Table 2.6-14). The ranges observed for the TMI-2 ISFSI site are plotted in Figure 2.6-42 showing SPT (N)-Blows per foot vs. cyclic stress ratio [2.239]. The range of values in which liquefaction is possible is 4 - 35, and increases with increasing cyclic stress ratio. Although we do not know the cyclic stress ratio of INTEC and TMI-2 ISFSI soils, the figure shows that all but one or two tests have over 35 blows per foot, ranging up to 178 for depths of about 5 feet and to 224 for depths of about 20 feet. In fact, for depths of

about 20 feet the lowest blows per foot is about 70, twice the number below which liquefaction is possible.

Shear wave velocity is another parameter which can help evaluate the potential for liquefaction. Shear wave velocities were determined in 7 boreholes in and around the TMI-2 ISFSI site in the fall of 1997 (Table 2.6-15). The ranges of values measured are plotted in Figure 2.6-43 showing cyclic stress ratio verses shear wave velocity [2.238, 2.239]. Only one borehole (#5) has velocities low enough at a depth of about 5 feet to encroach on the liquefaction field, but the large grain size at that spot (57% gravel) precludes development of excess pore pressure and liquefaction will not occur.

The potential for liquefaction is also influenced by the grain size of the soil. Particle size distributions for samples from the boreholes at the TMI-2 ISFSI site Figure 2.6-44 show that the material consists of 48 to 68% gravel, the rest being made up of sand and silt. Soils in which liquefaction has been observed to occur are typically uniform, saturated sands. Gravels such as those at the TMI-2 ISFSI site have not been known to liquefy because the pore size is so large (due to the gravel-sized particles) that excess pore pressure cannot be maintained.

Lithologic logs (Figure 2.6-45) and seismic velocity profiles (Figure 2.6-46) for TMI-2 ISFSI boreholes drilled in 1997 are provided so that the spatial distribution of sediment types and seismic velocities can be better visualized. Using these figures in conjunction with the map of borehole locations and bedrock elevation contours (Figure 2.6-14) shows that most of the TMI-2 ISFSI is underlain by a moderate thickness (40 ft or less) of sandy gravel. In the northwest corner of the site the bedrock is deeper (up to about 55 feet) and a layer of silt occurs between the basalt bedrock and the overlying gravels. The seismic velocity profiles for the drill holes are arranged from deeper bedrock (northwest part of the site) to shallower bedrock (southeast part of the site). The velocity range in which liquefaction is possible in uniform sands is plotted on the velocity profiles to show that the velocities in only a few of the boreholes approach the low velocities necessary for liquefaction, and that is only in the upper few meters of the boreholes.

2.6.4.9 Earthquake design bases

See section 2.6.2.3.7.2 - Seismic Design Parameters.

2.6.4.10 Static Analysis

See section 2.6.2.3.7.2 - Seismic Design Parameters.

2.6.4.11 Techniques to improve subsurface conditions

No improvements in subsurface conditions are necessary

2.6.5 Slope Stability

Slopes in the ISFSI site area are very small (Figure 2.6-41), a few feet per mile at most, and pose no threat for instability or landsliding.

2.6.5.1 Slope Characteristics

The only slopes involved with the INEEL TMI-2 ISFSI are the slopes at the edges of the concrete pad. These slopes are due to the pad being raised slightly from grade due to flood considerations. These are engineered slopes and are discussed in the SAR.

2.6.5.2 Design Criteria and Analysis

See section 2.6.2.3.7.2 - Seismic Design Parameters.

2.6.5.3 Logs of Core Borings in Borrow Areas

No borrow areas are anticipated.

2.6.5.4 Compaction Specifications

The pad specification will require a proof rolling of the natural soil and backfill as required to provide a 5 ksf minimum strength for the subgrade.

2.6.6 Volcanism

2.6.6.1 Introduction

The regional tectonic framework of ESRP volcanism has previously been introduced in Section 2.6.1. Basaltic and rhyolitic volcanism has affected the ESRP for about the past 10 Ma, and has continued into geologically recent time. No historical eruptions have occurred on the ESRP, but lava flows issued as recently as 2,100 years ago from the Great Rift, about 25 km southwest of the INEEL. Other Holocene basaltic lava fields near the southern INEEL boundary are nearly as young, and range from about 5,000 and 13,000 years in age [2.167]. Many basaltic and three rhyolitic vents located within the present INEEL boundary erupted between about 200,000 and 1.2 million years ago [2.54]. For these reasons, an assessment of volcanic hazards at the ISFSI site is warranted, and such an evaluation is based on the record of past volcanism in the region.

In this section, information on the timing, distribution and eruptive character of volcanism that could affect the ISFSI site is summarized. Potential volcanic hazards are grouped into two categories: those related to volcanic sources within the INEEL area, and those related to distant, non-ESRP sources. For near-field volcanism, the volcanic history of the ESRP and the INEEL area (Figures 2.6-6, 2.6-10, and 2.6-12] dictates three varieties of volcanism be evaluated: (1) The formation of future silicic calderas and associate eruptions of voluminous ash and pumice, as occurred in the INEEL area between about 6.5 and 4.3 Ma, during passage of the Yellowstone mantle plume [2.32; Figure 2.6-6]. (2) The growth of new silicic lava domes near INEEL, as occurred at Big Southern Butte (0.3 Ma), East Butte (0.6 Ma) and elsewhere along the Axial Volcanic Zone near the southern INEEL (Figure 2.6-12) [2.54]. (3) Phenomena related to Quaternary ESRP basaltic volcanism, largely involving the effusion of lava flows and magma-induced ground fissuring across the INEEL area (Figure 2.6-10 and Table 2.6-16).

Potential impacts from distant volcanic sources include: (1) Pyroclastic flows or tephra fall from explosive-silicic eruptions of the Yellowstone Plateau, 100-200 km northeast of the INEEL; and (2) Tephra fall from the Cascade volcanoes and other explosive volcanic centers in the western U.S.

Up-to-date references on general aspects of volcanism and associate volcanic hazards include Wohletz and Heiken [2.181], Blong [2.182] and Latter [2.183]. Data and analysis specific to INEEL volcanic hazards have been compiled by Volcanism Working Group [2.184]. Subsequent, related publications address ESRP regional tectonics [2.127; 2.34; 2.126; 2.32; 2.33] and ESRP volcanism [2.185; 2.45; 2.108]. In addition, detailed geologic mapping [2.54; 2.114] has led to improved knowledge of basaltic-vent and fissure locations in the INEEL area.

2.6.6.2 Potential Volcanic Hazards of the INEEL Area and the ISFSI Site

Table 2.6-13 summarizes the important characteristics of volcanism in the INEEL area. The nature and timing of volcanism is reconstructed from interpretation of ESRP volcanic deposits, and from the results of K-Ar dating of volcanic rocks. Observations of historical volcanic phenomena are also useful toward understanding prehistoric INEEL volcanism, particularly the volcanic rift zone eruptions of Iceland and Hawaii, and the growth of silicic lava domes at various volcanic centers along the Pacific rim.

2.6.6.2.1 Formation of ESRP Silicic Calderas and Related Volcanism

Explosive, voluminous eruptions of silicic pumice and ash, and associated caldera collapse occurred on the ESRP during passage of the Yellowstone hotspot between about 6.5 and 4.3 Ma [2.34; 2.32; Figure 2.6-6]. Tephra-fall and pyroclastic-flow deposits from

these eruptions were dispersed over tens of thousands of square kilometers in southern Idaho and adjoining states, and are known as the Heise Volcanics [2.108].

The risk of explosive-silicic volcanism and caldera formation in the INEEL area and at the ISFSI site is considered negligible for these reasons [2.184]:

1. The mantle plume (Yellowstone hotspot) - which has been the apparent energy source of voluminous, caldera-forming, silicic volcanism on the ESRP - has now moved under the Yellowstone Plateau, 100 to 200 km northeast of the INEEL, and accounts for the Quaternary silicic volcanism and ongoing hydrothermal activity of that area [2.34; 2.32].
2. Thermal modeling [2.124] and geophysical studies of the ESRP crustal structure [2.84] show that the silicic magma chambers inferred to have existed in the shallow crust of the ESRP during late Tertiary time are now entirely solidified and are therefore incapable of erupting.
3. The recurrence intervals (quiescent periods) between major caldera eruptions on the ESRP and the Yellowstone Plateau were 0.5 to 1.7 Ma long. Two-and-one-half to eight recurrence intervals (4.3 Ma since latest such ESRP eruption) have therefore elapsed in the INEEL area, suggesting that caldera-related silicic volcanism has ceased.
4. The time-transgressive pattern of ESRP - Yellowstone silicic volcanism suggests that explosive silicic volcanism expires after basaltic lava flows have filled the calderas. On the ESRP, the late-Tertiary-silicic calderas are buried by up to several km of late-Tertiary-to-Quaternary basalt and sediment.
5. Geothermal, geophysical, and geodetic anomalies indicating the presence of large shallow silicic magma chambers occur at such places as Yellowstone National Park and Long Valley, California. The anomalies include extremely high heat flow [2.35], low seismic velocities at shallow crustal levels [2.85, 2.115; 2.36], abundant hot spring and geyser activity [2.86; 2.87], persistent swarms of seismic activity [2.85, 2.115; 2.186], and rapid rise and fall (meter-scale inflation and deflation within months to years) of land surface elevations [2.85, 2.115; 2.187]. None of these phenomena occur beneath the ESRP.

2.6.6.2.2 Growth of rhyolitic domes, intrusions and related phenomena

Volcanic domes are steep-sided mounds of lava, commonly of silicic (rhyolitic) composition, for which the magma is too viscous to flow more than a few kilometers from the vent (Figure 2.6-12). The growth of domes is predominately an effusive process, and blocks of the surrounding terrain can be uplifted and tilted as the viscous magma approaches the surface [2.188]. Growing domes are steep sided and rubbly, gravitatively unstable, and are therefore prone to slope failure. In addition, dome lavas commonly contain sufficient dissolved gas to generate small explosions. As a result, small-volume tephra-fall deposits and blocky pyroclastic flows are frequently associated with dome growth [2.189; 2.181].

Several small (< 7 km^3) rhyolite domes were emplaced in the INEEL area during the past 1.2 Ma, located along the axial volcanic zone (Table 2.6-16 and Figure 2.6-12): Big Southern Butte (0.3 Ma) [2.188; 2.190], Cedar Butte (0.4 Ma) [2.191], East Butte (0.6 Ma), Middle Butte (inferred as uplifted by a shallow silicic intrusion; uplifted basalt dated at 1.1 Ma), and an unnamed butte (1.2 Ma). The estimated recurrence interval for ESRP silicic-dome effusion in the INEEL area is 200 Ka (5×10^{-6} / yr), based on 5 domes (those cited above), emplaced within a one-million-year period (1.2 Ma to 0.3 Ma).

The Quaternary rhyolitic domes postdate the earlier caldera-related silicic volcanism by about 3 million years, and they are compositionally dissimilar to the caldera rhyolites [2.31], suggesting they are volcanologically distinct phenomena. Although tephra falls and small-volume pyroclastic flows are commonly associated with silicic-dome growth, no such deposits have been identified in the INEEL area, probably owing to coverage by younger basaltic lava and sediment. Several centimeters of tephra could accumulate 10 km or more downwind of growing volcanic domes. Given the flat terrain of the ESRP, the major effects of dome effusion, intrusion and uplift, pyroclastic volcanism and corrosive gases would likely be restricted to about 5 km from a growing volcanic dome. Any fumes and tephra associated with dome growth along the axial volcanic zone would probably be carried northeastward along the southern INEEL boundary, and eventually off-site, by prevailing southwesterly winds.

Based on the apparent 200-Ka recurrence interval (5×10^{-6} per yr) and the likely restriction of hazardous phenomena to near-vent areas, the probability of a silicic dome affecting the central and northern INEEL (including the ISFSI site) is judged to be very small ($<< 10^{-6}$ / yr). The most likely area of future silicic-dome emplacement is along the axial volcanic zone; hence, the probabilistic risk of impact on southern-INEEL facilities would be somewhat higher, but still $< 10^{-6}$ / yr.

2.6.6.2.3 Basaltic Volcanism and Related Phenomena

With the exception of localized and infrequent silicic dome volcanism (Figure 2.6-12 and Table 2.6-16) Quaternary volcanism of the INEEL area has been predominately basaltic. Potassium-argon (K-Ar) dating of lava flows [2.54] demonstrates that the ages of basaltic vents on the INEEL range from > 1 Ma on the northern INEEL, to about 0.2 Ma on the southern INEEL near the axial volcanic zone. Although their vents are not situated on the INEEL, four Holocene basalt lava fields erupted along the axial volcanic zone between about 13,000 and 5,000 years ago [2.167]. In one case, the 13.4 Ka Cerro Grande lava field crossed what is now the southern INEEL boundary. Quaternary basaltic volcanism on the ESRP has largely involved mild, effusive outpourings of fluid lava flows from eruptive fissures and small, low-lying shield volcanoes [2.192; 2.45].

2.6.6.2.3.1 Volcanic Rift Zones

Basaltic vents are not randomly disseminated across the INEEL area, but tend to concentrate in northwest-trending, linear belts [2.185; 2.45], known as volcanic rift zones (Figures 2.6-9 and 2.6-10). These belts are marked by basaltic vents as well as open fissures, monoclines and small normal faults - structures that were produced during propagation of vertical dikes (0 to 4 km deep) that fed the surface eruptions (Figure 2.6-48) [2.135; 2.165; 2.33; 2.59]. ESRP volcanic-rift zones are inferred to be underlain by basaltic-dike swarms, based on their surface-deformation features and their equivocal correspondence with positive aeromagnetic- and gravity anomalies [2.193]. ESRP volcanic-rift zones are polygenetic features, i.e., were apparently active through numerous cycles of volcanism. The Great Rift (Figure 2.6-10) has well-developed volcanic landforms and surface-deformation features that formed during eight cycles of Holocene volcanism [2.194]. The Arco volcanic-rift zone is more diffuse and diachronous, with fissures and vents dispersed across an 8-km-wide belt (Figures 2.6-10 and 2.6-49), formed by multiple cycles of volcanism during the period 600 Ka to 10 Ka. The Lava Ridge - Hells Half Acre volcanic-rift zone is a strongly diachronous feature; its northern portion is occupied by lavas > 1 Ma in age, and its southern terminus is marked by the 5.2 Ka Hells Half Acre lava field and dike-induced fissures (Figures 2.6-10 and 2.6-49). Its central region is poorly developed, and is marked by a single monocline that was likely induced by dike intrusion (Figure 2.6-49). The Howe - East Butte volcanic rift zone [2.169] is poorly expressed surficially, and is largely covered by fluvial and lacustrine sediment on the central INEEL; five vents and several isolated fissures Figure 2.6-49) are associated with a positive, northwest-trending aeromagnetic anomaly [2.193].

2.6.6.2.3.2 Axial Volcanic Zone

The most voluminous and recent volcanism in the INEEL area occurred during the past 1.2 Ma along the axial volcanic zone, which is a broad, northeast-trending constructional-volcanic highland consisting of coalesced basaltic shield volcanoes, tephra cones and isolated silicic domes. The axial volcanic zone forms a topographic divide along the ESRP axis. It differs from volcanic-rift zones because northwest-trending fissure swarms that typify volcanic-rift zones are rare, and its overall topographic orientation is perpendicular to the regional stress field. Basaltic-dike-intrusion processes along the axial volcanic zone are probably similar to those of volcanic-rift zones, but increased magma supply along the ESRP axis and the predominance of large shield volcanoes has apparently covered most of the dike-induced surface deformation along the axial volcanic zone.

2.6.6.2.3.3 Volcanic Hazards at the ISFSI site.

Table 2.6-17 lists hazards associated with ESRP basaltic volcanism, based on interpretation of the ESRP eruption products, and by analogy with historical observations of rift-zone volcanism in Hawaii and Iceland. [Note: seismicity related to basaltic dike intrusion along volcanic rift zones is discussed in sections 2.6.2.3.5.5 - ESRP Volcanic Zones] The most significant hazard is inundation or burning of facilities by lava flows.

Such flows vary greatly in volume and may cover a few square kilometers to 400 square kilometers or more [2.45]. On gentle terrain such as the ESRP, lava flows would generally move down-slope at a few meters per minute. Large lava flows on the ESRP seldom exceed 30 km in length, and most are < 12 km long. Borehole investigations and outcrop studies indicate that most ESRP basaltic lava flows are < 10 m thick, and taper to several-meter thickness at flow edges. They are therefore unlikely to surmount major topographic or manmade obstacles. The general topography and vent locations of the INEEL area (Figures 2.6-9 and 2.6-49) suggest that future lavas will most likely erupt from vents along the axial volcanic zone or at the intersections of that zone with the volcanic-rift zones, from which they could flow toward the central INEEL and the ISFSI site.

2.6.6.2.3.4 Volcanic Recurrence and Probabilistic Risk for the ISFSI site

Although volcanic hazards can be qualitatively identified on the basis of the geologic record, risk is more difficult to assess because risk is usually expressed quantitatively and in probabilistic terms. Volcanic hazards may exist, but there can be no risk unless life or property are threatened. Risk can be thought of as the product or interplay of (some hazardous phenomenon) x (its potential impact on life or property at a given location). Quantitative risk assessment requires not only detailed knowledge of the timing and nature of past volcanism, but also the conditional probability of its impact on human life or property. Conditional probabilities take into account not only volcanic-recurrence intervals, but also nonvolcanic parameters such as distance from vents, local-terrain configuration, and prevailing-wind directions.

Table 2.6-18 gives estimated volcanic recurrence intervals for INEEL volcanic zones and borehole sites, estimated by summation of individual vents and fissures in the respective volcanic zones, and dividing that sum by the total time period of volcanism within each zone. This approach gives minimum-recurrence estimates and is very conservative, because it is assumed that every vent or fissure (sometimes a set of fissures, when they could be confidently grouped as cogenetic) represents a single eruptive episode. It is more likely that each eruptive episode involved eruptions from several vents and the opening of multiple fissures, based on the record of Holocene volcanism and on analysis of ESRP magma generation, rise and storage [2.185; 2.33].

In general terms, Table 2.6-18, and Figures 2.6-10 and 2.6-49 suggest that the shortest recurrence intervals (16,000 to 17,000 years), the most recent volcanism (Holocene lava fields), and hence the most probable areas of future basaltic volcanism and ground deformation, are the axial volcanic zone and the Arco volcanic rift zone. Within this context, Volcanism Working Group [2.184] estimated the conditional probability of basaltic volcanism to affect a south-central INEEL site as being < 10^{-5} per year.

For the TMI-2 ISFSI site the probability of inundation can be more closely estimated by employing all of the parameters contributing to the probability. The parameters that are important to the estimation of probability include:

1. Volcanic recurrence interval of the source zone or zones
2. Topographic setting of the site and the potential sources
3. Statistics of lengths and areas of lava flows
4. Distance from the site to potential sources of lavas
5. The potential for mitigation of the lava flow hazard

The three cases below are provided to illustrate the estimation of inundation probability.

Volcanic Source Zone	**Case 1** Probability of an eruption somewhere within the source zone	**Case 2** Probability of inundation at a random site within the source zone	**Case 3** Inundation probability at TMI-2 ISFSI site
Combined Axial Volcanic Zone and Arco VRZ	~6 x 10^{-5}/yr	~2.6 x 10^{-6}/yr	~5.2 x 10^{-6}/yr without mitigation ~10^{-6} to 10^{-7}/yr with mitigation

In **Case 1**, the probability of an eruption somewhere (anywhere) within the volcanic source zone is simply based on the number of vents and fissure sets within the Arco Volcanic Rift Zone and the Axial Volcanic Zone and the age range of volcanism for those zones. It is simply the "source term", or "recurrence term" for a zone or region, and contains no information about the "magnitude" of the event. It is derived by dividing the number of vent/fissure sets into the age range of volcanism, as illustrated in Table 2.6-18. It is the highest probability of the three cases because it allows for the volcanism to occur anywhere within the combined area of the two zones, and makes no prediction for any particular spot. Therefore it is not applicable to any specific site.

Case 2 illustrates estimation of the probability of inundation of a random spot within the volcanic source zone. This case goes beyond Case 1 by incorporating a "magnitude" term, and making some assessment of the likelihood that some site will be affected. The assessment of likelihood is achieved by taking into account the area of coverage (the "magnitude") of the average lava flow (100 km^2 - Table 2.6-19) in relation to the total area of the source zone (~2270 km^2). Because it selects no specific spot, it ignores the effects of topography, the distance from potential sources, and the potential for mitigation. It is estimated by simply multiplying the result of Case 1 (6 x 10^{-5}/yr) by the ratio of average area covered by a typical ESRP lava flow to the total area of the volcanic source zone ($100km^2/2270km^2$). The result (2.6 x 10^{-6}/yr) is analogous to the estimation

made by the Volcanism Working Group [2.184], and is in fact less than 10^{-5}/yr, exactly as the group predicted.

Case 3 is the probability of inundation at the ISFSI site. This assessment goes beyond Case 2 because we are now dealing with a specific site. Therefore, the topographic setting, the statistics of lava flow length, and the potential for mitigation can all be brought to bear on the problem. The ISFSI site lies outside the volcanic source zone, and its topographic setting within the valley of the Big Lost River defines the specific part of the volcanic source zone which can send lava flows on a path towards the site. In Figure 2.6-50 that specific part of the volcanic source zone is called the "critical volcanic source area". It is defined on the south, southeast, and southwest by the topographic divide that separates the Big Lost River drainage basin from that of the Snake River. Lavas which erupt south of that divide will flow south, away from the ISFSI site, and are of no concern for lava inundation at the site. It is defined on the north by the northern edge of the volcanic source zone. Topography also shows that lavas originating from any place on the Axial Volcanic Zone northeast of East Butte will not flow in the direction of the ISFSI site. The critical volcanic source area encompasses 660 km^2 (or 29%) of the total 2270 km^2 area of the combined Arco volcanic rift zone and the Axial Volcanic Zone. In addition, the site is located over 10 km (50th percentile lava flow length - Table 2.6-20) from the closest approach of the critical volcanic source area (Figure 2.6-49) and most of the source area is farther than 16 km (70th percentile lava flow length - Table 2.6-20) from the site. Using the 70th percentile distance of 16 km (only 30% of flows from that distance will reach the site) we derive the annual probability of inundation at 5.2×10^{-6}. This is obtained by multiplying the Case 1 probability (6×10^{-5}/yr) by the percentage of the total area of the source zone that is encompassed by the critical volcanic source area (29%) and by the percentage of lava flows from the critical volcanic source area that will reach the site (30%). This estimated annual probability of inundation at the site (5.2×10^{-6}) is conservative for several reasons.

1. Almost all of the critical volcanic source area is farther from the site than the 70th percentile distance (some of it is twice that distance) and therefore much smaller percentages of lava flows will reach the site from those distances.
2. The probability of eruption within the volcanic source zone is conservative because we double-counted the vents in the overlap zones of the volcanic rift zones with the Axial Volcanic Zone. Removing this conservatism alone will reduce the annual probability of inundation at the site to 3.8×10^{-6}.
3. No allowance is made for mitigation. Although the effectiveness of mitigation is difficult to assess, there are reasons to believe that actions can be taken to mitigate the hazard. First, the INEEL seismic network is well suited to detect seismicity associated with rising magma from the mantle, and has appropriate station spacing to accurately locate the most likely areas of eruption. Seismicity-detected ascent rates of basaltic magmas from source regions at 40-60 km depth beneath Kilauea and Mauna Loa volcanoes, Hawaii, show that several weeks to several months are required for magma to rise to upper crustal chambers beneath the volcano summits [2.240, 2.241]. Since the magma source beneath the ESRP is at 50-200 km depth [2.242] our seismic

network may provide similar warning time even though the tectonic setting of the ESRP is different from Hawaii's. Second, basaltic lava flows on the ESRP have relatively low flow velocities because of low topographic gradients. Analogy to flow velocities in other areas of the world in similar terrains shows that velocities of about 2 km/day are most likely, and thus it would take several days for lava from most of the critical volcanic source area to reach the site. Therefore, the warning time that would likely be available to us would be in the range of weeks to months. During that time any of a number of mitigation actions could be taken, and given a month or more of warning, mitigation strategies are likely to be successful. Potential mitigation actions include removal of the fuel storage modules from the area, building of earthen berms around the facility, building of earthen berms in the flow path to slow or divert the advance, cooling of the lava flow front with water sprays to slow or divert the advance, and use of explosives at or near the vent area to create opportunities for lava to flow in other directions. Some of these strategies have been used successfully in Iceland and in Italy, and are likely to be successful here. Even if mitigation were successful only half the time the inundation probability would be further reduced to less than $2x10^{-6}$/year; higher potential of success is more likely and would reduce the probabilities into the 10^{-6} to 10^{-7} range.

2.6.6.3 Potential Volcanic Hazards from Distant Sources

The locations and general characteristics of potentially hazardous volcanoes in the western U.S. are summarized by Bailey and others [2.195] and Wright and Pierson [2.196], and potential impacts to the INEEL from eruptions of those volcanoes are addressed by Volcanism Working Group [2.184]. The selective analysis given below supports the general conclusion that significant impacts to the INEEL from distant volcanic eruptions are highly improbable.

2.6.6.3.1 Yellowstone Plateau

Geologic and geophysical investigations [2.36] indicate that the mantle plume that has left its 15-million-year track across southern Idaho and formed the Snake River Plain, now resides beneath the Yellowstone Plateau, explaining the crustal structure, high heat flow, geothermal features, and explosive silicic volcanism of that area. The Yellowstone Plateau volcanic field has produced more than 6,000 km^3 of silicic tephra, in 3 cycles of explosive, caldera-related volcanism during the past 2.1 Ma, largely in the form of tephra-fall and pyroclastic-flow deposits [2.37]. Ash layers from Yellowstone have been identified in the Quaternary stratigraphic record across much of western North America [2.197]. Eruptions of this magnitude are rare in the worldwide geologic record, and the three climactic Yellowstone eruptions occurred at 2.1 Ma, 1.3 Ma and 0.6 Ma [2.37], for an average recurrence interval of 700,000 years.

Hazards at the ISFSI site from potential Yellowstone eruptions include blanketing by pyroclastic flows or volcanic ash. The facility lies about 160 km from the Yellowstone caldera rim, and more than 200 km from the Hot Springs Basin area of northeastern Yellowstone, a likely site of future eruptions. For comparison, maximum-runout distances of large-volume pyroclastic flows (ignimbrites) from Yellowstone, the ESRP and elsewhere, traveling on relatively flat terrain, generally range from 100 to 150 km. Hence, the likelihood of pyroclastic flows from even the largest Yellowstone eruptions reaching the INEEL is essentially nonexistent, because of the great distance and intervening topographic barriers.

Although there is no direct relationship between ashfall thickness and damage parameters [2.182], the historical eruptions of Mt. St. Helens demonstrate that about 8 cm of ash can generally be accommodated by the infrastructure of a technologically advanced nation, without serious long-term consequences [2.198]. Ash-fall thickness from Yellowstone could exceed 8 cm if there were a large (> 40 km^3) eruption, and if wind conditions were to disperse the ash cloud directly over the INEEL. Such conditions are conceivable in light of past Yellowstone volcanism, but are highly improbable because prevailing winds would not likely direct ash toward INEEL and because the recurrence intervals of such events are extremely long (0.5 to 1 Ma). It is worth noting that less than 5 cm of Yellowstone ash have been found on the ESRP at INEEL-equivalent distances [2.197].

2.6.6.3.2 Cascade volcanoes and other western-U.S. centers

The Cascade volcanoes of Northern California, Oregon and Washington have produced many Quaternary tephra layers, some of them widely dispersed across the western U.S. [2.199]. These centers lie 700 to 800 km west of the INEEL, at distances and prevailing-wind directions that prevent all but the largest ashfall eruptions from impacting the INEEL area. The Mazama ash is a voluminous (ca. 40 km^3) and widespread ash layer that erupted from what is now Crater Lake, Oregon, and is a product of the largest-known Cascade eruption. In the INEEL area, the Mazama ash is 0.5 - 2 cm thick [2.200]. Theoretical considerations and field measurements indicate that < 6 cm of Mazama ash would have fallen on the INEEL, if the dispersal axis of the cloud were directly overhead. This effectively eliminates all Cascade volcanoes as sources of significant (> 8 cm) ashfall at the INEEL.

A similar conclusion is reached for other western-U.S. volcanoes, such as the Long Valley caldera which erupted about 600 Ka and produced the 600-km^3 Bishop Tuff . Long Valley is more than 800 km southwest of the INEEL. As per the Yellowstone analysis given above, significant (> 8 cm) ash fall could be expected only for improbable conditions and at extremely long recurrence intervals.

2.6.6.4 Conclusions

Hazards associated with INEEL-area volcanism as well as distant volcanic sources are evaluated. The most significant hazards and risks to the ISFSI site are associated with basaltic volcanism and related phenomena from ESRP vents.

For volcanic areas such as the ESRP, with no historical volcanism and an incomplete chronologic record of prehistoric volcanism, assessments of potential volcanic hazards and volcanic risk are based on interpretation of the long-term geologic record, and on the documented effects of historical eruptions in analog regions such as Iceland and Hawaii. Volcanic hazards to the ISFSI site are related to future basaltic and rhyolitic eruptions along volcanic-rift zones and the axial volcanic zone. The most significant volcanic hazard to INEEL is the inundation or burning of facilities by basaltic lava flows from volcanic-rift zones. A significant, related hazard is disruption of facilities due to ground deformation accompanying magma intrusion along volcanic-rift zones: opening of fissures, normal faulting, broad-region tilting and uplift within several km of vents (see section 2.6.3 - Surface Faulting). Other, less significant basaltic hazards include volcanic-gas emission and disruption of groundwater.

Available geologic-map data and geochronometry of INEEL basalt lava flows suggest minimum (most conservative) volcanic-recurrence intervals of 10^{-4} to 10^{-5} per year, for the Axial volcanic zone, and the Arco and Lava Ridge-Hells Half Acre volcanic-rift zones. The probabilistic risk of basalt-lava inundation or intrusion-related ground disturbance is therefore estimated to be $< 10^{-5}$ per year, for the ISFSI site and other sites on the southern INEEL. Risk from these phenomena at northern-INEEL sites is still lower, because volcanism there has been less frequent and less recent. The probability of significant impact from all other volcanic phenomena, such as growth of new rhyolite domes on the ESRP or thicker than 8-cm tephra fall from non-ESRP vents, is estimated to be $< 10^{-5}$ per year, due to the combined effects of great distance, infrequency, low volume, and topographic or atmospheric barriers to the dispersal of tephra on the INEEL.

2.7 Summary of Site Conditions Affecting Construction and Operating Requirements

The INEEL TMI-2 ISFSI will be constructed on the INEEL. The INEEL is a large DOE controlled area which has nuclear facilities and performs research activities. The INEEL TMI-2 ISFSI will not add appreciably to the impact of the INEEL on the local environment, infrastructure, labor, or population.

The following is a listing of the design bases related to the Site Characteristics for the INEEL TMI-2 ISFSI (see SAR Chapter 3).

- The INEEL TMI-2 ISFSI is designed withstand the temperature extremes of 103°F to -50°F.
- The INEEL TMI-2 ISFSI is designed for the maximum snow load of 30 psf.
- The INEEL TMI-2 ISFSI is designed to be above the PMF at 4917 ft asl.
- The INEEL TMI-2 ISFSI is designed to withstand the Region III tornado (200 mph) with NUREG-0800 tornado generated missile.
- The INEEL TMI-2 ISFSI is designed to withstand a 0.36g horizontal seismic acceleration earthquake.

2.8 References

2.1 LITCO (1995), *Idaho Chemical Processing Plant Safety Analysis Report, Part I, General Safety Analysis. Chapter 1, Site Characteristics*, March 1995.

2.2 DOE (U.S. Department of Energy), (1995), *Department of Energy Programmatic Spent Nuclear Fuel Management and Idaho National Engineering Laboratory Environmental Restoration and Waste Management Programs Final Environmental Impact Statement*, April.

2.3 DOE-ID (U.S. Department of Energy Idaho Operations Office), (1993b), *Idaho National Engineering Laboratory Long-Term Land Use Future Scenarios*, DOE/ID-10440, Revision 1, Idaho Falls, ID.

2.4 Lee, L. G., J. M. Mines, and B. B. Webb, (1994), *Assessment of Aircraft Impact Probabilities at the Idaho Chemical Processing Plant*, Westinghouse Idaho Nuclear Company (WINCO-1137), Revision 1.

2.5 NOAA, 1984, *Climatography of the Idaho National Engineering Laboratory, Site Specific Summary NPR Primary and Alternate Site (Draft)*, IDO-12048B, G.E. Start, Ed., November, 1984 IDO-12048B.

2.6 Clawson, K.L., G.E. Start, and N.R. Ricks, (1989), *Climatography of the Idaho National Engineering Laboratory 2nd Edition*, DOE/ID-12118, U.S. Department of Commerce, National Oceanic and Atmospheric Administration, Environmental Research Laboratories, Air Resources Laboratory, Field Research Division, Idaho Falls, ID, p. 155.

2.7 Coats, D. W., and R. C. Murray, (1985). Natural phenomena hazards modeling project: *Extreme wind/tornado hazard models for Department of Energy sites*. UCRL-53526, Rev. 1 Lawrence Livermore National Nat. Lab., Livermore, Ca.

2.8 Sagendorf, J. F., (1996), *Precipitation Frequency and Intensity at the Idaho National Engineering Laboratory*, NOAA Technical Memorandum, National Oceanic and Atmospheric Administration, Environmental Research Laboratories, Idaho Falls, Idaho, June 21, 1996.

2.9 Hershfield, D. M., (1961), *Rainfall Frequency Atlas of the United States*, U.S. Weather Bureau Technical Paper No. 40, U.S. Department of Commerce, Washington, D. C.

2.10 DEQ, 1996, *Statewide Background Values -- Ambient Concentrations for Pollutants for which National Ambient Air Quality Standards Have Been Established*, Idaho Department of Environmental Quality, Boise, Idaho, April 29, 1996.

2.11 Sagendorf, et al, (1982), *XOQDOQ: Computer Program for the Meteorological Evaluation of Routine Effluent Releases at Nuclear Power Stations*, NUREG/CR-2919, J.F. Sagendorf, J. T. Goll, and W. F. Sandusky, U. S. Nuclear Regulatory Commission, Washington, DC, 1982.

2.12 Briggs, (1971), *Some Recent Analyses of Plume Rise Observations, Proceedings of the Second International Clean Air Act Congress*, edited by H.M. England and W.T. Barry, Academic Press, N.Y., 1971.

2.13 Briggs, (1972), "Discussion on Chimney Plumes in Neutral and Stable Surroundings," *Atmospheric Environment*, 6, pp. 507 - 510, 1972.

2.14 Start, G.E. and L.L. Wendell, (1974), *Regional Effluent Dispersion Calculations Considering Spatial and Temporal Meteorological Variations*, NOAA Technical Memorandum ERL-ARL-44, National Oceanic and Atmospheric Administration, Washington, DC.

2.15 Barraclough, J.T. and R.G. Jensen, *Hydrologic Data for the Idaho National Engineering Laboratory Site, 1971 to 1973*, U.S. Geological Survey Open File Report 75-318 (IDO-22052), January 1975.

2.16 Fischer, D.R., R.G. Jensen and J.R. Pittman, *Hydrologic Conditions at the Idaho National Engineering Laboratory, 1982-1985*, U.S. Geological Survey Open File Report 89-4008, DOE/ID-22078, December 1989.

2.17 Bennett, C.M., (1986), *Capacity of the Diversion Channel Below the Flood-Control Dam on the Big Lost River at the Idaho National Engineering Laboratory*, U.S. Geological Survey, Water-Resources Investigations Report 86-4204.

2.18 McKinney, J. D., 1985, *Big Lost River 1983-1984 Flood Threat*, EG&G Report PPD-FPB-002.

2.19 Carrigan, P.H., Jr., *Probability of Exceeding Capacity of Flood Control System at the National Reactor Testing Station, Idaho*, U.S. Geological Survey Open file Report IDO-22052, January 1972.

2.20 Lamke, R.D., (1969), *Stage-Discharge Relations on the Big Lost River within the National Reactor Testing Station, Idaho*, IDO-22050, U.S. Geological Survey, Water Resources Division, Idaho Falls, ID.

2.21 Koslow, K.N. and J.A. Tullis, (1983), *Characterization of Big Lost River Floods with Recurrence Intervals Greater than 25 Years*, RE-PB-83-044, (EG&G Idaho), November.

2.22 Martineau, R.C., D.H Hoggan, K.N. Keck, , and T.R. Wood, (1990), *Hydrologic Modeling Study of Potential Flooding at the Subsurface Disposal Area from a Hypothetical Breach of Dike 2 at the Idaho National Engineering Laboratory*, EGG-WM-9502, EG&G Idaho, Inc., Idaho Falls, ID.

2.23 Niccum, M. R.(1973). *Flooding Potential at the Idaho Chemical Processing Plant.*

2.24 Koslow, K.N. and D.H. Van Haaften, (1986), *Flood Routing Analysis for a Failure of Mackay Dam*, EGG-EP-7184, EG&G Idaho Inc., Idaho Falls, ID.

2.25 LITCO, (1994), *ICPP Safety Analysis Report*, INEL-94/022.

2.25a State of Idaho, 1978, *Phase I Inspection Report, National Dam Safety Program, Mackay Dam*, Department of Water Resources.

2.26 U.S. Department of the Army Corps of Engineers, (1977), "National Program of Inspection of Dams Report, vol. 1, Appendix D," *Recommended Guidelines for Safety Inspection of Dams*, Office of the Chief of Engineers.

2.27 Cecil, D. and Orr, B.R., (1991), *Hydrologic Conditions and distribution of Selected Chemical Constituents in Water, Snake River Plain Aquifer, Idaho National Engineering Laboratory, Idaho 1986 to 1988*, U.S. Geological Survey Open File Report 91-4047, DOE/ID-22096, August 1991.

2.28 Kirkham, V.R.D. (1931) "Snake River downwarp;" *Journal of Geology*, v.39, p.456-487.

2.29 Morgan, W.J. (1972) *Plate motions and deep mantle convection*; Geological Society of America Memoir 132, p. 7-22.

2.30 Armstrong, R. L., W. P. Leeman, and H. E. Malde (1975). "Quaternary and Neogene volcanic rocks of the Snake River Plain, Idaho", *American Journal of Science* 275, 225-251.

2.31 Leeman, W.P. (1982) "Development of the Snake River Plain-Yellowstone Plateau Province, Idaho and Wyoming: An overview and petrologic model;" in Bonnichsen, B. and Breckenridge, R.M., *Cenozoic Geology of Idaho*, Idaho Geological Survey Bulletin 26, p.155-178.

2.32 Pierce, K.L. and Morgan, L.A. (1992) "The track of the Yellowstone hot spot: Volcanism, faulting, and uplift," in P.K. Link et al., editors, *Regional Geology of Eastern Idaho and Western Wyoming*: Geological Society of America Memoir 179, 1-54.

2.33 Hackett, W. R. and R.P. Smith (1992). "Quaternary volcanism, tectonics, and sedimentation in the Idaho National Engineering Laboratory area," *in* J.K. Wilson editor, *Field Guide to Geologic Excursions in Utah and Adjacent Areas of Nevada, Idaho, and Wyoming*, Utah Geological Survey, Miscellaneous Publlication 92-3, p. 1-17.

2.34 Malde, H.E. (1991) "Quaternary geology and structural history of the Snake River Plain, Idaho and Oregon;" in Morrison, R.B., editor, *Quaternary non-glacial geology, conterminous United States*; Boulder Colorado, Geological Society of America, The Geology of North America, v.K-2, p.251-281.

2.35 Morgan, P., Blackwell, D.D., Spafford, R.E., and Smith, R.B. (1977) "Heat flow measurements in Yellowstone Lake and the thermal structure of the Yellowstone caldera;" *Journal of Geophysical Research*, v.82, p.3719-3732.

2.36 Smith, R.B. and R.L. Christiansen (1980) "Yellowstone Park as a window on the Earth's interior," *Scientific American*, v. 242, no. 2, p. 104-117.

2.37 Christiansen, R.L. (1984) "Yellowstone magmatic evolution: Its bearing on understanding large-volume explosive volcanism;" *in Explosive Volcanism: Inception, Evolution, and Hazards*; National Academy Press, Washington, D.C., p.84-95.

2.38 Thelin, G.P. and Pike, R.J. (1991) *Landforms of the conterminous United States - A digital shaded relief portrayal*; U.S. Geological Survey Miscellaneous Investigations Map 2206, scale 1:3,500,000.

2.39 Link, P.K., Skipp, B., Hait, M.H., Janecke, S.U., and Burton, B.R. (1988) *Structural and stratigraphic transect of south-central Idaho: A field guide to the Lost River, White Knob, Pioneer, Boulder, and Smoky Mountains*; Idaho Geological Survey Bulletin 27, p.5-42.

2.40 Skipp, B. and Hait, M.H. (1977) *Allochthons along the northeast margin of the Snake River Plain, Idaho*; Wyoming Geological Association 29th Annual Field Conference Guidebook, p.499-515.

2.41 Oldow, J.S., A.W. Bally, H.G. Ave'Lallement, and W.P. Leeman (1989). "Phanerozoic evolution of the North American cordillera: United States and Canada, in The Geology of North America: An overview," A.W. Bally and A.R. Palmer, editors, *Geol. Soc. Am., Decade of North American Geology*, v. A, p. 139-232.

2.42 Eaton, G.P. (1982) "The Basin and Range Province: Origin and tectonic significance;" *Annual Reviews of Earth and Planetary Science*, v.10, p.409-440.

2.43 Zoback, M. L. and M. D. Zoback (1989). "Tectonic stress field of the continental United States," in *Geophysical framework of the Continental United States*, Pakiser, L. C., and Mooney, W. D., editors, Geol. Soc. Am. Memoir 172, 523-539.

2.44 Nace, R.L., Voegely, P.T., Jones, J.R., and Deutsch, S. (1975) *Generalized geologic framework of the National Reactor Testing Station, Idaho*; U.S. Geological Survey Professional Paper 725-B, 49p.

2.45 Kuntz, M. A., H. R. Covington, and L. J. Schorr (1992). *An overview of basaltic volcanism of the eastern Snake River Plain, Idaho, in Regional Geology of Eastern Idaho and Western Wyoming*, Link, P. K. Kuntz, M. A., and Platt, L. B. editors, Geol. Soc. Am. Memoir 179, 227-267.

2.46 Doherty, D.J. (1979) *Drilling data from exploration well 1, NE 1/4, sec.22, T.2N., R. 32E., Bingham County, Idaho*; U.S. Geological Survey Open-file Report 79-1225, 1 sheet.

2.47 Doherty, D.J. (1979) *Drilling data from exploration well 2-2A, NW 1/4, sec.15, T.5N., R.31E., Idaho National Engineering Laboratory, Butte County, Idaho*; U.S. Geological Survey Open-file Report 79-851, 1 sheet.

2.48 Doherty, D.J., L.A. Morgan, and M.A. Kuntz (1979) *Preliminary geologic interpretation and lithologic log of the exploratory geothermal test well (INEL-1), Idaho National Engineering Laboratory, eastern Snake River Plain, Idaho*; U.S. Geological Survey Open-file Rep. 79-1248, 10p.

2.49 Bennett, C.M. (1990). *Streamflow losses and ground-water level changes along the Big Lost River at the Idaho National Engineering Laboratory, Idaho*, U.S. Geol. Surv. Water-Resources Invest. Rept. 90-4067.

2.50 Hull, L.C. (1989) *Conceptual model and description of the affected environment for the TRA warm waste pond (Waste Management Unit TRA-03);* EG&G Informal Report, EGG-ER-8644.

2.51 Woodward-Clyde Consultants (1990). *Earthquake strong ground motion estimates for the Idaho National Engineering Laboratory: Final Report, Volume I: Summary, Volume II: Methodology and Analyses, and Volume III: Appendices*, EG&G Idaho, Inc. Informal Report EGG-BG-9350.

2.52 Woodward-Clyde Consultants (1992a). *Earthquake strong ground motion evaluations for the proposed New Production Reactor at the Idaho National Engineering Laboratory, Volume I: Deterministic Evaluation and Volume II: Probabilistic Evaluation*, EG&G Idaho, Inc. Informal Report EGG-GEO-10304.

2.53 Woodward-Clyde Federal Services (1996a) *Site Specific Probabilistic Seismic Hazard Analysis for the INEL*, Final Report, Lockheed Idaho Technologies Company, Technical Report INEL-95/0536, two volumes.

2.54 Kuntz, M. A., B. Skipp, M.A. Lanphere, W. E. Scott, K.L. Pierce, G.B., Dalrymple, D.E. Champion, G.F. Embree, W.R. Page, L.A. Morgan, R.P. Smith, W.R. Hackett, and D.W. Rodgers (1994) *Geologic map of the Idaho National Engineering Laboratory and adjoining areas, eastern Idaho*; U.S. Geolological Survey Miscellaneous Investigations Map I-2330, 1:100,000 scale.

2.55 Scott, W. E. (1982). *Surficial Geologic Map of the Eastern Snake River Plain and Adjacent Areas, Idaho and Wyoming*; U. S. Geological Survey Miscellaneous Investigation Map I-1372, scale 1:250,000.

2.56 Golder Associates (1992b) *High level waste tank farm replacement project geotechnical investigation*; Report prepared for Westinghouse Idaho Nuclear Company under contract C90-132739.

2.57 Anderson, S.R. (1991). " Stratigraphy of the unsaturated zone and uppermost part of the Snake River Plain aquifer at the Idaho Chemical Processing Plant and Test Reactors Area, Idaho National Engineering Laboratory, Idaho," *U.S. Geol. Surv. Water Resources Invest. Report* 91-4010, 71 p.

2.58 Lanphere, M.A., D.E. Champion, and M.A. Kuntz (1993) *Petrography, age, and paleomagnetism of basalt lava flows in coreholes Well 80, NRF 89-05, and ICPP 123, Idaho National Engineering Laboratory*; U.S. Geological Survey Open-File Report 93-327, 40p.

2.59 Smith, R.P, C.F. Hersley, and S.M. Jackson (1996) *Summary of information relating to correlation of strata beneath the Idaho Chemical Processing Plant and the Test Reactor Area, Idaho National Engineering Laboratory; Idaho National Engineering Laboratory*, Engineering Design File TRA-ATR-1163, 15p.

2.60 Anderson, S. R., D. J. Ackerman, M. J. Liszewski, and R. M. Freiberger, (1996), "Stratigraphic Data for Wells at and near the Idaho National Laboratory, Idaho," U. S. Geological Survey Open - File Report 96-248 (DOE/ID 22127) 27p, 1 diskette.

2.61 Sbar, M.L. and Barazangi, M. (1970*) Tectonics of the Intermountain Seismic Belt, western United States, Part I: Microearthquake seismicity and composite fault plane solutions*; Geological Society of America Abstracts with Programs, v.2, p.675.

2.62 Smith R. B., and M. L. Sbar (1970). *Seismicity and tectonics of the Intermountain seismic western United States, Part II: Focal mechanism of major earthquakes*; Geological Society of America, Abstracts with Programs v. 2, p. 657.

2.63 Smith R. B., and M. L. Sbar (1974). "Contemporary tectonics and seismicity of the western United States with emphasis on the Intermountain seismic belt," *Geol. Soc. Am. Bull*. 85, 1205-1218.

2.64 Arabasz W.J. and R.B. Smith (1981). "Earthquake prediction in the Intermountain seismic belt: An intraplate extensional regime, in Earthquake Prediction: An International Review," D.W. Simpson and D.W. Richards, editors, *American Geophysical Union*, Maurice Ewing Series 4, p. 238-258.

2.65 Smith, R. B. and W. J. Arabasz (1991) "Seismicity of the Intermountain seismic belt, in Neotectonics of North America," D. B. Slemmons, E. R. Engdahl, M. D. Zoback, and D. D. Blackwell, editors, *Geol. Soc. Am., Decade Map Volume 1*, Boulder Colorado, p.185-228.

2.66 Stickney, M. C. and M. J. Bartholomew (1987). "Seismicity and late Quaternary faulting of the northern Basin and Range province, Montana and Idaho," *Bull. Seis. Soc. Am*. v. 77, 1602-1625.

2.67 Jackson, S.M., Wong, I.G., Carpenter, G.S., Anderson, D.M., and Martin, S.M. (1993) "Contemporary seismicity in the eastern Snake River Plain, Idaho based on microearthquake monitoring;" *Bulletin of the Seismological Society of America*, v.83, p. 680-695.

2.68 Peyton, S. L., R. B. Smith, and J. C. Pechmann (1991). "Seismotectonics of the Yellowstone-Hebgen Lake region from earthquake focal mechanisms and stress field inversion;" *EOS* 72, 335-336.

2.69 Eddington, P. K., R. B. Smith, and C. R. Renggli (1987). "Kinematics of Basin and Range intraplate extension," *in Continental Extensional Tectonics*, Coward, M.P., Dewey, J.F., and Hancock, P.L., editors, Geological Society Special Publication No. 28, 371-392.

2.70 Hackett, W.R., R.P. Smith, and N.E. Josten (1991). *Interaction of Quaternary volcanic and tectonic processes, eastern Snake River Plain*; Geological Society of America, Abstracts with Programs v. 23, p. 32.

2.71 Youngs, R.R., F.H. Swan, M.S. Power, D.P. Schwartz, and R.K. Green (1987). *Probabilistic analysis of earthquake ground shaking hazard along the Wasatch Front, Utah in Assessment of regional earthquake hazards and risk along the Wasatch Front, Utah*, U.S. Geol. Surv. Open-file Rept. 87-585, v. II, p. M1-M110.

2.72 Geomatrix Consultants (1989). *Seismotectonic evaluation for Little Wood River Dam Site*, unpublished report, U.S. Bureau of Reclamation.

2.73 Engdahl, E.R. and W.A. Rinehart (1988) "Seismicity map of North America, Continent-scale Map-004," *Decade of North American Geology*, Geological Society of America, Scale 1:5,000,000, 4 sheets.

2.74 Doser, D.I. (1985b). "Source parameters and faulting processes of the 1959 Hebgen Lake, Montana, earthquake sequence," *Journal of Geophysical Research*, v. 90, no. B6, p. 4537-4555.

2.75 Gorman, V. W. and R. C. Guenzler (1983) *The 1983 Borah Peak earthquake and INEL structural performance*, EG&G Informal Report EGG-EA-6501, 76 p.

2.76 Crone, A.J., M.N. Machette, M.G. Bonilla, J.J. Lienkaemper, K.L. Pierce, W.E. Scott, and R.C. Bucknam (1987) "Surface faulting accompanying the Borah Peak earthquake and segmentation of the Lost River fault, central Idaho;" *Bulletin Seismological Society of America*, v.77, no.3, p.739-770.

2.77 Richins, W. D., J. C. Pechmann, R. B. Smith, C. J. Langer, S. K. Goter, J.E. Zollweg, and J. J. King (1987). "The 1983 Borah Peak, Idaho earthquake and its aftershocks," *Bull. Seis. Soc. Am.*, v. 77, no. 3, p. 694-723.

2.78 Stover, C. W. (1985). "The Borah Peak, Idaho earthquake of October 28, 1983 - Isoseismal map and intensity distribution," *Earthquake Spectra*, 2, No. 1, 11-21.

2.79 Jackson, S. M. (1985). *Acceleration data from the 1983 Borah Peak, ID earthquake recorded at the Idaho National Engineering Laboratory, in Workshop XXVIII on the Borah Peak, ID earthquake*, U. S. Geol. Surv. Open-File Rept, 85-290, p. 385-400.

2.80 Jackson, S. M., J.J. King, D.M. Anderson, G.S. Carpenter, and H.A. Adams (1991b) *Strong ground motion data recorded at the Idaho National Engineering Laboratory during the 1983 Borah Peak, Idaho earthquake*; EG&G Idaho, Inc., Idaho Falls, Idaho Informal Report EGG-BG-9249, 136 p.

2.81 Anders, M.H., J.W. Geissman, L.A. Piety, and J.T. Sullivan (1989) "Parabolic distribution of circumeastern Snake River Plain seismicity and latest Quaternary faulting: Migratory pattern and association with the Yellowstone Hotspot;" *Journal of Geophysical Research*, v.94, no.B2, p.1589-1621.

2.82 Bankey, V., Webring, M, Mabey, D.R., Kleinkopf, M.D., and Bennett, E.H. (1985) *Complete bouguer gravity anomaly map of Idaho;* U.S. Geological Survey Map MF-1773.

2.83 Zeitz, I., Gilbert, F.P., and Kirby, J.R. (1978). *Aeromagnetic map of Idaho*, U.S. Geological Survey Map GP-920.

2.84 Sparlin, M. A., L. W. Braile, and R. B. Smith (1982). "Crustal Structure of the Eastern Snake River Plain Determined from Ray Trace Modeling of Seismic Refraction Data," *Journal of Geophysical Research*, v. 87, no. B4, p. 2619-2633.

2.85 Smith, R.B. and Braile, L.W. (1993) "Topographic signature, space-time evolution, and physical properties of the Yellowstone-Snake River Plain volcanic system: the Yellowstone hotspot," in Snoke, A.W., Steidtmann, J.R., and Roberts, S.M., editors, *Geology of Wyoming*: Geological Survey of Wyoming Memoir No. 5, p.694-754.

2.86 Christiansen, R.L.(1989) "The Yellowstone Plateau-Island Park Region;" *in Ruebelmann, K.L., editor, Snake River Plain-Yellowstone Volcanic Province, Field Trip Guidebook T305*, 28th International Geological Congress, American Geophysical Union, Washington, D.C., p.14-37.

2.87 White, D.E., Fournier, R.O., Muffler, L.J.P., and Truesdale, A.H. (1975) *Physical results of research drilling in thermal areas of Yellowstone National Park, Wyoming*; U.S. Geological Survey Professional Paper 892, 70p.

2.88 Iyer, H.M., Evans, J.R., Zandt, G., Stewart, R.M., Coakley, J., and Roloff, J. (1981) "A deep magma body under the Yellowstone caldera: Delineation using teleseismic P-wave residuals and tectonic interpretation;" *Geological Society of America Bulletin*, v.92, p.1471-1646.

2.89 Evans, J.R. (1982) "Compressional wave velocity structure of the upper 350 km under the eastern Snake River Plain near Rexburg, Idaho;" *Journal of Geophysical Research*, v.87, p.2654-2670.

2.90 Smith, R. B. and R. L. Bruhn (1984) "Intraplate extensional tectonics of the eastern Basin-Range: Inferences on structural style from seismic reflection data, regional tectonics, and thermal-mechanical models of brittle-ductile deformation," *Journal of Geophysical Research*, v. 89, p. 5733-5762.

2.91 Janecke, S.U. (1992) "Kinematics and timing of three superimposed extensional systems, east central Idaho: Evidence for an Eocene tectonic transition;" *Tectonics*, v.11, no.6, p.1121-1138.

2.92 Scott, W. E., K. L. Pierce, and M. H. Hait, Jr (1985) "Quaternary tectonic setting of the 1983 Borah Peak earthquake, central Idaho;" *Bulletin of the Seismological Society of America*, v.75, no.4, p.1053-1066.

2.93 Doser, D.I. and R.B. Smith (1985). "Source parameters of the 28 October 1983 Borah Peak, Idaho earthquake from body wave analysis," *Bull. Seis. Soc. Am.* 75, 1041-1051.

2.94 Woodward-Clyde Consultants (1992b). *Paleoseismic investigations of the southern Lemhi Fault, Idaho*, EG&G Idaho, Inc., Informal Report EGG-GEO-10178, 32 p.

2.95 Bruhn, R.L, Wu, D., and Lee, J-J (1992) *Final Report on the structure of the southern Lemhi and Arco fault zone, Idaho*; EG&G Idaho, Inc., Informal Report EGG-NPR-10680, 6 plates, 26 p.

2.96 Jackson, S.M., Carpenter, G.S., Smith, R.P., and Casper, J.L. (1995) *Seismic reflection project near the southern terminations of the Lost River and Lemhi faults, eastern Snake River Plain, Idaho*; Idaho National Engineering Laboratory Technical Report, INEL-95/0489 (in preparation).

2.97 Wu, D. and Bruhn, R.L. (1994) *Structural and rupture characteristics of the southern Lost River fault zone, Idaho; University of Utah*, Report to Woodward-Clyde Federal Services, April, 33p. plus figures, tables, and plates.

2.98 Woodward-Clyde Federal Services (1995) *Paleseismic investigation of the southern Lost River fault zone, Idaho*; Lockheed Idaho Technologies Company, Technical Report INEL-95/0508, 82p. plus figures, tables, and appendices.

2.99 Haller, K. M. (1988). *Segmentation of the Lemhi and Beaverhead faults, east-central Idaho, and Red Rock fault, southwest Montana, during the late Quaternary*, M.S. Thesis, University of Colorado, 141 p.

2.100 Embree, G.F. (1989) *Neogene fault activity in southern Beaverhead Range adjacent to the eastern Snake River Plain and Birch Creek Valley, Idaho*, unpublished report and map, submitted to EG&G Idaho Inc., Idaho Falls, Idaho.

2.101 Piety, L. A., C. K. Wood, J. D. Gilbert, J. T. Sullivan, and M. H. Anders (1986). *Seismotectonic study for Palisades Dam and Reservoir, Palisades Project*: U. S. Bureau of Reclamation, Engineering Research Center, Seismotectonic Division, Denver, Colorado, and Pacific Northwest Region Geology Branch, Boise Idaho, Seismotectonic Report 86-3, 198 pp.

2.102 McCalpin, J.P., L.A. Piety, and M.H. Anders (1990). *Part 1. Latest Quaternary faulting and structural evolution of Star Valley, Wyoming, in Geologic field tours of western Wyoming and parts of adjacent Idaho, Montana, and Utah*, S. Roberts, editor, Geol. Surv. Wyoming Public Information Circular No. 29, p. 5-14.

2.103 Williams, E. J. and G. F. Embree (1980). "Pleistocene movement on Rexburg fault, eastern Idaho (Abstract)," *Geol. Soc. Am. Abstr. with Prog*., Rocky Mountain Section, v. 12, no. 6, p. 308.

2.104 EG&G Idaho, Inc. (1985) *INEL Environmental Characterization Report; EG&G Idaho, Inc.* Informal Report EGG-NP-6688, Three Volume Set.

2.105 Pankratz, L. W. and H. D. Ackerman (1982). "Structure along the northwest edge of the Snake River Plain interpreted from seismic refraction," *Journal of Geophysical Research*, v. 84, no. B4, p. 2676-2682.

2.106 Myers, W. B. and W. Hamilton (1964). *Deformation accompanying the Hebgen Lake earthquake of August 17, 1959*, U. S. Geol. Surv. Bull. 435-I, 55-98.

2.107 Morgan, L.A. (1988). *Explosive rhyolitic volcanism of the eastern Snake River Plain* (unpublished, Ph.D. Thesis), Manoa, University of Hawaii, 191 p.

2.108 Morgan, L.A. (1992). "Stratigraphic relations and paleomagetic and geochemical correlations of ignambrites of the Heise Volcanic Field, eastern Snake River Plain, Idaho and Wyoming," in Link, P.K., Kuntz, M.A., and Platt, L.B., editors, *Regional Geology of Eastern Idaho and Western Wyoming*, Geol. Soc. Am. Memoir 179, 215-226.

2.109 Hackett, W. R. and L. A. Morgan (1988). "Explosive basaltic and rhyolitic volcanism of the eastern Snake River Plain, Idaho," in P.K. Link and W.R. Hackett, editors, *Guidebook to the Geology of Central and Southern Idaho*, Idaho Geological Survey, Bulletin 27, 283-301.

2.110 Rodgers, D.W. and N.C. Zentner (1988). "Fault geometries along the northern margin of the eastern Snake River Plain, Idaho," *Geol. Soc. Am. Abstr. with Programs* v. 20, p. 465-466.

2.111 Zentner, N.C. (1989). *Neogene normal faults related to the structural origin of the eastern Snake River Plain, Idaho*, unpublished M.S. Thesis, Idaho State University, 48 p.

2.112 Breckenridge, R. M. and K. L. Othberg (1991) *Geologic interpretation of a trench excavation near Arco Hills on the northwest margin of the INEL, Snake River Plain, Idaho*; Idaho Geological Survey Technical Report 91-2, 20 p.

2.113 Morin-Jansen, A. (1987) *Study of the Principle Lineament and associated lineaments*; Masters Thesis, Idaho State University, Pocatello.

2.114 Golder Associates (1992a) *New Production Reactor Site Characterization, Volume I: Volcanic Zones Mapping Report, Volume II: Regional Geomorphic Study, and Volume III: NPR Site Geologic Report*; EG&G Informal Report EGG-NPR-10625.

2.115 Smith, R.B. and Braile, L.W. (1994) "The Yellowstone hotspot," *Journal of Volcanology and Geothermal Research*, v.61, p.121-187.

2.116 Engdahl, E.R. and W.A. Rinehart (1991) "Seismicity map of North America Project;" in Slemmons, D.B, Engdahl, E.R., Zoback, M.D., and Blackwell, D.D., editors, *Neotectonics of North America*, Geological Society of America Decade Map Volume 1, p. 21-27.

2.117 Oaks, S.D. (1992*) Historical seismicity investigation for the November 11, 1905 earthquake*; EG&G Informal Report EGG-GEO-10203, 106p.

2.118 King, J. J., T. E. Doyle, and S. M. Jackson (1987). "Seismicity of the eastern Snake River Plain region, Idaho, prior to the Borah Peak, Idaho earthquake: October 1972 - October 1983," *Bull. Seis. Soc. Am.*, v. 77, no. 3, p. 809-818.

2.119 Jackson, S. M., G. S. Carpenter, and I. G. Wong, (1990) *Microearthquake investigations of the eastern Snake River Plain, Idaho* (abstract), Seismological Research Letters, v.61, p.41.

2.120 Pelton, J. R., R. J. Vincent, and N. J. Anderson (1990). "Microearthquakes in the Middle Butte/East Butte area, eastern Snake River Plain, Idaho," *Bull. Seis. Soc. Am.*, v. 80, no. 1, p. 209-212.

2.121 Smith, R.B. (1978) "Seismicity, crustal structure, and intraplate tectonics of the interior of the western cordillera," in Smith, R.B. and Eaton, G.P., editors, *Cenozoic Tectonics and Regional Geophysics of the Western Cordillera*, Geological Society of America Memoir 152, p.111-144.

2.122 Smith, R. B., W. D. Richins, and D. I. Doser (1985). "The 1983 Borah Peak, Idaho earthquake: Regional seismicity, kinematics of faulting, and tectonic mechanism," in *Proceedings of Conference XXVIII on the Borah Peak, Idaho Earthquake*, U. S. Geological Survey Open-File Report 85-290, p. 236-263.

2.123 Brott, C. A., D. D. Blackwell, and J. P. Ziagos (1981). "Thermal and tectonic implications of heat flow in the eastern Snake River Plain, Idaho," *Journal of Geophysical Research*, v.86, p.11709-11734.

2.124 Blackwell, D.D. (1989) "Regional implications of heat flow of the Snake River Plain, northwestern United States," *Tectonophysics*, v.164, p.323-343.

2.125 Blackwell, D. D. (1992). *Heat flow modeling of the Snake River Plain*, EG&G Informal Report EGG-C91-103450, 109 pp.

2.126 Parsons, T. and G. Thompson (1991). "The role of magma overpressure in suppressing earthquakes and topography: Worldwide examples," *Science*, v. 253, p. 1399-1402.

2.127 Rodgers, D.W., Hackett, W.R., and Ore, H.T. (1990) "Extension of the Yellowstone plateau, eastern Snake River Plain, and Owyhee plateau," *Geology*, v.18, p. 1138-1141.

2.128 Anders, M. H. and N. H. Sleep (1992). "Magmatism and extension: The thermal and mechanical effects of the Yellowstone hotspot," *J. Geophys. Res*. 97, 15379-15393.

2.129 Brandsdottir, B. and P Einarsson (1979) "Seismic activity asociated with the September 2977 deflagration of the Krafla central volcano in northeastern Iceland," Journal of Volcanology and Geothermal Reaseach, v. 6, p. 197-212.

2.130 Einarsson, P. and B. Brandsdottir (1980). "Seismological evidence for lateral magma intrusion during the July 1978 deflation of the Krafla volcano in NE-Iceland," *J. Geophy*., v. 47, p. 160-165.

2.131 Klein, F. W., R. Y. Koyanagi, J. S. Nakata, and W. R. Tanigawa (1987). *The seismicity of Kilauea's magma system, in Volcanism in Hawaii*, R. W. Decker, T. L. Wright, and P. H. Stauffer eds., U. S. Geological Survey Professional Paper 1350, p. 1019-1185.

2.132 Mastin, L. G. and D. D. Pollard (1988). "Surface deformation and shallow dike intrusion processes at Inyo Craters, Long Valley, California," *J. Geophy. Res*., v. 93, p. 13,221-13,235.

2.133 Ryan, M. P. (1987) "Neutral buoyancy and the mechanical evolution of magmatic systems," in *Magmatic Processes: Physiochemical Principles*, The Geochemical Society Special Publication No. 1, B.O. Mysen, editor, p. 259-287.

2.134 Rubin, A. M., and D. D. Pollard (1987) *Origins of blade-like dikes in volcanic rift zones, in Volcanism in Hawaii*, R. W. Decker, T. L. Wright, and P. H. Stauffer eds., U. S. Geol. Sur. Prof. Paper 1350, p. 1449-1470.

2.135 Rubin, A. M., and D. D. Pollard (1988). "Dike-induced faulting in rift zones of Iceland and Afar," *Geology*, v. 16, p. 413-417.

2.136 Rubin, A. M. (1990). "A comparison of rift-zone tectonics in Iceland and Hawaii," *Bull. Volcanol*. v. 52, p. 302-319.

2.137 Rubin, A. M. (1992). "Dike-induced faulting and graben subsidence in volcanic rift zones," *J. Geophys. Res*. v. 97, p. 1839-1858.

2.138 Smith, R.P., S.M. Jackson, and W.R. Hackett (1996) "Paleoseismology and seismic hazards evaluations in extensional volcanic terrains," *Journal of Geophysical Research*, v.101, p.6277-6292.

2.139 Hackett, W. R., S.M. Jackson, and R.P. Smith (1996) "Paleoseismology in volcanic environments," *in* McCalpin, J.P., editor, *Paleoseismology*, Academic Press, New York.

2.140 Jackson, S. M. (1994). *Magnitudes of Earthquakes Associated with Basalt Dike Intrusion for use in INEL Seismic Hazards Evaluations*, Informal Report, INEL 94/0132, 44p, Lockheed Idaho Technologies Company, Idaho Falls, ID.

2.141 Bjornsson, A., K. Saemundsson, P. Einarsson, E. Tyggvason, and K. Gronvald (1977). "Current rifting episode in north Iceland," *Nature*, v. 266, p. 318-323.

2.142 Wells, D.L. and Coppersmith, K.J. (1994) "New empirical relationships among magnitude, rupture length, rupture area, and surface displacement," *Bulletin of the Seismological Society of America*, v.84, p.974-1002.

2.143 Filson, J., Simkin, T, and Leu, L-K (1973), "Seismicity of a caldera collapse: Galapagos Islands 1968," *Journal of Geophysical Research*, v.78, p.8591-8622.

2.144 Stein, R. S., P. Briole, J. C. Ruegg, P. Tapponnier, and F. Gasse (1991). "Contemprary, Holocene, and Quaternary deformation of the Asal rift, Djibouti: Implications for the mechanics of slow-spreading ridges," *J. Geophys. Res*. v. 96, p. 21789-21806.

2.145 Daz, S. and Scholz, C.H. (1983) "Why large earthquakes do not nucleate at shallow depths;" *Nature*, 305, 621-623.

2.146 Mori, J., McKee, C., Itikarai, I., Lowenstein, P., de Saint Ours, P., and Tali, B., (1989), "Earthquakes of the Rabaul seismo-deformational crisis September 1983 to July 1985: Seismicity on a caldera ring fault," in J.H. Latter, editor, *Volcanic Hazards: IAVCEI Proceedings in Volcanology* 1, p.429-462.

2.147 Shenon, P. J. (1936). "The Utah earthquake of March 12, 1934 (extracts from unpublished report)," *in* Neumann, F., *United States Earthquakes*, 1934, U. S. Coast and Geodetic Survey, Serial 593, 43-48.

2.148 dePolo, C.M., D.G. Clark, D.B. Slemmons, and W.H. Aymard (1989). *Historical Basin and Range province surface faulting and fault segmentation in Fault segmentation and controls of rupture initiation and termination*, D.P. Schwartz and R.H. Sibson, editors, Proceedings Conference XLV, Palm Springs, U.S. Geol. Surv. Open-file Rept. 89-315, p. 131-162.

2.149 Doser, D. I. (1989b). "Extensional tectonics in northern Utah-southern Idaho, U.S.A., and the 1934 Hansel Valley sequence," *Physics of the Earth and Planetary Interiors*, v. 54, p. 12-134.

2.150 Westaway, R. and R. B. Smith (1989). "Source parameters of the Cache Valley (Logan), Utah earthquake of 30 August 1962," *Bull. Seis. Soc. Am.*, v. 79, no. 5, p. 1410-1425.

2.151 Bache, T.C., D.G. Lambert and T.G. Barker (1980). "A source model for the March 28, 1975, Pocatello Valley earthquake from time-domain modeling of teleseismic P waves," *Bull. Seis. Soc. Am.*, v. 70, p. 405-418.

2.152 Cook, K. L. and R. K. Nye (1979). *Effects of the Pocatello Valley (Idaho-Utah border) earthquake of March 28, 1975 (UTC)*, Earthquake Studies in Utah 1850 to 1978, W. J. Arabasz, R. B. Smith, and W. D. Richins, editors, p. 445-457.

2.153 Arabasz W.J., W.D. Richins, and C.J. Langer (1979). "The Pocatello Valley (Idaho-Utah border) earthquake sequence of March to April 1975," in *Earthquake Studies in Utah 1850 to 1978*, W.J. Arabasz, R.B. Smith, and W.D. Richins, editors, University of Utah Special Publication, p. 339-374.

2.154 Eppley, R.A. and W.K. Cloud (1961). *United States earthquakes 1959*, U.S. Coast and Geodetic Survey, 115 p.

2.155 Witkind, I. J. (1964). *Reactivated faults north of Hebgen Lake*, U.S. Geol. Surv. Professional Paper 435, p. 37-50.

2.156 Pitt, A.M., Weaver, C.S., and Spence, W. (1979) "The Yellowstone Park earthquake of June 30, 1975," *Bulletin of the Seismological Society of America*, 69, 187-205.

2.157 Pardee, J.T. (1926). *The Montana earthquake of June 27, 1925*, U.S. Geol. Surv. Professional Paper 147-B, 17 p.

2.158 Doser, D. I. (1989a). "Source parameters of Montana earthquakes (1925-1964) and tectonic deformation in the northern Intermountain Seismic Belt;" *Bulletin of the Seismological Society of America*, v.79, No. 1, p.31-50.

2.159 Dewey, J.W., W.H. Dillinger, J. Taggart, and S.T. Algermissen (1973). "A technique for seismic zoning: Analysis of earthquake locations and mechanisms in northern Utah, Wyoming, Idaho, and Montana," in *Contributions to seismic zoning*, S.T. Harding, editor, NOAA Technical Rept. ERL 267-ESL 30, p. 541-575.

2.160 Turko, J. M. (1988). *Quaternary Segmentation History of the Lemhi Fault, Idaho*, M.S. Thesis, State University of New York at Bringhamton.

2.161 Baltzer, E. M., P. L. K. Knuefer, and M. J. Turko (1989). "Late Quaternary slip events along the central Lemhi fault, Idaho (Abstract)," *Geol. Soc. Am. Abstr. Progr*., v. 21, no. 5, p. 53.

2.162 Crone, A.J., and K. M. Haller, (1991), "Segmentation and coseismic behavior of basin-and-range normal faults; Examples from east-central Idaho and southwestern Montana, USA.", *Journal of Structural Geology*, v.13, p.151-164.

2.163 Jackson, S.M., Carpenter, G.S., Smith, R.P., and Casper, J.L. (1996) *Seismic reflection project near the southern terminations of the Lost River and Lemhi faults, eastern Snake River Plain, Idaho*; Idaho National Engineering Laboratory Technical Report, INEL-95/0489 (in preparation).

2.164 Pierce, K. L. (1985). *Quaternary history of faulting on the Arco segment of the Lost River fault, central Idaho, in Proceedings of Conference XXVIII on the Borah Peak, Idaho Earthquake*, U. S. Geol, Surv., Open-File Rept. 85-290, p. 195-206.

2.165 Smith, R. P., W. R. Hackett, and D. W. Rogers (1989). "Geological Aspects of seismic hazards assessments at the INEL, Southeastern Idaho," in *Proceedings of the second DOE Natural Hazards Mitigation Conference, Knoxville, Tennessee*, 282-289.

2.166 Kuntz, M. A., B. Skipp, M.A. Lanphere, W. E. Scott, K.L. Pierce, G.B., Dalrymple, D.E. Champion, G.F. Embree, W.R. Page, L.A. Morgan, R.P. Smith, W.R. Hackett, and D.W. Rodgers (1994) *Geologic map of the Idaho National Engineering Laboratory and adjoining areas, eastern Idaho*; U.S. Geolological Survey Miscellaneous Investigations Map I-2330, 1:100,000 scale.

2.167 Kuntz, M. A., D. E. Champion, E. C. Spiker, and R. H. Lefebvre (1986). "Contrasting magma types and steady-state, volume-predictable, basaltic volcanism along the Great Rift, Idaho;" *Geological Society of America Bulletin*, v. 97, p. 579-594.

2.168 Forman, S.L., Smith, R.P., Hackett, W.R., Tullis, J.A., and McDaniel, P.A. (1993) "Timing of late Quaternary glaciations in the western United States based on the age of loess on the eastern Snake River Plain, Idaho;" *Quaternary Research*, v.40, p.30-37.

2.169 Kuntz, M. A. (1978). *Geology of the Arco-Big Southern Butte area, eastern Snake River Plain, and potential volcanic hazards to the Radioactive Waste Management Complex and other waste storage and reactor facilities at the Idaho National Engineering Laboratory, Idaho*, U. S. Geol. Surv. Open-File Report 78-691, 70 p.

2.170 Doser, D. I. (1985a). "The 1983 Borah Peak, Idaho and 1959 Hebgen Lake, Montana earthquakes: Models for normal fault earthquakes in the Intermountain seismic belt;" *in Proceedings of Conference XXVIII on the Borah Peak, Idaho Earthquake*, U. S. Geol, Surv., Open-File Rept. 85-290, p. 368-384.

2.171 Arabasz, W. J., Richins, W. D., and C. J. Langer (1981). "The Pocatello Valley (Idaho-Utah border) earthquake sequence of March to April 1975', *Bull. Seis. Soc. Am.* 71, 803-826.

2.172 Singh, S. and Herrman R.B. (1983) "Regionalization of crustal coda Q in the continental U.S.," *J. Geophys. Res*. v. 88, p. 527-538.

2.173 Braile, L. W., R. B. Smith, J. Ansorge, M. R. Baker, M. A. Sparlin, C. Prodehl, M. M. Schilly, J. H. Healy, S. T. Mueller, and K. H. Olsen, (1982), "The Yellowstone-Snake River Plain Seismic Profiling Experiment; Crustal Structure of the Eastern Snake River Plain," Journal of Geophysical Research, v.87, no.B4, p.2597-2610.

2.174 EG&G, 1982, *INEL Architectural Engineering Standards*, Revision 3, June 15, 1982.

2.175 Woodward-Lungren and Associates, (1971), *Preliminary Seismic Risk Evaluation for the National Reactor Testing Station, Idaho*, prepared for the Idaho Nuclear Corporation, Idaho Falls, Idaho, 91p.

2.176 Woodward-Clyde Consultants, (1975) *A Seismic Hazards Study for the LOFT Reactor Facility at the INEL, Idaho*, unpublished report prepared for Energy research and Development Agency.

2.177 Allied Chemical Corporation, (1975), *Preliminary Safety Analysis Report for the New Waste Calcining Facility*, unpublished report prepared for th4e Idaho national Engineering Laboratory.

2.178 Agbabian Associates, (1977), Evvaluation of Seismic Criteria Used in the Design of INEL Facilities, manuscript prepared for Idaho National Engineering Laboratory, Research and Development Administration, Report R-7741d-4509, 151p.

2.179 Woodward-Clyde Federal Services (1996b) Development of Design Basis Earthquake Parameters for the TMI Fuel Interim Storage System, Draft Letter Report for review, July 8.

2.180 Silva, W. J., I. G. Wong, R. B. Darragh, (1996), "Engineering Characterization of Earthquake Strong Ground Motions in the Pacific Northwest," in *Assessing Earthquake Hazards and Reducing Risk in the Pacific Northwest*, Editors: A. M. Rogers, W. J. Kockelman, G. R. Priest, and T. J. Walsh, US Geological Survey Professional Paper 1560.

2.181 Wohletz, K. and G. Heiken (1992). *Volcanology and Geothermal Energy*, University of California Press, 432 p.

2.182 Blong, R.J. (1984). *Volcanic Hazards: A source book on the effects of eruptions*, Academic Press, p. 1-424.

2.183 Latter, J.H. (1989). *Volcanic Hazards: Assessment and monitoring*, Springer-Verlag, 625 p.

2.184 Volcanism Working Group (1990). *Assessment of potential volcanic hazards for New Production Reactor Site at the Idaho National Engineering Laboratory*, EG&G Idaho, Inc. Informal Report EGG-NPR-10624, 98 p.

2.185 Kuntz, M. A. (1992). *A model-based perspective of basaltic volcanism, eastern Snake River Plain, Idaho, in Regional Geology of Eastern Idaho and Western Wyoming*, Link, P. K., Kuntz, M. A., and Platt, L. B. editors, Geol. Soc. Am. Memoir 179, 289-304.

2.186 Rundle, J.B. and Hill, D.P. (1988) "The geophysics of a restless caldera--Long Valley, California," *Annual Reviews of Earth and Planetary Science*, v. 16, p.251-271.

2.187 Yamashita, K.M., Kleinman, J.W., Iwatsubo, E.Y., Ewert, J.W., Dzurisin, D., Rundle, J.B., and Stein, R.S. (1992) "Results of 1992 leveling survey at Long Valley, California (Abstract)," *EOS*, v.73, p.347.

2.188 Spear, D.B. and J.S. King (1982) *The geology of Big Southern Butte, Idaho; in Cenozoic Geology of Idaho*, edited by Bill Bonnichisen and R. M. Breckenridge, Idaho Bureau of Mines and Geology Bulletin, 26, p. 395-403.

2.189 Fink, J.H. (1990). *Lava flows and domes: Emplacement mechanisms and hazard implications*, Springer-Verlag, 249 p.

2.190 Fishel, M.L. (1993) *Geology and petrology of uplifted mafic lavas on the north flank of Big Southern Butte, eastern Snake River Plain, Idaho*; Masters thesis, Idaho State University, Pocatello.

2.191 Hayden, K.P. (1992) *Geology and petrology of the Cedar Butte eruptive center, eastern Snake River Plain, Idaho*; Masters thesis, Idaho State University, Pocatello.

2.192 Greely, R. (1982). "The style of basaltic volcanism in the eastern Snake River Plain, Idaho;" *in* Bill Bonnichsen and Roy M. Breckenridge, editors, *Cenozoic Geology of Idaho*, Idaho Bureau of Mines and Geology Bulletin 26, p. 407-422.

2.193 Josten, N.E., W.R. Hackett, and R.P. Smith (1993). "The trouble with geophysics," abstr, *Am. Geophys*. Union Front Range Branch annual meeting, Golden, Colorado, p. 12-13.

2.194 Kuntz, M. A., D. E. Champion, R. H. Lefebvre, and H. R. Covington (1988) *Geologic map of the Craters of the Moon, Kings Bowl, Wapi lava fields and the Great Rift volcanic rift zone, south-central Idaho*; U. S. Geological Survey Miscellaneous Investigations Series Map I-1632, scale 1:100,000.

2.195 Bailey, R.A., P.R. Beauchemin, F.P. Kapinos, and D.W. Klick (1983). "The Volcano Hazards Program: Objectives and long-range planning," *U.S. Geol. Surv. Open-file Report* 83-400, p. 1-33.

2.196 Wright, T. L., and Pierson, T. C., 1992, *Living with volcanoes - the U.S. Geological survey's Volcano-Hazard Program* - U. S. Geological Survey Circular 1073, 57 p.\

2.197 Izett, G.A. and R.E. Wilcox (1982). *Map showing localities and inferred distributions of the Huckleberry Ridge, Mesa Falls, and Lava Creek ash beds (Pearlette family ash beds) of Pliocene and Pleistocene age in the western United States and southern Canada*, U.S. Geol. Surv. Map I-1325.

2.198 Warrick, R.A., J. Anderson, T. Downing, J. Lyons, J. Ressler, M. Warrick, and T. Warrick (1981) *Four communities under ash after Mount St. Helens*, Program on Tech. Envir. and Man, Monograph No. 34, Inst. of Behavioral Sciences, University of Colorado, p. 1-143.

2.199 Izett, G.A. (1981). "Volcanic ash beds: Recorders of upper Cenozoic silica pyroclastic volcanism in the western United States," *J. Geophys. Res*. v. 86, p. 10,200-10,222.

2.200 Mehringer, P. J., E. Blinman, and K. L. Peterson, (1977), "Pollen Influx and Volcanic Ash," *Science*, v. 198, no. 4, p. 257-261.

2.201 DOE (U.S. Department of Energy), (1996), *Comprehensive Facility and Land Use Plan*, DOE/ID-10514, U.S. Department of Energy, Idaho Operations Office, Idaho Falls, ID, March.

2.202 Stover, C. W., G. E. Reagor, and S. T. Algermissen (1986). *Seismicity map of the state of Idaho*, U. S. Geological Survey Map MF1857.

2.203 Golder Associates, 1991, Geotechnical Soils Testing Laboratory Results for the New Production Reactor; EGG-NPR-10688)

2.204 Weston Geophysical Corporation, 1991, Geophysical Investigation, New Production Reactor Complex, Idaho National Engineering Laboratory; EGG-NPR-10689

2.204 Campbell, K.W. (1982), A preliminary methodolgy for the regional zonation of peak ground acceleration, Proceedings of 3rd International Conference on Earthquake Microzonation 1, Seattle, p. 365-376.

2.206 Campbell, K.W. and Y. Bozorgnia (1994), Near-source attenuation of peak horizontal acceleration from worldwide accelerograms recorded from 1957 to 1993, Fifth U.S. International Conference on Earthquake Engineering, Chicago, Illinois.

2.207 Corbett, M.K. (1975), Structural development of the eastern Snake River Plain, Idaho as an intracontinental rift, Geological Society of America Abstracts with Programs 7, p. 599-600.

2.208 Cornell, C.A. (1968), Engineering seismic risk analysis, Bulletin of the Seismological Society of America 58, p. 1583-1606.

2.208 Der Kiuergahian, A. and A. H-S. Ang (1977), A fault-rupture model for seismic risk analysis, Bulletin Seismological Society of America 67, p. 1173-1194.

2.210 Dewey, J. (1994), Letter transmittal of the 1994 Draney Peak, Idaho earthquake isoseismals, U.S. Geological Survey, March 4, Denver Colorado.

2.211 DOE (1978), INEL Architectural Engineering Standards, Idaho Falls, Idaho, Original Issue, December.

2.212 Geomatrix Consultants (1995), Seismic design mapping for the State of Oregon, unpublished Final Report prepared for the Oregon Department of Transportation.

2.213 Hamiton, W. (1987), Plate-tectonic evolution of the western U.S.A., Episodes 10, p. 271-301.

2.214 Harris, B.G. (1989), Seismic design criteria at the Idaho National Engineering Laboratory (INEL), Proceedings of the Second DOE Natural Phenomena Hazards Mitigation Conference, Knoxville, Tennessee, p.

2.215 Idriss, I.M. (1991), earthquake ground motions at soft soil sites, Second International Conference on Recent Advances in Geotechnical Earthquake Engineering and Soil Dynmaics 3, p. 2265-2272.

2.216 Joyner, W.B. and D.M. Boore (1982), Prediction of earthquake response spectra, U.S. Geological Survey Open-File Report 82-977.

2.217 Mabey, D.R. (1978), Regional gravity and magnetic anomalies in the eastern Snake River Plain, Idaho, U.S. Geological Survey, Journal of Research 6, p. 553-562.

2.218 Morgat and Shah (1979)

2.219 Mortgat, C.P., T.C. Zsutty, H.C. Shah, and l. Lubetkin (1977), A study of seismic risk for Costa Rica, John A. Blume Earthquake Engineering Center, Stanford University, California, Report 25.

2.220 Nava, S.J., W.J. Arabasz, and J.C. Pechmann (1994), The M 5.9 Draney Peak, Idaho (Idaho-Wyoming border) earthquake of February 3, 1994: A preliminary report, Seismological Research Letters 65, No. 3-4, p. 239.

2.221 Parsons, T., G.A. Thompson, and R.P. Smith (1998), More than one way to stretch: A tectonic model for extension along the plume track of the Yellowstone Hotspot and adjacent Basin and Range Province, U.S.A., accepted for publication in Tectonics.

2.222 Pechmann, J.C., D.A. Brumbaugh, S.J. Nava, T.G. Skelton, G.P. Fivas, W.J. Arabasz, and S.M. Jackson (1997), The 1994 Draney Peak, ID earthquake and its aftershocks, Eos, Transactions, American Geophysical Union, 78, No. 46, p. F480.

2.223 Sadigh, K., C-Y. Chang, N.A. Abrahamson, S.J. Chiou, and M.S. Power (1993), Specification of long-period ground motions: Updated attenuation relationships for rock site conditions and adjustment factors for near-fault effects, in Proceedings of ATC-17-1 Seminar on Seismic Isolation, Passive Energy Dissipation, and Active Control 1, p. 59-70.

2.224 Seed, I., M. Idriss, and F.W. Kiefer (1969), Characteristics of rock motions during earthquakes, Journal of the Soil Mechanics and Foundations Division, American Society of Civil Engineers 95, No. SM5, September.

2.225 Silva, W.J. and K. Lee (1987), WES RASCAL code for synthesizing earthquake ground motions, State-of-the-Art for Assessing Earthquake Hazards in the United States, Report 24, U.S. Corps of Engineers Waterways Experiment Station, Misc. Paper S-73-1, 120 p.

2.226 Singh, S. and R.B. Herrmann (1983), Regionalization of crustal coda Q in the continental U.S., Journal of Geophysical Research 88, p. 527-538.

2.227 Stanley, W.D. (1982), Magnetotelluric soundings on the Idaho National Engineering Laboratory Facility, Idaho, Journal of Geophysical Research 87, p. 2683-2691.

2.228 Stover, C.W., R.B. Simson, and W. Person (1977), Earthquake in the United States, April-June 1975, U.S. Geological Survey Circular 749-B, 29 pp.

2.229 Tera Corporation (1978), Influence of seismic modeling on seismic exposure evaluation, Tera Corporation, Berkeley, California.

2.230 Tera Corporation (1984), Seismic hazard analysis for Area 410, Nevada Test Site, Tera Corporation, Berkeley, California.

2.231 Tera Corporation (1984), Seismic hazard analysis for the Idaho National Engineering Laboratory, unpublished report prepared for Lawrence Livermore National Laboratory, 55 p.

2.232 Youngs, R.R. and K.J. Coppersmith (1990), Keeping pace with the science: Seismic hazard analysis in the western U.S., Proceedings of the Second Natural Phenomena Hazards Mitigation Conference, p. 262-270.

2.233 Woodward-Clyde Federal Services (1997), Letter transmittal of update earthquake catalog 1884-1995, Ivan Wong Letter, December 30, Oakland, California.

2.234 Anderson, S.R. and B.D. Lewis (1989) Stratigraphy of the unsaturated zone at the Radioactive Waste Management Complex, Idaho National Engineering Laboratory, Idaho; U.S. Geological Survey Water Resources Investigations Report 89-4065, IDO-22080, 54p.

2.235 Champion, D. E., M. A. Lanphere, and M. A. Kuntz (1988) Evidence for a new geomagnetic reversal from lava flows in Idaho - discussion of short polarity reversals in the Brunhes and late Matuyama polarity chrons; Journal of Geophysical Research, v. 93, no. B10, p. 11,667-11,680.

2.236 Smith, R.P, C.F. Hersley, and S.M. Jackson (1996) Summary of information relating to correlation of strata beneath the Idaho Chemical Processing Plant and the Test Reactor Area, Idaho National Engineering Laboratory; Idaho National Engineering Laboratory, Engineering Design File TRA-ATR-1163, 17p.

2.237 Dames and Moore (1976) Report on soil response spectra for proposed building and pipelines adjacent to the proposed Waste Calcining Facility near Idaho Falls, Idaho for the Energy Research and Development Administration; prepared for Facilities System Engineering Corporation, Los Angeles.

2.238 Kayen, R.E., et al. (1992) Evaluation of the SPT-CPT- and shear wave-based methods for liquefaction potential assessment using Loma Prieta Data; Proceedings of the 4th Japan-US workshop on Earthquake Resistance Design of Lifetime Facilities and Counter Measures for Liquefaction, v.1.

2.239 Seed, R.B., Idress, I.M., and Arango, I. (1983) Evaluation of liquefaction potential using field performance data; Journal of Geotechnical Engineering Division, ASCE, v.97, no.3.

2.240 Eaton, J.P. and Murata, K.J. (1960) How volcanoes grow; Science, v.132,no.3432, p.925-938.

2.241 Klein, F. W., R. Y. Koyanagi, J. S. Nakata, and W. R. Tanigawa (1987) The seismicity of Kilauea's magma system; in Volcanism in Hawaii, R. W. Decker, T. L. Wright, and P. H. Stauffer eds., U. S. Geol. Sur. Prof. Pap. 1350, Chapter 43, p. 1019-1185.

2.242 Humphreys, E.D. and Dueker, K.G. (1994a) Western U.S. upper mantle structure; Journal of Geophysical Research, v.99, p.9615-9634.

2.243 Seed, R.B. and Idress, I.M. (1970) Soil moduli and damping factors for dynamic response analyses; University of California, Earthquake Engineering Research Center, Berkeley, Report # EERC 70-10.

Tables

Table 2.1-1. The Typical Work Force at INEL Facilities[a}

Item	Location	Number of Employees
1	Test Area North (TAN)	335
2	Naval Reactor Facility (NRF)	1022
3	Argonne National Laboratory West Area (EBR-II)	750
4	EBR-I National Monument	0
5	Auxiliary Reactor Area (ARA)	0
6	Special Power Excursion Reactor Test (SPERT) and Power Burst Facility (PBF) and Waste Reduction Operations	116
7	Central Facilities Area (CFA)	854
8	Idaho Chemical Processing Plant (ICPP)	1157
9	Test Reactor Area (TRA)	430
10	Radioactive Waste Management Complex (RWMC)	196
	Total	4860

[a] Approximate number of employees as of March 1996.

Table 2.3.1

PERIOD OF RECORD MONTHLY AND ANNUAL TEMPERATURE AVERAGES AND EXTREMES AVERAGES[a]

	MAXIMUM			AVERAGE			MINIMUM		
	High	**Average**	**Low**	**High**	**Average**	**Low**	**High**	**Average**	**Low**
January	37.9	27.6	19.5	25.1	15.8	6.5	13.1	3.8	- 8.8
February	45.9	34.0	25.6	34.2	21.6	9.9	22.4	9.1	- 6.5
March	51.5	42.9	33.6	37.5	30.7	19.1	24.6	8.4	4.5
April	64.7	55.3	46.1	45.9	41.3	35.4	32.0	27.2	22.5
May	76.1	66.3	59.9	58.3	51.3	46.7	40.7	36.2	33.3
June	85.3	76.1	69.9	67.5	59.9	56.2	49.7	43.7	40.4
July	91.2	87.0	82.5	71.8	68.2	66.1	53.1	49.3	46.5
August	90.2	84.8	75.4	70.2	65.9	60.3	53.4	47.1	43.2
September	81.2	73.4	64.1	61.1	55.5	48.6	45.2	37.4	31.9
October	67.7	60.5	53.7	49.2	43.5	38.2	32.1	26.5	21.2
November	50.7	42.5	37.8	36.4	29.9	24.5	24.3	17.3	10.3
December	37.1	31.2	22.3	26.8	19.6	10.2	17.6	7.5	- 1.9
Annual	59.5	59.0	53.8	44.3	41.8	39.1	29.9	28.1	24.0

a. Temperature in °F, based on NWS archived CFA data from April 1954 through December 1982.

Table 2.3.2

AVERAGE, HIGHEST, AND LOWEST TOTAL MONTHLY AND ANNUAL PRECIPITATION AT CFA FROM JANUARY 1950 TO DECEMBER 1988.[A]

Month	Average (in.)	Highest (in.)	Lowest (in.)
January	0.69	2.56	0.00
February	0.64	2.40	0.00
March	0.60	1.44	0.07
April	0.73	2.50	0.00
May	1.20	4.42	0.07
June	1.18	3.89	0.02
July	0.53	2.29	0.00
August	0.57	3.27	0.00
September	0.63	3.52	0.00
October	0.52	1.67	0.00
November	0.68	1.74	0.00
December	0.75	3.43	0.02
Annual	8.71	14.40	4.50

a. Clawson et al. (1989).

Table 2.3.3

SNOWFALL AMOUNTS EXPECTED AT TMI-2 ISFSI SITE[a]

	MONTHLY			
	Average[b] (in.)	**Maximum (in.)**	**Minimum (in.)**	**Maximum 24-h Period[c] (in.)**
January	7.7	18.1	1.4	8.5
February	5.3	15.0	0.1	7.5
March	3.5	10.2	0.8	8.6
April	2.4	11.9	0.0	6.7
May	1.1	8.3	0.0	4.7
June	0.0	Trace	0.0	Trace
July	0.0	0.0	0.0	0.0
August	0.0	0.0	0.0	0.0
September	0.1	1.0	0.0	1.0
October	0.7	7.2	0.0	4.5
November	3.0	12.3	0.0	6.5
December	6.4	22.3	Trace	7.0
SEASONAL	26.0	40.9	11.3	8.6

a. Based on CFA data from January 1950 through December 1982.
b. Average based on data measured during period from March 1954 through December 1982.
c. Based on data measured from January 1950 through September 1983.

Table 2.3.4

MONTHLY AND ANNUAL AVERAGES OF DEW POINT TEMPERATURES APPLICABLE TO TMI-2 ISFSI SITE[a]

	Average Air Temperature (°F)	Average Wet Bulb (°F)	Average Dew Point (°F)
January	16.5	14.7	7.4
February	22.0	19.6	12.5
March	31.5	26.4	16.1
April	41.9	33.0	19.0
May	52.3	41.0	27.8
June	61.3	46.2	31.0
July	69.0	47.9	33.5
August	66.4	47.9	29.3
September	56.2	41.7	23.8
October	44.1	34.4	19.7
November	27.9	23.7	14.0
December	22.0	19.2	10.8
ANNUAL	42.6	33.2	20.4

a. Computed from average air temperatures and average wet bulb temperatures measured at CFA during the period from April 1955 through April 1961.

Table 2.3.5

HOURLY AVERAGE WINDSPEEDS EXPECTED AT TMI-2 ISFSI SITE[a]

	Average Speed (mph)		Highest Hourly Average Speed (mph)			
			20-ft Level[d]		250-ft Level[e]	
	20-ft[b] Level	250-ft[c] Level	Speed	Direction	Speed	Direction
January	5.6	9.7	48	WSW	65	SW
February	6.9	11.3	36	SW	52	WSW
March	8.7	13.8	51	WSW	67	WSW
April	9.3	14.6	39	WSW	49	WSW-SW
May	9.3	14.3	41	SW	47	WSW-SW
June	8.9	14.2	36	SW	46	WSW-SW
July	8.0	13.5	35	WSW	47	WSW
August	7.7	13.1	40	WSW	54	SW
September	7.2	12.8	42	WSW	56	WSW
October	6.8	12.3	44	WSW	58	WSW
November	6.4	11.6	40	WSW	54	WSW
December	5.1	9.6	43	SW	56	SW
ANNUAL	7.5	12.6	51	WSW	67	WSW

a. Based on CFA data.
b. April 1950 through October 1964.
c. July 1951 through October 1964.
d. April 1950 through October 1983.
e. July 1951 through October 1983.

Table 2.3.6

EXTREMES OF DAILY TEMPERATURES FOR TMI-2 ISFSI SITE

	Highest Daily Maximum[a] (°F)	Lowest Daily Maximum[a] (°F)	Highest Daily Average[b] (°F)	Average Dew Point (°F)
January	51	-40	44	-19
February	58	-32	44	-11
March	70	-28	54	-6
April	82.9	6	60	23
May	91	13	71	30
June	97	23	79	30
July	101	29	80	52
August	99	28	80	52
September	96	12	74	30
October	82	3	64	22
November	67	-24	52	-9
December	51	-40	44	-23
ANNUAL	101	-40	80	-23

a. CFA -- January 1950 through December 1982.

b. CFA -- January 1950 through September 1983.

Table 2.3.7

MEAN AND MAXIMUM OF DAILY TEMPERATURE RANGE FOR TMI-2 ISFSI SITE[a]

	Mean Range (°F)	Maximum Range (°F)
January	23	52
February	24	50
March	24	50
April	28	57
May	30	55
June	32	54
July	38	56
August	38	57
September	36	58
October	34	58
November	25	51
December	23	45
ANNUAL	31	58

a. CFA--January 1950 through September 1983.

Table 2.3.8

FREEZE AND THAW CYCLES APPLICABLE TO TMI-2 ISFSI SITE[a]

	Days on which Maximum was above 32°F and Minimum was below 32°F		
	Average Number of Days -- Period of Record	**Maximum Number of Days**	**Minimum Number of Days**
January	10	22	1
February	16	28	4
March	25	31	13
April	22	28	15
May	9	18	0
June	1	5	0
July	0	1	0
August	0	3	0
September	7	16	0
October	22	30	11
November	23	28	15
December	14	25	5
ANNUAL	149	183[b]	101[b]

a. CFA -- January 1950 through September 1983.

b. CFA -- January 1950 through August 1964.

Table 2.3.9

MONTHLY AND ANNUAL DEGREE DAYS APPLICABLE TO TMI-2 ISFSI SITE[a]

	Total Accumulated Degree Days			Daily Degree Days	
	Mean	**Highest**	**Lowest**	**Highest**	**Lowest**
January	1,504	1,797	1,086	84	22
February	1,220	1,600	864	77	22
March	1,071	1,425	854	71	11
April	711	889	574	43	5
May	432	610	234	35	0
June	190	291	44	25	0
July	28	76	1	24	0
August	56	192	4	20	0
September	285	493	142	36	0
October	657	832	493	44	0
November	1,051	1,232	860	74	14
December	1,411	1,704	1,181	88	21
ANNUAL	8,616				

a. CFA -- January 1950 through September 1983.

Table 2.3.10

PEAK GUSTS EXPECTED AT TMI-2 ISFSI SITE BASED ON THE GREATER OF CFA AND TAN RECORDED SPEEDS

	20-ft Level[a]		250-ft Level[b]	
	Direction	**Speed (mph)**	**Direction**	**Speed (mph)**
January	SW	78	SW	79[c]
February	WSW	62	SW	66
March	WSW	78	SW	87[d]
April	S	67	SW	76
May	SW	62	SSW	67
June	SSW	67	SSW	75
July	N	68	S	73
August	WSW	64	SW	72
September	WSW	61	WSW	73
October	WSW	66	WSW	76
November	WSW-SW	60	WSW	78
December	SW	64	SSW	80
Period of Record	WSW	78	SW	87

a. April 1950 through October 1964, TAN, and through October 1983, CFA.

b. July 1951 through October 1964, TAN and through October 1983, CFA.

c. January 11, 1972, 20-ft peak gust = 70 mph, 250-ft peak gust = 79 mph from SW.

d. March 1, 1974, 20-ft peak gust = 52 mph, 250-ft peak gust = 87 mph from SW.

Table 2.3-11

INEL DESIGN BASIS TORNADO

Maximum Wind Speed	175 mph
Rotational Speed	145 mph
Translational Speed	30 mph (maximum)
Pressure Drop	0.65 psi
Rate of Pressure Drop	0.25 psi/sec

TMI-2 ISFSI DESIGN BASIS TORNADO

Maximum Wind Speed	200 mph
Rotational Speed	160 mph
Translational Speed	40mph (maximum)
Radius od Max. Rotational Speed	150 ft
Pressure Drop	1.5 psi
Rate of Pressure Drop	0.6 psi/sec

Table 2.3.12

GREATEST PRECIPITATION AMOUNTS EXPECTED AT TMI-2ISFSI SITE

	1-h[a] (in.)	24-h[b] (in.)
January	0.18	1.08
February	0.18	0.96
March	0.17	0.61
April	0.24	1.51
May	1.00	1.78
June	1.15	1.73
July	0.24	1.33
August	0.45	1.44
September	0.55	1.55
October	0.34	1.12
November	0.25	1.02
December	0.23	1.18
ANNUAL	1.15	1.78

a. For period from January 1950 through December 1964, hourly amounts were not available from 1965 through 1982.

b. For period January 1950 through December 1982.

Table 2.3-13

INEL MAXIMUM STORM EVENTS

Storm Duration	Return Period	Precipitation Amount (inches)
1 hour	10 years	1.5x 0.241= 0.36
	50 years	2.0x 0.241=0.48
	100 years	2.5x 0.241=0.63
3 hour	10 years	1.5x 0.423= 0.63
	50 years	2.0x 0.423=0.85
	100 years	2.5x 0.423=1.06
6 hour	10 years	1.5x 0.580= 0.87
	50 years	2.0x 0.580= 1.16
	100 years	2.5x 0.580= 1.45
12 hour	10 years	1.5x 0.769= 1.15
	50 years	2.0x 0.769= 1.54
	100 years	2.5x 0.769= 1.92
24 hour	10 years	1.5
	50 years	2.0
	100 years	2.5

Table 2.3.14

AVERAGE NUMBER OF DAYS WITH PRECIPITATION OF SPECIFIED AMOUNTS APPLICABLE TO THE TMI-2 ISFSI SITE[a]

	Trace or More	0.01 in. or More	0.10 in. or More	0.50 in. or More	1.0 in. or More
January	12.3	7.7	2.2	0.2	0.0
February	9.0	5.9	2.0	0.2	0.0
March	9.8	6.5	2.1	0.0	0.0
April	9.3	6.0	2.2	0.1	0.0
May	10.7	7.4	3.9	0.5	0.0
June	10.1	7.0	3.2	0.6	0.1
July	5.4	3.4	1.2	0.1	0.0
August	6.4	4.0	1.6	0.3	0.1
September	5.7	3.8	1.8	0.3	0.1
October	6.1	3.7	1.7	0.2	0.0
November	8.0	5/5	2/0	0.2	0.0
December	10.7	7.3	2.7	0.1	0.0
ANNUAL	103.5	68.2	27.6	2.8	0.2

a. CFA – January 1950 through September 1983.

Table 2.3.15

NUMBER OF DAYS WITH SPECIFIED SNOWFALL AMOUNTS, AVERAGES, AND EXTREMES EXPECTED AT TMI-2 ISFSI SITE[a]

	≥ 0.1 in.			≥ 1.0 in			3.0 in.		
	Average	**Maximum**	**Minimum**	**Average**	**Maximum**	**Minimum**	**Average**	**Maximum**	**Minimum**
January	9.3	19	0	1.8	5	0	< 1	2	0
February	5.8	12	0	1.0	4	0	< 1	2	0
March	5.3	13	0	1.1	3	0	< 1	2	0
April	3.4	11	0	0.5	3	0	< 1	2	0
May	0.5	2	0	< 1.0	2	0	< 1	2	0
June	0.0	0	0	0	0	0	0	0	0
July	0.0	0	0	0	0	0	0	0	0
August	0.0	0	0	0	0	0	0	0	0
September	0.3	0	0	0	0	0	0	0	0
October	1.1	6	0	< 1.0	1	0	< 1	1	0
November	4.2	10	0	< 1.0	3	0	< 1	3	0
December	7.5	16	1	2.7	6	0	< 1	2	0
SEASONAL	37.4	0	0	0	0	0	0	0	0

a. Based on CFA data from January 1950 through September 1983. Day is from midnight to midnight.

Table 2.3.16

MAXIMUM SNOW DEPTHS ON THE GROUND EXPECTED AT TMI-2 ISFSI SITE[a]

	Average Maximum[b] (in.)	Highest Maximum (in.)	Lowest Maximum (in.)
January	7.0	13	Trace
February	6.7	22	Trace
March	3.6	27	Trace
April	1.3	6	0
May	0.4	5	0
June	0.0	Trace	0
July	0.0	0	0
August	0.0	0	0
September	0.0	Trace	0
October	0.0	3	0
November	1.7	6	0
December	4.1	13	Trace

a. Based on data from 1950 through 1983.

b. Average for period from April 1954 through December 1981.

Table 2.3-17

DEQ-ESTIMATED PLANNING-LEVEL AMBIENT CONCENTRATIONS - INEL AIRSHED

	1-hr	**8-hr**	**24-hr**	**Annual**	**Quarterly**
PM-10	NA	NA	86 ug/m^3	32.7 ug/m^3	NA
TSP	NA	NA	130 ug/m^3	36.7 ug/m^3	NA
Pb	NA	NA	NA	NA	0.17 ug/m^3
CO	10 ppm (11450 ug/m^3)	4.5 ppm (5153 ug/m^3)	NA	NA	NA
NO_2	NA	NA	NA	40 ug/m^3	NA
SO_2	NA	0.208 ppm (544 ug/m^3)	0.055 ppm (144 ug/m^3)	0.009 ppm (23.6 ug/m^3)	NA
0_3	40 ppb (78.5 ug/m^3)	NA	NA	NA	NA

Table 2.3.18

ATMOSPHERE PRESSURE CFA APPLICABLE TO TMI-2 ISFSI SITE

	Station Pressure (in. of mercury)					
	Average	**Average Daily High**	**Average Daily Low**	**Highest**	**Lowest**	**Maximum Monthly Range**
January	25.08	25.18	25.00	25.69	24.26	1.43
February	25.07	25.15	24.98	25.58	24.27	1.31
March	24.99	25.08	24.90	25.61	24.26	1.35
April	24.98	25.07	24.91	25.44	24.46	0.98
May	25.00	25.07	24.94	25.48	24.51	0.97
June	25.02	25.09	24.96	25.39	24.55	0.84
July	25.09	25.15	25.04	25.44	24.71	0.73
August	25.09	25.15	25.03	25.37	24.72	0.65
September	25.09	25.16	25.03	25.59	24.54	0.82
October	25.11	25.19	25.03	25.59	24.54	1.02
November	25.12	25.21	25.04	25.65	24.46	1.19
December	25.13	25.23	25.04	25.66	24.29	1.37
Period of Record	25.06	25.14	24.99	25.69	24.26	1.43[a]

a. Greatest monthly range over the period of record

Table 2.3.19

XOODOQ INPUT DATA AND PROGRAM OPTIONS USED IN TMI-2 ISFSI DISPERSION ANALYSES

Parameter	Option	TMI-2 ISFSI Site
Stability	Various	NRC (ÙT) Grid 3
Wind	Various	PBF (1982)
Plume Spread parameters	Reference 2 and 15	Reference 2
Release height	Elevated or ground level or mixed mod	Ground level
Stack effluent momentum, temperature	Momentum and/or buoyancy	N/A (surface release)
Building wake effects	Dimensions, relation to release point	Not used (design not available)
Transport level wind height	May be extrapolated through planetary boundary layer	Not adjusted (e.g., 15.2m used)
Topography	Input for modified effective plume height	Not used (assume flat terrain)
Radioactive decay	Incorporate varied half lives	Not used (no inventory available)
Dry deposition	Incorporate depletion factors	Not used
Recalculation or stagnation	Tune X/Q, D/Q values	Not considered
Receptor grid	Standard or custom	Standard

Table 2.3.20

MESODIF INPUT DATA AND PROGRAM OPTIONS USED IN TMI-2 ISFSI DISPERSION ANALYSES

Parameter	Option	TMI-2 ISFSI Site
Stability	Various	NRC (ÙT) Grid 3
Wind	Various telemetered stations	All stations
Plume spread parameters	As input	Reference 2
Release height	As input	Surface
Stack effluent momentum, temperature	As input	Ambient
Building wake effects	Option not available	Not considered
Topography	Option not available	Not considered directly (Effects in windfield)
Radioactive decay	Option not available	Not considered
Deposition decay	Option not available	Not considered
Recirculation or stagnation	Considered directly	Yes--in windfield

Table 2.3.21

Example Grid 3 Data Output

Date (YYMMDD),Time (hhmm),GRI BVlt (Volts),GRI CRTmp (Degrees F.),GRI DPts,GRI HVol,GRI NRad (microR/hr),GRI 15S (MPH),GRI 15D (Degrees),GRI 15SD (Degrees),GRI 15G (MPH),GRI 2Tmp (Degrees F.),GRI 15Tmp (Degrees F.),GRI 2MaxT (Degrees F.),GRI 2MinT (Degrees F.),GRI 2RH (Percent),GRI SRad (Watts/m2),GRI Rain (Inches),GRI TopS (MPH),GRI TopD (Degrees),GRI TopSD (Degrees),GRI TopG (MPH),GRI TopT (Degrees F.),GRI BP (Inches Hg)

971124,555,12.94,18.09,300,0,16.51,3.5,208,4.5,4.1,11.75,15.46,11.86,11.62,98.6,0.7,0,4.2,348,3.4,4.6,27.02,25.09
971124,600,12.94,18.05,300,0,15.97,3.2,219,4,3.9,11.66,15.08,11.79,11.52,98.6,0.7,0,5.2,352,8.3,5.8,26.72,25.089
971124,605,12.92,18.05,300,0,16.4,3.4,212,8.6,3.7,11.39,14.16,11.57,11.25,98.3,0.8,0,5.2,356,7.7,6,26.5,25.092
971124,610,12.93,18.01,300,0,16.68,3.2,208,3.9,3.7,11.28,13.62,11.35,11.19,98.4,0.7,0,4.8,354,3.5,5.8,25.73,25.094
971124,615,12.92,17.97,300,0,17.76,3.6,213,5.1,4.2,11.32,13.21,11.39,11.23,98.5,0.9,0,4.3,358,4.5,5,25.63,25.095
971124,620,12.94,17.93,300,0,16.12,3.8,215,5.1,4.5,11.28,13.86,11.41,11.16,98.4,0.7,0,3.9,357,8.1,4.9,25.39,25.096
971124,625,12.94,17.93,300,0,17.01,3.8,215,3,4.2,11.12,12.81,11.26,11.01,98.2,0.8,0,3.4,9,7.4,4.2,25.05,25.098
971124,630,12.94,17.9,300,0,16.61,3.7,215,5.5,4.1,10.94,12.47,11.08,10.81,98.1,0.7,0,3.4,1,11.3,4.5,25.35,25.098
971124,635,12.94,17.82,300,0,17.28,3.4,224,4,3.9,10.83,12.24,10.98,10.67,98.1,0.9,0,4.2,352,12.6,4.8,26.03,25.097
971124,640,12.94,17.74,300,0,17.17,3.2,211,6.3,3.5,10.62,12.04,10.72,10.47,97.9,0.8,0,3.9,9,11.3,4.9,25.68,25.098
971124,645,12.94,17.7,300,0,16.44,3.3,205,2.1,3.5,10.4,12.04,10.53,10.26,97.8,0.7,0,3.5,16,5.9,3.8,25.68,25.1
971124,650,12.93,17.62,300,0,16.71,3.3,197,5.8,3.5,10.36,12.07,10.47,10.26,98,0.8,0,3.5,38,9.7,3.9,25.4,25.099
971124,655,12.93,17.55,300,0,17.14,3.3,206,4.2,3.6,10.53,12.15,10.8,10.31,98.3,0.9,0,2.9,37,6,3.5,24.53,25.102
971124,700,12.93,17.47,300,0,16.76,3.5,205,3.5,3.7,10.87,12.18,10.99,10.74,98.4,1,0,3.6,36,4.6,3.9,24.81,25.102
971124,705,12.93,17.38,300,0,16.14,3.1,205,3.4,3.4,10.9,12.15,10.98,10.81,98.2,0.9,0,4,31,4,5,24.7,25.103
971124,710,12.93,17.31,300,0,16.97,3.1,210,4.2,3.5,10.72,11.97,10.85,10.53,98,0.9,0,3.6,33,7.5,4.7,24.32,25.105
971124,715,12.93,17.28,300,0,17.48,3.2,208,6.3,3.8,10.35,11.71,10.56,10.15,97.6,1,0,3.7,39,7.7,5,24.05,25.105
971124,720,12.93,17.15,300,0,16.33,3.2,211,6.5,3.4,10.08,11.71,10.22,9.9,97.6,1.2,0,3.6,43,9.9,4.9,24,25.105
971124,725,12.93,17.11,300,0,16.15,3.4,202,3.9,3.7,9.73,11.95,10,9.5,97.3,2,0,2.8,59,8.1,3.6,23.81,25.106
971124,730,12.92,17.01,300,0,16.66,3.8,199,5.3,4.2,9.68,12.38,9.86,9.59,97.7,4.6,0,2.9,50,9.5,3.6,23.72,25.107
971124,735,12.92,16.92,300,0,14.6,4.2,198,3.9,5,10.06,12.49,10.49,9.77,98.2,7.8,0,2.2,63,17.5,3.1,24.06,25.105
971124,740,12.92,16.84,300,0,16,4.5,196,2.9,5,10.94,12.56,11.37,10.44,99,11.4,0,1,101,19.1,1.9,24.26,25.104
971124,745,12.92,16.81,300,0,17.14,4,193,4.4,4.5,11.75,12.51,12.13,11.35,99.3,14.2,0,1.8,105,16.5,2.5,24.3,25.103
971124,750,12.92,16.77,300,0,17.18,3.3,202,8.2,3.9,12.31,12.54,12.45,12.07,99.3,17,0,1.9,80,24.3,2.3,24.46,25.103
971124,755,12.92,16.77,300,0,15.87,3.4,217,6,4.4,12.43,12.43,12.52,12.36,99.1,27.5,0,1.4,62,63.1,3.1,24.79,25.103
971124,800,12.92,16.81,300,0,16.02,2.9,208,7,3.4,12.54,12.47,12.65,12.42,99.1,35.2,0,1.2,39,19.7,3.2,25.32,25.103
971124,805,12.92,16.84,300,0,17.61,3.6,211,7.4,4.6,12.72,12.69,12.81,12.6,99.2,44.9,0,1.6,54,91.1,3.2,25.35,25.103
971124,810,12.92,16.93,300,0,16.3,3.7,216,9.4,4.3,12.92,12.97,13.14,12.76,99.5,58.6,0,0.8,334,86.8,2,26.11,25.102
971124,815,12.92,17.01,300,0,16.9,3.2,211,7.1,3.9,13.32,13.21,13.6,13.08,99.7,73.1,0,0.6,345,17.1,1.6,26.72,25.104
971124,820,12.92,17.17,300,0,16.2,3.4,218,8.6,4.1,14.02,13.87,14.43,13.57,100.3,85.9,0,0.6,275,70.7,0.6,26.4,25.109
971124,825,12.92,17.35,300,0,15.89,3.3,222,6.7,4,14.79,14.61,15.13,14.38,100.7,100.3,0,0.6,283,35,0.6,26.62,25.111
971124,830,12.92,17.63,300,0,16.04,3.2,220,8,3.9,15.48,15.21,15.91,15.08,101,120,0,1.5,245,29.5,2.7,26.19,25.113
971124,835,12.92,17.97,300,0,16.22,3.1,220,6.5,3.7,16.34,16.11,16.88,15.87,101.6,116.1,0,0.9,257,12.1,1.8,26.73,25.111
971124,840,12.92,18.36,300,0,16.84,3.2,206,11,4.1,17.53,17.37,18.21,16.84,102.3,133.7,0,1.7,227,12.3,2.7,27.56,25.111
971124,845,12.93,18.86,300,0,16.29,3.1,206,10.3,4.2,18.97,18.78,20.06,18.16,103.3,191.9,0,3.4,214,4.6,4.1,27.64,25.11
971124,850,12.93,19.4,300,0,16.76,3.5,191,6.9,4.3,20.65,20.25,21.29,19.97,103.9,201.2,0,4.5,198,7.2,5,27.29,25.11
971124,855,12.93,20.05,300,0,16.45,2.9,186,7.6,4,22.04,21.44,22.76,21.2,104.5,222,0,4.5,182,3.9,6.2,27.14,25.109
971124,900,12.92,20.81,300,0,14.27,3.3,186,8,4.7,23.22,22.46,23.65,22.65,104.7,226.5,0,5,181,2.3,6.7,27.02,25.108
971124,905,12.92,21.64,300,0,15.36,3.4,178,7.3,4.5,24.17,23.42,24.71,23.49,105.1,205.1,0,6,179,3.2,7.2,26.34,25.109
971124,910,12.93,22.5,300,0,16.59,2.7,172,10.2,4.1,24.98,24.3,25.25,24.64,105.2,174.2,0,6.6,183,4.6,8,25.92,25.111
971124,915,12.93,23.44,300,0,16.51,2.5,170,11.7,3.7,25.02,24.29,25.17,24.83,104.7,171.4,0,7.2,193,4.1,7.6,25.45,25.112
971124,920,12.93,24.34,300,0,15.97,2.6,170,14.1,4.2,25.09,24.31,25.54,24.79,105,251.4,0,7.1,196,7.6,7.7,25.52,25.109
971124,925,12.92,25.23,300,0,16,3,190,11.2,3.9,25.71,25.02,26.25,25.35,105.4,268.8,0,6.8,209,3.3,7.6,25.77,25.11
971124,930,12.93,26.13,300,0,14.76,3.2,197,8.4,3.9,26.59,26.04,26.98,26.17,105.9,302.7,0,6.3,205,7.1,7.3,25.68,25.112
971124,935,12.94,27.02,300,0,14.69,3.2,183,8.7,4.3,27.3,26.64,27.59,26.86,106.1,325.3,0,5.4,202,8.6,6.9,25.98,25.112
971124,940,12.93,27.91,300,0,15.22,3.2,188,7.4,3.9,27.58,26.71,27.78,27.35,106,300.3,0,4.7,203,13.2,6.2,26.02,25.114
971124,945,12.93,28.79,300,0,16.16,2.9,189,12.5,4.2,27.61,26.79,27.87,27.46,105.9,266.2,0,4.9,206,10.5,5.9,26.07,25.118
971124,950,12.93,29.68,300,0,15.58,2.2,190,15.7,3.7,27.73,27.06,27.9,27.56,106,346.4,0,4.6,208,7.1,7,26.67,25.12
971124,955,12.93,30.57,300,0,15.48,2.1,190,13.6,3.1,28.12,27.65,28.39,27.82,106.3,298.7,0,3.6,223,12.5,4.7,27.05,25.121
971124,1000,12.93,31.45,300,0,17.16,2.5,180,15,3.8,28.65,28.05,29.01,28.02,106.6,371.5,0,3.6,198,14.5,4.6,27.44,25.12
971124,1005,12.93,32.37,300,0,16.75,3,182,20.3,5,29.18,28.57,29.45,28.79,106.7,371.5,0,3.3,206,20,4.9,27.94,25.121
971124,1010,12.93,33.34,300,0,16.04,3.2,188,20.7,5.6,29.56,29.05,29.97,29.32,106.8,371.6,0,4,207,11.6,5.7,28.3,25.122
971124,1015,12.94,34.3,300,0,14.41,3.5,176,10.2,4.7,30,29.39,30.1,29.92,106.9,367,0,3.2,191,13.9,4.2,28.95,25.123
971124,1020,12.94,35.41,300,0,15.06,2.5,164,15.9,4.8,30.26,29.54,30.53,30.05,106.9,380.1,0,3.2,160,15,4.3,29.46,25.122

Table 2.4-1. Monthly Discharge of the Big Lost River at Lincoln Boulevard near the ICPP

Year	Jan	Feb	Mar	Apr	May	Jun	Jul	Aug	Sep	Oct	Nov	Dec	Annual
1965	0	0	2,380	10,300	15,400	29,600	31,100	16,900	10,900	0	0	0	116,580
1966	0	0	0	3,660	981	0	0	0	0	0	0	0	4,641
1967	0	0	0	0	2,030	20,180	18,376	4,400	9,050	8,740	0	0	62,776
1968	0	0	2,280	3,390	16	524	0	1,053	1,130	3,290	4,500	0	16,183
1969	0	0	0	3,960	33,000	33,500	21,800	4,780	9,840	6,710	3,290	0	116,880
1970	0	0	501	1,650	793	13,800	17,700	1,510	6,080	5,280	4,750	8	52,072
1971	0	0	0	10,600	12,300	17,200	20,800	7,760	13,400	14,400	13,100	0	109,560
1972	0	0	1,540	4,920	504	1,710	861	84	2,990	3,520	3,099	0	19,228
1973	0	0	0	2,830	405	0	0	0	0	0	0	0	3,235
1974	0	0	3,240	5,520	6,940	16,200	9,390	1,170	1,160	3,760	4,200	0	51,580
1975	0	0	0	3,180	12,000	12,100	18,700	3,560	6,520	8,210	7,990	0	72,260
1976	0	0	333	1,450	1,660	1,120	0	0	300	620	1,100	76	6,659
1977	0	0	0	0	0	0	0	0	0	0	0	0	0
1978	0	0	0	0	0	0	0	0	0	0	0	0	0
1979	0	0	0	0	0	0	0	0	0	0	0	0	0
1980	0	0	0	0	0	0	1,140	0	0	0	0	0	1,140
1981	0	0	0	1,300	5,092	7,560	0	0	0	0	0	0	13,952
1982	0	0	0	5,930	17,200	13,400	15,100	4,820	8,190	10,500	5,740	600	81,480
1983	600	600	900	12,800	15,800	18,900	18,200	9,780	7,320	6,200	5,660	1,200	97,960
1984	1,200	1,200	1,200	2,200	2,230	4,550	3,950	5,790	5,140	5,980	8,710	2,120	44,360
1985	3	0	0	7,170	6,430	0	0	0	9,950	10,707	1,275	0	35,535
1986	0	96	537	8,370	14,825	20,315	2,900	1,016	14,753	8,220	1,190	2	72,224
1987	0	0	531	491	0	0	0	0	0	0	0	0	1,022
1988	0	0	0	0	0	0	0	0	0	0	0	0	0
1989	0	6	0	0	0	0	0	0	0	0	0	0	0
1990	0	0	0	0	0	0	0	0	0	0	0	0	0
1991	0	0	0	0	0	0	0	0	0	0	0	0	0
1992	0	0	0	0	0	0	0	0	0	0	0	0	0
1993	0	0	0	0	0	5,116	0	0	0	0	0	0	5,116
1994	0	0	0	0	0	0	0	0	0	0	0	0	0

Source: Monthly discharge (cubic feet) value for 1965-88 from Bennett, Streamflow Losses and Groundwater Level Changes Along the Big Lost River at the Idaho National Engineering Laboratory, Idaho. USGS Water-Resources Investigations Report 90-4067. Data from 1989-94 from USGS printout.

Table 2.4-2 Mackay Dam and INEL Diversion Dam and reservoir characteristics Koslow and Van Haaften, 1986).

	Mackay Dam	INEL Diversion Dam
Dam crest elevation (ft msl)	6,076.0	5,064.7
Dam crest length (ft)	1,430	500
Dam height (ft)	79	22
Spillway	Ungated overflow crest, 75 ft long	none
Spillway crest elevation (ft msl)	6,066.5	NA
Gate centerline elevation (ft msl)	6,036.6 (upper) 6,007.8 (lower)	5,045.6
Dam base elevation (ft msl)	5,997.0	5,042.6
Spillway maximum capacity (cfs)	6,588	NA
Gate maximum capacity (cfs)	2,960	1,121
Reservoir capacity[a] (ac-ft)	55,091 @ 6,076.0 44,500 @ 6,066.5 8,750 @ 6,030.0 500 @ 6,010.0	18,200 @ 5,040.0 58,000 @ 5,050.0

a. It has been estimated that Mackay Reservoir has lost 22% of its mid and late-season irrigation capacity due to sedimentation of the reservoir (Butte Soil Conservation District, 1982). Reservoir capacity given for INEL diversion dam is for the spreading areas; no water is held immediately behind the diversion dam.

Table 2.4-3. Average, highest, and lowest total monthly and annual precipitation at CFA from January 1950 to December 1988.[a]

Month	Average (in.)	Highest (in.)	Lowest (in.)
January	0.69	2.56	0.00
February	0.64	2.40	0.00
March	0.60	1.44	0.07
April	0.73	2.50	0.00
May	1.20	4.42	0.07
June	1.18	3.89	0.02
July	0.53	2.29	0.00
August	0.57	3.27	0.00
September	0.63	3.52	0.00
October	0.52	1.67	0.00
November	0.68	1.74	0.00
December	0.75	3.43	0.02
Annual	8.71	14.40	4.50

a. Clawson et al. (1989).

Table 2.4-4. Results of PMF-induced overtopping failure of Mackay Dam (Koslow and Van Haaften, 1986).

Location (approximate elevation, ft msl)	Streambed elevation (ft msl)	Peak water surface elevation (ft msl)	Peak flood flow (cfs)	Peak water velocity (ft/s)	Time of wave arrival (hr)
Mackay Dam (6076)	5997	6078	306,700	8.5	0.0
Arco (5310-5410)	5309	5319	147,720	5.6	6.7
INEL Diversion (5065)	5043	5073	71,850	1.0	10.0
CFA (4928-4940)	4935	4942	67,830	3.4	12.8
TRA (4920-4925)	4919	4924	67,170	2.8	13.2
ICPP (4914-4930)	4911	**4917**	66,830	2.7	13.5
NRF (4845-4850)	4846	4851	61,620	1.9	16.4
TAN (4780-4795)	4778	4786	34,810	1.1	34.5

Total flow to INEL diversion spreading areas: 27,460 ac-ft
Total Mackay Reservoir release: 142,330 ac-ft.

Table 2.4-5. Results of seismic-induced failure of Mackay Dam during 25-yr flood (Koslow and Van Haaften, 1986).

Location (approximate elevation, ft msl)	Streambed elevation (ft msl)	Peak water surface elevation (ft msl)	Peak flood flow (cfs)	Peak water velocity (ft/s)	Time of wave arrival (hr)
Mackay Dam (6076)	5997	6067	107,480	5.8	0.0
Arco (5310-5410)	5309	5317	74,240	4.8	8.3
INEL Diversion (5065)	5043	5070	45,410	1.4	11.8
CFA (4928-4940)	4935	4942	40,520	3.0	14.8
TRA (4920-4925)	4919	4923	39,580	2.5	15.3
ICPP (4914-4930)	4911	**4916**	39,080	2.4	15.8
NRF (4845-4850)	4846	4850	31,690	1.5	18.9
TAN (4780-4795)	4778	4782	4,440	0.7	42.5

Total flow to INEL diversion spreading areas: 8,480 ac-ft
Total Mackay Reservoir release: 44,830 ac-ft.

Table 2.4-6. Dam Failure Characteristics of four hypothetical failure scenarios (Koslow and Van Haaften, 1986).

	Seismic	100-yr Piping	500-yr piping	Overtopping PMF
Mackay Dam:				
Breach Type	Trapezoid	Triangle	Trapezoid	Trapezoid
Breach bottom width, ft	31.6	0.0	31.6	140.0
Breach side slope, x/y	0.6	0.6	0.6	0.6
Failure mode	Internal (seismic)	Internal (piping)	Internal (piping)	Hydrologic (overtopping)
Failure time, hr	1.0	1.0	1.0	1.0
Reservoir inflow hydrograph	25-yr flood	100-yr flood	500-yr flood	PMF
Peak reservoir inflow, cfs	4,030	4,870	5,760	82,100
Reservoir level at failure, ft msl	6,066.5	6,066.5	6,066.5	6,077.0
INEL Diversion Dam:				
Breach type	Trapezoid	Trapezoid	Trapezoid	Trapezoid
Breach bottom width, ft	60.0	60.0	60.0	60.0
Breach side slope, x/y	0.6	0.6	0.6	0.6
Failure mode	Overtopping	Overtopping	Overtopping	Overtopping
Failure time, hr	0.1	0.1	0.1	0.1
Initial water level, ft msl	5,059.6	5,059.6	5,059.6	5,059.6
Flow losses, percent of total flow	40	40	40	40

Table 2.5-1: INEEL Production Wells and Annual Volume Pumped

Well Name	Depth of well (ft bls)[a]	Depth to Water (ft bls)	Annual Volume (gal)
ANP-01	360	208	2.561E+06
ANP-02	340	211	1.433E+06
ANP-08	309	218	3.908E+05
Badging Facility well	644	489	5.760E+04
CFA-1	639	468	1.473E+07
CFA-2	681	471	1.448E+05
CPP-01	586	460	1.834E+08[b]
CPP-02	605	460	1.834E+08[b]
CPP-04	700	462	1.834E+08[b]
CPP-05	695	447	1.834E+08[b]
EBR-1	1075	596	4.491E+04
EBR II-1	745	632	2.767E+06[c]
EBR II-2	753	630	2.767E+06[c]
FET-1	330	199	1.427E+06
FET-2	455	200	5.067E+05
Fire Station well	516	420	1.057E+04
NRF-1	535	363	2.594E+06
NRF-2	529	362	9.368E+06
NRF-3	546	363	9.802E+04
NRF-4	597	363	1.649E+07
Rifle Range well	620	508	9.115E+04
RWMC Production	685	568	4.824E+05
SPERT-1	653	456	3.871E+05
SPERT-2	1217	463	3.450E+05
TRA-01	600	453	3.595E+07
TRA-03	602	456	2.074E+06
TRA-04	965	463	9.006E+07

a. Feet below land surface (ft bls)
b. Annual volume data is the total for wells CPP-1, CPP-2, CPP-4, and CPP-5.
c. Annual volume data is the total for both wells EBR II-1 and EBR II-2.
Note: All wells are withdrawing water from the main body of the Snake River Plain Aquifer and are used as drinking water wells with the exception of wells ANP-08, Fire station well, and NRF-4 which are production wells for facility operations.

Table 2.6-1. Summary of geologic units in the INEL area.

Age	Unit, thickness, distribution	Physical character	Origin	Reference
Holocene to Late Pleistocene	Eolian deposits, <30m; covers much of INEL, sand dunes in NE part and loess blankets elsewhere	Fine sand and silt, dune forms and blankets	Sand from Lake Terreton beaches; loess from glacial and alluvial fan deposits	Scott 1982, Nace et al. 1975
	Playa deposits, <10m, in sinks areas of northern INEL and scattered small playas across INEL	Poorly sorted clayey, sandy silt, some with high carbonate content	Deposited in closed depressions during wet periods	Scott 1982; Nace et al 1975; Kuntz et al. 1994
	Alluvium and alluvial fans, up to 30m, along streams and at base of mountains	Gravels with varying content of sand, silt, clay	Mainstream deposits along rivers, debris flows and intermittent stream deposits in fans	Scott 1982; Nace et al. 1975; Kuntz et al. 1994
	Holocene Lava fields, up to 30m, in Great Rift and along Axial Volcanic Zone	Olivine tholeiite basalt to rhyodacite and ferroliatite	Erupted from VRZs and AVZ	Kuntz et al 1986, 1994
Pleistocene	Lake Terreton deposits, <50m, northeastern INEL and Mud Lake area	Sandy and clayey light colored silt with lenses of pure sand, silt, and clay	Deposited in beaches, bars, and floor of Pleistocene Lake Terreton	Nace et al. 1975; Scott 1982
	Rhyolite Domes, along axis of ESRP	Porphyritic to aphric rhyolite flows and minor pyroclastics	Dome building eruptions at Big Southern, East, Middle, Cedar, and unnamed butte.	Armstrong, Leeman, and Malde 1975; Hackett and Smith 1992; Hayden 1992

Table 2.6-1. (continued)

Age	Unit, thickness, distribution	Physical character	Origin	Reference
Late Tertiary to Quaternary	Snake River Group basalts and interbedded sediments ~1km, ESRP	Porphyritic to aphyric olivine tholeiites, fractured and vesicular, flows ~20 ft thick, interbedded with alluvial, eolian, and lacustrine sediments	Erupted from numerous vents and fissures in VRZs and AVZ of ESRP	Armstrong, Leeman, and Malde 1975; Malde 1991; Hacket and Smith 1992
Late Tertiary	Heise Volcanics, Several thousand meters, buried beneath ~1km of ESRP basalt and outcrops along margins of ESRP	Ash flow tuffs and rhyolitic lavas	Erupted from calderas buried beneath the basalts of the ESRP	Morgan 1988; Hackett and Morgan 1988; Hackett and Smith 1992
Late Precambrian to Paleozonic	Carbonate and clastic sedimentary rocks, >5,000m, mountains north and south ESRP	Quartzites overlain by middle to upper Palezoic carbonates	Marine deposition followed by Mesozoic thrusting	Link et al. 1988; Skipp and Hait 1977.

Table 2.6-2. Chemical analyses and ion exchange capacities of Eastern Snake River Plain basalts.

Chemical analysis		Ion exchange capacity[a]	
SiO_2	47.04	4 mm	0.98
$Ti0_2$	2.70	2 mm	0.89
Al_20_3	15.11	1 mm	0.73
Fe0	13.51	0.5 mm	0.61
Mn0	0.20	0.25 mm	0.86
Mg0	7.65	0.125 mm	1.32
Ca0	10.06	0.062	2.80
Na_20	2.54	<230 mesh	2.30
K_20	0.61		
P_20_5	0.58		

a. Meg per 100 g of rock

TABLE 2.6-3. TIME PERIODS OF EARTHQUAKE DATA COMPLETENESS

Magnitude Interval	Completeness Period
2.0-4.0	1975-1995
4.0-5.0	1963-1995
5.0-5.5	1950-1995
5.5-6.0	1925-1995
6.0-6.5	1900-1995
6.5-7.0	1875-1995
7.0 +	1850-1995

Modified from Woodward-Clyde Consultants [2.52].

TABLE 2.6-4. EARTHQUAKES WITH MAGNITUDES GREATER THAN 5.5 WITHIN 200 MILES OF INEEL

EARTHQUAKE DATE & TIME (HR:MN - UTC)[A]	MAGNITUDE[B]	MODIFIED MERCALLI INTENSITY[C]		GEOGRAPHICAL LOCATION[D]	RADIAL DISTANCE (KM)[E]	REFERENCES
		EPICENTER	ISFSI SITE			
1884 November 10 08:50						
1905 November 11 21:26	5.5 M_L	VII	IV	Shoshone, Idaho	164	2
1909 October 6 02:50	6.3 M_I	VIII		Hansel Valley, Utah	216	1
1914 May 13 17:15	5.7 M_I	VII		Ogden, Utah	283	1
1925 June 28 01:21 ~~July 10 14:45~~	6.8 M 6.6 M_w	VI		Clarkston, Montana	275 ~~201~~	3,4,5
1925 June 29 01:12	6.3 M			Clarkston, Montana	292	20
1930 June 12 09:15	5.8 M_L	VI		E of Soda Springs, Idaho	190	5
1934 March 12 15:05	6.6 M_L 6.6 M_w	IX		Hansel Valley, Utah	222	1,3,6
1934 March 12 18:20	6.2 M_L 5.9 M_w	VII		Hansel Valley, Utah[f]	222	1,3,6
1934 April 14 21:26	5.6 M_L	VII		Hansel Valley, Utah[f]	245	1

TABLE 2.6-4. EARTHQUAKES WITH MAGNITUDES GREATER THAN 5.5 WITHIN 200 MILES OF INEEL

EARTHQUAKE DATE & TIME (HR:MN - UTC)[A]	MAGNITUDE[B]	MODIFIED MERCALLI INTENSITY[C]		GEOGRAPHICAL LOCATION[D]	RADIAL DISTANCE (KM)[E]	REFERENCES
		EPICENTER	ISFSI SITE			
1934 May 06 08:09	5.6 M_L	VI		Hansel Valley, Utah[f]	222	1
1944 July 12 19:30	6.1 M_b	VII		N of Stanley, Idaho	235	7
1945 February 14 03:01	6.0 M_L	VI		N of Stanley, Idaho	235	7
1947 November 23 00:46 ~~December 17~~	6.3 M 6.1 M_w			Virginia City, Montana	138~~225~~	3,4
1959 August 18[g] 06:37	7.5 M_s 6.3, 7.3 M_w	X	VI	Hebgen Lake, Montana	187	3,8,9,10
1959 August 18 07:56	6.5 M			Hebgen Lake, Montana	208	3
1959 August 18 08:41	6.0 M			Hebgen Lake, Montana	208	3
1959 August 18 11:03	5.6 M			Hebgen Lake, Montana	182	3
1959 August 18 15:26	6.5 M_b 6.3 M_w			Hebgen Lake, Montana	209	10
1959 August 19 04:04	5.9 M_s 6.0 M_w			Hebgen Lake, Montana	209	4,10
1962 August 30 13:35	5.7 M_s 5.9 M_w	VII		Cache Valley, Utah	208	1,3,11

TABLE 2.6-4. EARTHQUAKES WITH MAGNITUDES GREATER THAN 5.5 WITHIN 200 MILES OF INEEL

EARTHQUAKE DATE & TIME (HR:MN - UTC)[A]	MAGNITUDE[B]	MODIFIED MERCALLI INTENSITY[C]		GEOGRAPHICAL LOCATION[D]	RADIAL DISTANCE (KM)[E]	REFERENCES
		EPICENTER	ISFSI SITE			
1964 October 21 07:38	5.8 M_b 5.6 M_w			Hebgen Lake, Montana[h]	154	3,4
1975 March 28 02:31	6.1 M_b 6.2 M_w	VIII	III	Pocatello Valley, Utah	183	3,12
1975 June 30 18:54	6.1 M_L	VII	NF	Yellowstone Park, Wyoming	209	3,13
1976 December 8 14:40	5.5 M_b			Yellowstone Park, Wyoming	198	5
1983 October 28 14:06	7.3 M_s 6.8 M_w	IX	VI	N W of Mackay, Idaho[i]	93	3,8,9,14
1983 October 28 19:51	5.8 M_L 5.4 M_w			N W of Mackay, Idaho[i]	98	3,15
1983 October 29 23:29	5.8 M_L 5.5 M_w			N W of Mackay, Idaho[i]	121	3,15
1984 August 22 09:46	5.8 M_L 5.6 M_w			Challis, Idaho[i]	127	3,15
1994 February 309:05	5.9M_w 5.7M_w	V	NF	W of Afton, Wyoming	172	16,17,18

Table 2.6-4

NOTES:

a - UTC - Universal Time Coordinated (Greenwich Mean Time).

b - Highest magnitude value is reported in this Table. Moment magnitudes are included, if calculated. Magnitude Scales: M_I - Conversion from Intensity; M_L - Local or Richter; M - magnitude type not specified; M_w - Moment; M_b - Body-wave; M_s - Surface-wave.

c - Modified Mercalli intensity for epicenter is based on Wood and Neumann, 1931. Modified Mercalli intensity at ISFSI site was obtained from available intensity maps. "NF" indicates "Not Felt" where documented. Blanks indicate no information available.

d - Latitude and Longitude coordinates are listed in Table 3.7-4.

e - Radial distances based on coordinates 43° 42.0', 112° 48.0'.

f - Aftershock following the M_L = 6.6, 1934 Hansel Valley, Utah earthquake.

g - Hebgen Lake usually referred to as M_s 7.5, but is actually a two events having magnitudes of M_w 6.3 and 7.3 per Doser, 1985.

h - Aftershock following the M_s = 7.5, 1959 Hebgen Lake, Montana earthquake.

i - Aftershock following the M_s = 7.3, 1983 Borah Peak, Idaho earthquake.

References: (1) Richins, 1979; (2) Oaks, 1992; (3) Doser and Smith, 1989; (4) Doser, 1989a; (5) National Earthquake Information Center, unpublished data; (6) Doser, 1989b; (7) Stover et al., 1986; (8) Doser, 1985a; (9) Stover, 1985; (10) Doser, 1985b; (11) Westaway and Smith, 1989; (12) Arabasz et al., 1979; (13) Pitt et al., 1979; (14) Doser and Smith, 1985; (15) Richins et al., 1987; (16) Dewey, 1994; (17) Nava et al, 1994; (18) Pechmann et al., 1997; (19) Cook and Nye, 1979; (20) Stover et al., 1977.

Table 2.6-5. Ground motions recorded during the Borah Peak earthquake at CPP-601 (~1000 feet north of the TMI-2 ISFSI site).

Location		**Acceleration** (g)	**Velocity** (cm/sec)	**Displacement** (cm)
CPP-601 1st Floor	L	0.043	1.38	0.25
	T	0.065	2.76	0.13
	V	0.033	1.28	0.16
CPP-601 2nd Basement	L	0.038	1.32	0.12
	T	0.044	2.19	0.16
	V	0.038	1.46	0.11
CPP-601 Free Field	L	0.078	2.03	0.23
	T	0.058	2.80	0.34
	V	0.035	1.39	0.25

TABLE 2.6-6. BASIN AND RANGE FAULTS AROUND THE ESRP

For each segment or fault, the information under IMPORTANT POINTS is presented as follows: Most recent event (MRE) in thousands of years (Ka), type of study, displacement per last event (D), length (L), slip rate (SR), and recurrence interval (RI). ND = no data available.

FAULT	REFERENCE	IMPORTANT POINTS
Sawtooth, White Cloud Peaks area	Dewey (1987), Jackson and Zollweg (1988), Smith et al (1985).	Contemporary earthquake swarms, maximum magnitude = 6.1, several mapped normal faults.
Lost River Fault	Pierce (1985, 1988), Scott et al. (1985), Crone et al. (1987), Schwartz (1988), Malde (1987), Piety et al. (1986)	**Arco Segment** - MRE~30 Ka, trenching, D~2-3 m, L~10 km, SR~0.12 mm/y, RI~30-40 Ka. **Pass Creek Segment** -MRE~30-50 Ka, scarp morphology, ND, L~30 km, RI~30-50 Ka? **Mackay Segment** -MRE~4.3-6.8 Ka, trenching, ND, L~22 km, SR~0.3 mm/yr, RI~4-7 Ka. **Thousand Springs Segment** - MRE=1983, trenching/earthquake, D=2.7 m, L=36 km, SR=0.3 mm/yr, RI=6-7Ka. **Warm Spring Segment** - MRE~5.5-6.2 Ka, trenching, ND, L~15 km, SR=0.3 mm/yr, RI<15 Ka. **North Segment** - MRE>Late Quaternary, scarp morphology, ND, L~20 km., ND, ND, low structural relief.

Lemhi Fault	Woodward-Clyde Consultants (1992a, 1992b), Knuepfer (1989), Turko (1988), Baltzer et al. (1989), Malde (1987), Haller (1988), Scott et al. (1985), Bruhn et al. (1992)	**Southern Segments (Howe and Fallert Springs segments) -** MRE~15-24Ka, trenching/scarp morphology, D~2-3 m, L~25km, SR~0.1mm/yr, RI=3.3Ka(ave.) **Sawmill Gulch Segment** - MRE<10Ka, trenching, D=1.7 m, L=43 km, ND, ND. **Goldburg Segment** - MRE~10-15 Ka, scarp morphology, ND, L=12 km, ND, ND. **Patterson Segment** - MRE<10 Ka?, scarp morphology, ND, L~23 km, ND, ND. **May Segment** - MRE~15-30 Ka?, scarp morphology, ND, L~23 km, ND, ND.
Beaverhead Fault	Haller (1988), Stickney and Bartholomew (1987).	**Blue Dome Segment** - MRE>30 Ka, scarp morphology, ND, L~25 km, ND, ND. **Nicholia Segment** - MRE~10-15 Ka, scarp morphology, ND, L~42 km, ND, ND. **Baldy Mountain Segment** - MRE>30 Ka, scarp morphology, ND, L~21 km, ND, ND. **Leadore Segment** - MRE<10 Ka, scarp morphology, ND, L~23 km, ND, ND. **Mollie Gulch Segment** - MRE~10-15 Ka?, scarp morphology, ND, L~20 km, ND, ND. **Lemhi Segment** - MRE>30 Ka, scarp morphology, ND, L~20 km, ND, ND.
Red Rock Fault	Haller (1988), Stickney and Bartholomew (1987).	**Sheep Creek Segment** - MRE<10 Ka, scarp morphology, ND, L~16 km, ND, ND. **Timber Butte Segment** - MRE~10-15 Ka, scarp morphology, ND, L~11 km, ND, ND.
Centennial Fault	Stickney and Bartholomew (1987), Johnson (1981).	**Western Centennial Valley Segment** - MRE<10 Ka, scarp morphology, ND, L~23 km, ND, ND. **Red Rocks Lake Segment** - MRE>20 Ka?, scarp morphology, ND, L~24 km, ND, ND. **Henrys Lake Segment** - MRE<10 Ka, scarp morphology, ND, L~1 km, ND, ND.

Madison Fault	Stickney and Bartholomew (1987), Schneider (1985)	**Madison Canyon Segment** - MRE~Late Holocene (1947?, 1959?), scarp morphology, ND, L~34 km (total fault length = 117 km). Additional scarps exist but no segments have been delineated (a short segment of this fault ruptured in 1959).
Hebgen Fault and Red Canyon Fault	Stickney and Bartholomew (1987), Doser (1985b).	**Hebgen Fault** - MRE=1959, scarp morphology, D=6.7m, L~13 km (+ 14 km on R.C.Fault), ND, ND. **Red Canyon Fault** - MRE=1959, scarp morphology, D=6.7m, L~45 km, SR~1.2-1.5 mm/yr (pre-1959), RI=4.3 Ka.
Yellowston e area	Pitt et al (1979), U.S. Geological Survey (1972), Doser (1984).	Numerous north-trending normal faults around Yellowstone Caldera with Quaternary movement. Contemporary seismicity, maximum magnitude = 6.1. RI = 700-750 years for M7 earthquakes based on seismic moment rates.
Teton Fault	Piety et al. (1986), Smith et al. (1990), Byrd et al. (1988), Susong et al. (1987), Gilbert et al. (1983)	**South Segment** - MRE~7Ka, trenching and scarp morphology, D=4.1m, L~24 km, SR~1.7-2.2 mm/yr, RI~1.4-2.3Ka. **Middle Segment** - MRE<11-14Ka, scarp morph., D~3m, L~20 km, SR~1.7-2.2 mm/yr, RI~1.4-2.3Ka. **North Segment** - MRE<11-14Ka, scarp morph., D~3m, L~20 km, SR~1.7-2.2 mm/yr, RI~1.4-2.3Ka.
Grand Valley Fault	Anders et al. (1989), Piety et al. (1986).	**Grand Valley Fault** - MRE>15-30 Ka, scarp morphology, ND, L~72 km, SR~0.02-0.04 mm/yr, ND.

Snake River Fault	Anders et al. (1989), Piety et al. (1986).	**Snake River Fault** - MRE>15-30 Ka, scarp morphology, ND, L~50 km, SR~0.001 mm/yr, ND
Star Valley Fault	Anders et al. (1989), Piety et al. (1986), McCalpin et al. (1990).	**Northern Segment** - MRE<9Ka, scarp morphology, D~3.6-6.3, L~30 km, SR~0.8-1.2mm/yr, RI~5-7Ka. **Southern Segment** - MRE<9Ka, trenching and scarp morphology, D~5.0-6.3 m, L~28 km, SR~0.6-1.1 mm/yr, RI~5-7 Ka.
Northern Wasatch Fault Segments	Schwartz (1988), Machette et al. (1992), Swan et al. (1980), Piety et al. (1986).	**Collinston Segment** - MRE>13 Ka, scarp morphology, ND, L~25 km, ND, ND. **Brigham City Segment** - MRE=3400 yrs, trenching, ND, L~40 km, ND, ND. **Weber Segment** - MRE~500 years, 1.7-3.7 m, trenching, D~1.7-3.7m, L~50 km, SR~1.2-2.8 mm/yr, RI~1Ka?

TABLE 2.6-7. EARTHQUAKES WITHIN 200 MILES THAT HAVE OCCURRED ON TECTONIC STRUCTURES

Earthquake Date & Time (Hr:Mn - UTC)[a]	Seismic Moment[b] ($x10^{25}$ dyne-cm)	Focal Mechanism Strike/Dip/Rake[c] (Degrees)	Tectonic Structure, Source Parameters and Dimensions, and References[d]
1925 June 28 01:21	10 ± 2 B	30 80 -175 FM 250 56 - 38 BW	Associated with a fault oriented in an oblique manner north of the Clarkston Valley Fault north of Bozeman, Montana. Z=9±5 km (LP); RL=25±5 km (BW), 59±5 km (SF); SD=2.0±1.0 m (v). (1,2)
1934 March 12 15:05	0.95 G 8.6 ± 2 B	7 80 - 70 FM 40 87 - 11 BW 0 73 -110 SF	Caused a fault scarp along an unnamed fault in Hansel Valley, Utah. Z= 8±2 km (LP); RL=11±3 km (BW), 6±2 km (SF); BWD= -2.1±0.1 m (h), 0.2±0.05 m (v); SD= -0.2 (h), 2.0±1.0 m (v); GD= 0.4±0.1 m (v). (1,3)
1934 March 12 18:20	0.77 ± 0.3 B	25 85 - 20 BW	Aftershock to March 12, 1934 earthquake. Z= 8±7 km (LP); RL=7±3 km (BW); BWD= -0.5±0.1 m (h). (1,4)
1947 November 23 09:46	1.8 ± 0.5 B	120 60 -120 FM 104 48 -170 BW	Possibly associated with the Madison Fault northwest of Hebgen Lake, Montana. Z= 8±2 km (LP); RL=9±2 km (BW); BWD= -0.7±0.2 m (h). (1,2,5)
1959 August 18 06:37 (M_s 7.5)	41 G 150 L 120 S	102 60 - 90 SW 120 70 - 90 SF 132 45 - 90 GE	Caused a fault scarp along the Hebgen and Red Canyon faults near Hebgen Lake, Montana. No distinction between subevents: Z= 11±2 km (LP); RL=24±4 km (SF), 40±4 km (GE); SD= 4.4 m (v); GD= 7.4±0.4 m (v). (1,6)
1959 August 18 06:37 (M_w 6.3)	2.8 B	102 60 - 90 FM 95 42 - 90 BW	Subevent 1: Z= 10±2 km (LP); RL=7±1 km (BW); BWD= 0.95 m (v). (1,6)
1959 August 18 06:37 (M_w 7.3)	92 B	100 54 - 90 FM 95 42 - 90 BW	Subevent 2: Z= 15±3 km (LP); RL=21±5 km (BW); BWD= 6.8 m (v). (1,6)

TABLE 2.6-7 Continued. EARTHQUAKES WITHIN 200 MILES THAT HAVE OCCURRED ON TECTONIC STRUCTURES

Earthquake Date & Time (Hr:Mn - UTC)[a]	Seismic Moment[b] ($x10^{25}$ dyne-cm)	Focal Mechanism Strike/Dip/Rake[c] (Degrees)	Tectonic Structure, Source Parameters and Dimensions, and References[d]
1959 August 18 07:56	nd	70 55 - 45 FM	Aftershock to August 18, 1959 earthquake. nd. (1)
1959 August 18 08:41	nd	70 65 - 15 FM	Aftershock to August 18, 1959 earthquake. nd. (1)
1959 August 18 11:03	nd	50 64 31 FM	Aftershock to August 18, 1959 earthquake. nd. (1)
1959 August 18 15:26	3.10 B 5.5 S	90 60 - 70 FM 83 50 - 90 BW	Aftershock to August 18, 1959 earthquake. Z= 10±2 km (LP); RL=9±1 km (BW). (1)
1959 August 19 04:04	1.1 ± 0.3 B 4.8 S	60 75 -155 FM 57 80 -161 BW	Aftershock to August 18, 1959 earthquake. Z= 8±2 km (LP); RL=11±2 km (BW). (1)
1962 August 30 13:35	0.52 ± 0.2 B	185 58 - 85 FM 201 49 -108 BW	Associated with the Temple Ridge fault, Cache Valley, Utah. Z= 12±2 km (LP); RL=3±1 km (BW); BWD= 0.55 ± 0.2 m (h). (1,7)
1964 October 21 07:38	1.10 ± 0.3 B	310 60 18 FM 307 56 14 BW	Aftershock to August 18, 1959 earthquake. RL=3±1 km (BW). (1)
1975 March 28 02:31	1.23 ± 0.6 B 2.4 L 1.2 S	225 39 - 53 FM 200 38 - 70 BW 210 60 - 90 GE	Associated with an unnamed fault in Pocatello Valley, Utah. Z= 9±2 km (LP), 5±2 km (SP), 12 km (GE); RL=12±2 km (BW), 18±2 km (GE); BWD= 0.75 ± 0.25 m (v); GD= 0.50 m (v). (1,8,9)
1975 June 30 18:54	0.75 S	302 71 -129 FM	Associated with an unnamed fault near the north-central boundary of the Yellowstone Caldera, Wyoming. Z= 6±1 km (SP); GD= 0.12 m (v). (1,9,10)

TABLE 2.6-7 Continued. EARTHQUAKES WITHIN 200 MILES THAT HAVE OCCURRED ON TECTONIC STRUCTURES

Earthquake Date & Time (Hr:Mn - UTC)[a]	Seismic Moment[b] ($x10^{25}$ dyne-cm)	Focal Mechanism Strike/Dip/Rake[c] (Degrees)	Tectonic Structure, Source Parameters and Dimensions, and References[d]
1983 October 28 14:06	28 G 21 B 29 L	138 45 - 60 FM 155 50 - 65 BW 160 70 - 70 SF 152 49 nd GE	Caused a fault scarp along the Thousand Springs segment of the Lost River Fault in central Idaho. Z= 16±4 km (LP), 12±2 km (SP), 14 km (GE); RL= 21±2 km (BW), 19±2 km (SF), 20±2 km (GE); BWD= -0.20 m (h), 1.30 m (v); SD= -0.30 m (h), 1.50 m (v); GD= 2.10 m (v). (1,11)
1983 October 28 19:51	0.13 B 0.24 S	287 58 -165 FM 282 48 -159 BW 286 70 -155 SF	Aftershock to October 28, 1983 earthquake. Z= 10 km (LP), 10 km (SP), 10 km (GE); RL= 6±2 km (BW). (1)
1983 October 29 23:29	0.20 B	309 51 - 65 FM 317 45 - 90 BW	Aftershock to October 28, 1983 earthquake. Z= 19±9 km (LP), 10 km (SP); RL= 8±1 km (BW). (1)
1984 August 22 09:46	0.24 B	170 70 - 5 FM 348 85 -160 BW	Aftershock to October 28, 1983 earthquake. Associated with the Challis segment of the Lost River fault and possibly caused slip (M 5.0) on an antithetic fault, the Lone Pine fault, central Idaho. Z= 10 km (LP), 10 km (SP); RL= 7±1 km (BW). (1,12)
1994 February 3 09:05	0.51 W	355 41 - 91 WI	Mainshock associated with unknown fault located 18 km west of the west-dipping Star Valley normal fault. Z= 8 km (13,14, 15)

a - UTC - Universal Time Coordinated (Greenwich Mean Time).

b - Seismic moments based on: G - geology; B - body-wave analysis; L - Geodetic observations; S surface-wave analysis from Doser and Smith, 1989 and W - Waveform inversion.

c - Focal mechanisms based on: FM - first motions; BW - body-wave analysis; SF - surface-wave analysis; SF - surface faulting; GE - geodetic observations from Doser and Smith, 1989 and WI - Waveform Inversion.

d - Earthquake source parameters and dimensions: Z - focal depth from long-period waves (LP), short period waves (SP), and geodetic observations (GE); RL - rupture length from body waves (BW), surface faulting (SF), and geodetic observations (GE); BWD - body-wave displacement, SD - surface displacement, and GD - geodetic displacement for horizontal (h) and vertical (v) orientations. Numbers in parentheses corresponds to references listed below. For obtaining original references see Doser and Smith, 1989.

References: (1) Doser and Smith, 1989; (2) Doser, 1989a; (3) Shenon, 1936; (4) Doser, 1989b; (5) Dewey et al., 1973; (6) Doser, 1985b; (7) Westaway and Smith, 1989; (8) Cook and Nye, 1979; (9) Bache et al., 1980; (10) Pitt et al., 1979; (11) Crone et al., 1987; (12) Jackson et al., 1991a; (13) Jeroen Pitsema, personnal communications, 1994; (14) Nava et al., 1994, (15) U.S. Geological Survey, 1994.

TABLE 2.6-8. HISTORICAL EARTHQUAKES POSSIBLY LOCATED WITHIN THE ESRP[a]

Date	Origin Time (UTC)[b]	Intensity[c]	Magnitude	Location Error (km)[d]
11 November 1905	22:29[e]	MM VII	M_L 5.5[f]	± 100-200
20 February 1909	01:nd	MM II	nd	± 50-100
6 December 1925	16:16	Felt	nd	± 50-100
7 August 1927	nd	Felt	nd	± 50-100
5 September 1928	05:36	Felt	M_L 5.2[g]	≥ ± 100
6 June 1932	11:00	MM II	nd	± 50-100
21 December 1932	08:00	MM II	nd	± 50-100
28 April 1934	09:30	MM IV	nd	± 100-200
28 April 1934	10:00	MM III	nd	± 100-200
29 April 1934	06:10	MM III	nd	± 100-200
18 November 1937	23:50	nd	M_L 5.4[h]	nd
1 February 1954	03:33:19.[i]	nd	nd	± 50-100
20 January 1964	10:09:39.7[i]	nd	nd	± 22-56
28 February 1969	15:30:24.4[i]	nd	nd	± 22-56

a - Modified from Woodward-Clyde Consultants (1992a).
b - Origin time shown as hour:minute:second for Universal Time Coordinated (UTC), as reported in Stover et al. (1986).
c - MM = Modified Mercalli Intensity (Wood and Neumann, 1931). Felt = Earthquake felt but no intensity assigned.
d - Estimated from Stover et al. (1986).
e - According to Oaks (1992) Shoshone earthquake occurred at 22:29 and not 21:29 as reported by Stover et al. (1986).
f - Richter magnitude (M_L) calculated by Oaks (1992).
g - Magnitude obtained from Slemmons et al. (1965).
h - Information obtained from Engdahl and Rinehart (1988).
i - Instrumentally computed location.
nd - No data.

TABLE 2.6-9. MAXIMUM MAGNITUDES AND FOCAL DEPTHS OF EARTHQUAKES ASSOCIATED WITH DIKE INJECTION[a]

LOCATION	VOLCANIC EVENT[c] (Year)	MAXIMUM MAGNITUDE[d]	FOCAL DEPTH(S)[e] (km)	REFERENCES
Iceland				
Krafla	1975-76	5.0[f]	0 - 4	1.2
Krafla	1977	3.8[f]	0 - 6	3
Krafla	1978	4.1[f]	1 - 4	4
Hawaii, USA				
Kilauea Rift Zones				
East	1965	4.4 (M_L)	0 - 8	5
East	1968, Aug.	3.3	< 5	6
East	1968, Oct.	3.1	< 6	6
East	1969	4.7	< 7	7
Southwest	1975	3.0	nd	8
East	1976-77	4.0	< 10	8
East	1980, Aug.	3.0(M_c)[g]	0.5 - 3	9
East	1980, Nov.	3.1(M_c)[g]	0.7 - 4	9
Southwest	1981	3.4(M_c)[g]	1 - 2	9
East	1982	3.0(M_c)[g]	0.5 - 3	9
Japan				
Izu Pennisula[h]	1989	5.5(M_{JMA})	< 8	10.11.12
Africa				
Asal, Afar	1978	5.3(m_b)	0 - 6	13.14
New Zealand				
Taupo Volcanic Zone[i]	1964-65	4.6	4 - 8	15
Taupo Volcanic Zone[j]	1983	4.3	6 - 10	15
California, USA				
Mono Craters[k]	1325 + 20 AD	> 5.5(M_c)	nd	16
Italy				
Mt. Etna	1989	3.3(M_L)	< 4	17.18
Mt. Etna	1991	3.3(M_L)	< 6	19
Mean $\pm$1 sigma; n=19[l]	3.9 $\pm$ 0.8			

a - Modified from Hackett et al. (1995).
b - Worldwide dike-injection events associated with mafic magma except Mono craters which is associated with silicic magma and for Mt. Etna which is associated with intermediate magma. Composition of magma for New Zealand episodes are unknown.
c - An episode of dike-injection and associated seismicity having a known beginning and end.
d - Maximum magnitude reported for the dike-injection event. Magnitudes: M_L - Local or Richter; M_c - Coda; M_{JMA} - Japan Meteorological Agency; m_b - Body-wave; M_s - Surface-wave. No definition of magnitude scale was reported for values without magnitude designation.
e - Depth range of volcanic seismicity and maximum magnitude earthquake associated with the dike-injection event.
f - Einarsson (1991) reports earthquakes of magnitude $\geq$ 5.0 are usually associated with caldera deflation events and magnitude $\leq$ 4.0 with dike injection at Krafla.
g - Coda magnitudes greater than amplitude magnitudes for these events (Nakata et al., 1982; Tanigawa et al., 1981, 1983).
h - This earthquake is interpreted to have triggered magma movement, but was part of an earthquake swarm that began about 10 days prior to a dike-fed submarine eruption (10, 11, 12).
j - Associated with or triggered by dike intrusion, or possibly associated with tectonic subsidence of the basin (15).
k - Minimum estimate of the largest of five historic earthquakes based on liquefaction deposits produced by earthquakes equivocally associated with dike intrusion or tectonic faults (16).
l - Mean and one standard deviation computed based on magnitudes as presented without Mono Craters because its a minimum estimate.
nd - No data obtained.

References: (1) Einarsson & Bjornsson, 1979; (2) Bjornsson et al., 1977; (3) Brandsdottir and Einarsson, 1979; (4) Einarsson and Brandsdottir, 1980; (5) Bosher and Duennebier, 1985; (6) Jackson et al., 1975; (7) Swanson et al., 1976; (8) Dzurisin et al., 1980; (9) Karpin and Thurber, 1987; (10) Okada and Yamamato, 1991; (11) Takeo, 1992; (12) Oura et al., 1992; (13) Abdallah et al., 1979; (14) Lepine and Hirn, 1992; (15) Grindley and Hull, 1986; (16) Sieh and Bursik, 1986; (17) Bonaccorso and Davis, 1993; (18) Barberi et al., 1990; (19) Ferrucci and Patane, 1993.

TABLE 2.6-10. MAXIMUM MAGNITUDES BASED ON RUPTURE AREAS OF NORMAL FAULTS AND FISSURES IN ESRP VOLCANIC RIFT ZONES

Normal Faults or Fissures	Surface Length - SL (km)	Fault Widths: Depth to Dike Top[a] - DDT (km)	Fault Widths: Level of Neutral Buoyancy[b] - LNB (km)	Rupture Areas: SL x DDT (km^2)	Rupture Areas: SL x LNB (km^2)	Moment Magnitudes[c] **M**	Moment Magnitudes[c] **M**
Kings Bowl, Fissures[d]	11.5 E	0.6	4.0	6.9	46.0	4.9	5.7
	14.0 M			8.4	56.0	5.0	5.8
South of New Butte, Fissures[d]	19.0 E	1.0	4.0	19.0	76.0	5.3	5.9
	22.0 M			22.0	88.0	5.4	6.0
Southeast of New Butte, Fissures[d]	11.0	1.0	4.0	11.0	44.0	5.1	5.7
Railroad Monocline, Fault[e]	5.0	0.2	4.0	1.0	20.0	4.1	5.3
Jaylin Monocline Fault[e]	3.2	nc	4.0	nc	12.8	nc	6.4
Box Canyon, Fault[e]	3.0	0.2	4.0	6.0	12.0	4.8	5.6
East-West, Fault[e]	0.7	nc	4.0	nc	2.8	nc	5.6
Southeast Butte City, Fissure[e]	0.7	nc	4.0	nc	2.8	nc	5.6
Northwest of Tea Kettle Butte, Fissure[e]	2.3	nc	4.0	nc	9.2	nc	6.2
Northeast of Sixmile Butte, Fissure[e]	1.2	nc	4.0	nc	4.8	nc	5.9
Northeast of Tea Kettle Butte, Fissure[e]	0.3	nc	4.0	nc	1.2	nc	5.2
East of Tea Kettle Butte, Fissure[e]	0.5	nc	4.0	nc	2.0	nc	5.4
Northwest of Sixmile Butte, Fissure[e]	1.1	nc	4.0	nc	4.4	nc	5.8
Kath Fissure[e]	0.6	nc	4.0	nc	2.4	nc	5.5
NRF Fissure[e]	1.5	nc	4.0	nc	6.0	nc	6.0
Hells Half Acre, Fissures[e]	4.0 E	0.8	4.0	3.2	16.0	4.5	5.3
	15.0 M		4.0	12.0	60.0	5.1	5.8
Lapoint Monocline, Fissure[e]	1.4	nc	4.0	nc	5.6	nc	5.9

TABLE 2.6-10. Continued

Normal Faults or Fissures	Surface Length - SL (km)	Fault Widths: Depth to Dike Top[a] - DDT (km)	Fault Widths: Level of Neutral Buoyancy[b] - LNB (km)	Rupture Areas: SL x DDT (km^2)	Rupture Areas: SL x LNB (km^2)	Moment Magnitudes[c] **M**	Moment Magnitudes[c] **M**
East of Morgan Crater, Fault[f]	11.7	0.5	4.0	5.9	46.8	4.8	5.7
North of Morgan Crater, Fault[f]	9.2	1.3	4.0	12.0	36.8	5.1	5.6
West of High Point Butte, Fault[f]	10.0	1.0	4.0	10.0	40.0	5.1	5.6
Antelope Flat, Fault[f]	11.0	1.7	4.0	18.7	44.0	5.3	5.7
South of Antelope Flat, Fault[f]	3.7	0.3	4.0	1.1	14.8	4.1	5.2
Mean ±1 sigma; n= 11; n=22						4.9 ± 0.4	5.7 ± 0.3

E - Exposed surface length; corresponding magnitude not used to estimate the mean value.
M - Maximum surface length estimated from extrapolation of fissures beneath younger lava flows.
nc - Not calculated because only one fissure or fault exposed, and therefore the depth to the dike top could not be estimated.
a - Maximum depth calculated using: d=1/2W; where d=depth to dike top; W=width of graben (Pollard et al., 1983; Mastin and Pollard, 1988).
b - Depth extent based on Ryan (1987) and Rubin (1992).
c - Magnitudes calculated using **M**=4.07+0.98*Log(RA); where **M**=moment magnitude; RA=rupture area. Magnitudes are extrapolated if less the constant in the equation (Wells and Coppersmith, 1994).
d - Surface lengths obtained from Kuntz et al. (1988).
e - Surface lengths obtained from Golder Associates (1992a).
f - Surface lengths obtained from aerial photographs and topographic maps.

TABLE 2.6-11 DETERMINISTIC SEISMIC HAZARD STUDIES APPLICABLE TO THE ISFSI SITE

Seismic Hazard Study	Methodology	Input Parameters	Peak Horizontal Acceleration (g) Bedrock	Soil
Woodward-Lungren and Associates, 1971 [2.175] & Allied Chemical Corporation, 1975 [2.177]	Based on empirical attenuation relationship — maximum acceleration of rock as functions of magnitude and distance (Seed et al., 1969). Soil based on amplification factor of 1.4 derived from lumped-mass method incorporating representative dynamic soil properties.	M_L 7.75 earthquake at the southern end of the Lost River fault at a distance of 24 km to the ICPP. Representative soil profile 50 ft of gravel and sand. This evaluation was for the NWCF site at the ICPP located 320 m from the ISFSI site.	0.33	0.46
Agbabian Associates, 1977 [2.178]	Reviewed the deterministic study conducted by Allied Chemical Corporation [2.177] with respect to NRC regulations. Suggested an alternative deterministic evaluation that considered use of: 1) fault surface length versus earthquake magnitude; and 2) an empirical attenuation relationship developed from earthquakes worldwide (Woodward-Clyde Consultants, 1975 [2.176]). No soil values calculated.	M_L 6.75 earthquake at the southern end of the Lost River fault at a distance of 24 km to the ICPP. This evaluation was for the NWCF site at the ICPP located 320 m from the ISFSI site.	0.30	
Woodward-Clyde Consultants, 1990 [2.51]	Site-specific evaluation using the a stochastic numerical modeling technique known as the band-limited-white-noise ground motion model combined with random vibration theory. The ground motions are modeled as a point source described by M_w, stress drop $\Delta\sigma$, and source region V_s, and ρ_s; crustal attenuation described by Q_o and η; and the local site response based on V_s, intrinsic damping Q_s, and ρ_s. Ground motions were modeled to the ground surface for both rock and soil. Results are in the form of horizontal peak acclerations and response spectra for the 16th, 50th, and 84th percentiles. An evaluation of the vertical to horizontal ratio resulted in an average value of 0.72.	M_w 6.9 on the Lemhi fault at a distance of 21 km, the closest point of the rupture plane to ICPP. $\Delta\sigma$= 50 bars; V_s= 3.55 km/sec; ρ_s = 2.7 gm/cm3; Q_o = 450; and η = 0.2. Local site response based on V_s and V_p measurements in boreholes and empirical earthquake recordings. Sites selected for evaluation at the ICPP were called FPR for rock and SIS for soil, located approximately 500 m from each other and 200 m and 600 m from the ISFSI site, respectively.	0.20 (84th)	0.30 (84th)

TABLE 2.6-11 Continued. DETERMINISTIC SEISMIC HAZARD STUDIES APPLICABLE TO THE ISFSI SITE

Seismic Hazard Study	Methodology	Input Parameters	Peak Horizontal Acceleration (g)	
			Bedrock	Soil
Woodward-Clyde Federal Services, 1996b [2.179]	Incorporated results of detailed paleoseismic investigations at the southern end of the Lemhi fault [2.94]. Combined four empirical attenuation relationships [2.53] with an attenuation relationship based on the same stochastic modeling approach as in Woodward-Clyde Consultants [2.51] to calculate a weighted mean peak horizontal acceleration for a maximum credible earthquake. Soil value was estimated by using an amplification factor of 2 [2.53]. Results are in the form of peak horizontal accelerations at the 50th and 84th percentiles.	M_w 7.1 on the Lemhi fault at a distance of 22 km, the closest point of the rupture plane to ISFSI site. $\Delta\sigma$ = 75 bars; V_s= 3.55 km/sec; ρ_s = 2.7 gm/cm3; Q_o = 150; and η = 0.6. Local site response based on V_s and V_p measurements in boreholes drilled at the ISFSI site.	0.28 (84th)	0.56 (84th)

TABLE 2.6-12 PROBABILISTIC SEISMIC HAZARD STUDIES APPLICABLE TO THE ISFSI SITE

Seismic Hazard Study	Methodology	Input Parameters	Peak Horizontal Acceleration (g) Bedrock	Soil
Agbabian Associates, 1977 [2.178]	Calculated the probability of experiencing the design earthquake during the service life of the facility. Calculation procedure uses the mathematical model by Der-Kiureghian and Ang (1977). Evaluation performed for the NWCF site at the ICPP located 320 m from the ISFSI site.	Three source areas located around the ESRP having maximum magnitudes (6.75-7.5) corresponding to Modified Mercalli Intensities (MMI) IX-X, recurrence intervals based on the historical earthquake record, and intensity attenuation relationships developed from five regional earthquakes.	0.4 /MMI VIII-IX (0.01% chance of exceedance in 100 years)	None
Tera Corporation, 1984	Calculated probabilities of peak horizontal accelerations with return periods of 100, 1,000, and 10,000 yrs. Procedure uses the Tera (1978) model based on the work of Mortgat et al. (1977) and Mortgat and Shah (1979). Analysis done for Argonne National Laboratory site, but hazard maps include the ICPP.	Nine source regions, three are the major range-bounding faults northwest of the ESRP. Magnitudes range 6.5-7.75 and recurrence based on 17 years of earthquake data. Attenuation based on Campbell (1982) and Tera (1984) with Q_o=450, η=0.2 outside the ESRP; Q_o=150, η=0.55 inside the ESRP.	0.18 (1,000 yrs) 0.30 (10,000 yrs)	None
Woodward-Clyde Federal Services, 1996a [2.53]	Calculated annual exceedance probabilities (500, 1,000, 2,000, and 10,000) for peak horizontal accelerations. Procedure is based on Cornell (1968) and Youngs and Coppersmith (1990). Results are in the form of mean peak horizontal accelerations and uniform hazard spectra for rock. Evaluation performed for the ICPP.	Source zones: basin and range faults, M6.5-7.75; volcanic rift zones, M4.5-5.5; ESRP background seismicity, M5-6; northern basin and range background seismicity, M6.25-6.75. Recurrence based on earthquake catalog 1884-1992. Attenuation includes four empirical relationships and stochastic numerical modeling ($\Delta\sigma$ = 75 bars; V_s= 3.55 km/sec; ρ_s = 2.7 gm/cm3; Q_o = 150; and η = 0.6. Site response V_s and	0.10 (1,000 yrs) 0.13 (2,000 yrs) 0.22 (10,000 yrs)	None

		V_p measured in boreholes drilled at ICPP and INEEL).		

TABLE 2.6-12 Continued. PROBABILISTIC SEISMIC HAZARD STUDIES APPLICABLE TO THE ISFSI SITE

Seismic Hazard Study	Methodology	Input Parameters	Peak Horizontal Acceleration (g) Bedrock	Peak Horizontal Acceleration (g) Soil
Woodward-Clyde Federal Services, 1996b [2.179]	Developed seismic design parameters for the ISFSI site. Procedures include: deaggregation of mean uniform hazard spectra and adjustment of the normalized spectral shapes to produce bedrock response spectra; soil response analysis using a frequency-domain equivalent-linear formulation (Silva et al. [2.180]); and development of acceleration time histories by combining a Fourier amplitude spectrum with a phase spectrum from an observed strong ground motion record based on (Silva and Lee, 1987). Results in the form of peak horizontal and vertical accelerations for rock, preliminary peak horizontal and vertical accelerations for soil, smoothed response spectra, and time histories.	Mean uniform hazard spectra for bedrock at the ICPP developed by Woodward-Clyde Federal Services, 1996a [2.53]. Soil analysis includes: depths 7.5 - 18 m; shear wave velocites 234 - 604 m/s obtained from boreholes drilled at the ISFSI site. Acceleration time histories developed from strong ground motion rock records of the 1989 M_w 7.0 Loma Prieta, California and the 1980 M_w 6.9 Irpinia earthquakes.	0.10 (1,000 yrs) 0.13 (2,000 yrs) 0.22 (10,000 yrs)	0.23[a] (1,000 yrs) 0.30[a] (2,000 yrs) 0.47[a] (10,000 yrs)

a - This value is preliminary and may possibly change based on incorporation of recently acquired data from boreholes drilled at the ISFSI site.

Table 2.6-13 Properties of Soils (Sediments) and Bedrock at ICPP

Unit and depth of occurrence	Classification (USCS)	Dry Density (lbs/ft^3)	Moisture Content (%)	Relative Density (%)	Porosity (%)	Strength Characteristics	Vp ft/s, (m/s)	Vs ft/s (m/s)	Damping
Upper Alluvial Soils (0-20 ft)	Sandy Gravel (GW)	110-123	1-8	36-98	29	C=0 F=43	2000 (610)	1000 (300)	0.5%@10^{-4}% strain 15%@10^{-1}% strain
		131.5 - 133	6		29	C=0 F=38-43	2000 (610)- 2300 (700)	1000 (300)- 1150 (350)	
		117-142	2-20	13-100		C=0 F=38°	3300 (1000)	1400(425)	1%@10^{-4}%Strain
		98-135					1600 (490)- 1700 (520)	500 (150) 900 (275)	
							3665 (1120)- 5600 (1700)	650 (200) 1700 (520)	
Lower Alluvial Soils (20-40 ft)	Sandy Gravel (GW) and Poorly Graded Sand (SP)	112-123	1-8	49-98	29	C=0 F=43(gravel) F=35(sand)	2300(700)	1150 (350)	10^{-4}%@0.5%strain 10^{-1}%@15% strain
		131.5 - 133	6		29	C=0 F=38-43	2000 (610)- 2300 (700)	1000 (300)- 1150 (350)	
		117-142				C=0, F=38° (compacted gravel)	3300 (1000)	1400 (425)	1%@10^{-4}% strain
							2500 (760)- 3000 (910)	1400(425)- 1600 (490)	
Clay Soils (0 -14 ft) (variable just above bedrock)	Sandy clay Silty clay (CL) Sandy silt to clayey sand (ML-SC)	92-110	17-23		39	C=650-5000 psf F=0-25°	2600 (790)	1150 (350)	Similar to lower aluvial soils
		109	17		39	C=0-1500 psf F=25-38°	2600 (790)	1150 (350)	
Basalt Bedrock (>40 ft)	Vesicular olivine basalt	136-163				6-17x10^5 psf Uniax.Comp.Strength	6800 (2070)	3500 (1070)	
		140-165				1.3-1.7x10^{6}psf Uniax.Comp.Strength	6800 (2070)	3500 (1070)	
							9000 (2740)- 10000 (3050)	4000 (1200)- 5500 (1670)	
							7500 (2300)	4000 (1200)	
						5-16 x 10^5 psf	9200 (2800)	3900 (1200)	1%

Table 2.6-13(cont) **Properties of Soils (Sediments) and Bedrock at ICPP (continued)**

Unit and depth of occurrence	Shear Modulus (G)	Poisson's Ratio (n)	Static Modulus of Elasticity (E)	Bulk Modulus (K)	Consolidation Characteristics	Location (Facility)	Reference
Upper Alluvial Soils (0-20 ft)	2.2 x 10^6 psf 5.5 x 10^5psf	0.32	1.8x10^6psf@5000 psf load 2.5x10^6psf@10000 psf load	1.7x10^6psf@5000psf 2.3x10^6psf@10000psf	Elastic - dependent on E	New Waste Calcining Facl.	Dames and Moore (1976)
	6.8x10^5psf@5000psf 9.5x10^5psf@10000psf	0.32	1.8x10^6psf@5000 psf load 2.5x10^6 psf@10000 psf load		C_v=0.012 C_c=0.015	7th Bin Set & FPR	EG&G (1984a, b)
	8.2 x 10^6 psf	0.39	2.2x10^7 psf		slightly compressible	SIS	Northern Engineering and Testing (1987)
	1.1x10^6 to 3.1x10^6psf dynamic max. (G_{max})	0.27 - 0.30 (dyamic)	2.9x10^6 to 8.1x10^6 psf (dynamic)			HLWTF replacement	Golder Associates (1992b)
		0.41 - 0.45				FFTF	Dames and Moore (1977)
Lower Alluvial Soils (20-40 ft)	?? ??	0.32	1.8x10^6psf@5000 psf load 2.5x10^6 psf@10000 psf load	1.7x10^6psf@5000psf 2.3x10^6psf@10000psf	Elastic - dependent on E	New Waste Calcining Facl.	Dames and Moore (1976)
	6.8x10^5psf@5000psf 9.5x10^5psf@10000psf	0.32	1.8x10^6psf@5000 psf load 2.5x10^6 psf@10000 psf load		C_v=0.012 C_c=0.015	7th Bin Set & FPR	EG&G (1984a, b)
	8.2 x 10^6 psf	0.39	1x10^6 to 3x10^6 psf		slightly compressible	SIS	Northern Engineering and Testing (1987)
	7.6x$10^6$to 9.9x10^6 psf dynamic max. (G_{max})	0.27 - 0.30 (dyamic)	1.9x10^7 to 2.57x10^7psf (dynamic)			HLWTF replacement	Golder Associates (1992b)
		0.41 - 0.45				FFTF	Dames and Moore (1977)
Clay Soils (0 -14 ft) (variable just above bedrock)	Similar to lower alluvial soils	0.38			C_v=0.037@ 0-5000psf load C_v=0.065 @ 5000-10000psf	New Waste Calcining Facl.	Dames and Moore (1976)
	4.3x10^5 psf @8000 psf		1.2x10^6psf @ 8000psf	1.6x10^6 psf @ 8000 psf	C_v=0.001 C_c=0.016	7th Bin Set & FPR	EG&G (1984a, b)
Basalt Bedrock (>40 ft)		0.18-0.25 (calc)	1.3-3.1 x 10^8 psf 1.9-4.5x10^8 psf	1.6-3.7x10^8psf	Relatively incompressible	New Waste Calcining Facl.	Dames and Moore (1976)
	0.99-2.2x10^8 psf 0.73-1.7x10^8psf	0.115-0.136	2.1-5.9 x 10^8 psf	1.6-3.7x10^8psf	Relatively incompressible	7th Bin Set & FPR	EG&G (1984a, b)
	7.4x10^7 to 1.41x10^8 psf	0.28-0.38 (dynamic)	2.1-3.6 x 10^8 psf (dynamic)			HLWTF replacement	Golder Associates (1992b)
		0.25-0.30				FFTF	Dames and Moore (1977)
	7.1x10^7 psf	0.39	2.0x10^8psf		Incompressible	SIS	Northern Engineering and Testing (1987)

Table 2.6-14. Standard Penetration Test Results for Boreholes in Surficial Sediments at the TMI-2 ISFSI Site

Standard Penetration Test Results for TMI-2 ISFSI Site Boreholes at INTEC
November, 1997

Hole Number	Blows/ft at 5.5-6.5 ft	Blows/ft at 20.5-21.5 ft
1	106	69
1A	32	167
2	32	69
4A	178	90
5	31	79
7	28	108
11	30	121
12	62	98
13	59	188
14	62	224
16	18	166
19	62	113
22	53	135

Table 2.6-15. Seismic Velocities of Surficial Sediments and Basalts at the TMI-2 ISFSI Site. Data from Downhole Logging of Agbabian Associates, 1997

Depth	BH-1		BH-3		BH-5		BH-11		BH-14		BH-19		BH-22	
(m)	Vs	Vp	Vs	Vp	Vs	Vp	Vs	Vp	Vs	Vp	Vs	Vp	Vs	Vp
1	375	549	322	545	234	410							367	595
2	375	549	322	545	234	410			353	514	296	565	367	595
3	375	549	322	545	234	410			353	514	296	565	367	595
4	469	827	322	545	234	410	498	1328	497	1009	296	565	367	595
5	469	827	322	545	604	1018	498	1328	497	1009	296	565	367	595
6	469	827	586	864	604	1018	498	1328	497	1009	430	844	421	1127
7	469	827	586	864	604	1018	498	1328	497	1009	430	844	421	1127
8	469	827	586	864	604	1018	498	1328	497	1009	430	844	421	1127
9	469	827	586	864	1005	2444	498	1328	497	1009	430	844	421	1127
10	469	827	586	864	1005	2444	498	1328	857	2497	430	844	421	1127
11	469	827	586	864	1005	2444	882	2719	857	2497	430	844	679	2443
12	387	669	1215	2700	1005	2444	882	2719	857	2497	430	844	679	2443
13	387	669	1215	2700	1005	2444	882	2719	857	2497	430	844	679	2443
14	387	669	1215	2700	1005	2444	882	2719			430	844	679	2443
15	387	669	1215	2700							430	844	679	2443
16	387	669	1215	2700							430	844		
17	387	669									733	2291		
18	939	1857									733	2291		
19	939	1857									733	2291		
20	939	1857									733	2291		
21	939	1857									733	2291		
22	939	1857												
23	939	1857												

Table 2.6-16. Characteristics of volcanism in the INEL area.

	CALDERA FORMATION	RIFT-ZONE VOLCANISM	AXIAL-ZONE VOLCANISM	AREAS BETWEEN VOLCANIC ZONES
MAGMA TYPES	rhyolite (viscous and gas-rich)	basalt (fluid and gas-poor)	basalt and subordinate rhyolite	basalt (and minor rhyolite?)
VOLCANIC STYLE AND PRODUCTS	highly explosive; voluminous pumice and fine ash blankets entire regions	mild & effusive; erupt mainly lava flows from fissures, low shield volcanoes and small tephra cones	as per rift zones, but also local rhyolite domes & intrusions (Big Southern, Middle, East Buttes) with local explosive phenomena	as per volcanic rift zones and axial volcanic zone
STRATIGRAPHY	calderas filled with up to several km of welded, silicic ash-flow tuffs, lava flows and volcaniclastic sediment [Heise Volcanics]	piles of 1- to 30-m-thick basalt lava flows & minor interbedded sediment; total lava thickness up to1 km in INEL area [Snake River Group]	basaltic lava flows and dispersed small tephra cones; isolated rhyolite domes and intrusions [Snake River Group]	fine clastic sediment of fluvial, lacustrine and eolian origin; fewer lava flows than near VRZs [Snake River Group]
TECTONICS AND PHYSICAL CONFIGURATION	collapse: broad, oval depressions, 10s to 100 km wide and 1-2 km deep, ringed by inward-dipping fractures	extensional: NW-trending belts of open fissures, monoclines, small normal faults and basaltic vents	extensional, but magma-induced fissures or faults are rare; a diffuse, NE-trending, volcanic highland along the ESRP axis	subsidence(?): broad, low topographic basins between extensional and constructional volcanic highlands; seldom disturbed by magma intrusion
GEOLOGIC AGE IN INEL AREA	6.5 Ma to 4.3 million yrs in INEL area, now covered by younger basaltic lava. [2.1 to 0.6 million yrs on Yellowstone Plateau]	Surficial INEL basalts: 1.2 to 0.05 million yrs; most are 0.7 to 0.1 million yrs. Inception of major basaltic volcanism was ca. 4 million yrs ago.	Basalt: >1 million yrs (Middle Butte), to 5,400 yrs (Hells Half Acre). Rhyolite: >1 million yrs (near East Butte) to 300,000 yrs (Big Southern Butte)	as per VRZs
QUATERNARY ERUPTION FREQUENCY	zero in INEL area; Quaternary calderas closest to INEL occur on Yellowstone Plateau	low; one eruption per 10,000 to 100,000 yrs (see Table 3)	low: one basaltic eruption per 8,000 yrs (see Table 3); one rhyolitic intrusion or dome every 200,000 yrs or more	very low; by definition less frequent than within rift zones (one eruption per 100,000 yrs or more)

Table 2.6-17. Hazards associated with basaltic volcanism on the Eastern Snake River Plain. Entries are listed from highest to lowest relative hazard.

PHENOMENON	RELATIVE FREQUENCY	SIZE OR AREA OF INFLUENCE	COMMENTS
lava flow	common	0.1 km^2 to 400 km^2 in area, up to 25 km length based on sizes of ESRP lava flows of the past 400,000 years	significant hazard; typical basaltic phenomenon; lava from fissures or shield volcanoes may inundate large areas downslope of vents
ground deformation: fissuring, faulting and uplift	common; associated with virtually all shallow magma intrusion and eruption	fissuring could affect areas to 2 x 10 km; minor tilting & broad uplift in areas to 5 x 20 km	significant hazard; due to shallow dike intrusion; "dry" intrusion may occur without lava flows; affects smaller areas than for lava inundation
volcanic earthquakes	common; associated with magma intrusion before and during eruption	maximum M = 5.5 and most events M < 4; ground vibration may affect facilities within 25 km	low to moderate hazard; swarms of shallow earthquakes (<4 km focal depth) occur as dikes propagate underground
gas release (toxic and corrosive vapors)	common; associated with fissuring and lava eruption	restricted to near-vent areas; may affect several-square-km area downwind	low hazard; local plume of corrosive vapor, downwind from eruptive vent or fissure; cooled vapors may collect in local topographic depressions
tephra fall (volcanic ash and bombs)	uncommon	as per gas release	low hazard; basaltic eruptions are inherently nonexplosive and may form small tephra cones but little fine ash to be carried downwind
base surge (ground-hugging blast of steam and tephra)	rare	effects limited to radius of several km from vent; < 10 km^2 area	low hazard; steam explosions due to interaction between ascending magma and shallow groundwater; water table too deep under most of INEL
tephra flow (ground-hugging flow of hot, pyroclastic material)	extremely rare	near vent; may affect area < 1 km^2	very low hazard; as per tephra fall but affecting even smaller areas

Table 2.6-18. Estimated volcanic-recurrence intervals and corresponding annual eruption probabilities (in parentheses) for volcanic zones and boreholes of the INEL area.

VOLCANIC ZONE OR BOREHOLE	DATA SOURCES	TIME INTERVAL OF VOLCANISM [yrs before present]	NUMBER OF VENTS, FISSURES OR FLOW GROUPS	COMMENTS	ESTIMATED RECURRENCE INTERVAL
Great Rift (25 km southwest of INEL)	Kuntz et al., 1986, 1988	2,100 - 15,000 yrs (radiocarbon dating)	> 100 vents 8 Holocene eruptive periods (each lasting a few decades or centuries, and each including multiple flows and cones).	no impact on INEL; most recently and frequently active of all ESRP rift zones; thus provides minimum-recurrence for entire ESRP; most probable area of future ESRP volcanism	2,000 yrs (5×10^{-4} / yr)
Axial Volcanic Zone (southern INEL)	Kuntz et al., 1986, 1994	5,000 - 730,000 yrs (K-Ar dating; radiocarbon; paleomagnetic data)	73 vents & fissure sets; 4 Holocene lava fields, 3 of them shared by volcanic rift zones. 45 cogenetic vent/fiss gps	could affect much of southern INEL; most recently and frequently active of all volcanic zones that could impact INEL	16,000 yrs (6.2×10^{-5} / yr)
Arco Volcanic Rift Zone (southwestern INEL)	Kuntz, 1978; Smith et al., 1989; Kuntz et al., 1994	10,000 - 600,000 yrs (radiocarbon, K-Ar and TL dating; paleomagnetic data)	83 vents & fissure sets; 2 Holocene lava fields. 35 cogenetic vent/fiss gps	volcanism could affect southwestern INEL	17,000 yrs (5.9×10^{-5} / yr)
Lava Ridge-Hells Half Acre Volcanic Rift Zone (includes Circ Butte/Kettle Butte volc rift zone) (north & eastern INEL)	Kuntz et al., 1986, 1994	5,000 - 1,200,000 yrs (K-Ar dating; radiocarbon; paleomagnetic data)	48 vents & fissure sets; 1 Holocene lava field: Hells Half Acre. 30 cogenetic vent/fiss gps	could affect northern & eastern INEL; extremely long eruptive history; includes oldest and youngest basalts in the INEL area	40,000 yrs (2.5×10^{-5} / yr)
Howe-East Butte Volcanic Rift Zone (central INEL)	Kuntz, 1978, 1992; Golder Associates, 1992a	230,000 - 730,000 yrs (K-Ar dating; paleomagnetic data)	7 vents & fissure sets; no Holocene features. 5 cogenetic vent/fissure groups	old, poorly exposed and sediment-covered; identified in part by subsurface geophysical anomalies	100,000 yrs (1.0×10^{-5} / yr)
Borehole NPR SITE E (south-central INEL)	Champion et al., 1988	230,000 - 640,000 yrs (K-Ar dating; paleomagnetic data)	9 lava-flow groups (each group contains multiple flows, erupted over a short time)	dates from 600-foot interval of subsurface lavas give recur-rence estimate consistent with surficial geology of the area	45,000 yrs (2.2×10^{-5} / yr)
Borehole RWMC 77-1 (southwestern INEL)	Kuntz, 1978; Anderson & Lewis, 1989	100,000 - 565,000 yrs (K-Ar and TL dating; paleomagnetic data)	11 lava-flow groups (each group contains multiple flows, erupted over a short time)	dates from 600-foot interval of subsurface lavas give longer recurrence interval than nearby Arco & Axial zones, reflecting flow-group (sub-surface) vs. vent-counting (surface geology) approaches	45,000 yrs (2.2×10^{-5} / yr)

Table 2.6-19. Areas and Area Statistics for Lava Flows in the INEEL Area. Areas Measured from References [2.166] and [1.55].

	Area (km^2)	Lava flow name or location
Qba	5	North Robbers flow
	3	South Robbers flow
	175	Cerro Grande flow
	400	Hells-Half Acre flow
	325	Wapi Flow
	3.3	Kings Bowl flow
Qbb	50	Arco lava field
	100	Taber lava field
	150	Quaking Aspen Butte
	181	N. of Big Southern Butte
	77	Fingers Butte
	57	Near N. and S. Robbers
	55	SW of Big Southern Butte
Qbc	100	Table Legs Butte
	125	St. Marys Nipple
	41	Little Butte
	70	Little Butte South
	260	Kettle Butte
	65	Section 5, T3N, R34E
	311	ANL-W
	142	Mid Butte
	130	Section 35, T4N, R33E
	80	Near 2-2A
	130	Section 33, T4N, R33E
	111	Section 20, T4N, R33E
	67	EastButte Crater
	77	Section 14, T3N, R33E
	96	NW of Wildhorse Butte
	78	Just north of Twin Buttes
	1	Coyote Butte
Qbd	275	Crater Peak
	65	Sixmile Butte
	31	Lavatoo
	1	Small butte near Teakettle
	0.5	Small butte near Teakettle
	1	Small butte near Teakettle
	44	Butterfly Butte
	52	Butterfly Butte South
	93	Section 36, T5N, R34E
	34	Table Butte
	31	Cedar Butte (N. of Mud Lake)
	31	section 6, T4N, R.34E
	26	Crater Peak, SE

Descriptive Statistics	
Mean	96.51
Standard Error	14.37
Median	70
Mode	1
Standard Deviation	94.21
Sample Variance	8876
Kurtosis	2.298
Skewness	1.587
Range	399.5
Minimum	0.5
Maximum	400
Sum	4150
Count	43
95%Confidence Lev.	28.99

area	*Percentile*
400	100.00%
325	97.60%
311	95.20%
275	92.80%
260	90.40%
181	88.00%
175	85.70%
150	83.30%
142	80.90%
130	76.10%
130	76.10%
125	73.80%
111	71.40%
100	66.60%
100	66.60%
96	64.20%
93	61.90%
80	59.50%
78	57.10%
77	52.30%
77	52.30%
70	50.00%
67	47.60%
65	42.80%
65	42.80%
57	40.40%
55	38.00%
52	35.70%
50	33.30%
44	30.90%
41	28.50%
34	26.10%
31	19.00%
31	19.00%
31	19.00%
26	16.60%
5	14.20%
3.3	11.90%
3	9.50%
1	2.30%
1	2.30%
1	2.30%
0.5	.00%

Table 2.6-20. Lengths and Length Statistics for Lava Flows in the INEEL area. Lengths Measured from References [2.166] and [2.55]

	Length	Lava flow name or location
QBa	5.4	North Robbers flow
	3.5	South Robbers flow
	21	Cerro Grande flow south
	15	Cerro Grande flow north
	31	Hells-Half Acre flow
	21	Wapi Flow
	3	Kings Bowl flow
QBb	8	Arco lava field
	9	Taber lava field
	27	Quaking Aspen Butte
	17	North of Big Southern Butte
	12	Fingers Butte
	13	Near N. and S. Robbers
	18	SW of Big Southern Butte
QBc	18	Table Legs Butte
	18	St. Marys Nipple
	10	Little Butte
	27	Little Butte South
	28	Kettle Butte
	10	Section 5, T3N, R34E
	25	ANL-W (north)
	15	ANL-W (south)
	16	Mid Butte
	18	Section 35, T4N, R33E
	8	Near 2-2A
	7	Section 33, T4N, R33E
	8	Section 20, T4N, R33E
	10	Near Unnamed Rhyolite Dome
	15	EastButte Crater
	10	Section 14, T3N, R33E
	11	NW of Wildhorse Butte
	10	Just north of Twin Buttes
	0.5	Coyote Butte
QBd	27	Crater Peak
	10	Sixmile Butte
	5	Lavatoo
	0.5	Small butte near Teakettle
	0.1	Small butte near Teakettle
	0.5	Small butte near Teakettle
	7	Butterfly Butte
	6	Butterfly Butte South
	13	Section 36, T5N, R34E
	6	Table Butte
	7.5	Cedar Butte (N. of Mud Lake)
	10	section 6, T4N, R.34E
	12	Crater Peak, SE

Descriptive Statistics	
Mean	12.457
Standard Error	1.1713
Median	10
Mode	10
Standard Deviation	7.944
Sample Variance	63.107
Kurtosis	-0.26
Skewness	0.5889
Range	30.9
Minimum	0.1
Maximum	31
Sum	573
Count	46
95%Confidence Lev.	2.3591

length	*Percentile*
31	100.00%
28	97.70%
27	91.10%
27	91.10%
27	91.10%
25	88.80%
21	84.40%
21	84.40%
18	75.50%
18	75.50%
18	75.50%
18	75.50%
17	73.30%
16	71.10%
15	64.40%
15	64.40%
15	64.40%
13	60.00%
13	60.00%
12	55.50%
12	55.50%
11	53.30%
10	37.70%
10	37.70%
10	37.70%
10	37.70%
10	37.70%
10	37.70%
10	37.70%
9	35.50%
8	28.80%
8	28.80%
8	28.80%
7.5	26.60%
7	22.20%
7	22.20%
6	17.70%
6	17.70%
5.4	15.50%
5	13.30%
3.5	11.10%
3	8.80%
0.5	2.20%
0.5	2.20%
0.5	2.20%
0.1	.00%

WASHINGTON
MONTANA
OREGON
Boise
INEL
Idaho
Falls
Twin Falls
Blackfoot
WYOMING
26
Pocatello
Ogden
Reno
NEVADA
Ely
Salt Lake City
NTS
(Nevada Test Site)
UTAH
Las
Vegas
CALIFORNIA
ARIZONA
Miles
0 50 100 150
ICPP-A-4764X
(9-93)
Location Map of the INEL

Figure 2.1-1.

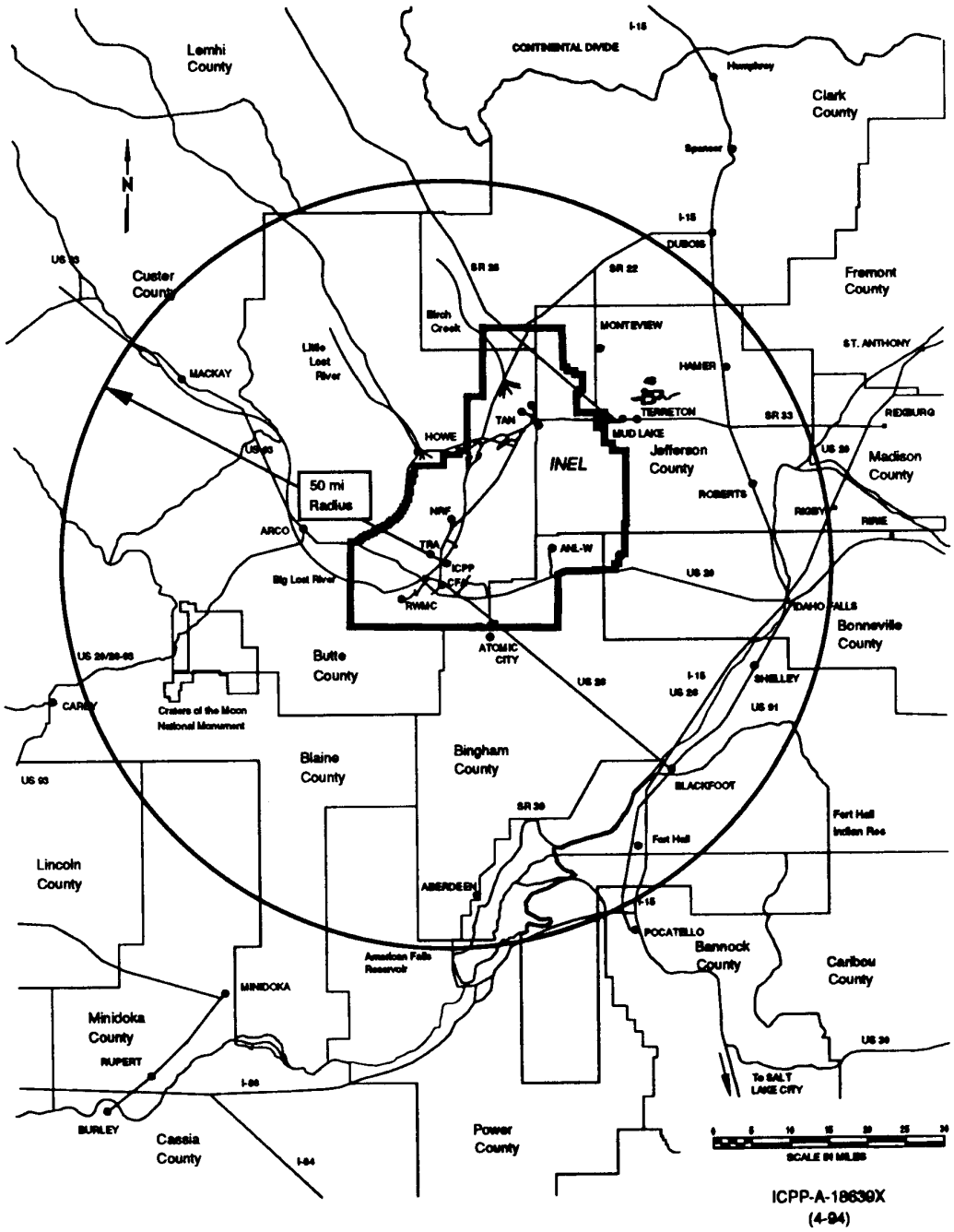

Figure 2.1-2. INEL Vicinity Map (with 50-mile radius line).

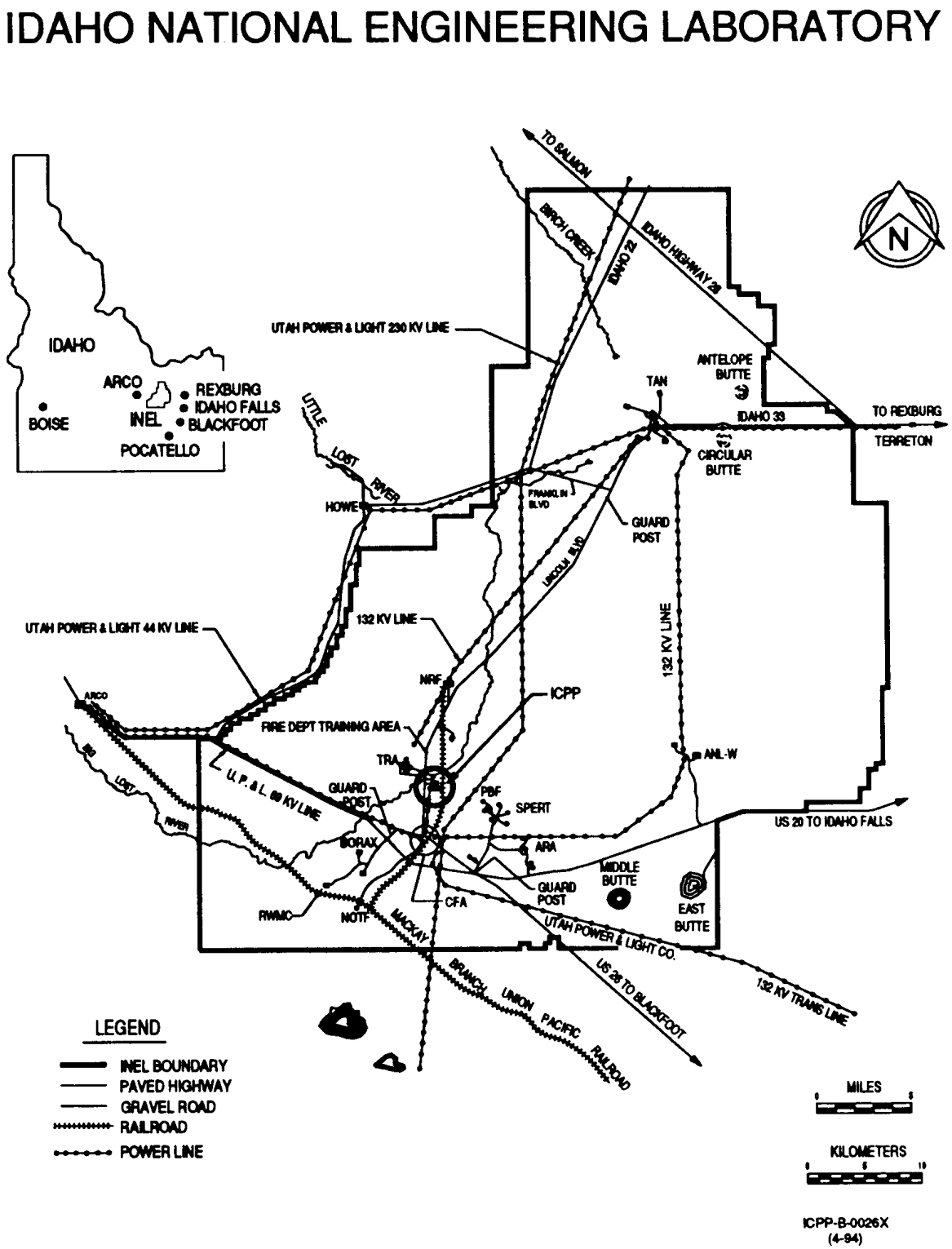

Figure 2.1-3. Map of INEL.

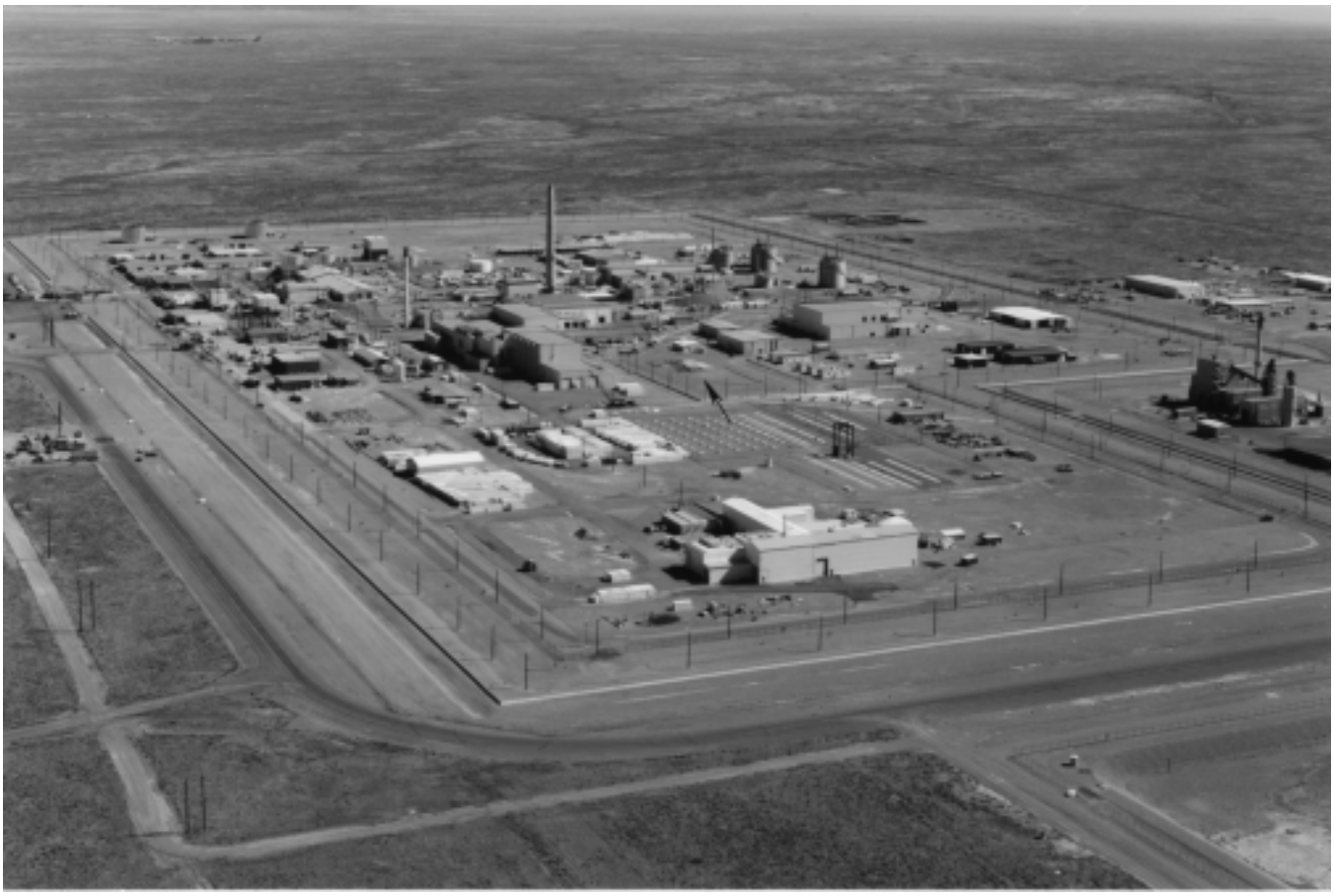

Figure 2.1-4. Aerial View of ICPP Showing ISFSI site. (Looking Northeast)

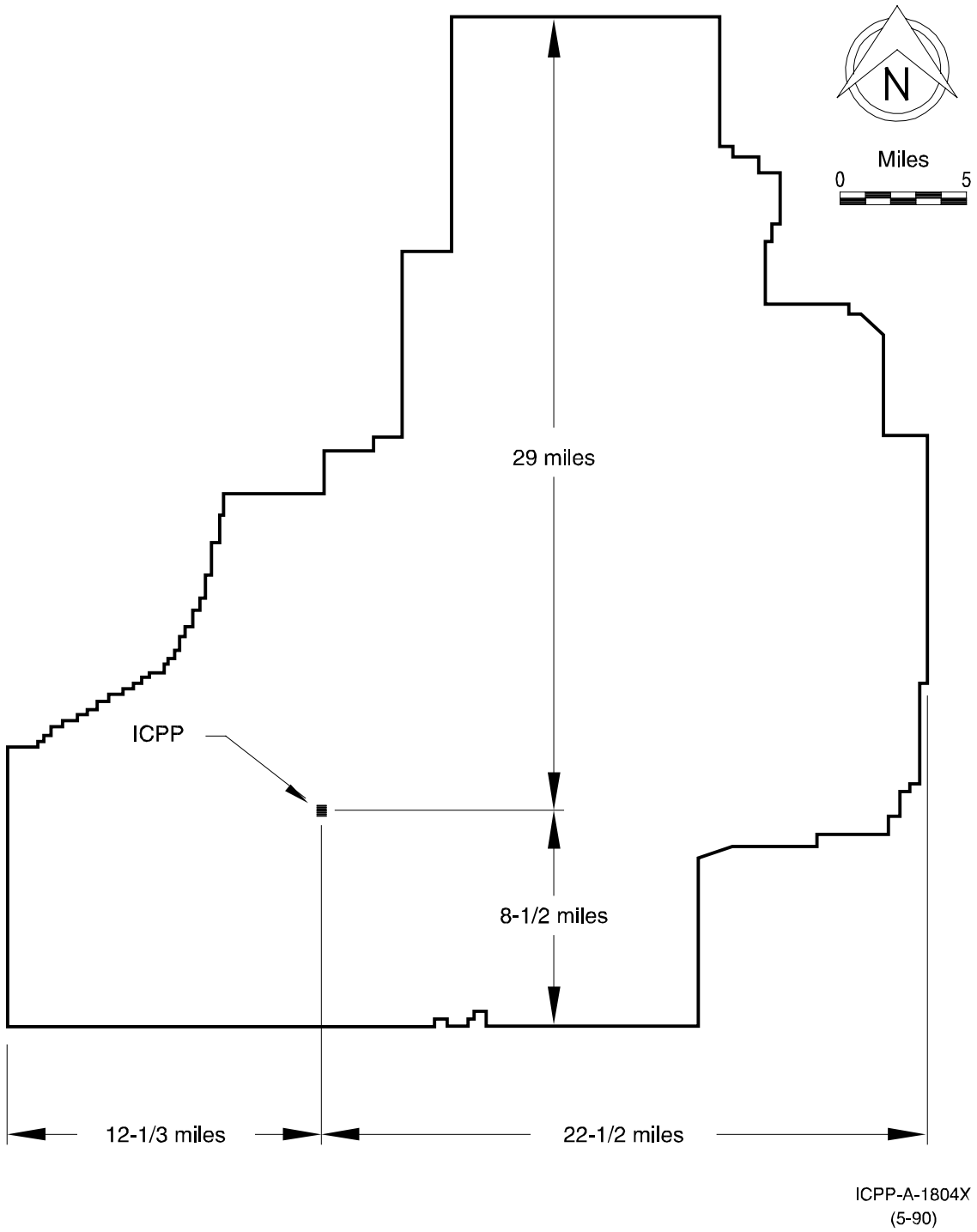

Figure 2.1-5. Distances from the TMI-2 ISFSI to the INEL Boundary (Controlled Area).

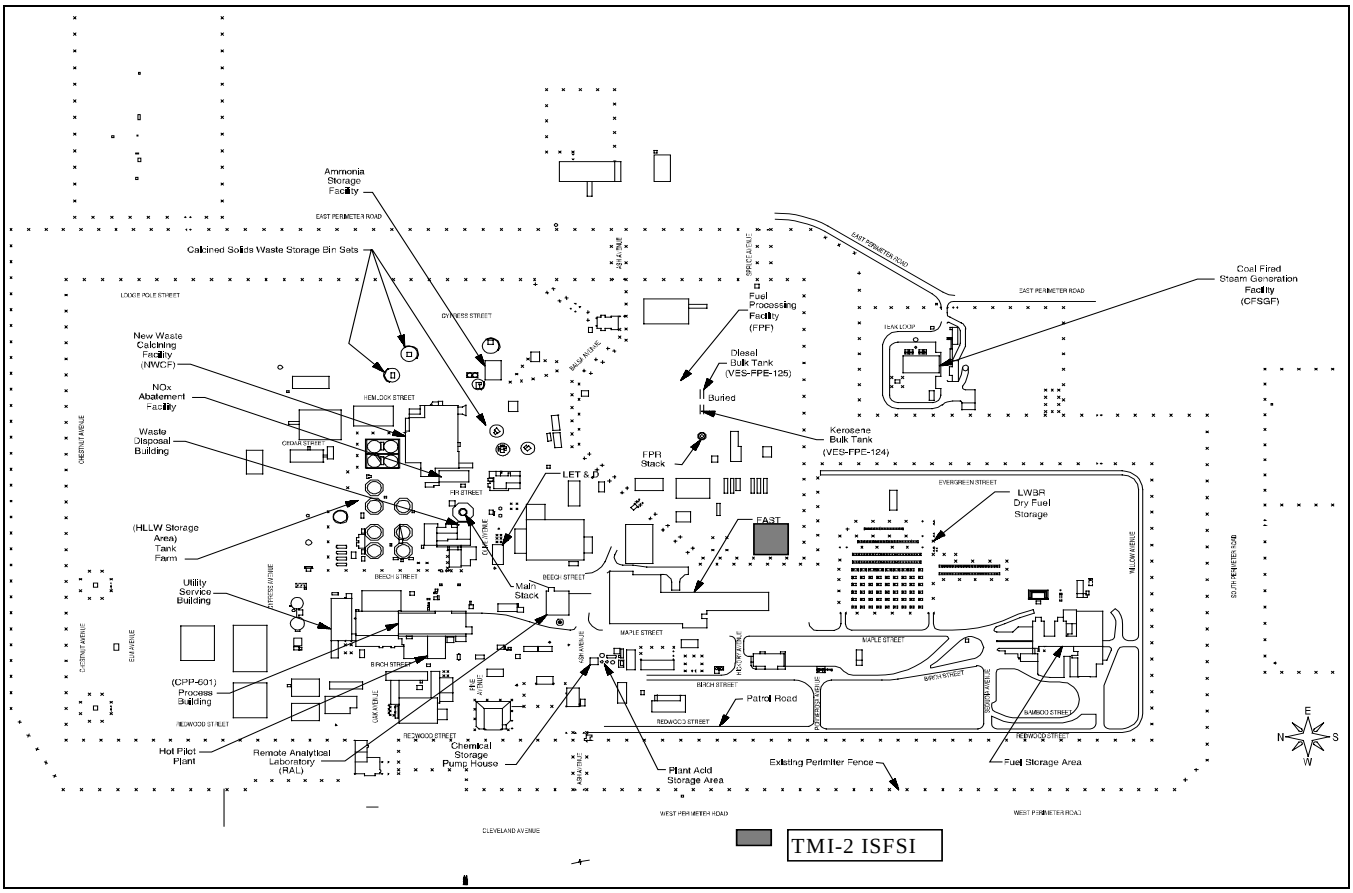

Figure 2.1-6. INTEC Area Plot Plan (not to scale).

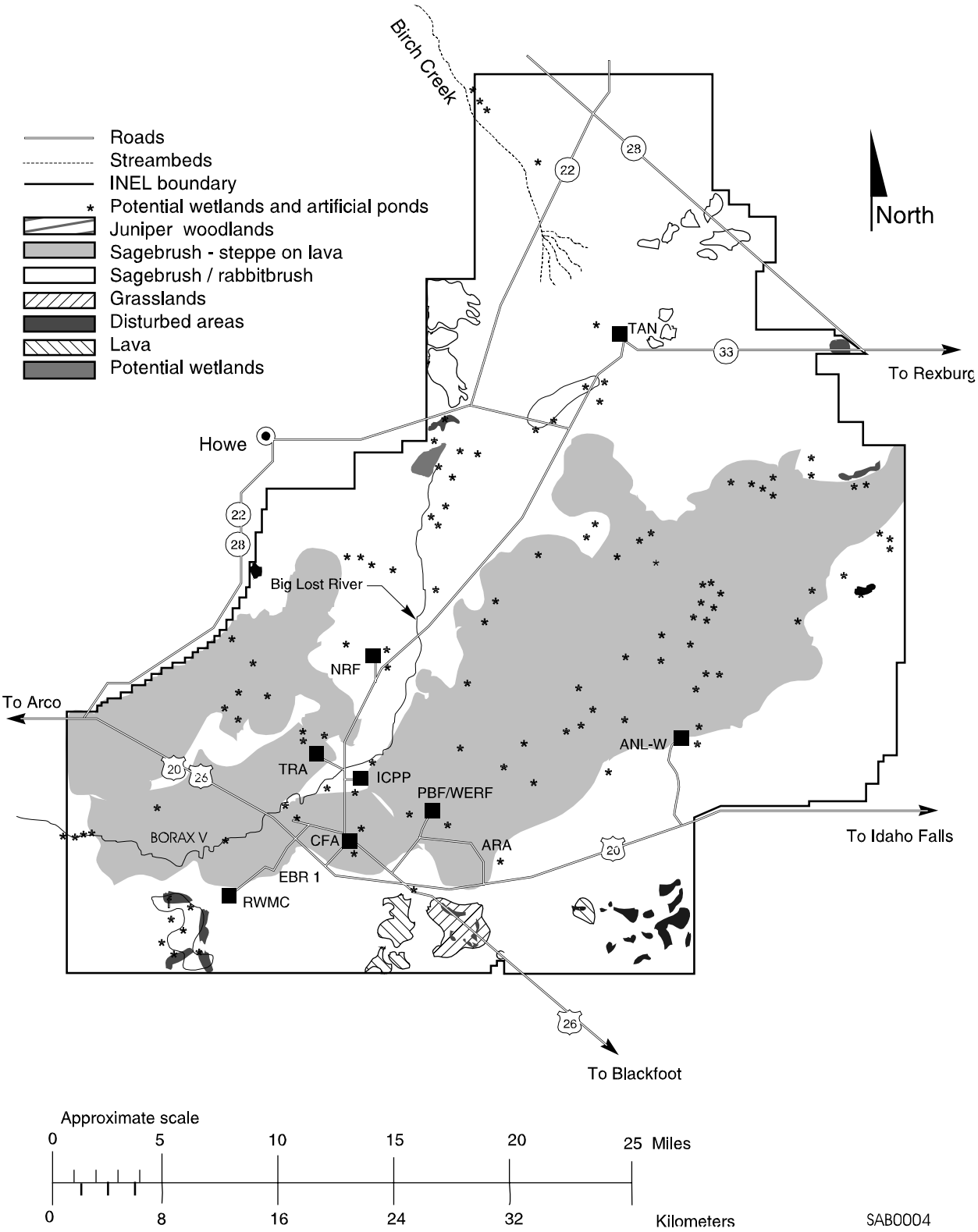

Figure 2.1-7. Approximate Distribution of Vegetation at the INEL.

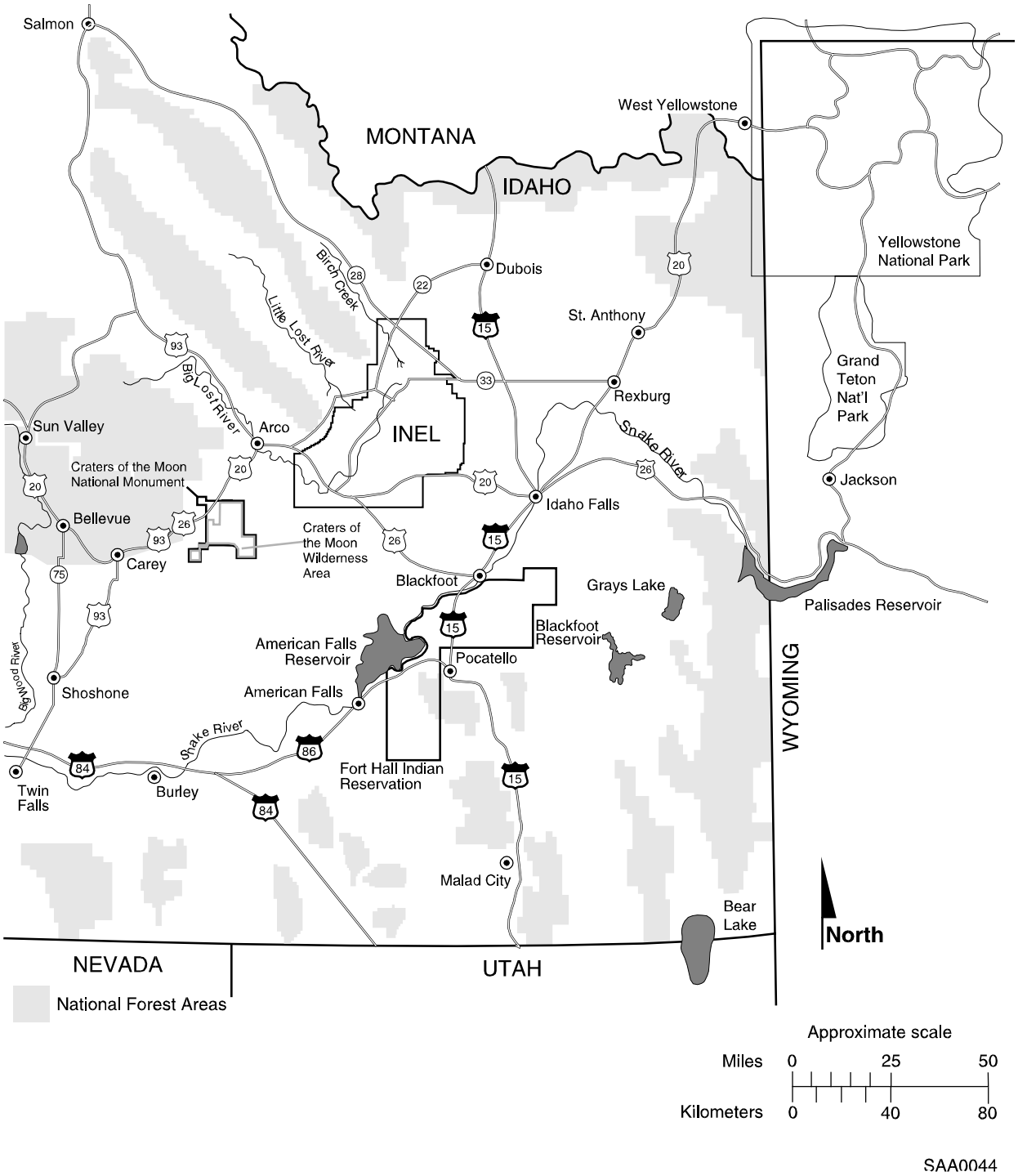

Figure 2.1-8. Location of the INEL in Southeastern Idaho.

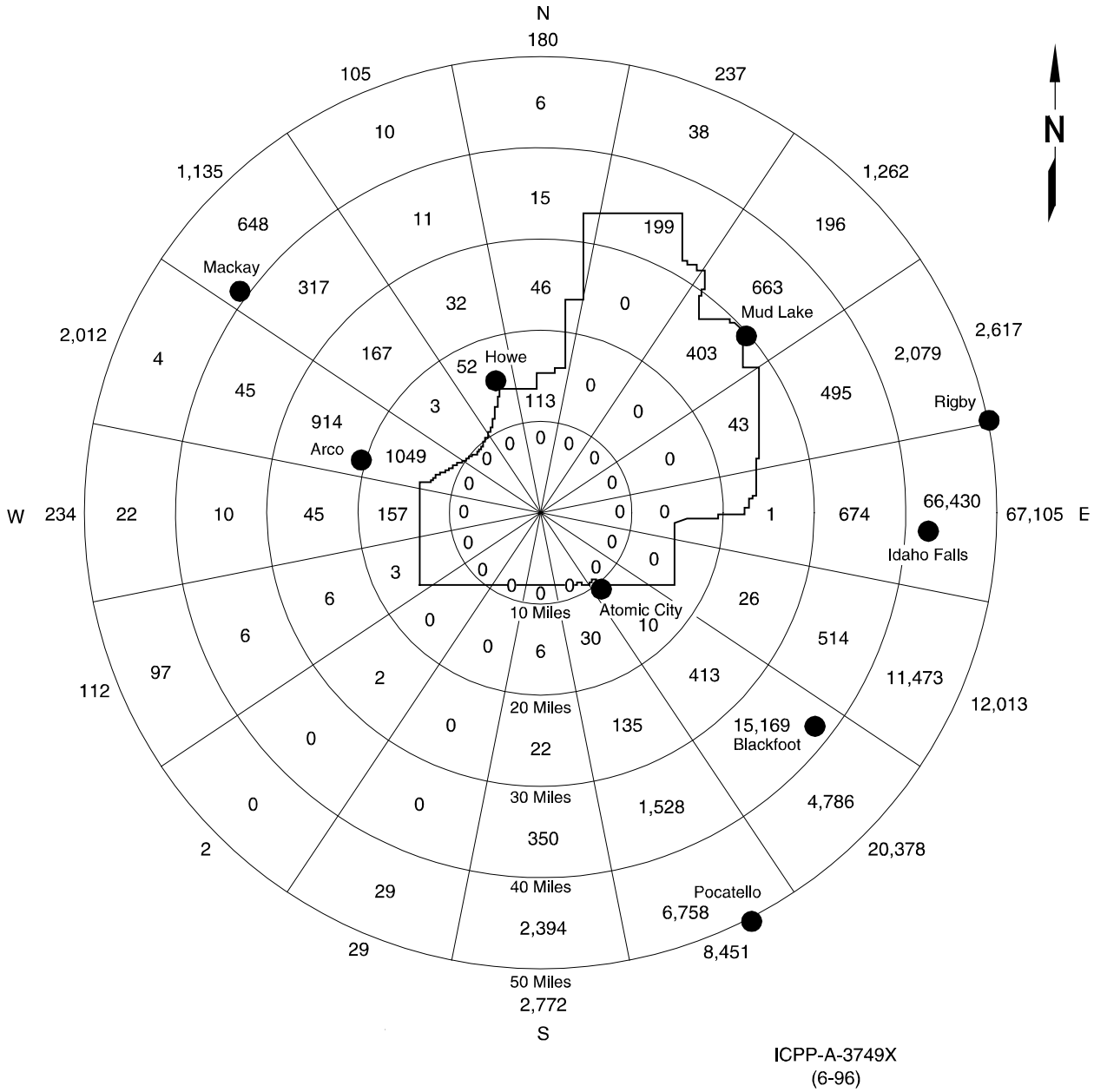

Total: 118,644

Figure 2.1-9. Population Distribution for 1990.

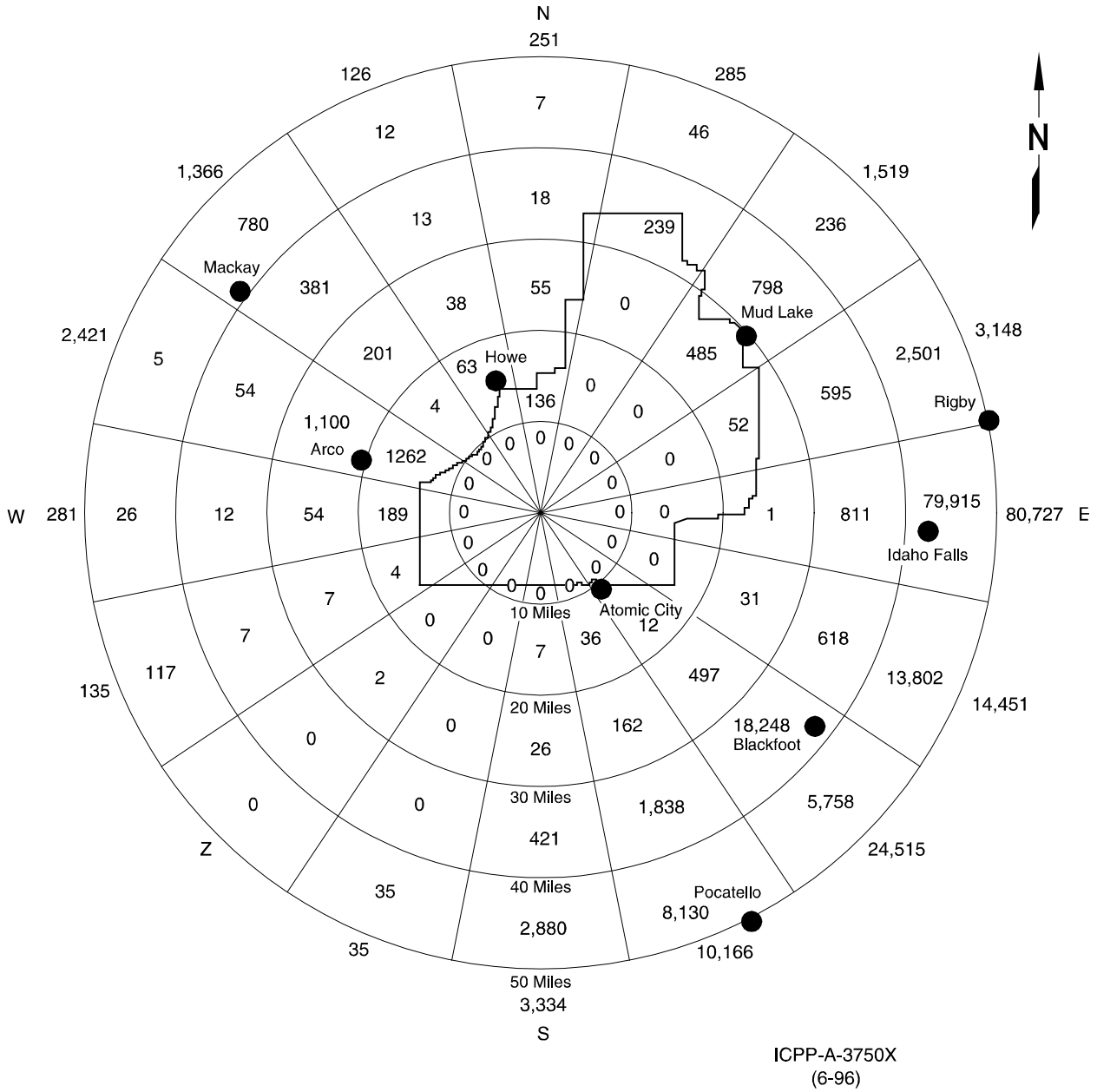

Total: 142,727

Figure 2.1-10. Population Distribution for 2000.

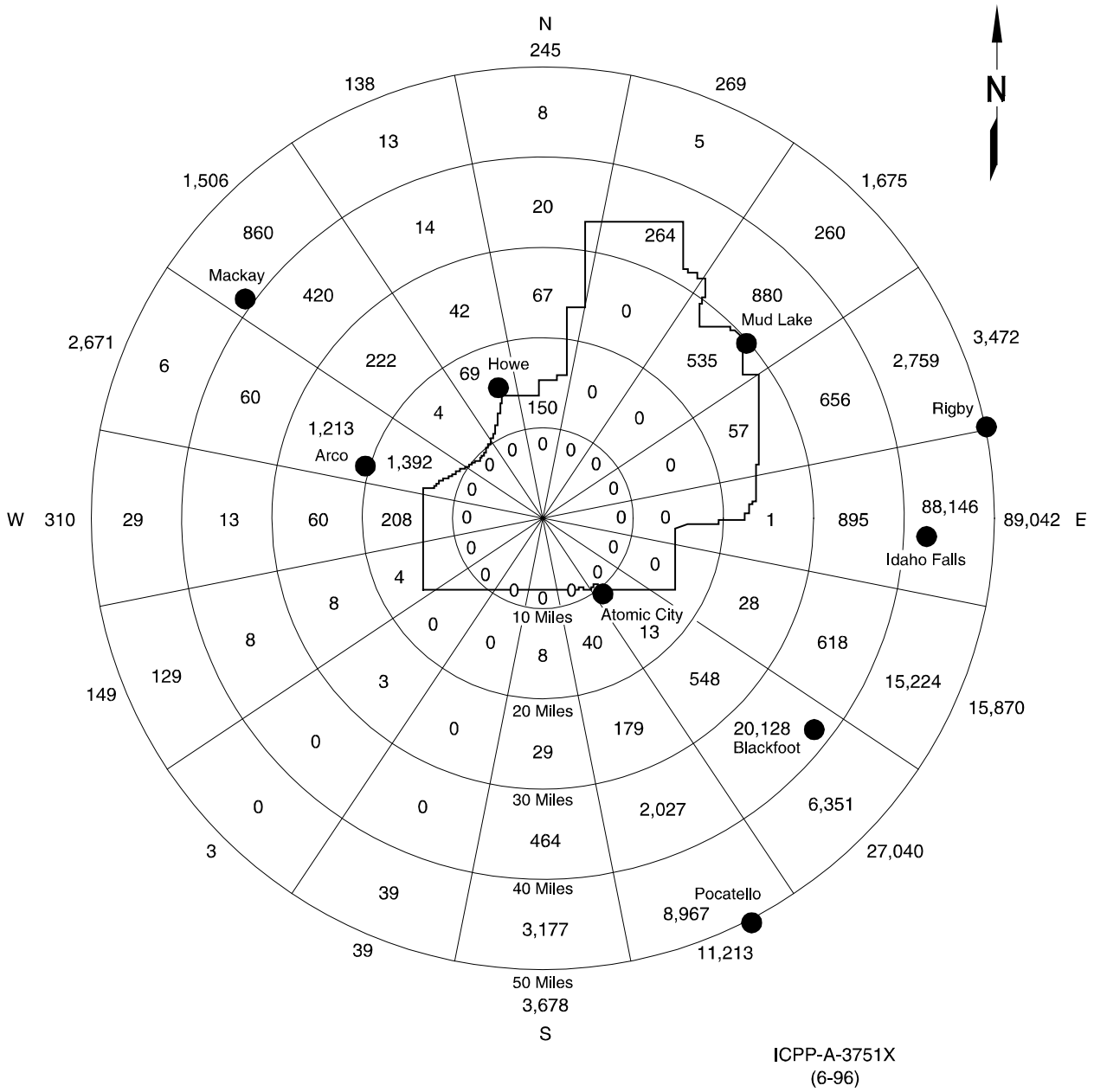

Total: 157,320

Figure 2.1-11. Population Distribution for 2010.

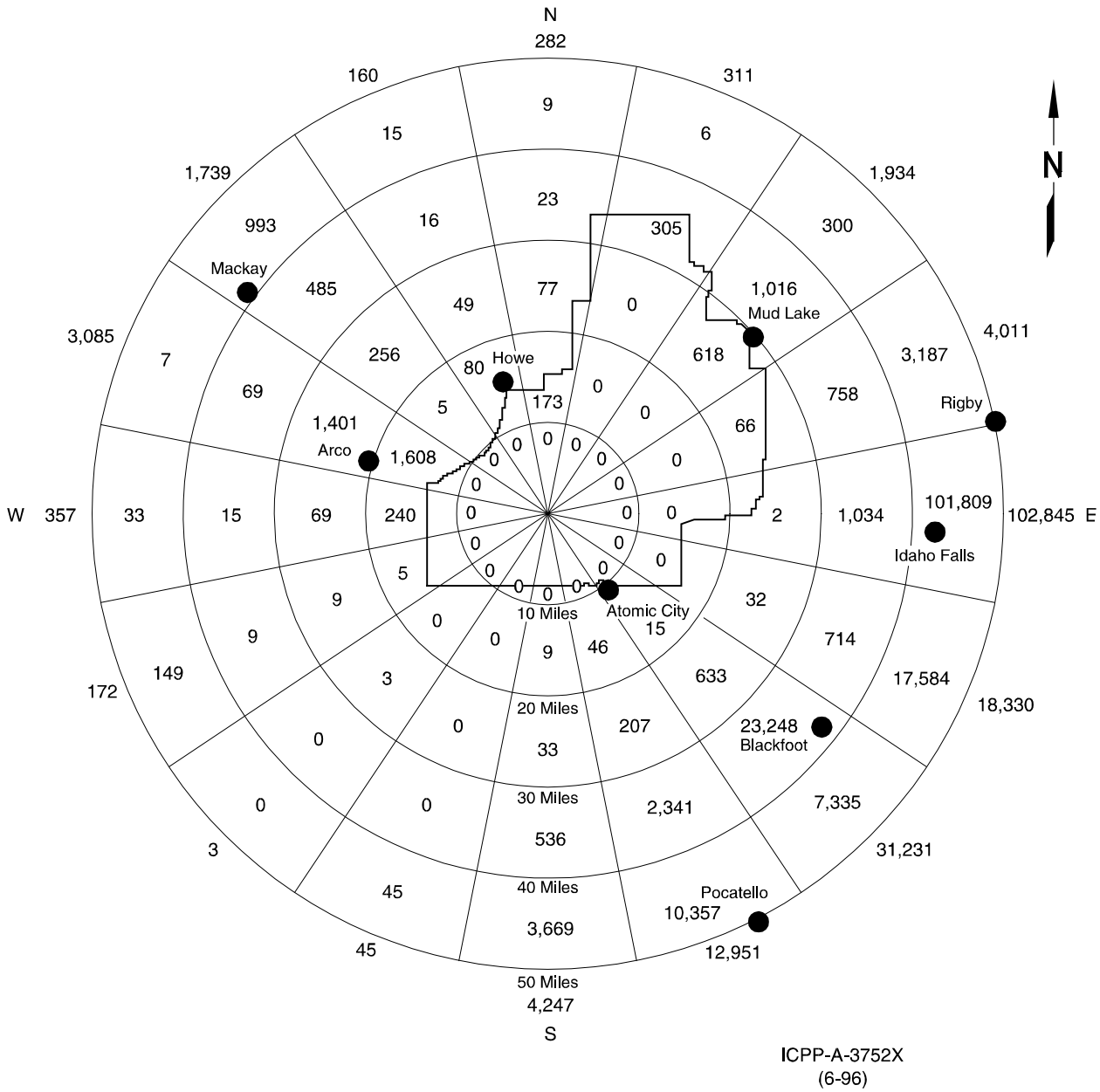

Total: 181,703

Figure 2.1-12. Population Distribution for 2020.

ANL-W Argonne National Laboratory-West
ARA Auxiliary Reactor Area
CFA Central Facilities Area
EBR-I Experimental Breeder Reactor - I
ICPP Idaho Chemical Processing Plant
NRF Naval Reactors Facility
PBF Power Burst Facility
RWMC Radioactive Waste Management Complex
TAN Test Area North
TRA Test Reactor Area
WERF Waste Experimental Reduction Facility

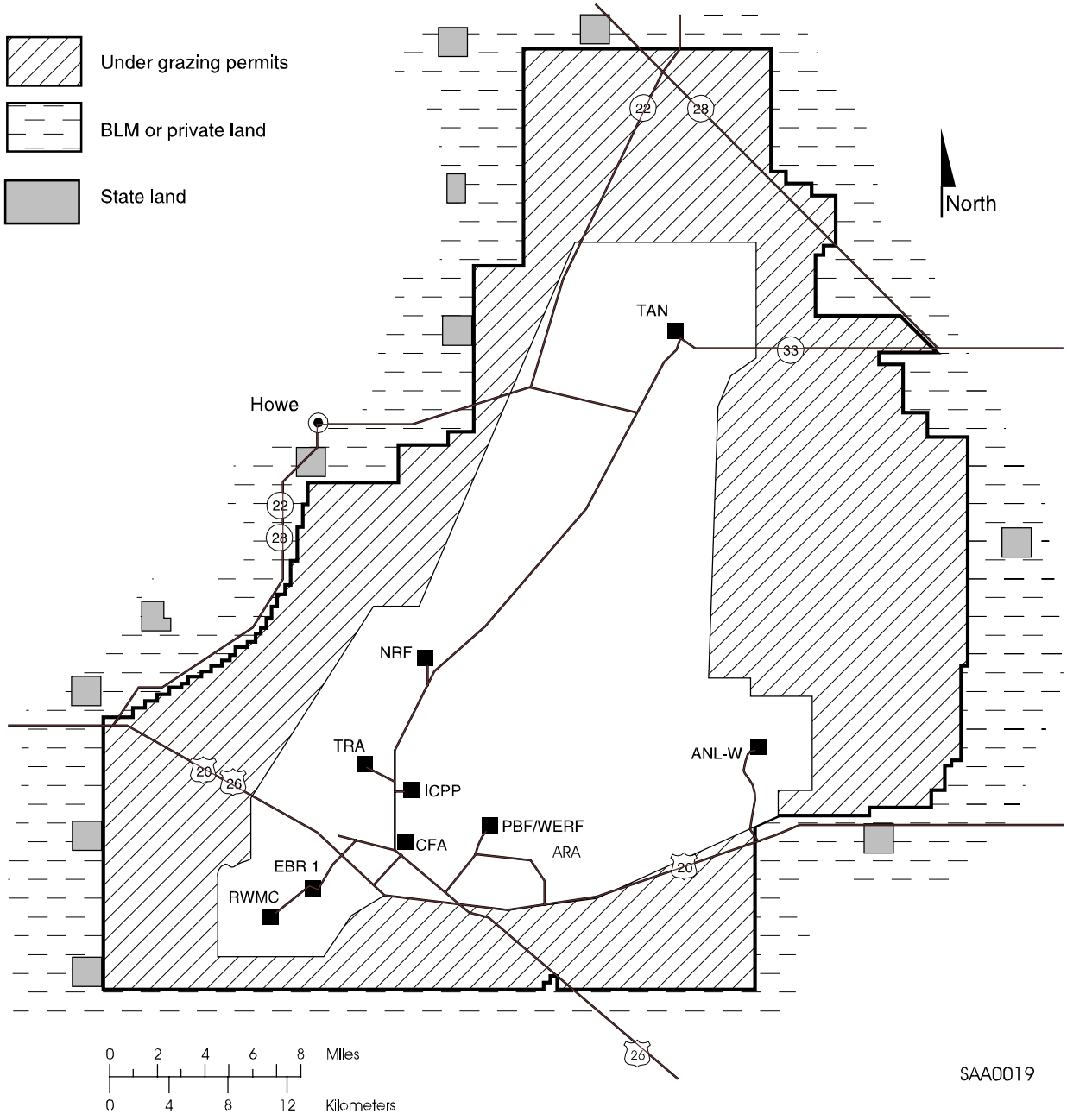

Figure 2.1-13. Selected Land Uses at the INEL and Surrounding Region.

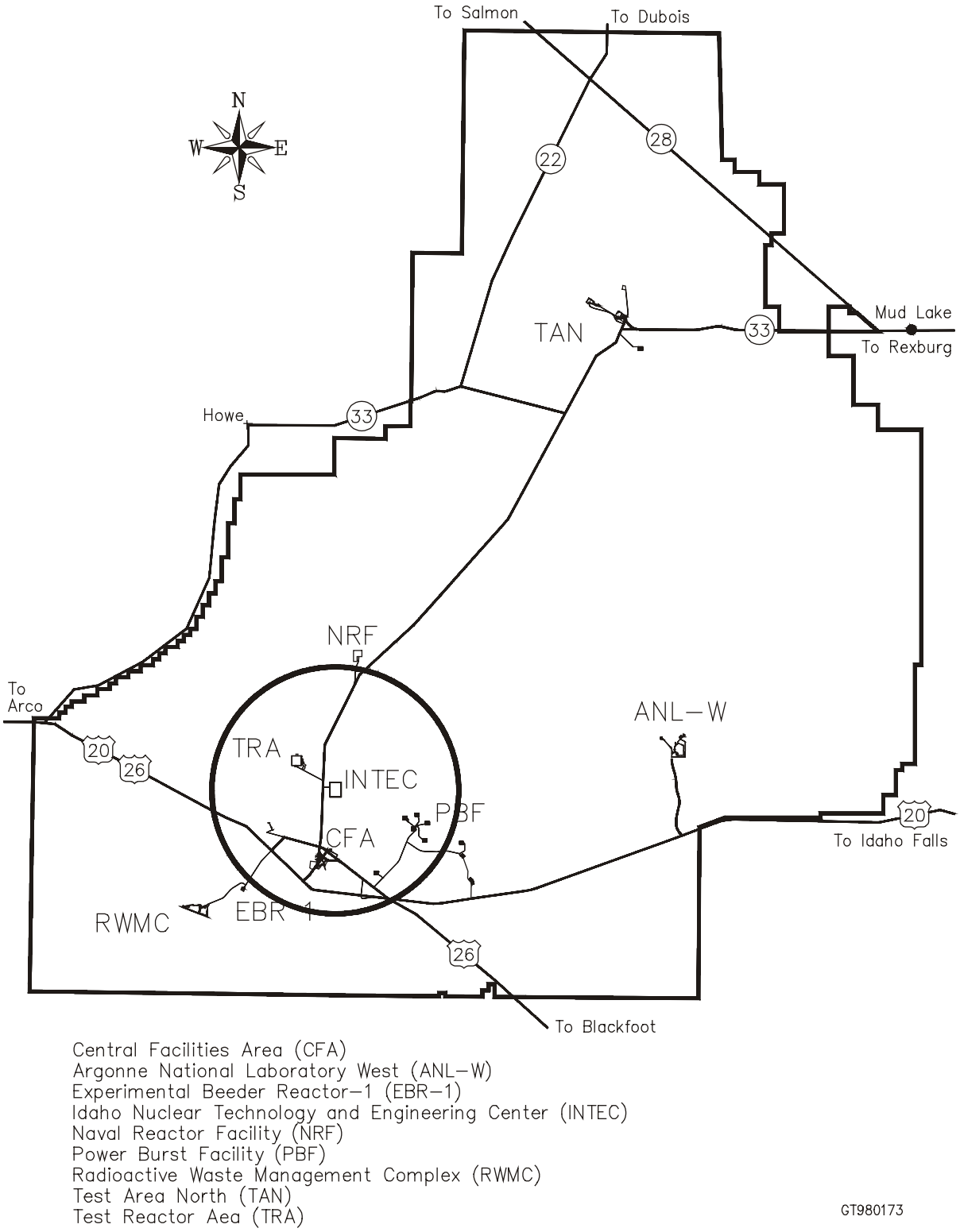

Figure 2.2-1. Idaho National Engineering and Environmental Laboratory's Primary Facility Areas (showing 5-mile radius from TMI-2 ISFSI).

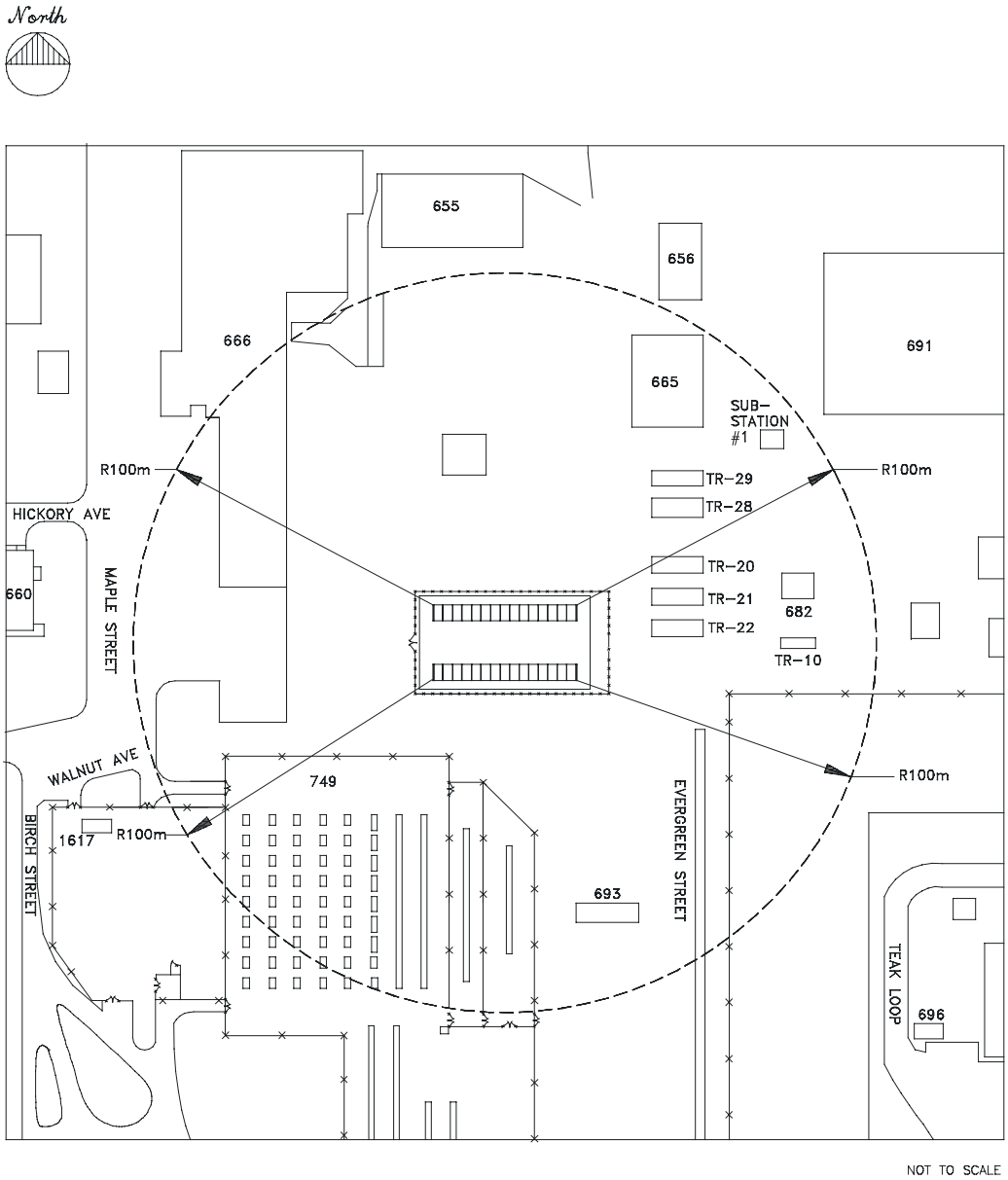

Figure 2.2-2. TMI-2 ISFSI Location with 100 meter Radius Line.

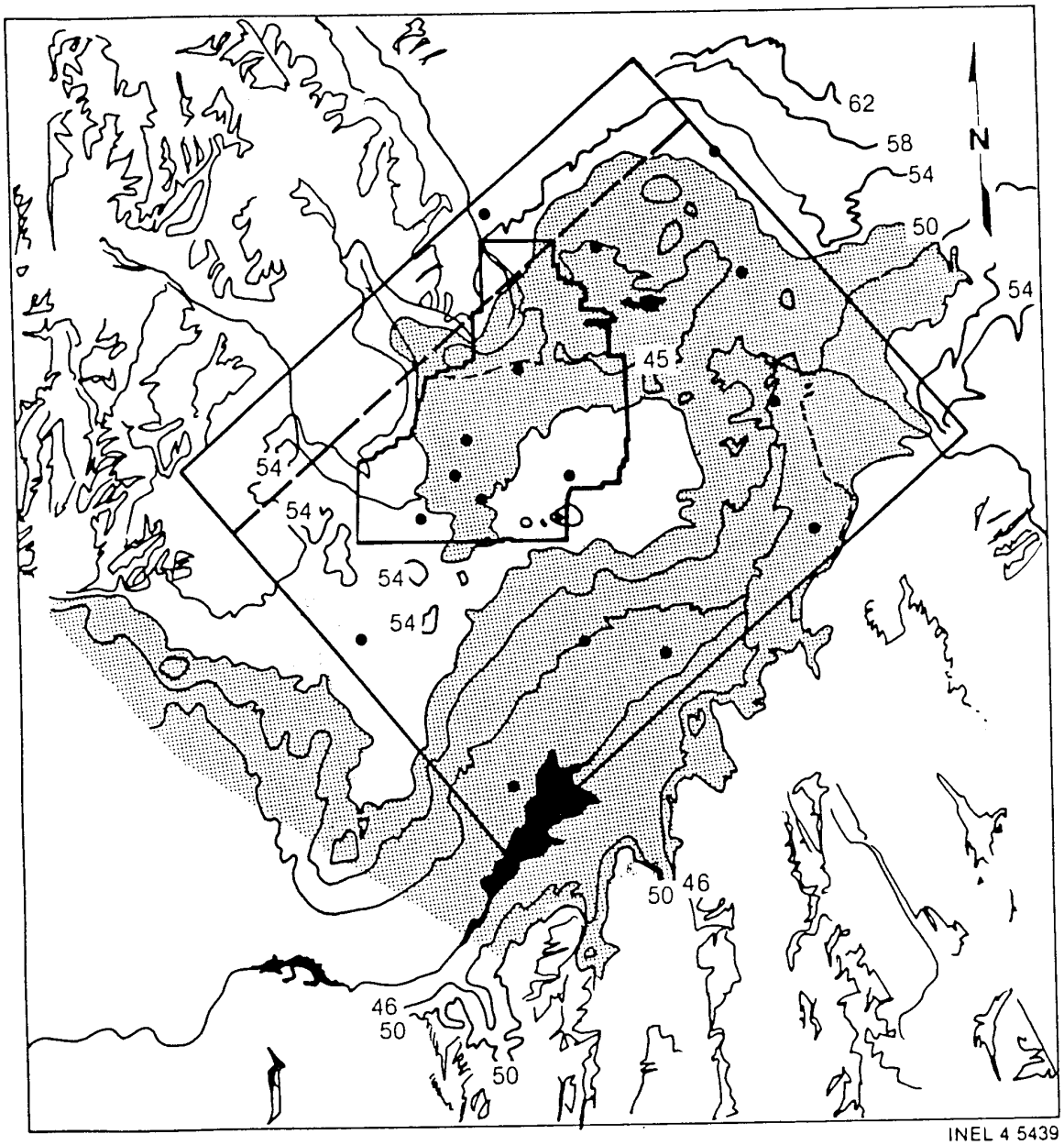

46-62 = Height values in hundreds of ft above mean sea level (msl)
▒ = Below 5000 ft msl
Tick marks = 8.6 km (computational grid mesh size)
• = Tower-mounted wind sensors

Figure 2.3-1. Relief map of the ESRP.

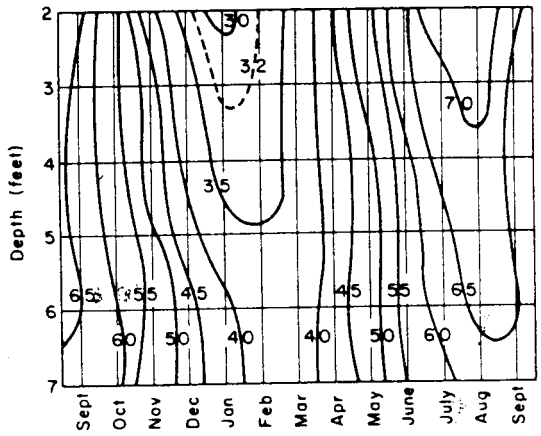

Figure 2.3-2. Average monthly subsoil temperatures (°F), sandy soil surface.

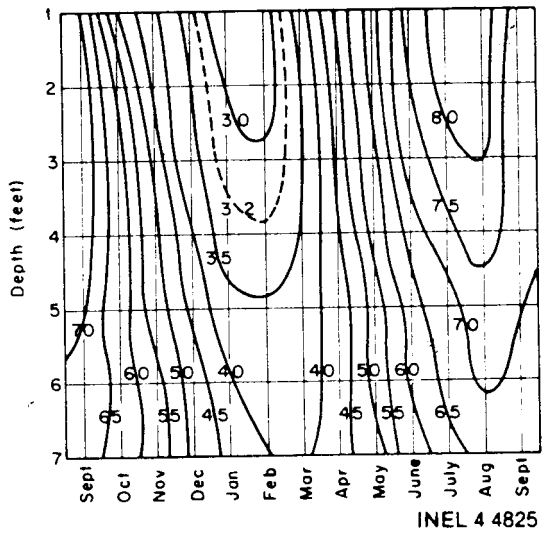

Figure 2.3-3. Average monthly subsoil temperatures (°F), asphalt surface.

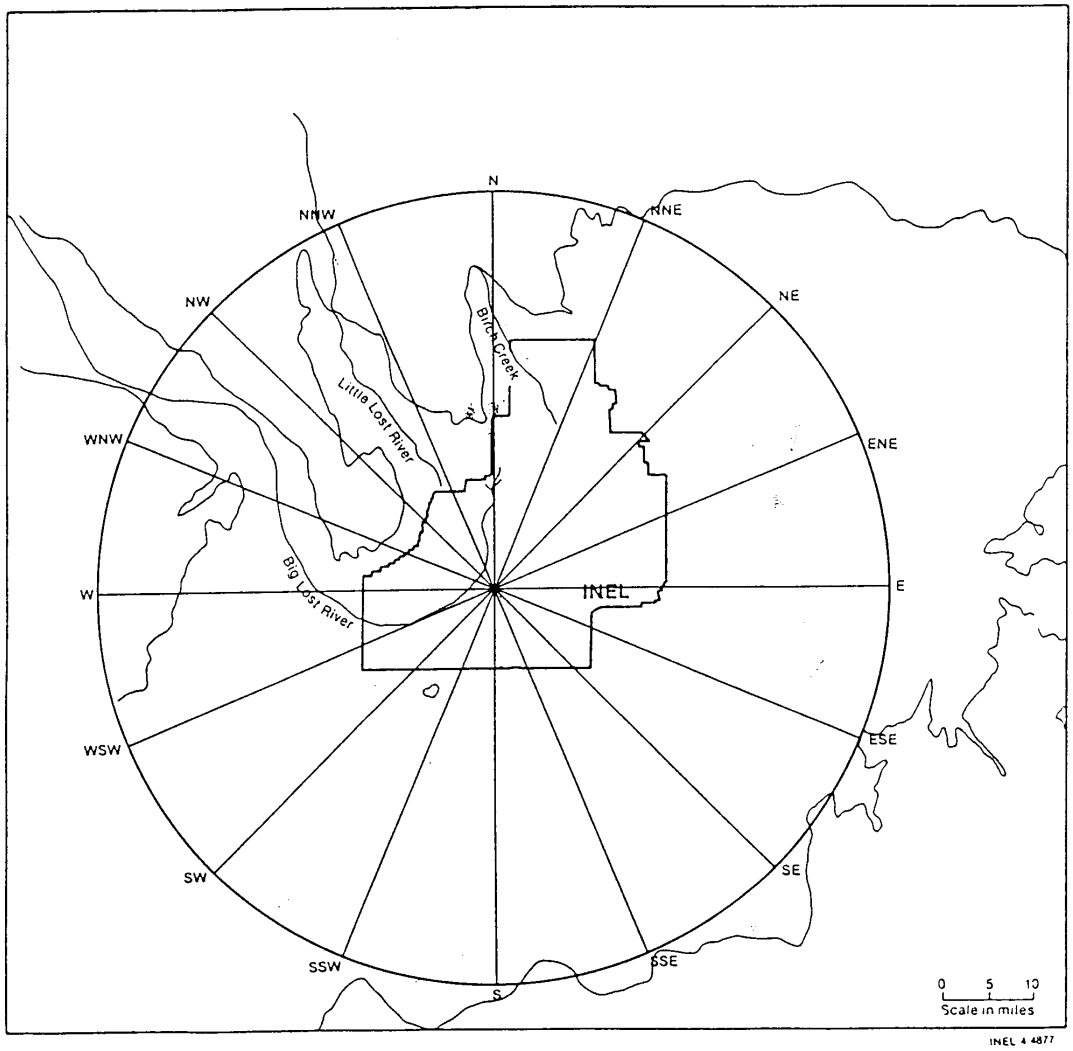

Figure 2.3-4. TMI-2 ISFSI site 50-mi radius.

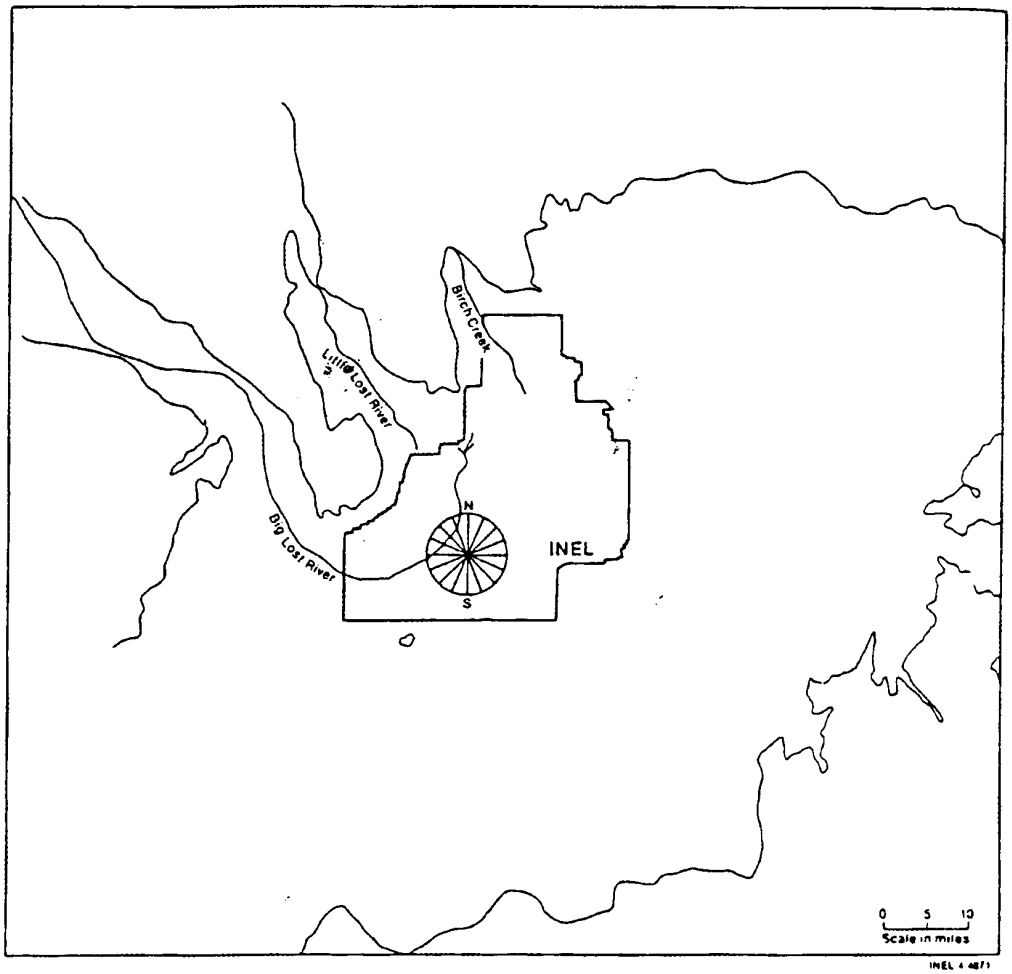

Figure 2.3-5. TMI-2 ISFSI site 5-mi radius.

Figure 2.3-6. Topographic cross-sections for TMI-2 ISFSI site--50 mi radius, north and east radials.

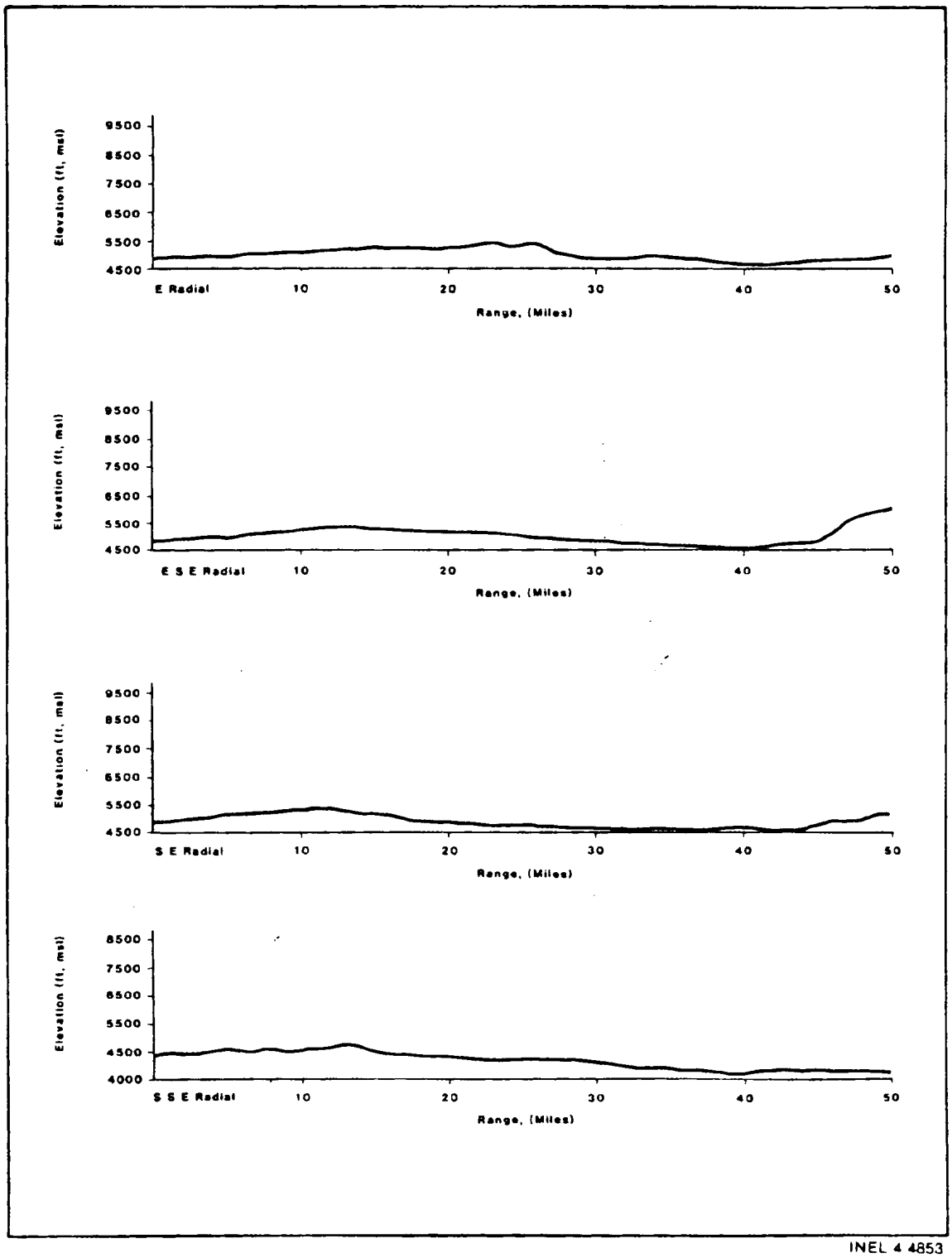

Figure 2.3-7. Topographic cross sections for the TMI-2 ISFSI site--50-mile south and east radials.

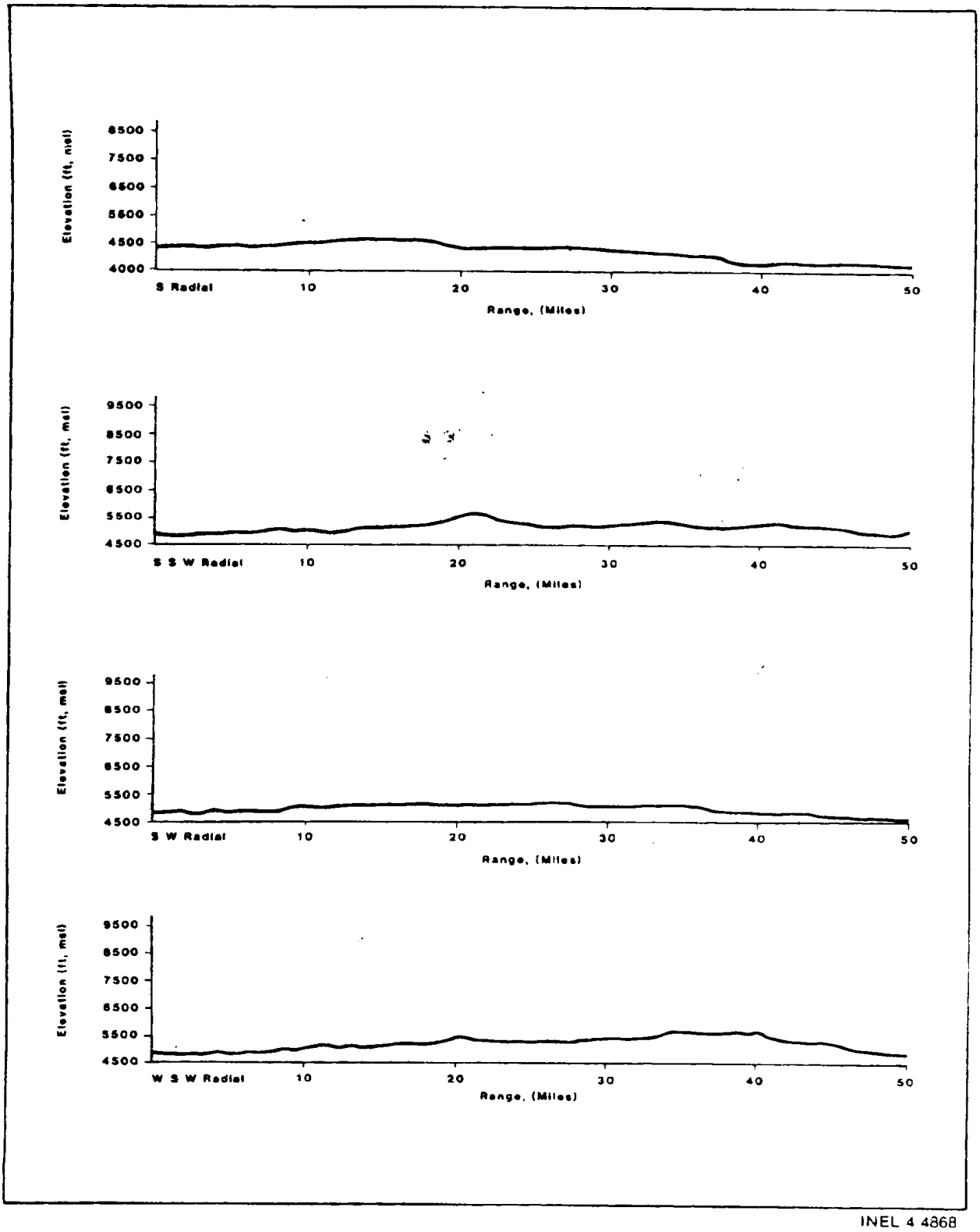

Figure 2.3-8. Topographic cross-sections for TMI-2 ISFSI site--50 mi radius, south and west radials.

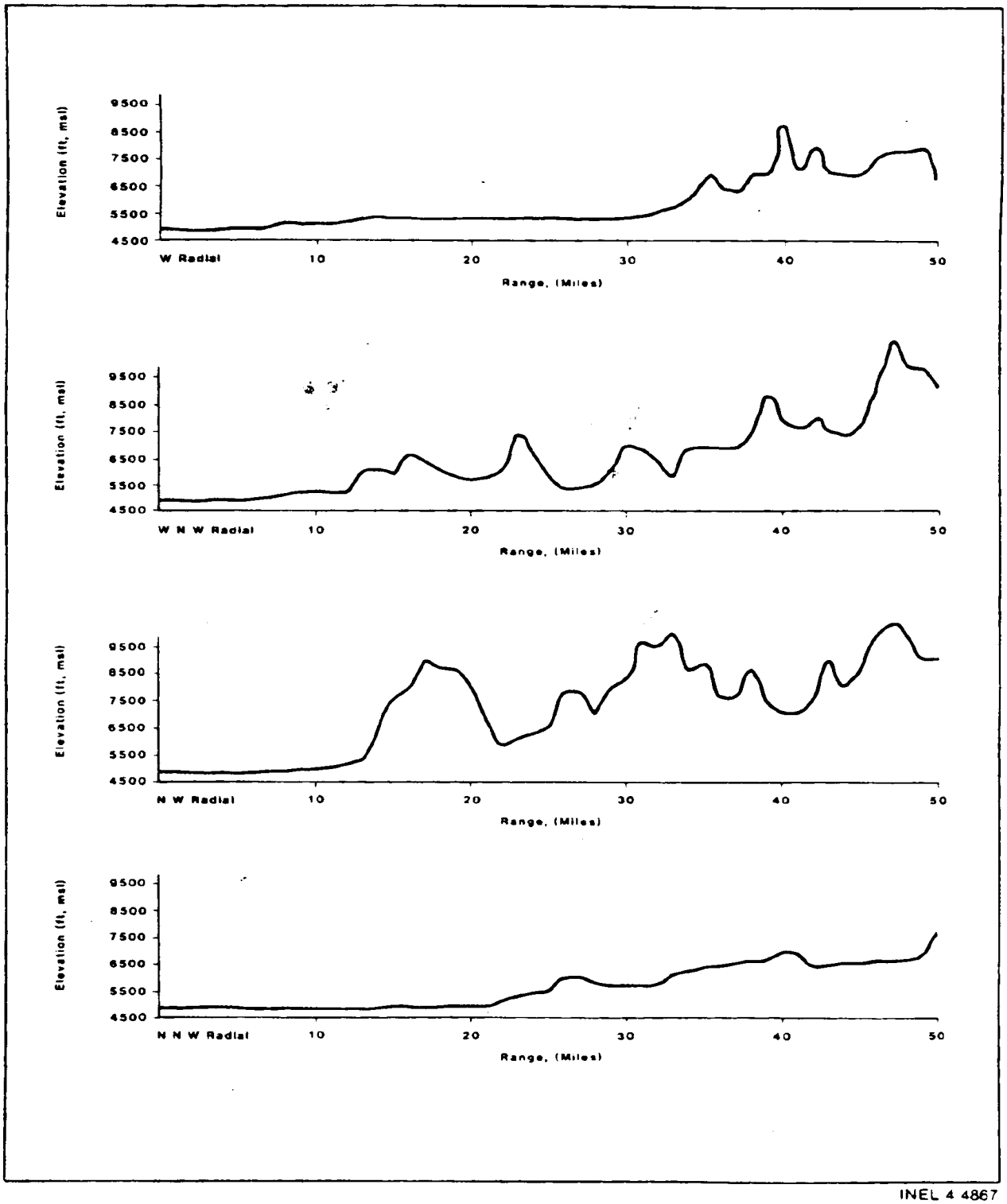

Figure 2.3-9. Topographic cross-sections for TMI-2 ISFSI site--50 mi radius, north and west radials.

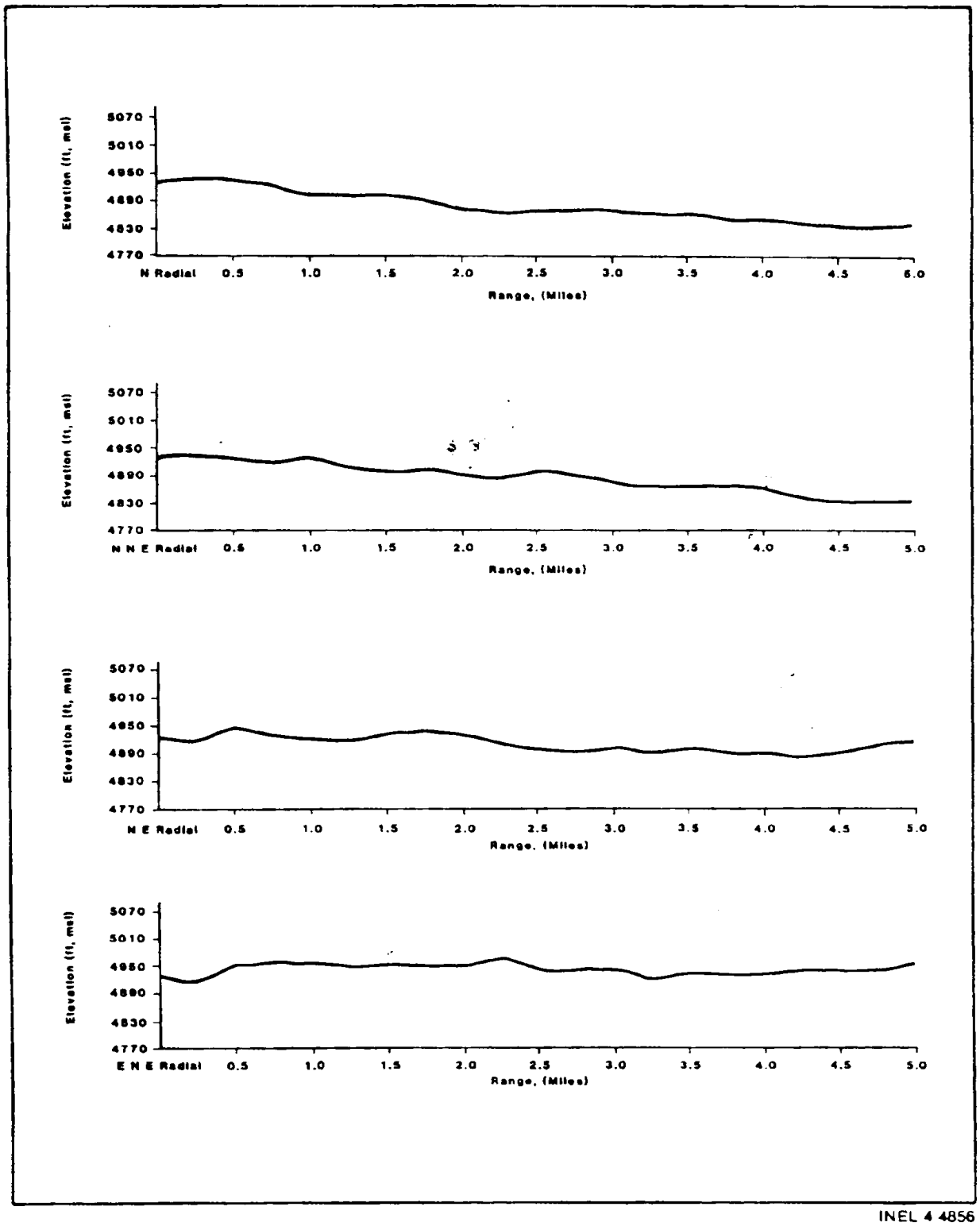

Figure 2.3-10. Topographic cross-sections for TMI-2 ISFSI site--5 mi radius, north and east radials.

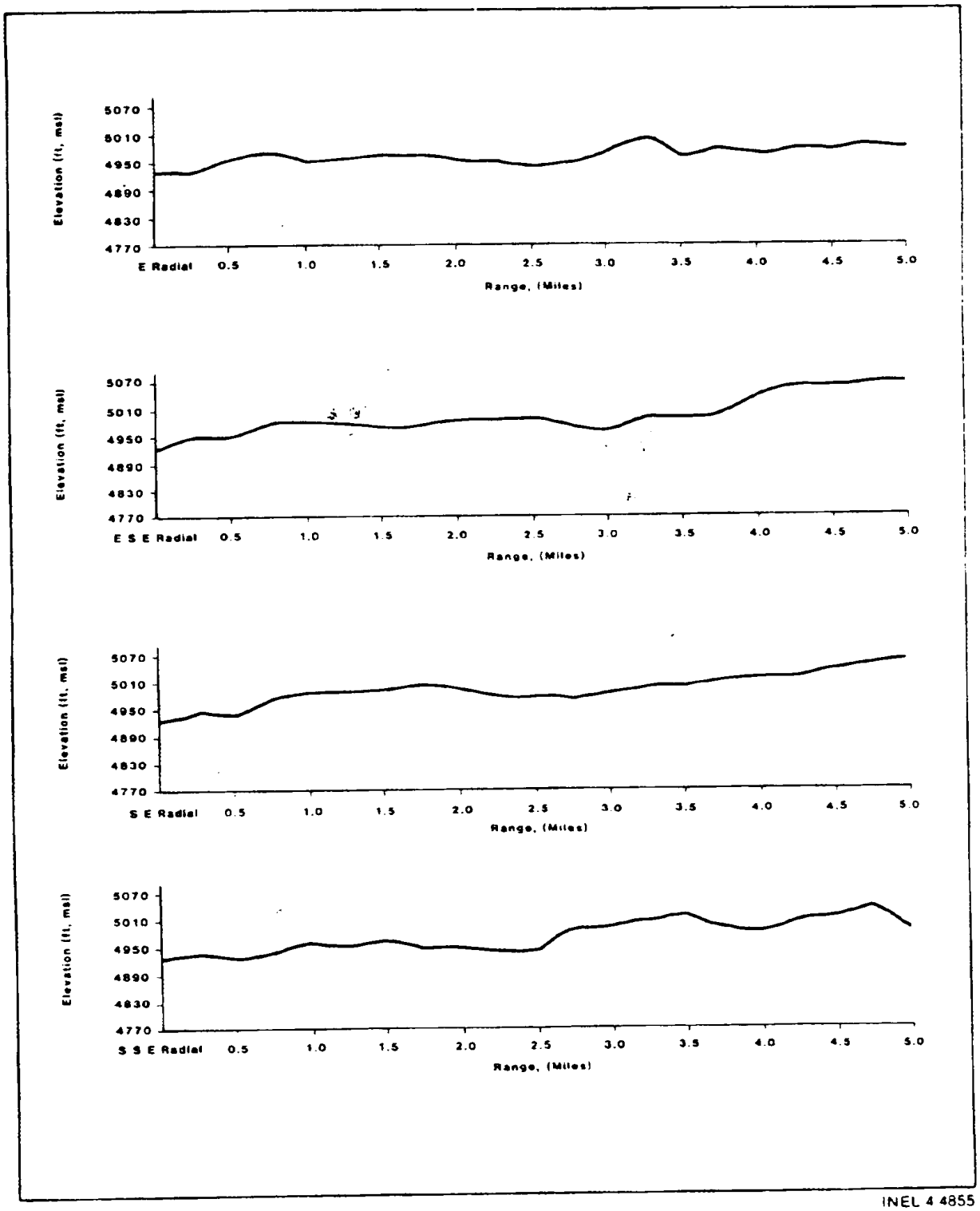

Figure 2.3-11. Topographic cross-sections for TMI-2 ISFSI site--5 mi radius, south and east radials.

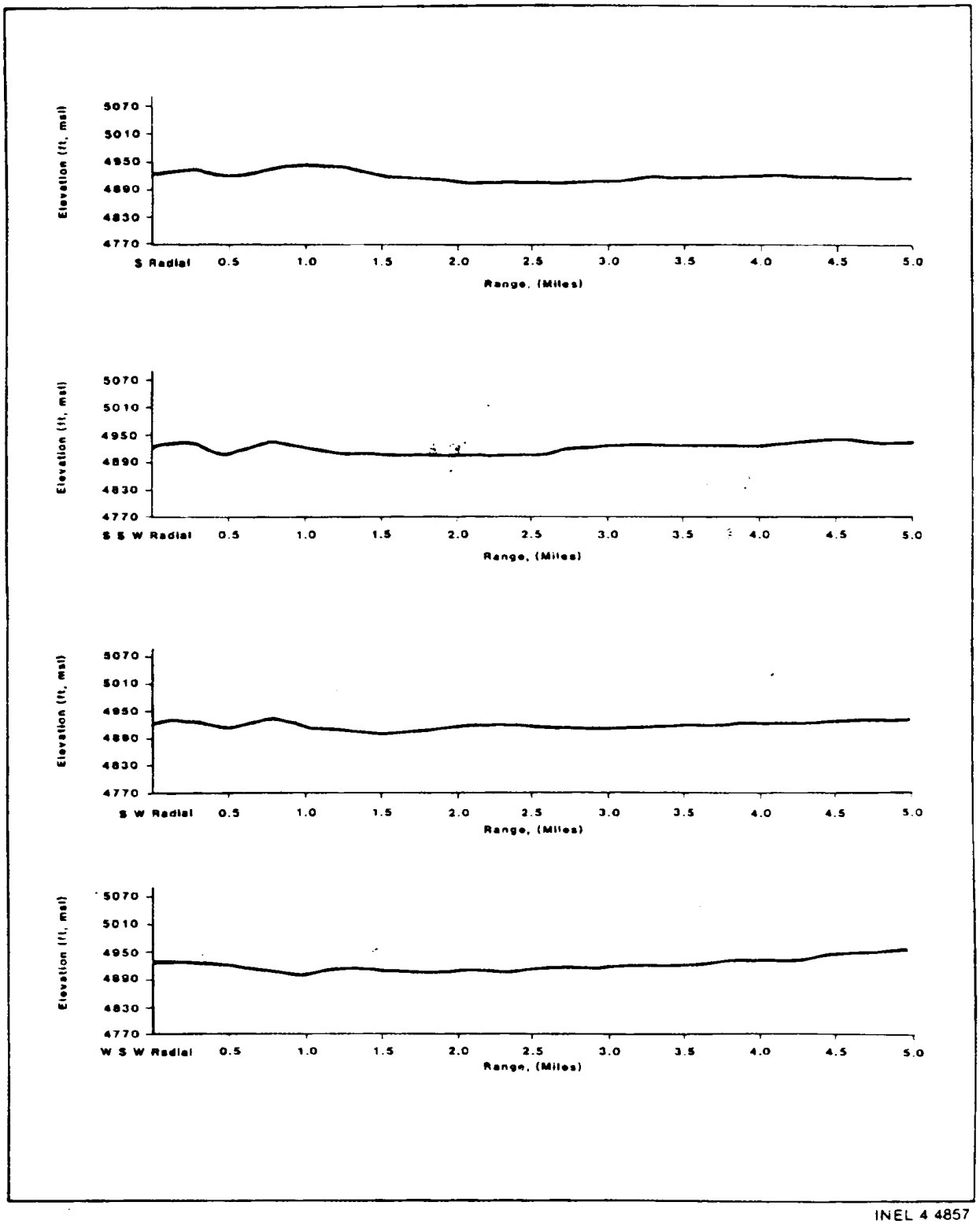

Figure 2.3-12. Topographic cross section for TMI-2 ISFSI site--5 mi radius, south and west radials.

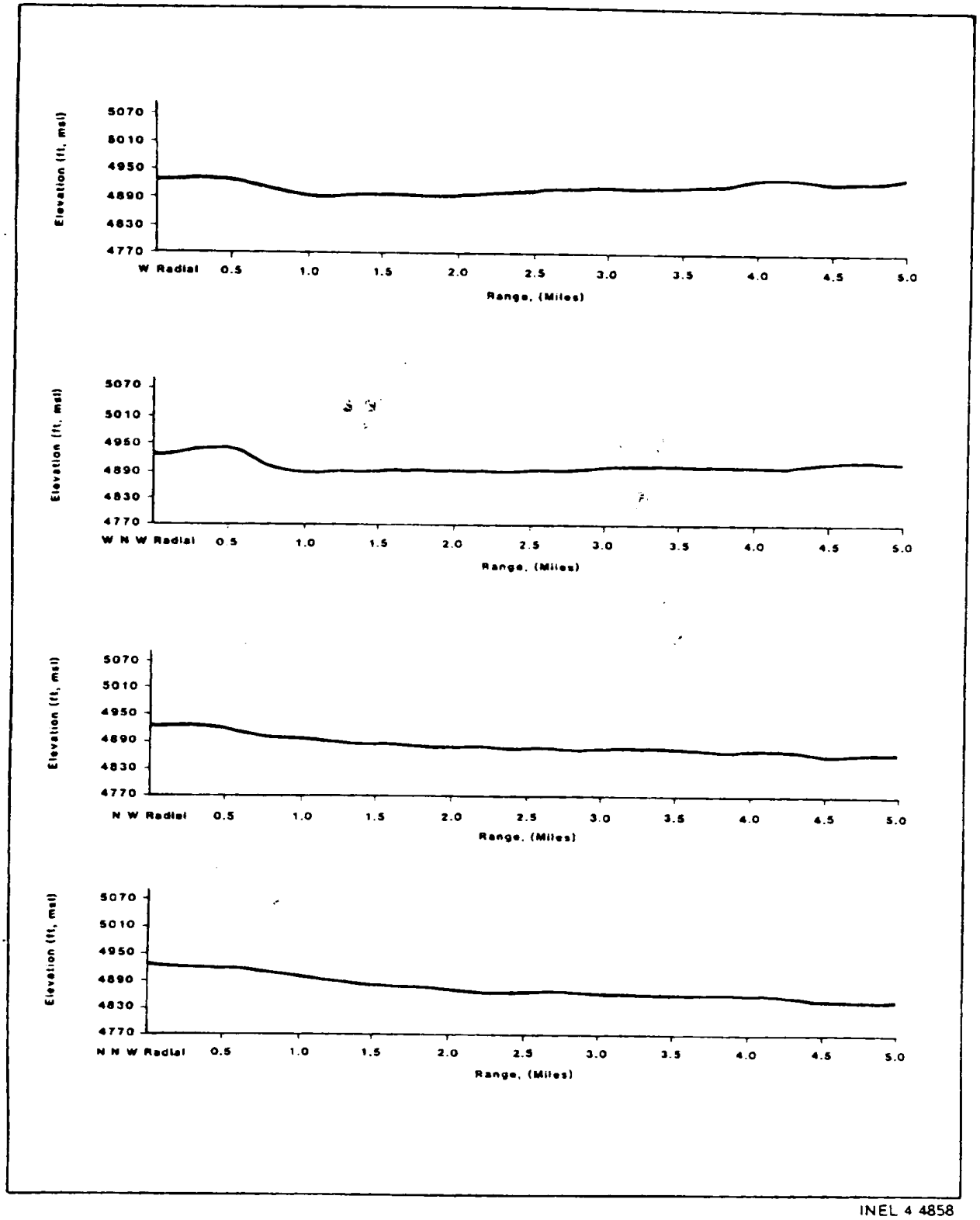

Figure 2.3-13. Topographic cross section for TMI-2 ISFSI site--5 mi radius, north and west radials.

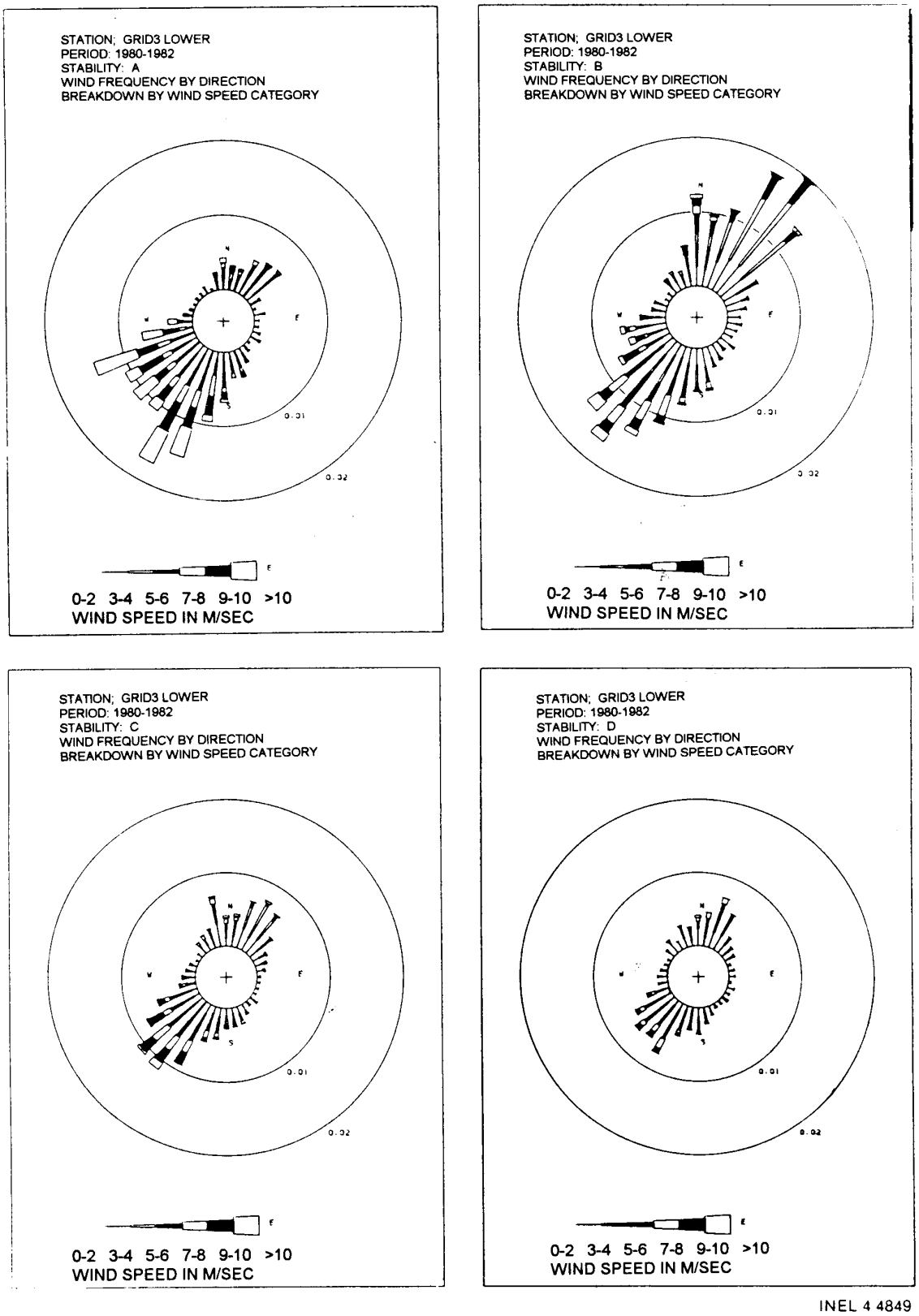

Figure 2.3-14. Grid 3, 10-m level annual wind roses, (1981-1982).

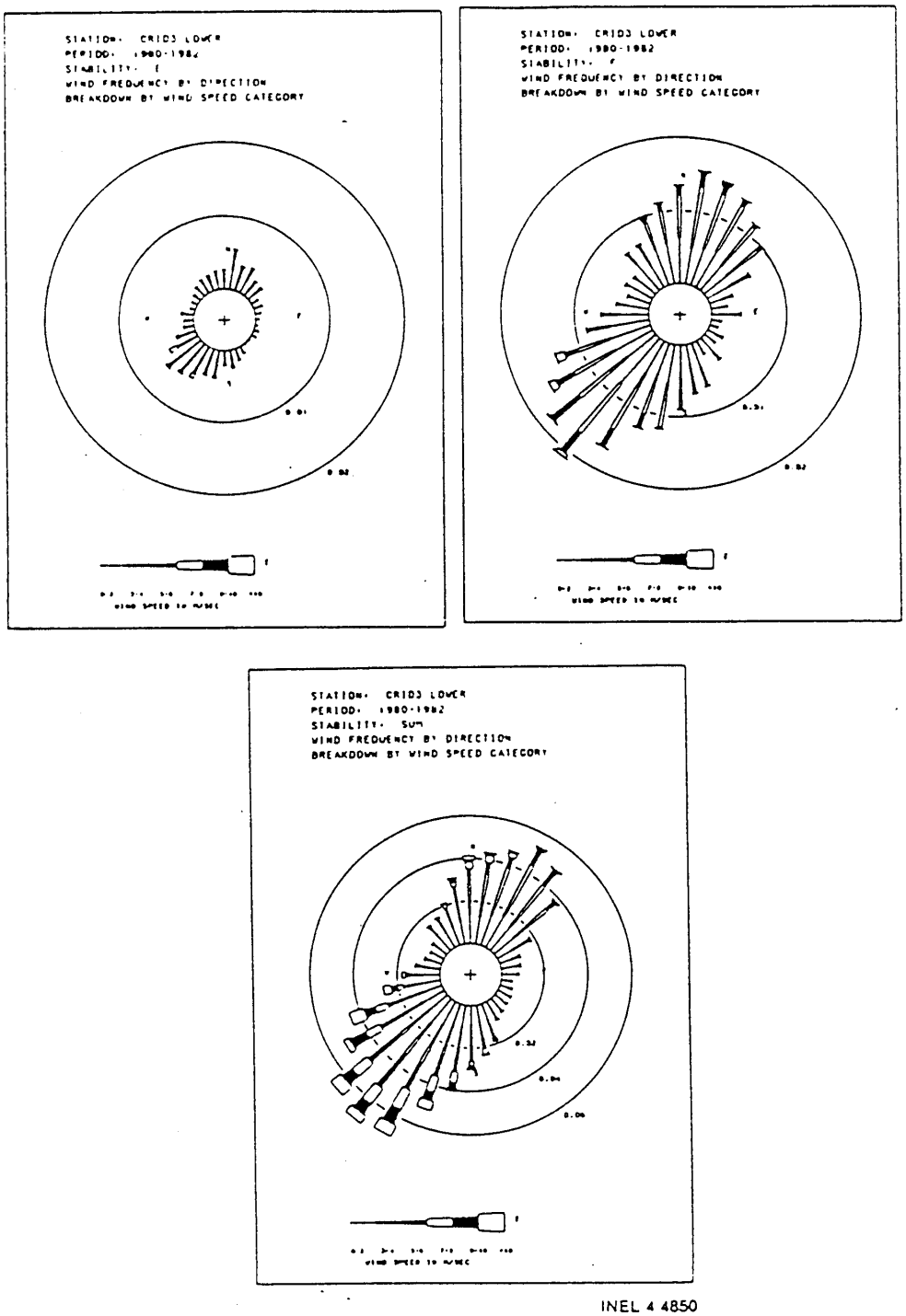

Figure 2.3-15. Grid 3, 10-m level annual wind roses, (1981-1982).

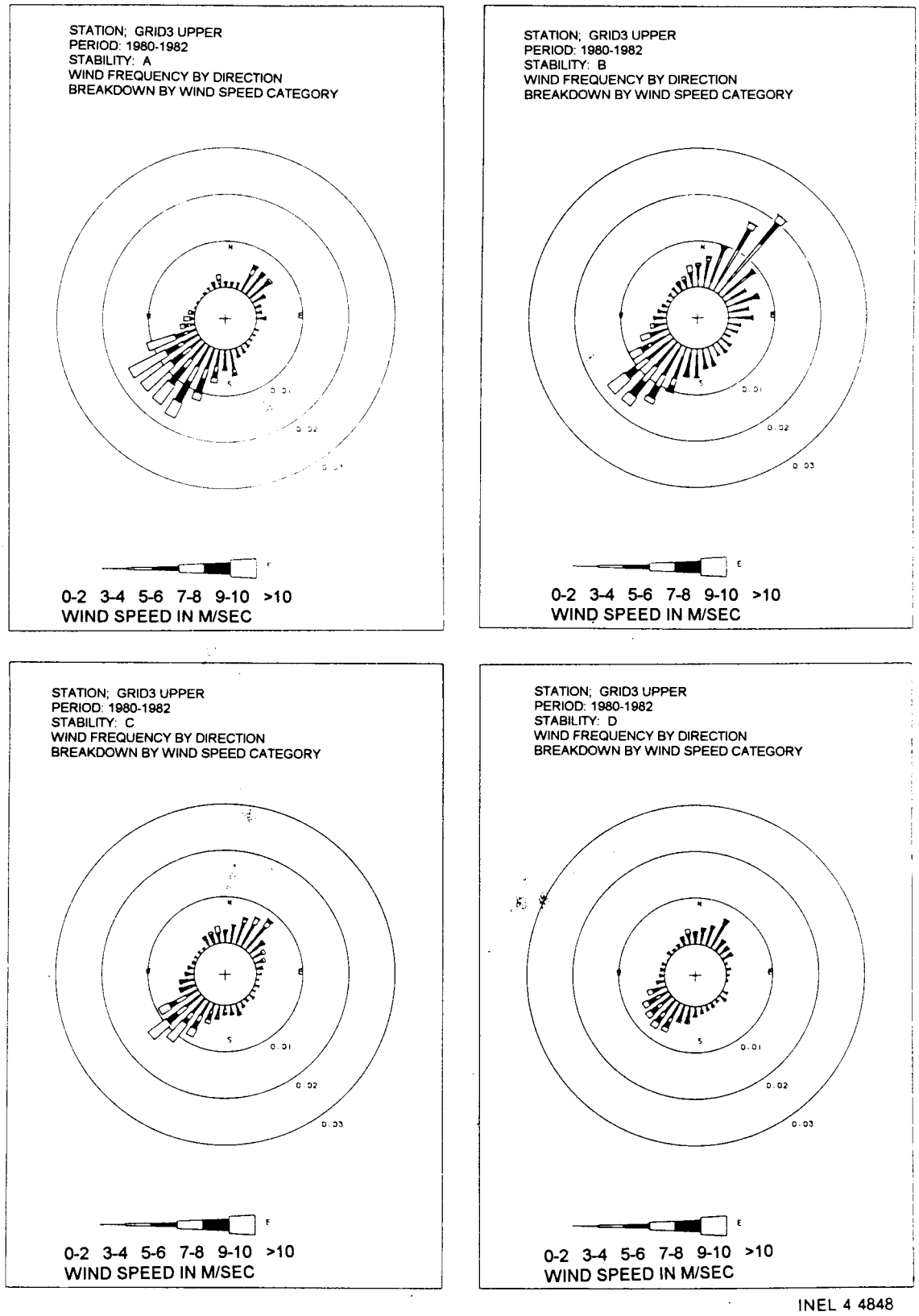

Figure 2.3-16. Grid 3, 61-m. level annual wind roses, (1981-1982).

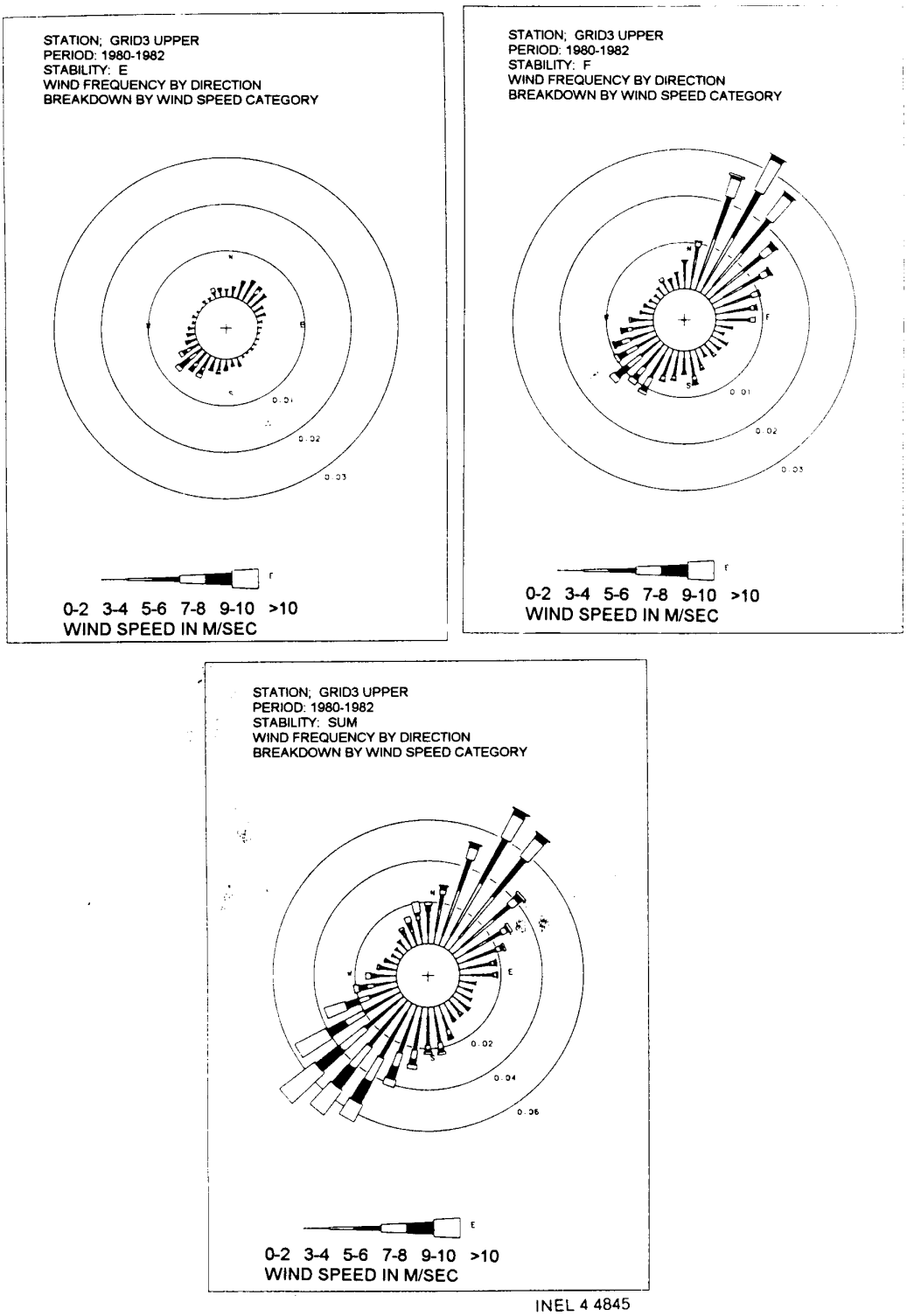

Figure 2.3-17. Grid 3, 61-m. level annual wind roses, (1981-1982).

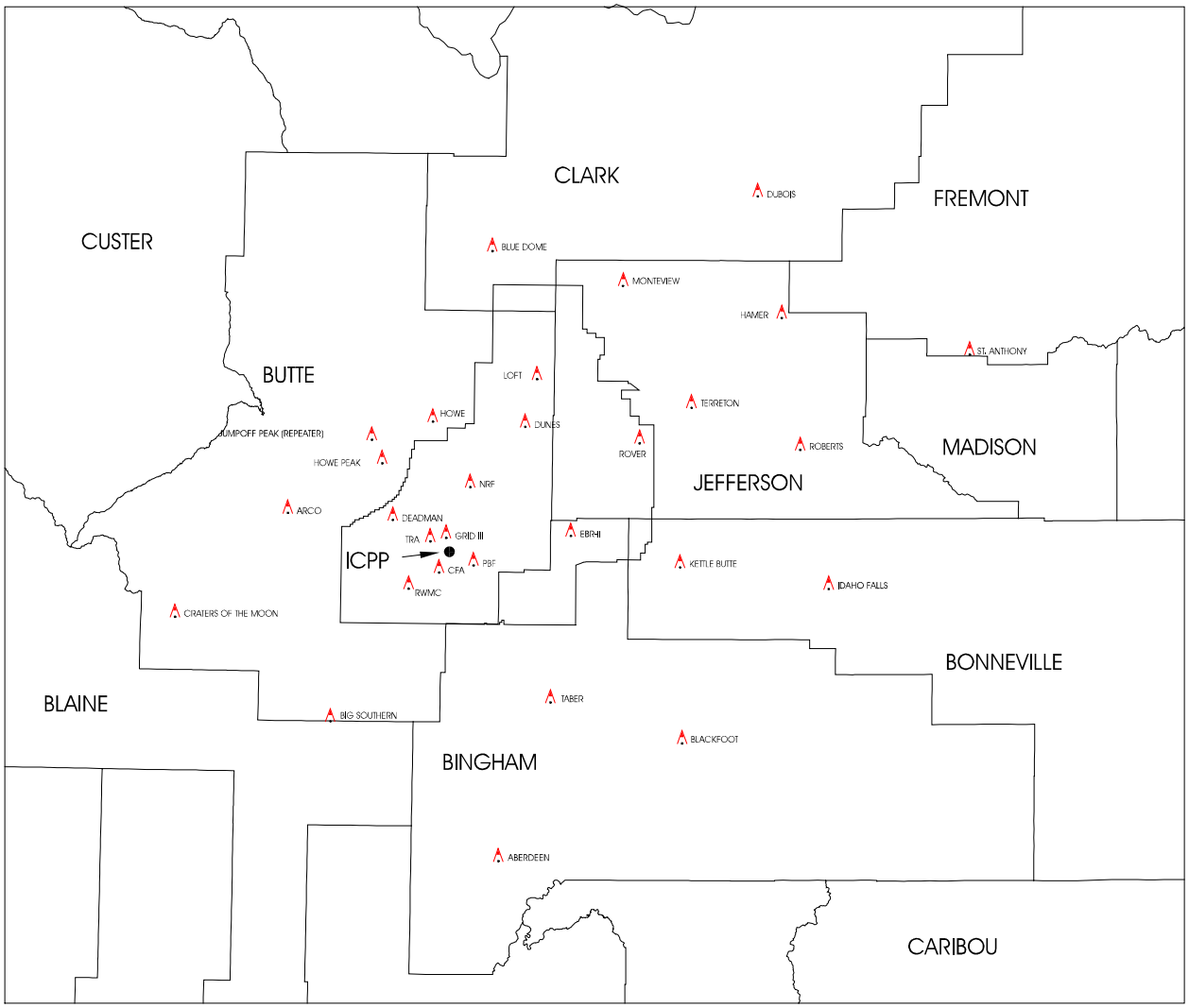

Figure 2.3-18. Wind observation locations within a 50-mi radius of the TMI-2 ISFSI site at ICPP.

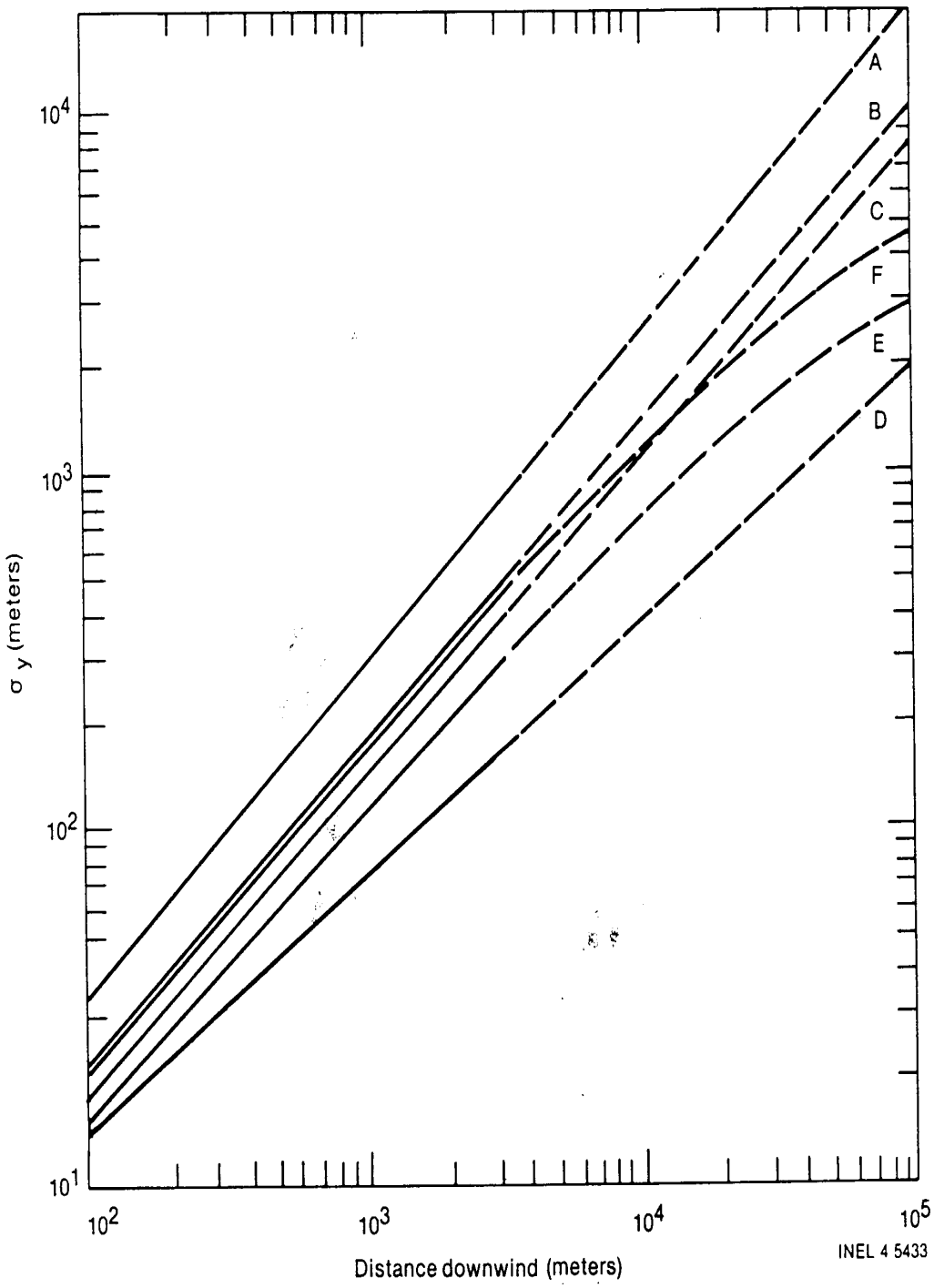

Figure 2.3-19. σ_y versus distance at INEL

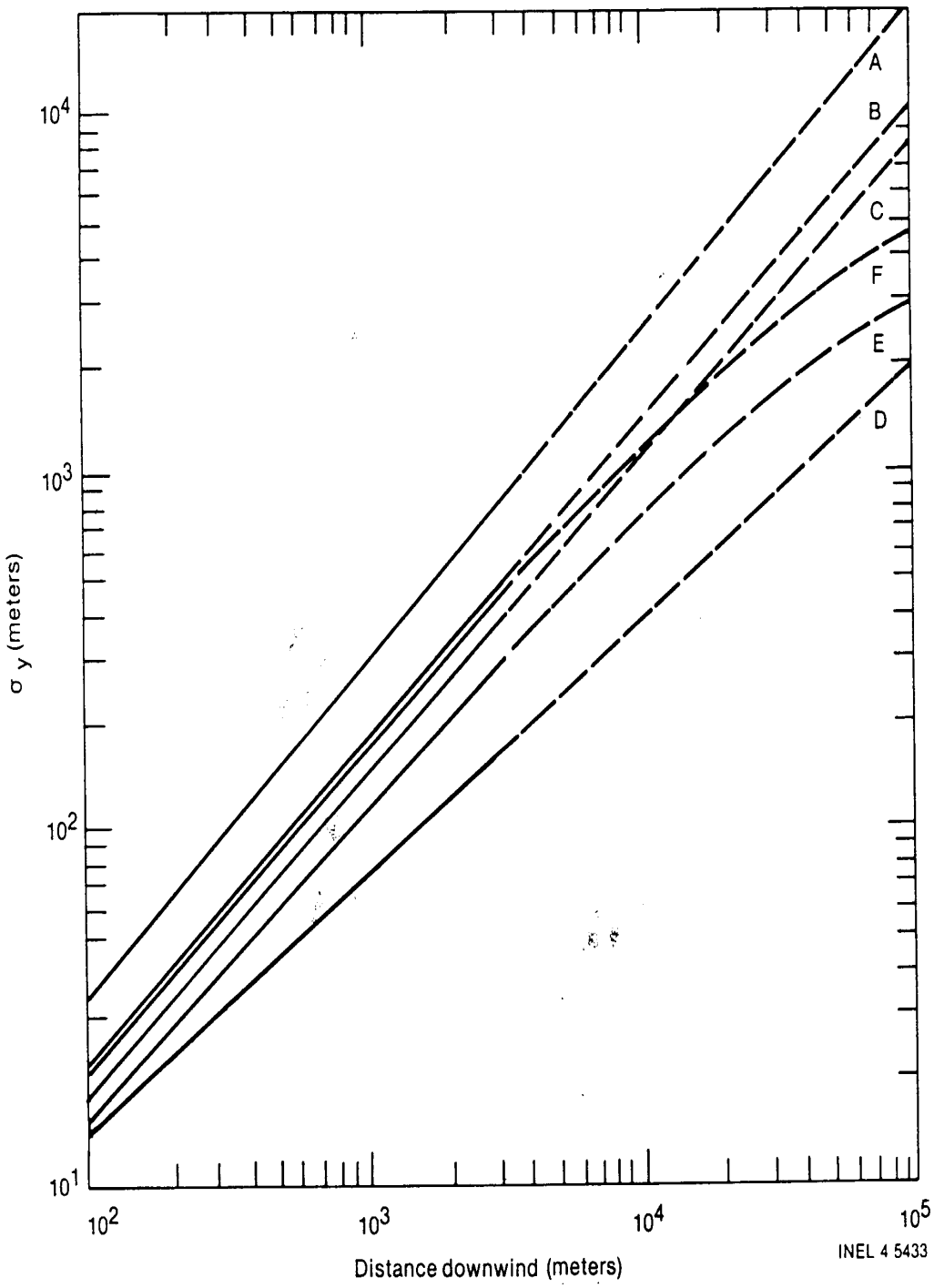

Figure 2.3-19. σ_y versus distance at INEL.

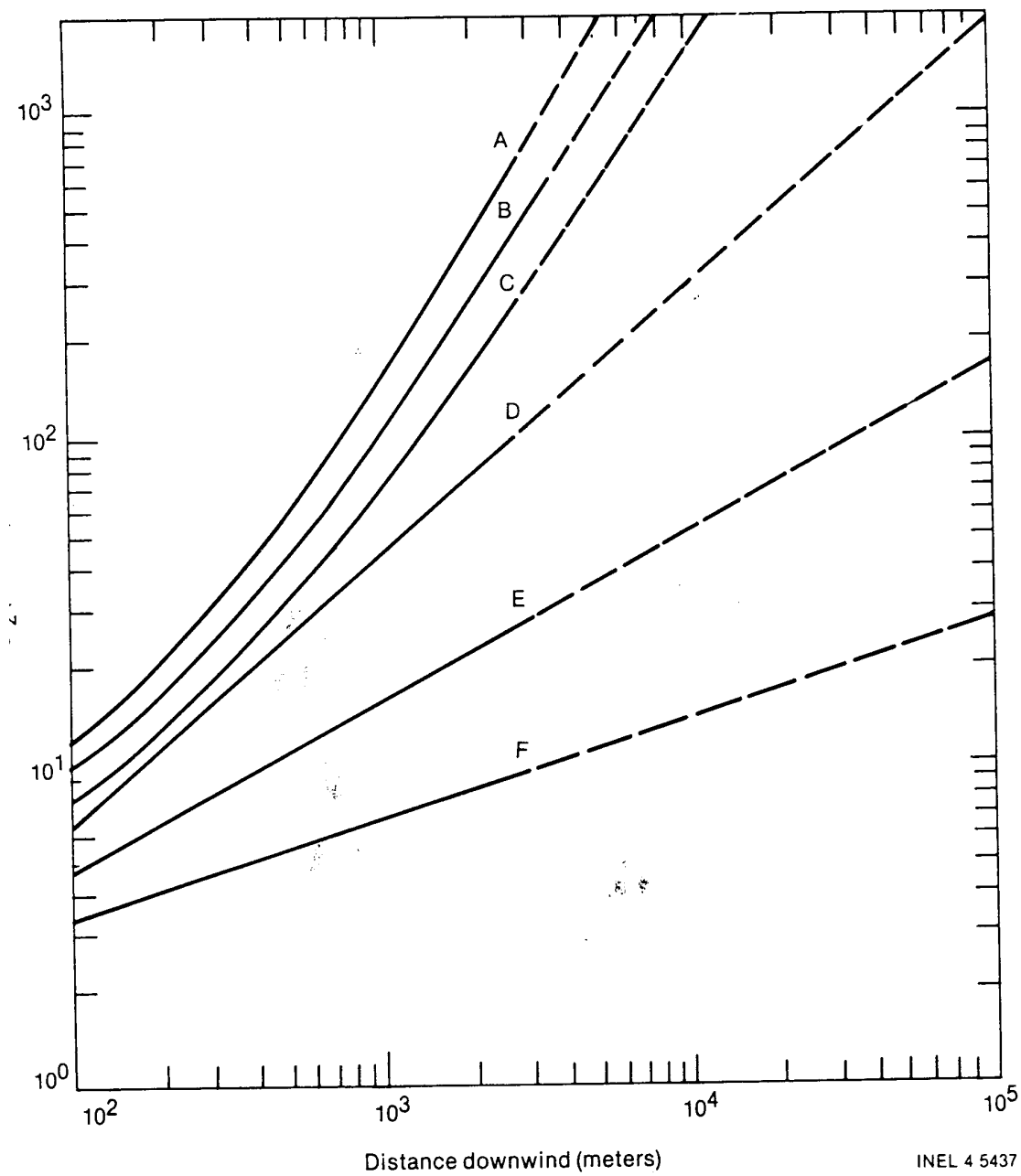

Figure 2.3-20. σ_y versus distance at INEL.

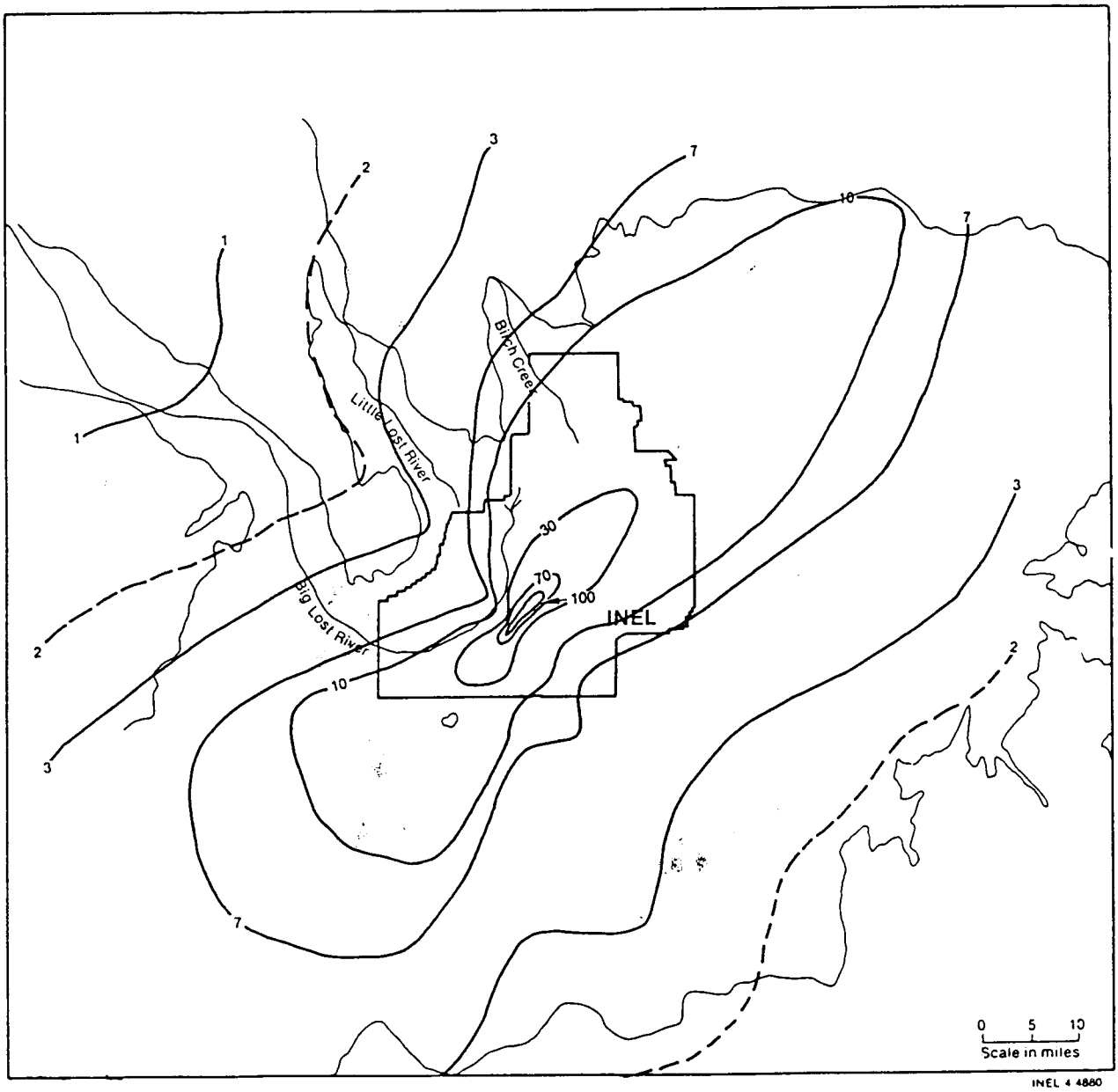

Figure 2.3-21. Annual normalized concentration ?/Q (s/m^3 x 10^{-9})
Source location: TMI-2 ISFSI site--50-mi 1982.

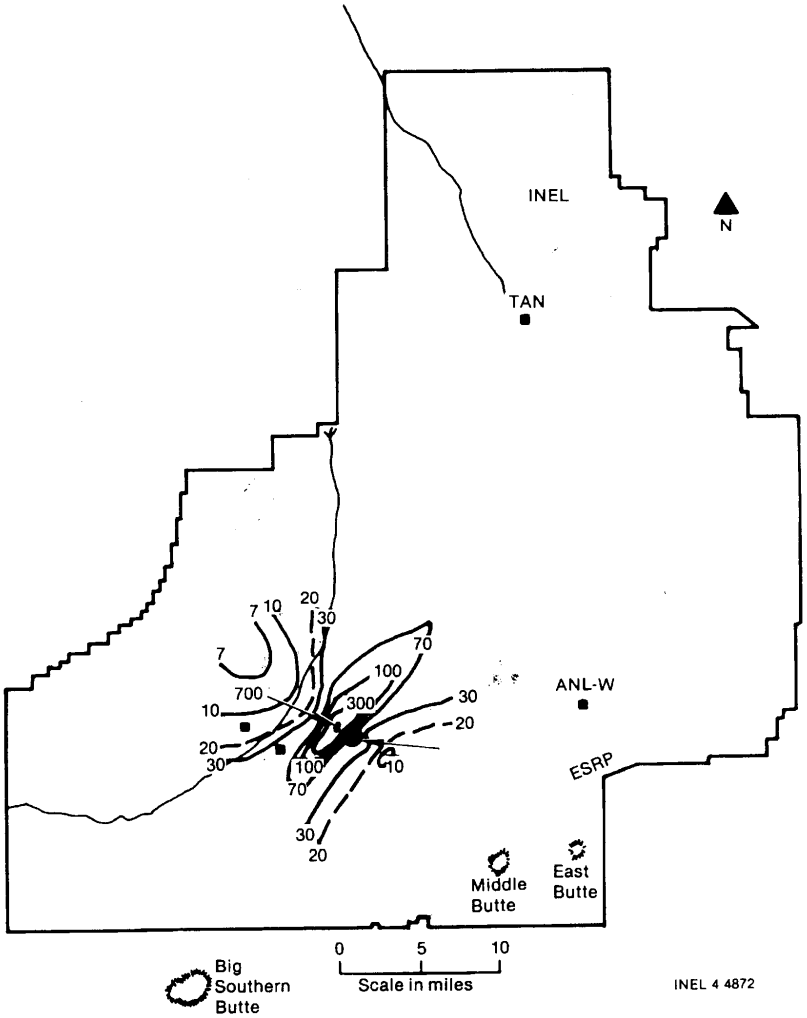

Figure 2.3-22. Annual normalized concentration ?/Q (s/m^3 x 10^{-9})
Source location TMI-2 ISFSI site -- 5-mi 1982.

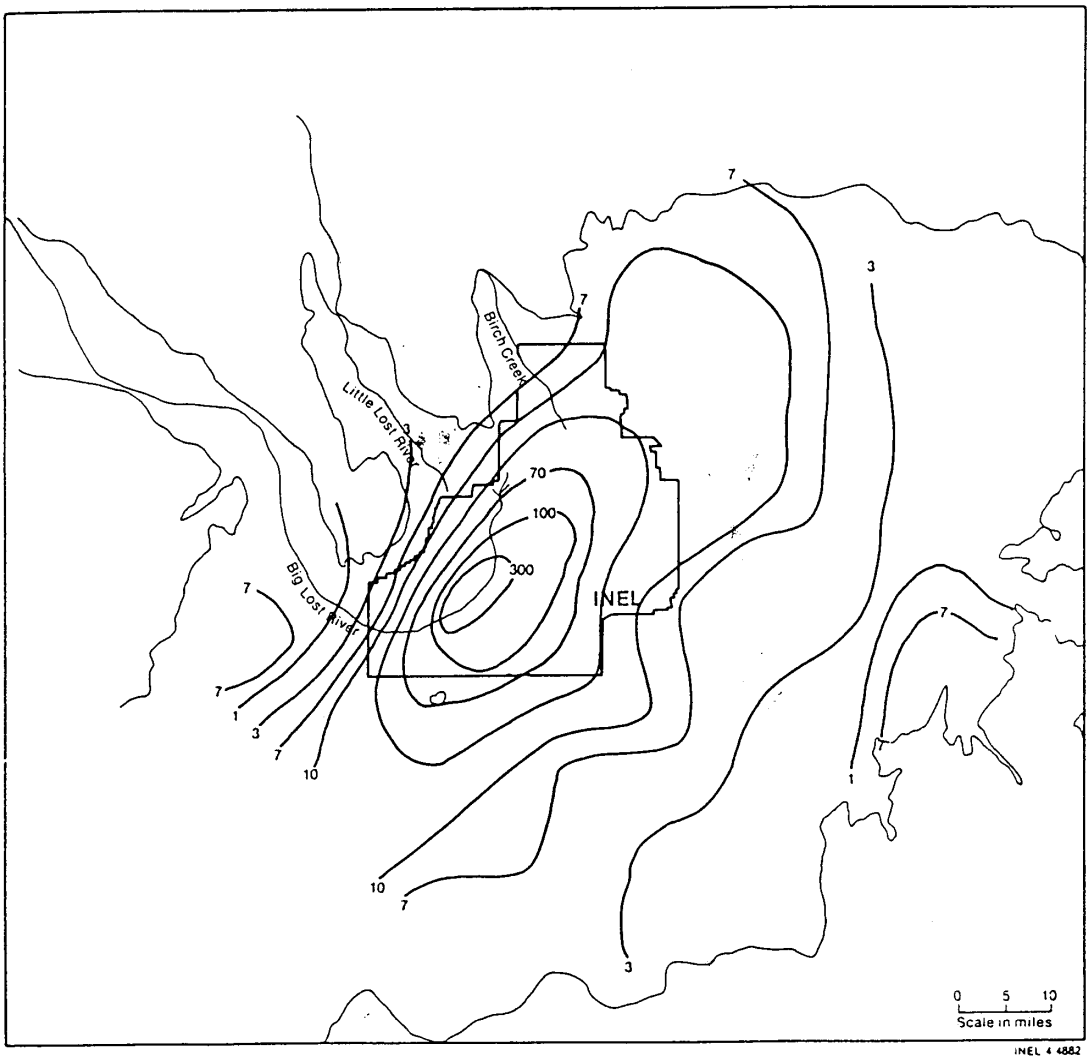

Figure 2.3-23. Annual normalized total integrated concentration ($h^2/m^3 \times 10^{-9}$)

Source location: ICPP 1980.

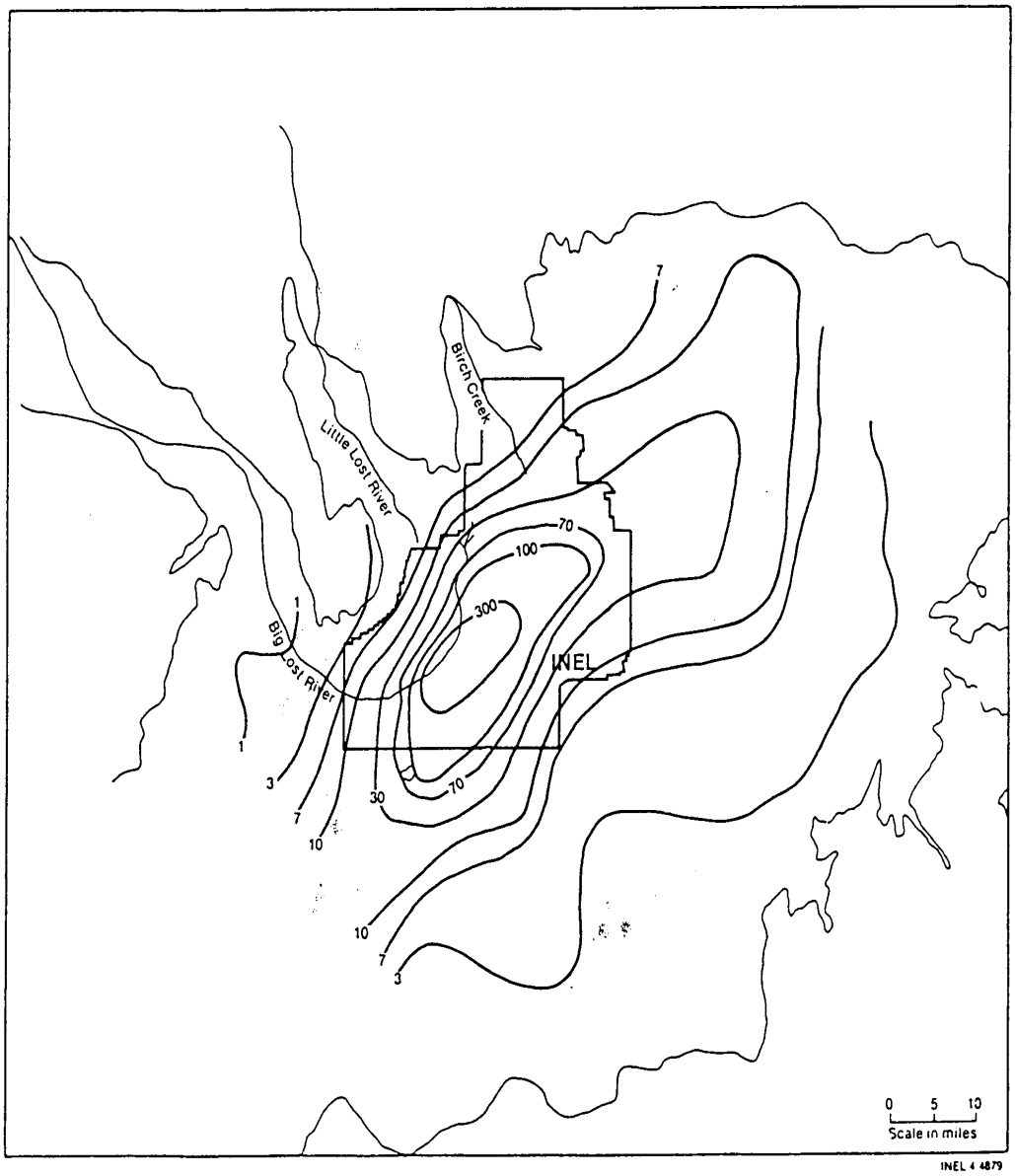

Figure 2.3-24. Annual normalized total integrated concentration ($h^2/m^3 \times 10^{-9}$)

Source location: ICPP 1981.

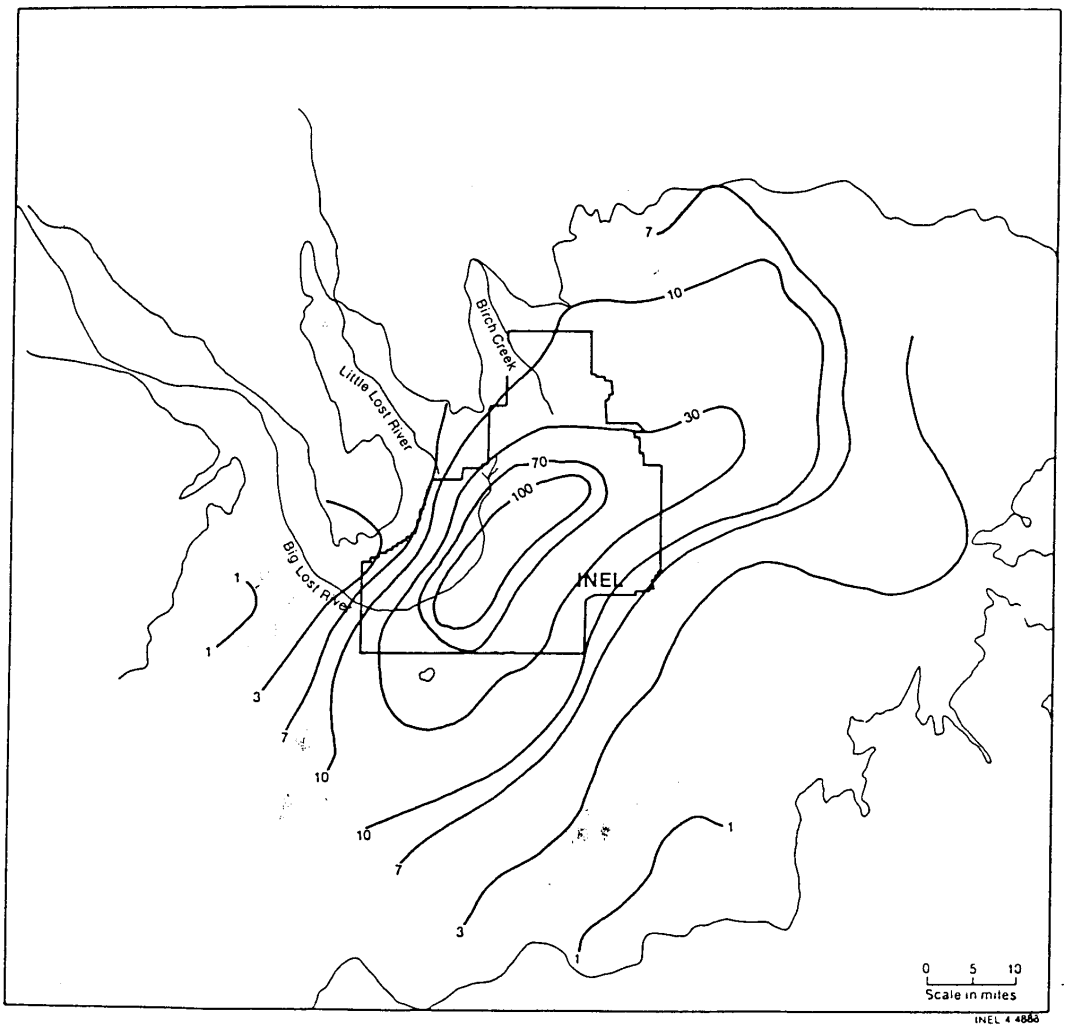

Figure 2.3-25. Annual normalized total integrated concentration ($h^2/m^3 \times 10^{-9}$)

Source location: ICPP 1982.

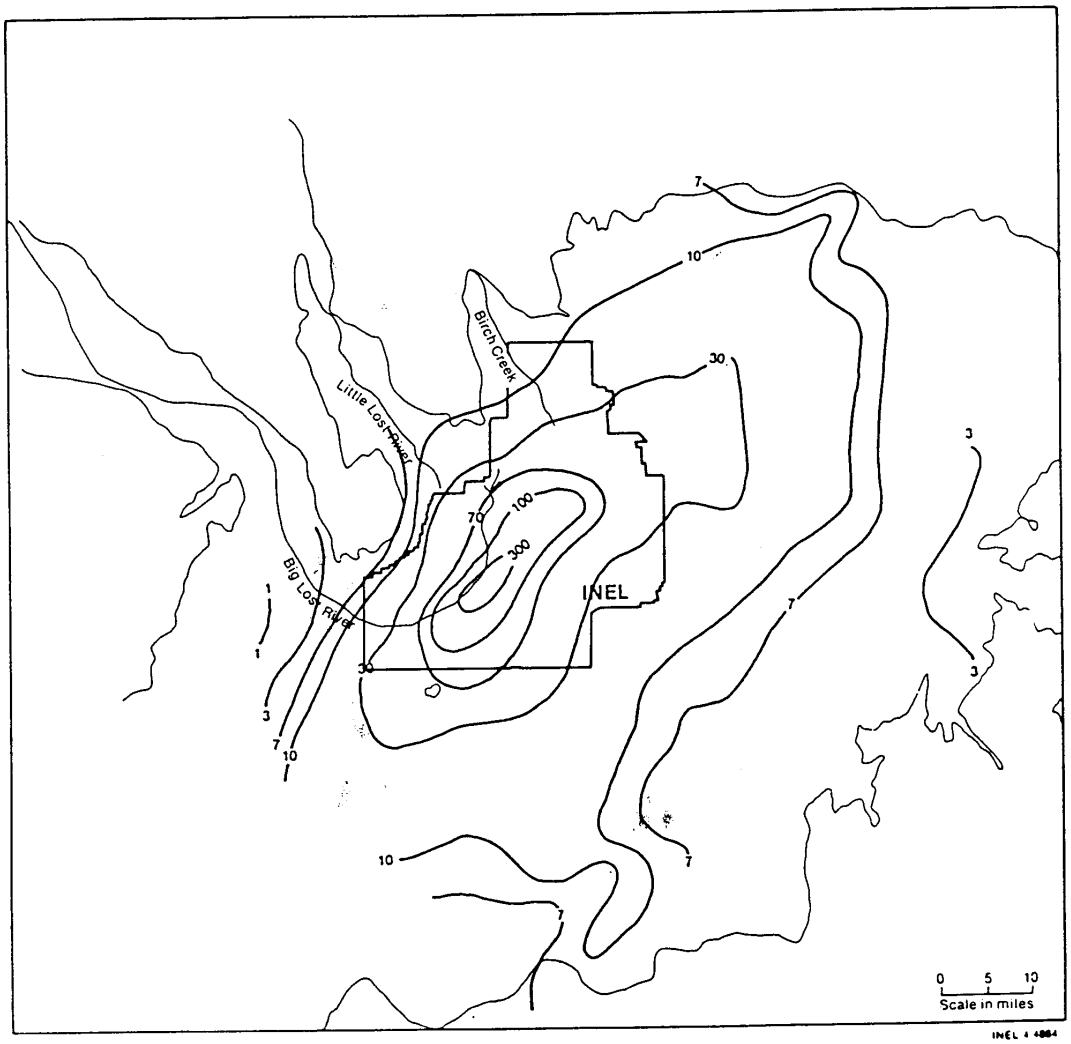

Figure 2.3-26. Normalized total integrated concentration ($h^2/m^3 \times 10^{-9}$)
Source location: ICPP 1974-1983.

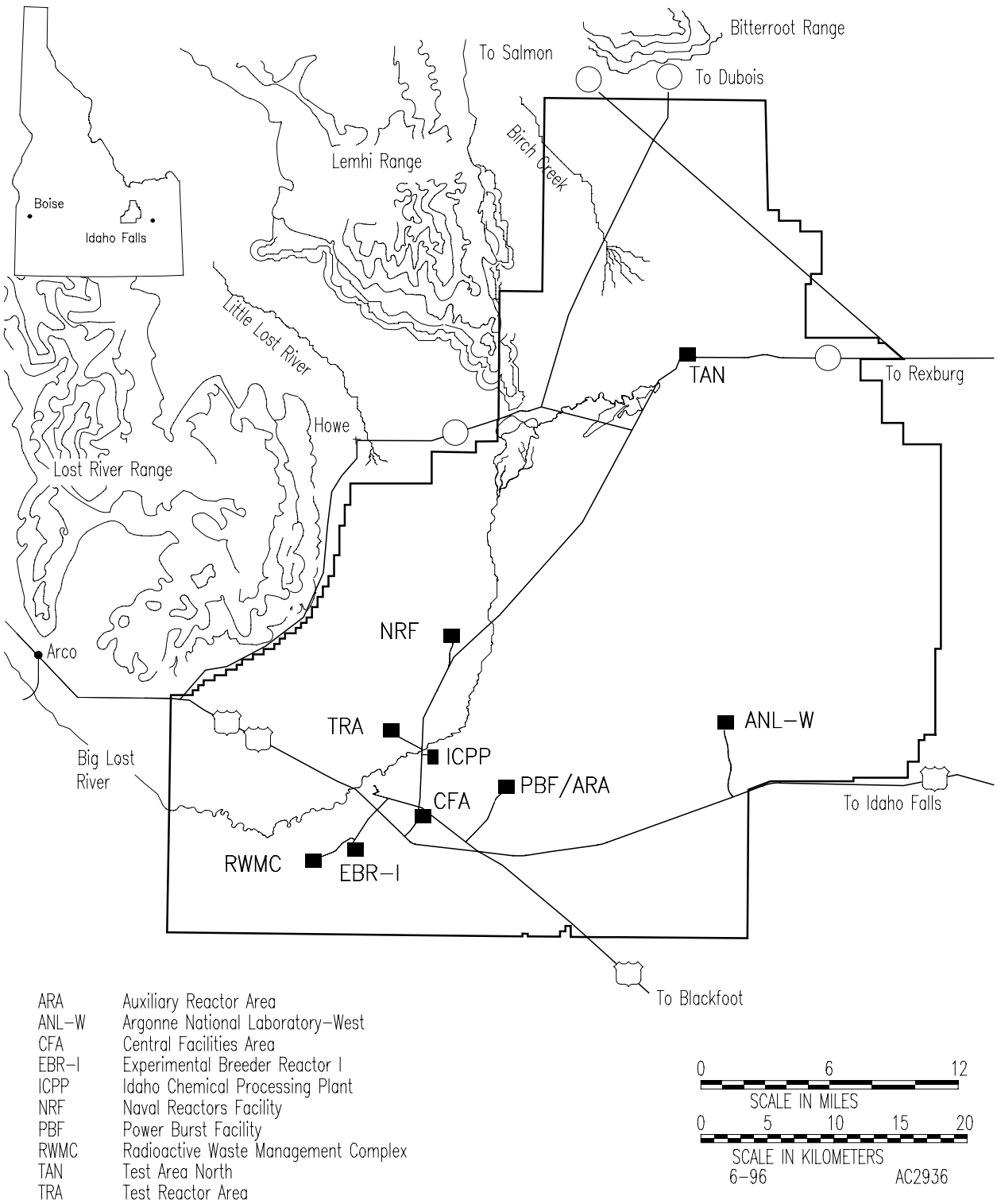

Figure 2.4-1. INEL site map with major drainages.

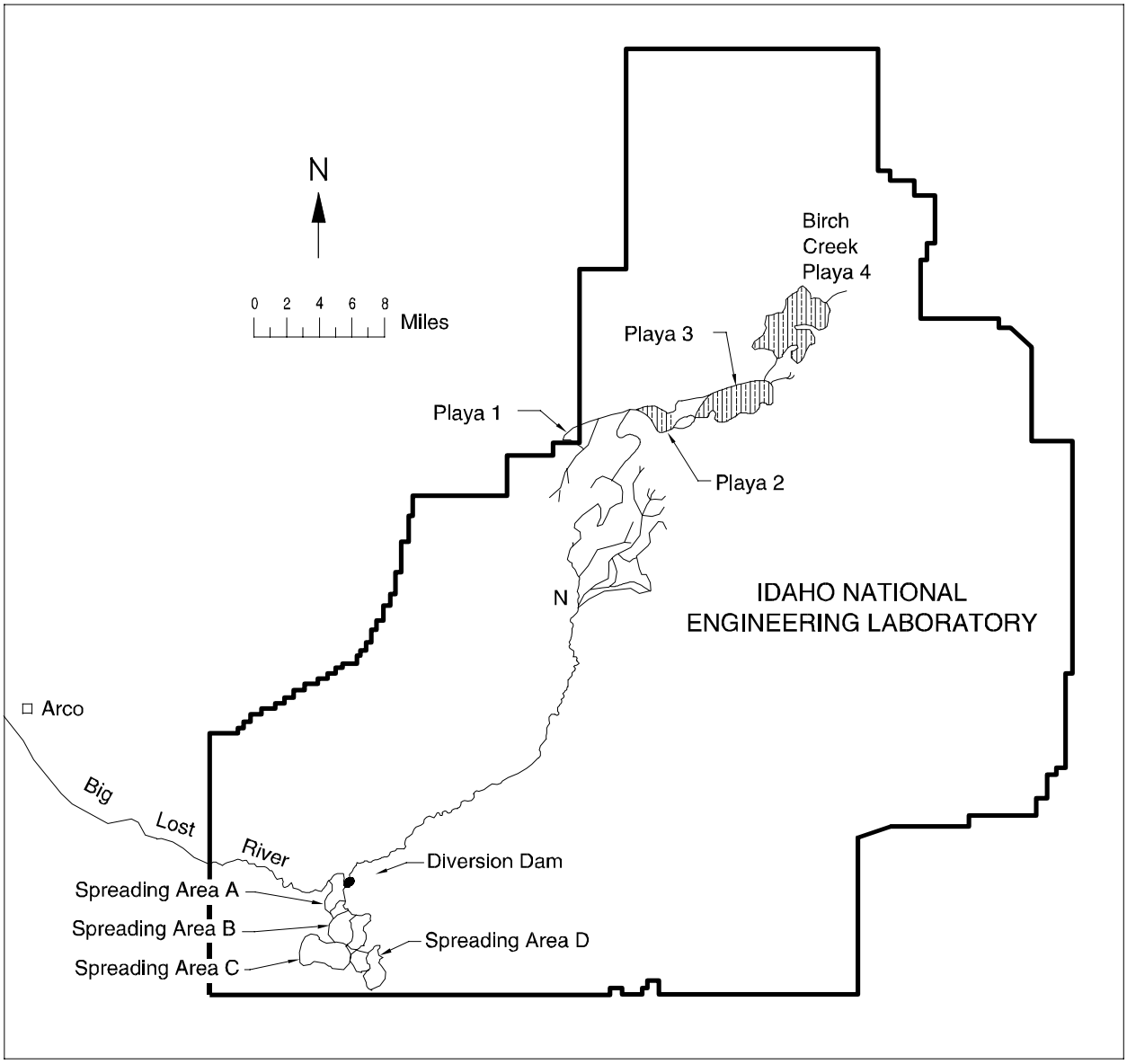

ICPP-A-16942X
(1-91)

Figure 2.4-2. Big Lost River System on the INEL (LITCO, 1995)

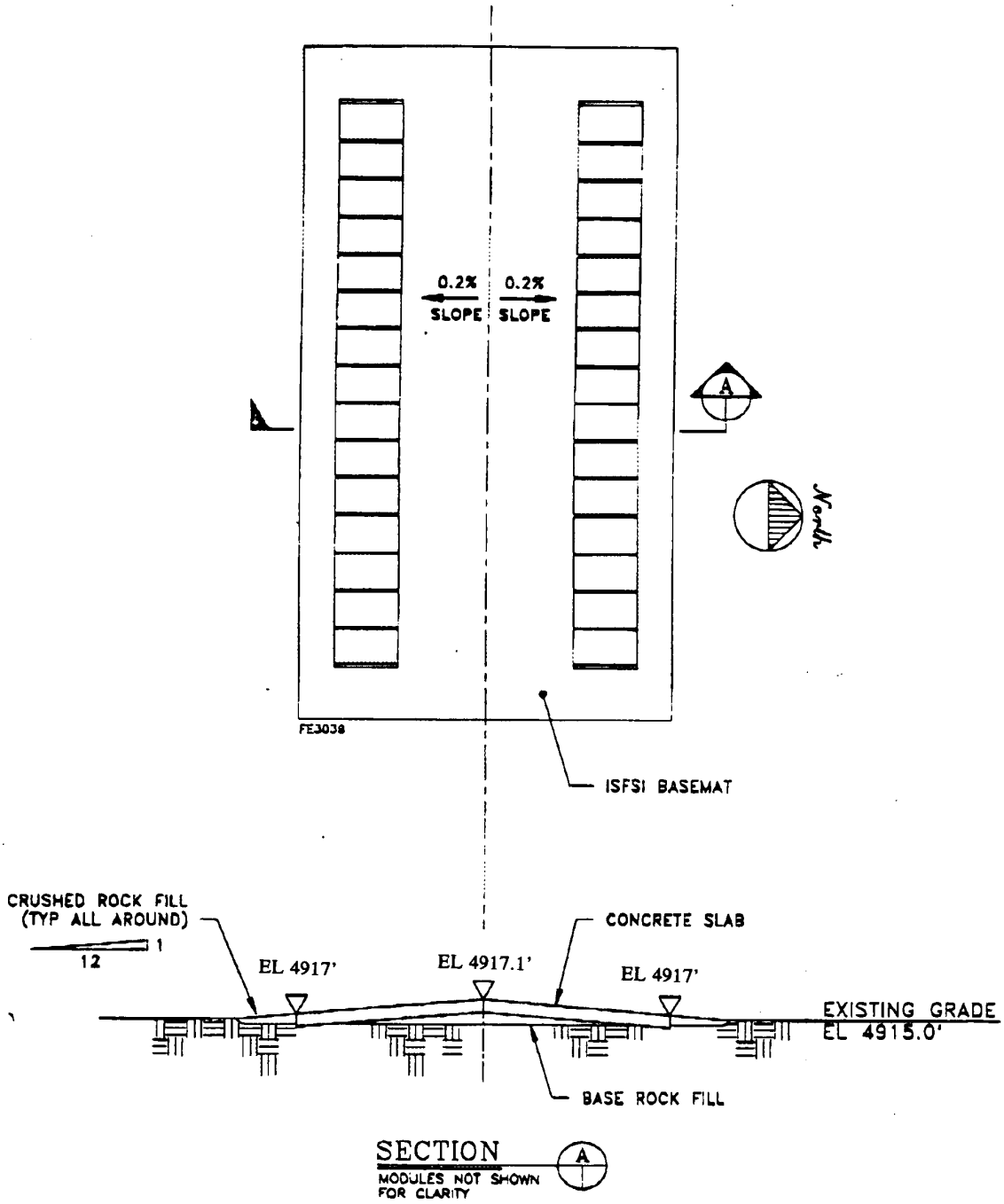

Figure 2.4-3. TMI-2 ISFSI Pad Cross Section.

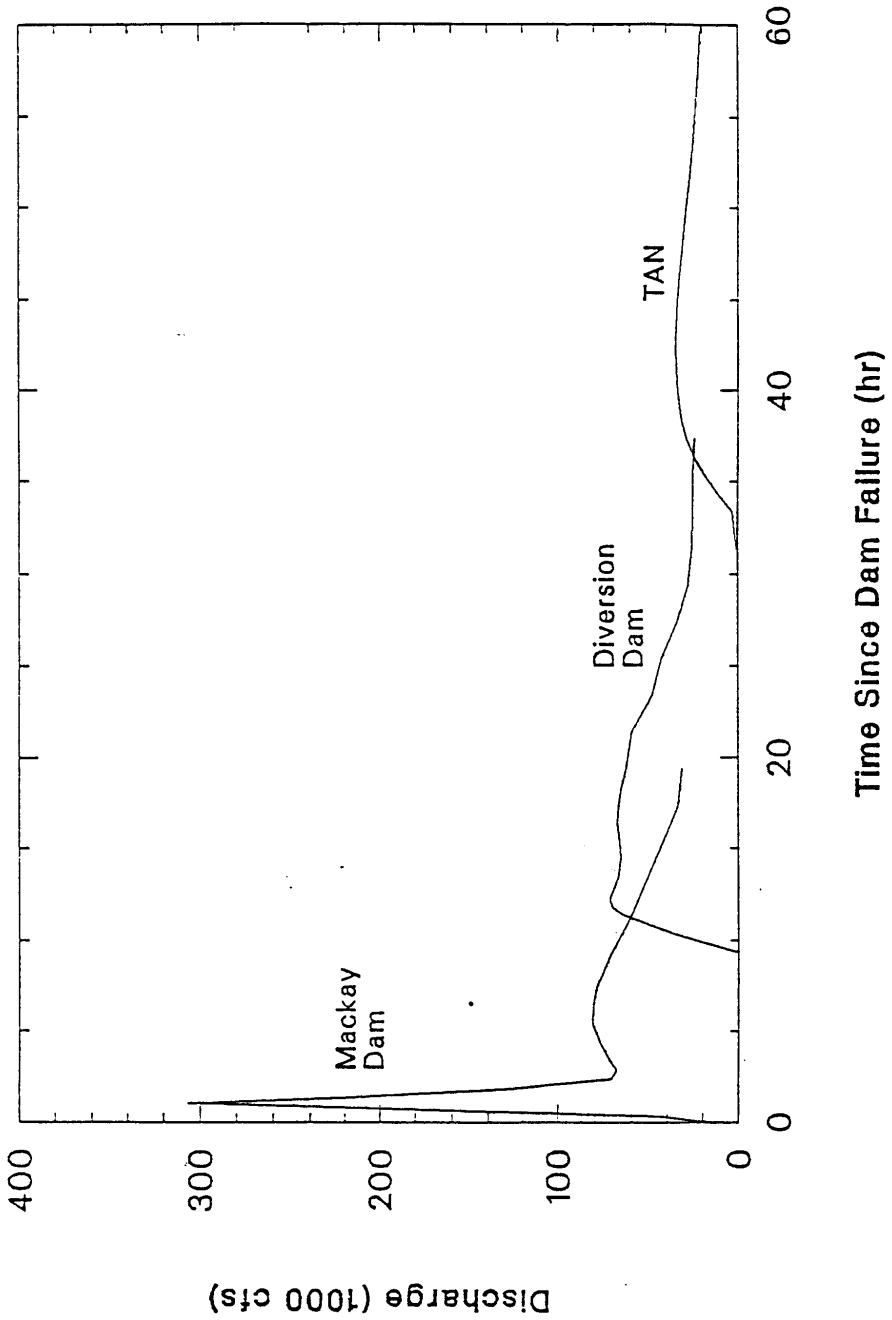

Figure 2.4-4. Hydrograph for the PMF-induced failure of the Mackay Dam (Koslow and Van Haaften, 1986)

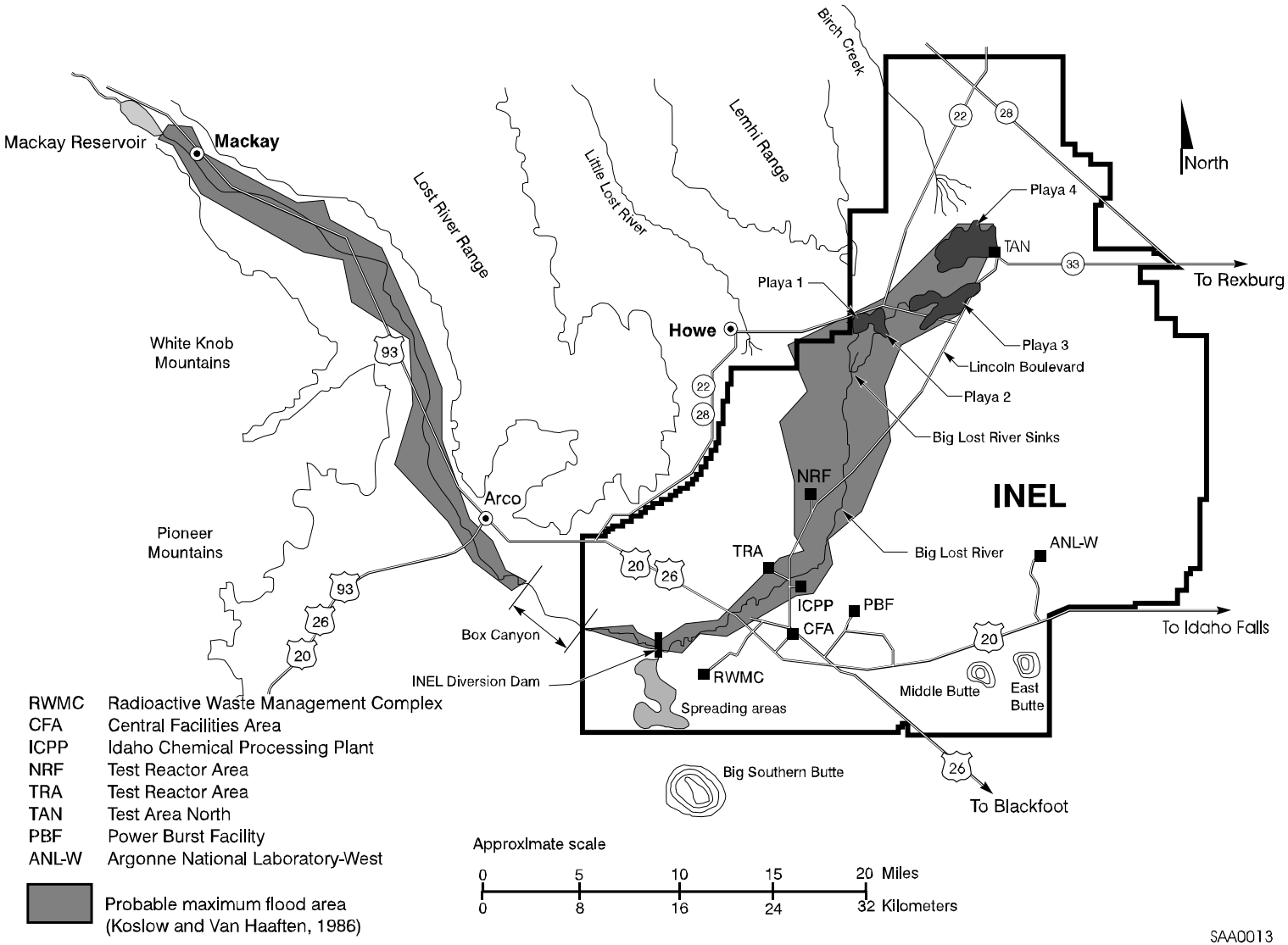

Figure 2.4-5. INEL facilities with the predicted inundation area for the probable maximum flood-induced overtopping of the Mackay Dam (Bennett 1990).

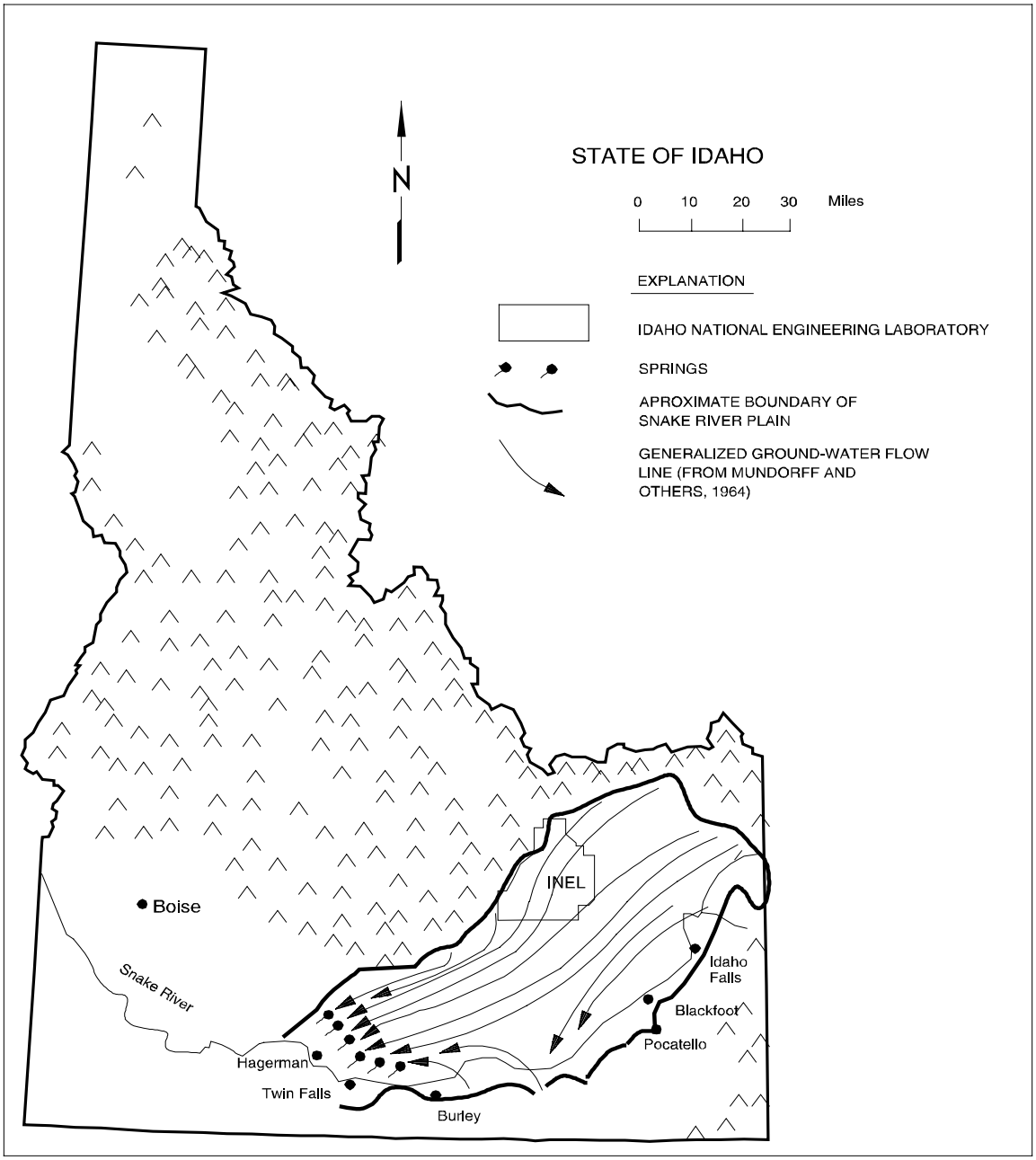

ICPP-A-4584X
(10-94)

Figure 2.5-1. Relief Map of Idaho With Groundwater Flow Lines.

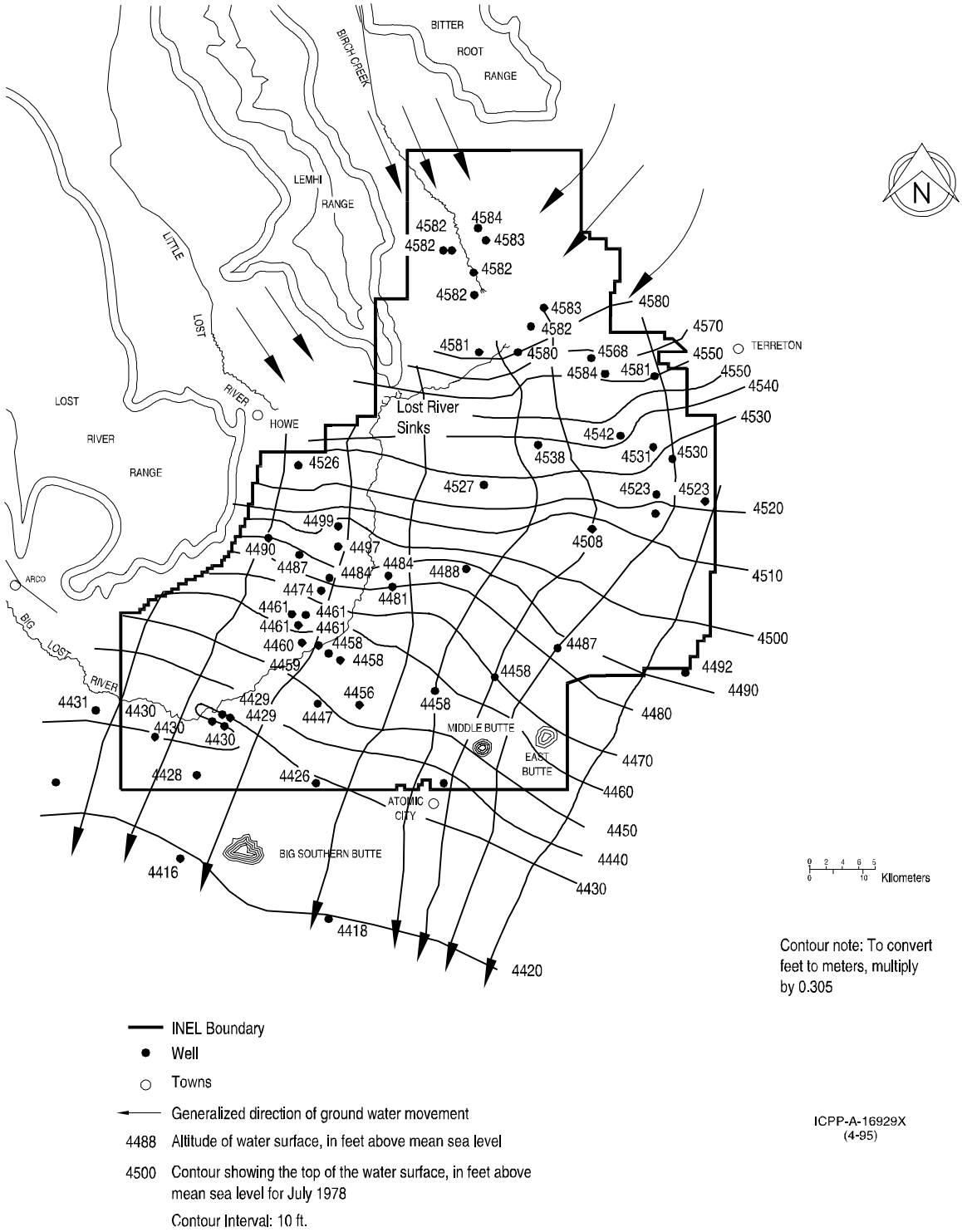

Figure 2.5-2. Groundwater Contours and Directions - INEL.

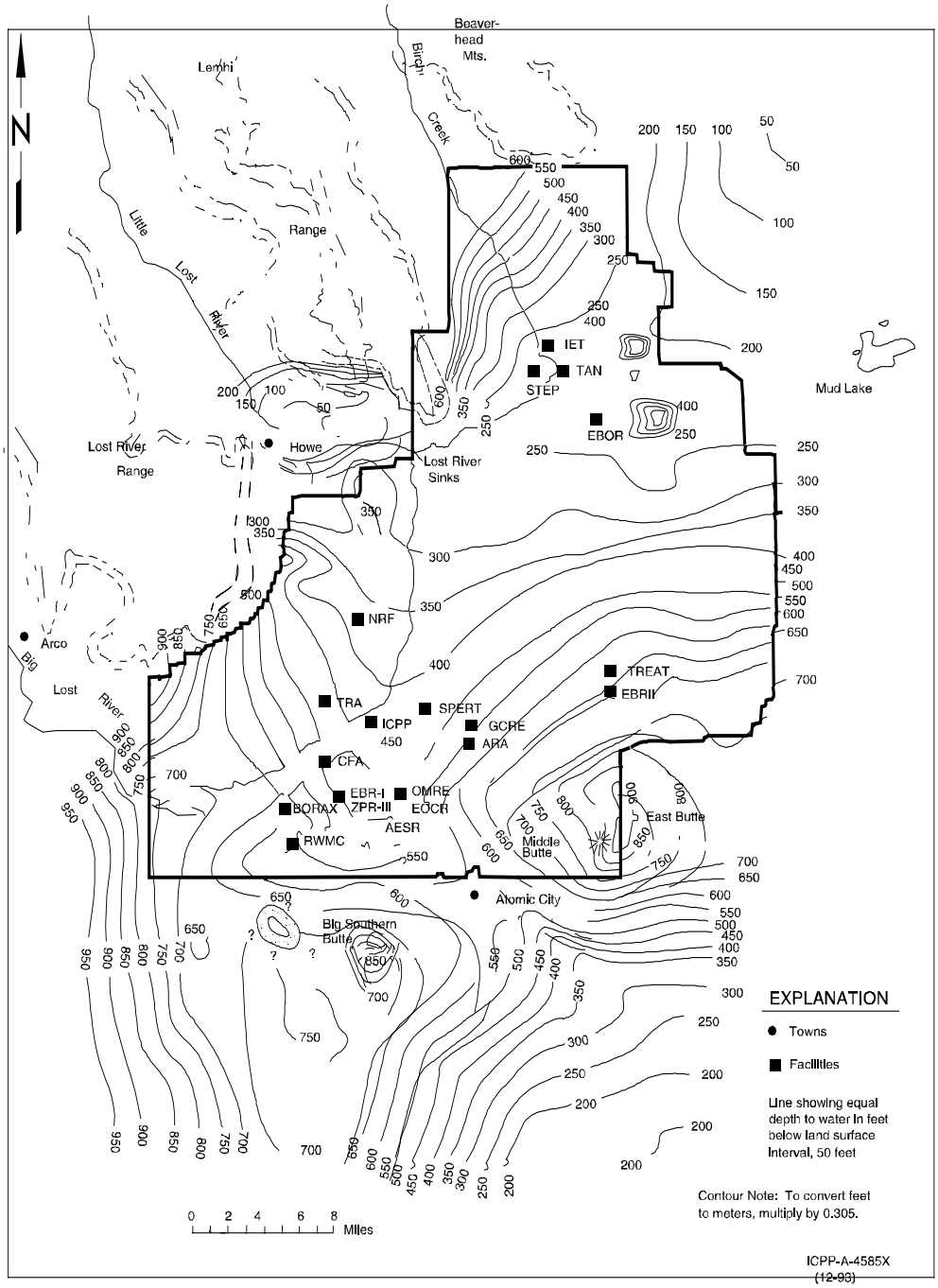

Figure 2.5-3. Depth to Water Table, INEL.

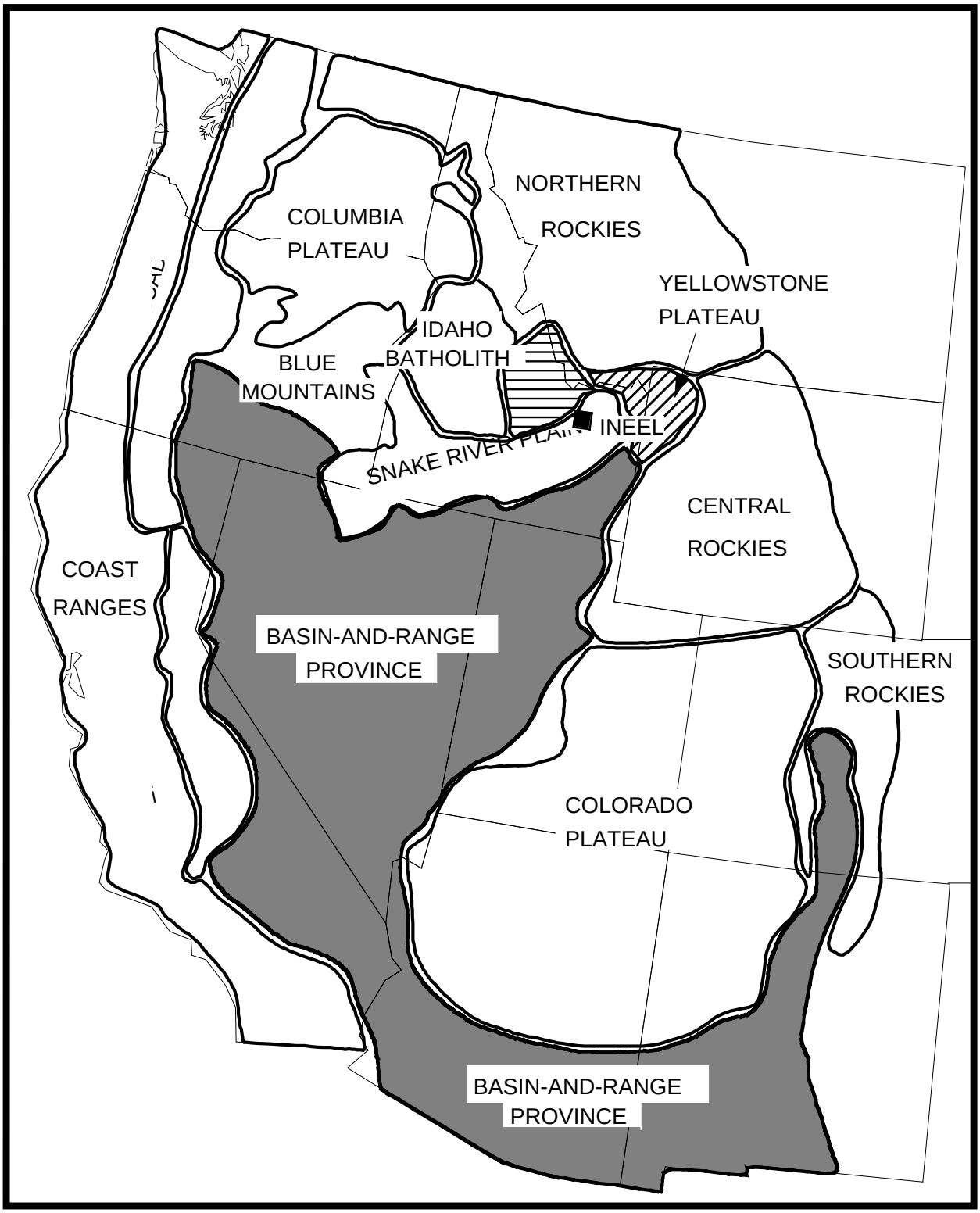

Figure 2.6-1. Physiographic Province Map of the Western United States Showing the Location of the ESRP and the INEL.

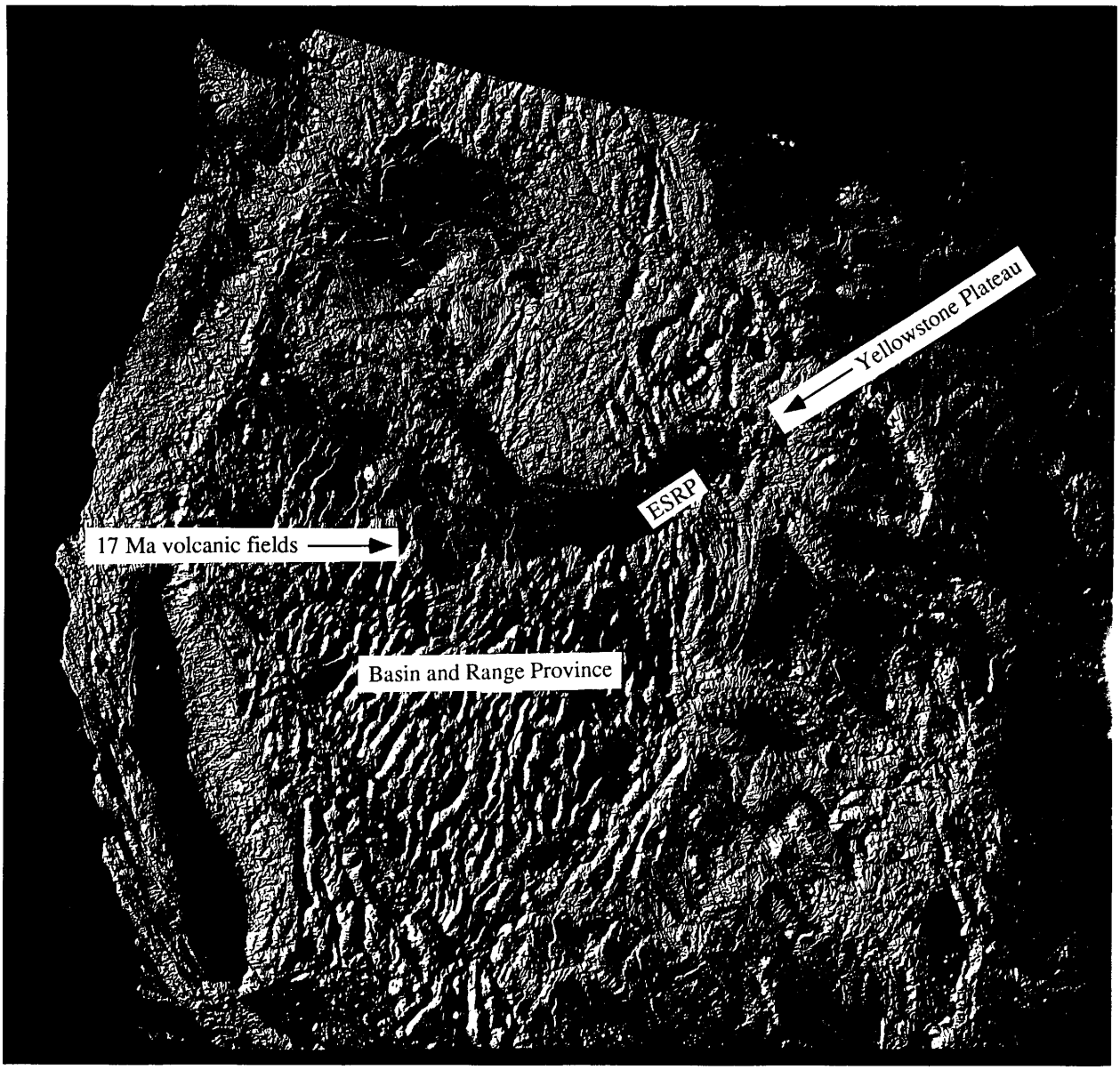

Figure 2.6-2. Shade relief topographical map of the Western United States showing the Eastern Snake River Plain (ESRP), the basin and range providence and the track of the Yellowstone hot spot from the 17MA volcanic fields of north central Nevada to the Yellowstone Plateau.

Geologic Age	Formation and Brief Description	Thickness (m)
Quaternary	Surficial deposits of playas (silty sand to clayey silt), floodplains (sandy gravel to silty sand), alluvial fans (sandy gravels to silty sands), and thin eolian blankets (loess and fine sand).	Playas: <30m Floodplains: ~20m on INEEL Eolian: 1-10m
	Rhyolitic lavas, breccias, and obsidians of Big Southern, East, and Cedar Buttes, and an unnamed butte along the axis of the ESRP. 0.3-1.2 Myr.	2500 at Big Southern Butte
Quaternary and Tertiary	**Snake River Group.** Interbedded clastic sediments and basaltic lava flows of the Snake River Plain. Sediments are unlithified to poorly lithified alluvial (gravels, sands, minor silt), lacustrine (silty clays to sandy silts), and eolian (silts and sands) deposits. Basaltic lavas are black to dark gray pahoehoe and minor a'a flows with near-vent scoria, cinder, and ash deposits. Age range - 2 kyr to ~4.5 Myr. Rocks and sediment older than about 1.2 Myr are present only in the subsurface. Comprises almost all of the rocks within the ESRP.	700-1500
Tertiary	Various basaltic lava flows of late-Tertiary age, rhyolitic ash flow tuffs of the **Heise volcanic field** (4.3-7 Myr), older rhyolitic ash flow tuffs (7-12 Myr), and Eocene **Challis volcanics**. All outcrop outside the ESRP in the mountains northwest of the INEEL. Heise and older tuffs occur in deep drill holes within the ESRP.	Total thickness unknown
Triassic	**Dinwoody Fm.** Siltstone and micaceous shale.	>55
Permian	**Phosphoria Fm.** Limestone, chert, phosphatic siltstone, phosphorite, and dolostone.	60
Permian to Mississippian	**Snaky Canyon Fm.** Interbedded limestone, dolostone, and minor sandstone.	1200
Pennsylvanian-Mississippian	**Bluebird Mt. Fm.** Sandstone w/interbedded limestone and minor dolostone. Straddles period boundary.	100
Mississippian	From younger to older, consists of **Bluebird Mtn., Arco Hills, Railroad Canyon, Surrett Canyon, South Creek, Scott Peak, and Middle Canyon Fms.** Mostly fossiliferous limestones w/interbedded sandstones, siltstones, and shales.	1000-1500
Mississippian - Devonian	**McGowan Creek and Three Forks Fms.** Gray argillites, siltstones, and limestones.	64-163
Devonian	**Jefferson Fm.** Sandy to silty gray dolostone and limestone.	60-300
Ordovician	**Fish Haven Dolostone.** Gray, massive dolostone.	18-300
	Kinnikinic Quartzite. Vitreous orthoquartzite.	100-230
	Summerhouse Fm. Quartzite w/calcareous sandstone and siltstone.	0-60
Cambrian	**Tyler Peak Fm.** Sandstone, shale, and quartzite.	265
Precambrian	**Swager Fm, Lemhi Group, and Wilbert Fm.** Arkosic, conglomeratic sandstones and quartzites.	320-400

Notes: ESRP = eastern Snake River Plain. Double lines = unconformities. Precambrian to Triassic units outcrop only in the mountains north and south of the ESRP.

Figure 2.6-3. Stratigraphic Section of the Precambrian, Paleozoic, and Mesozoic Rocks Exposed in the Ranges North and South of the ESRP.

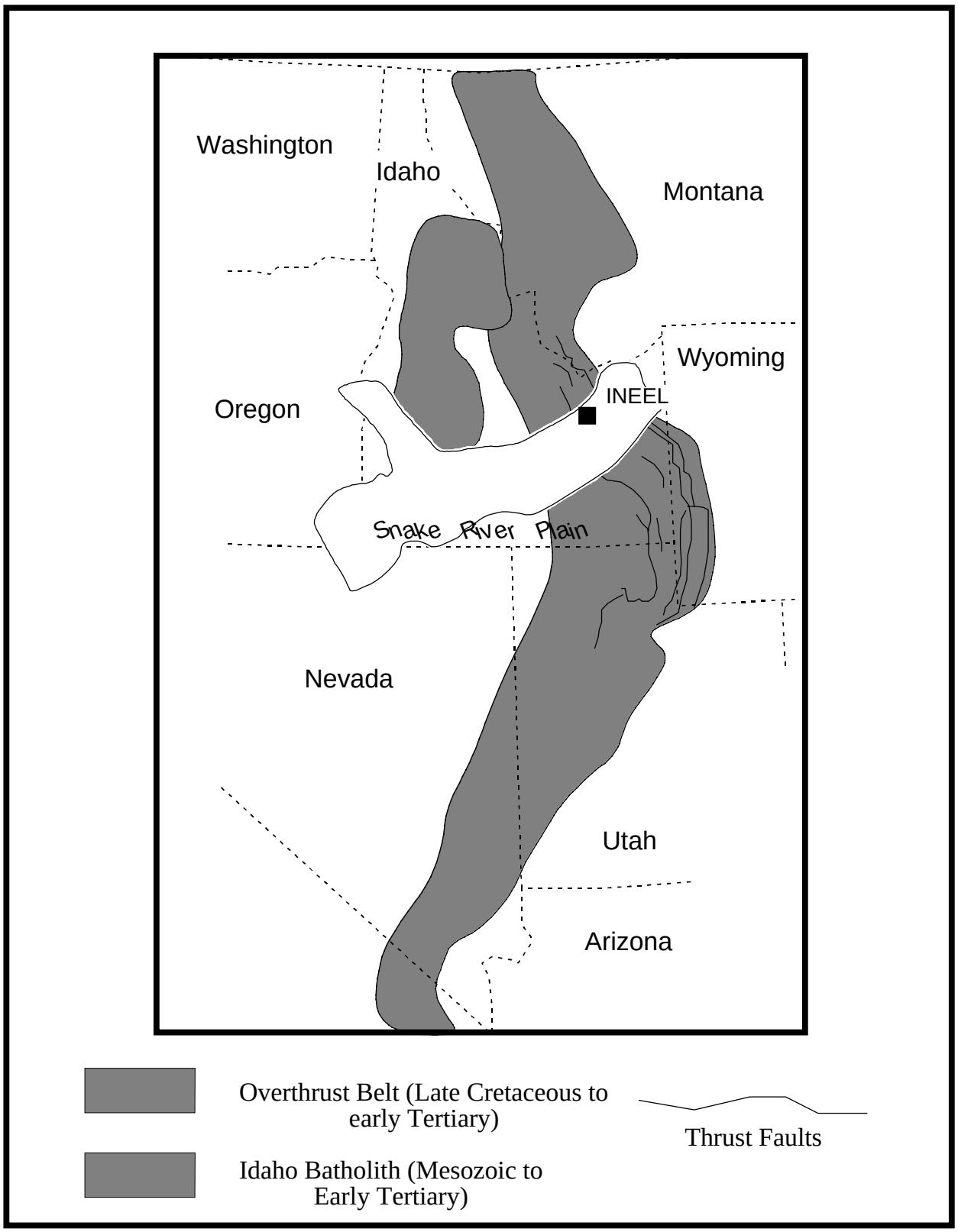

Figure 2.6-4. Map of the Overthrust Belt.

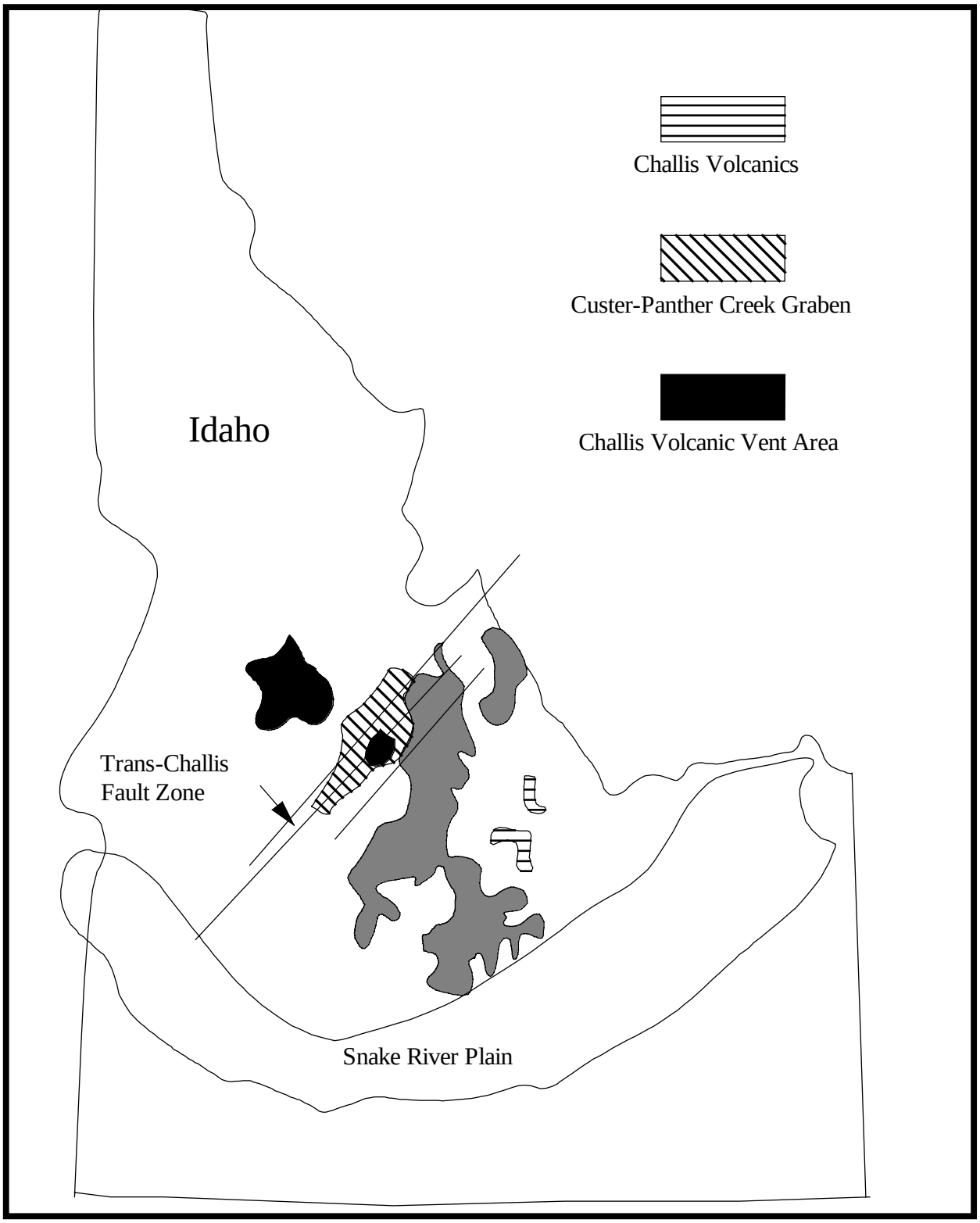

Figure 2.6-5. Map Showing Trans-Challis Fault Zone and Challis Volcanic Field.

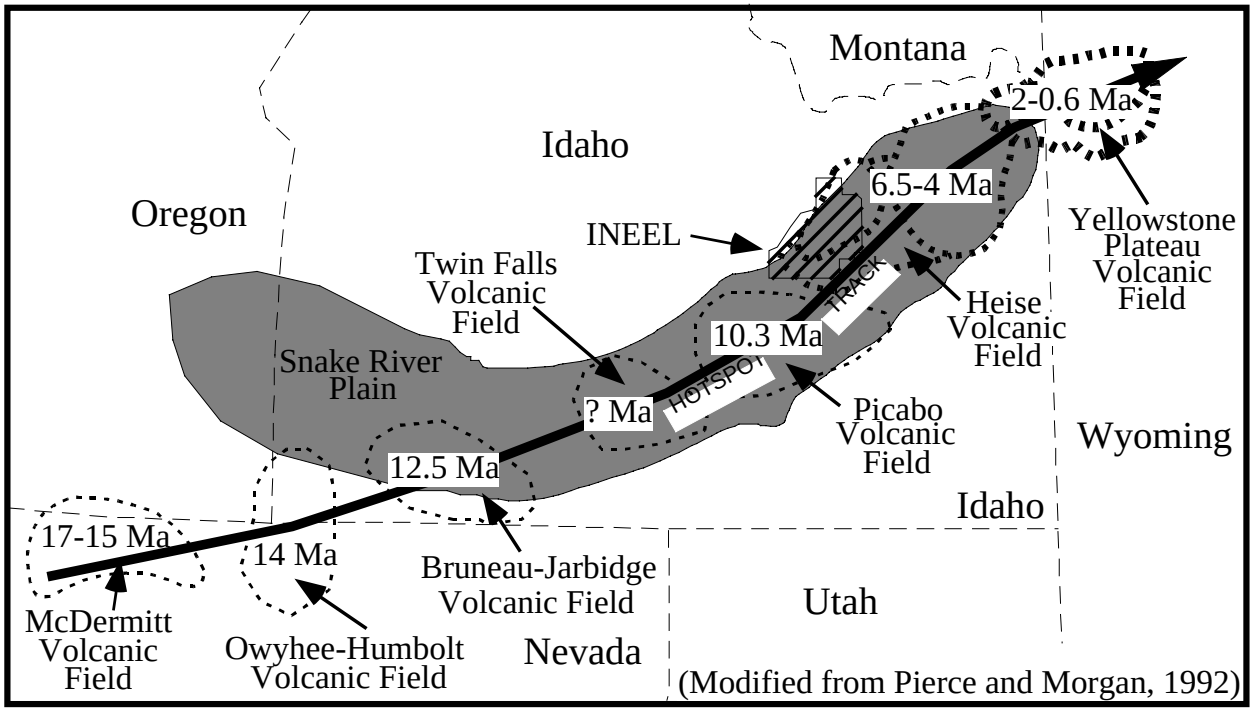

Figure 2.6-6. Calderas in the Track of the Yellowstone Hotspot (modified from Pierce and Morgan, 1992).

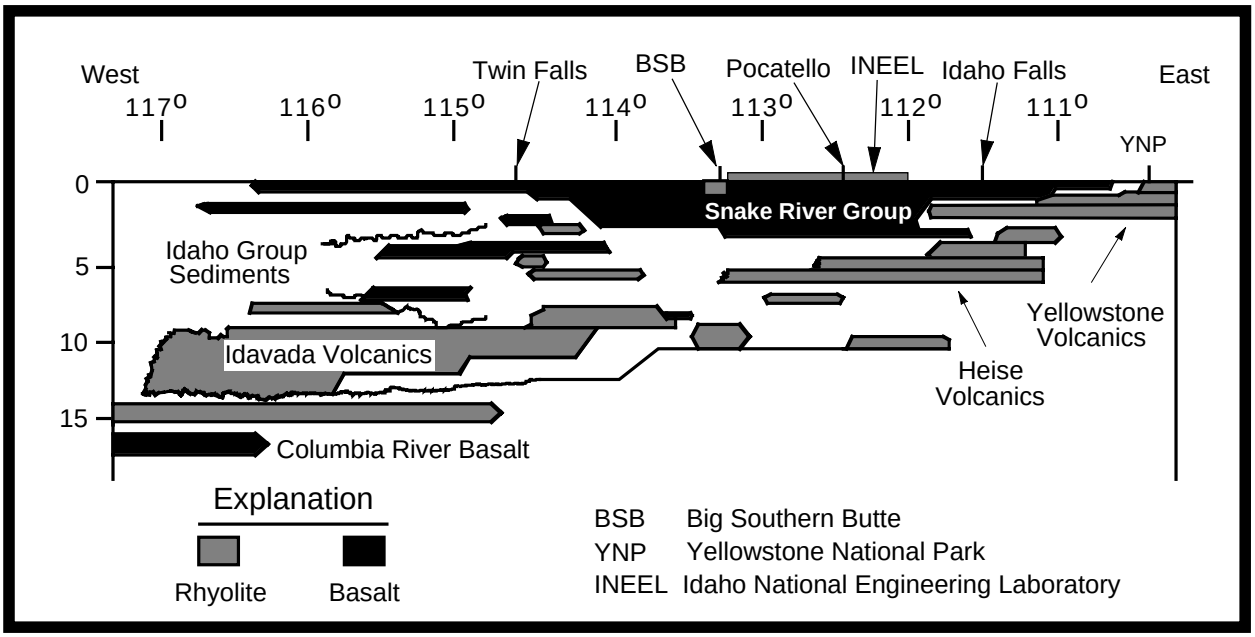

Figure 2.6-7. Armstrong Diagram

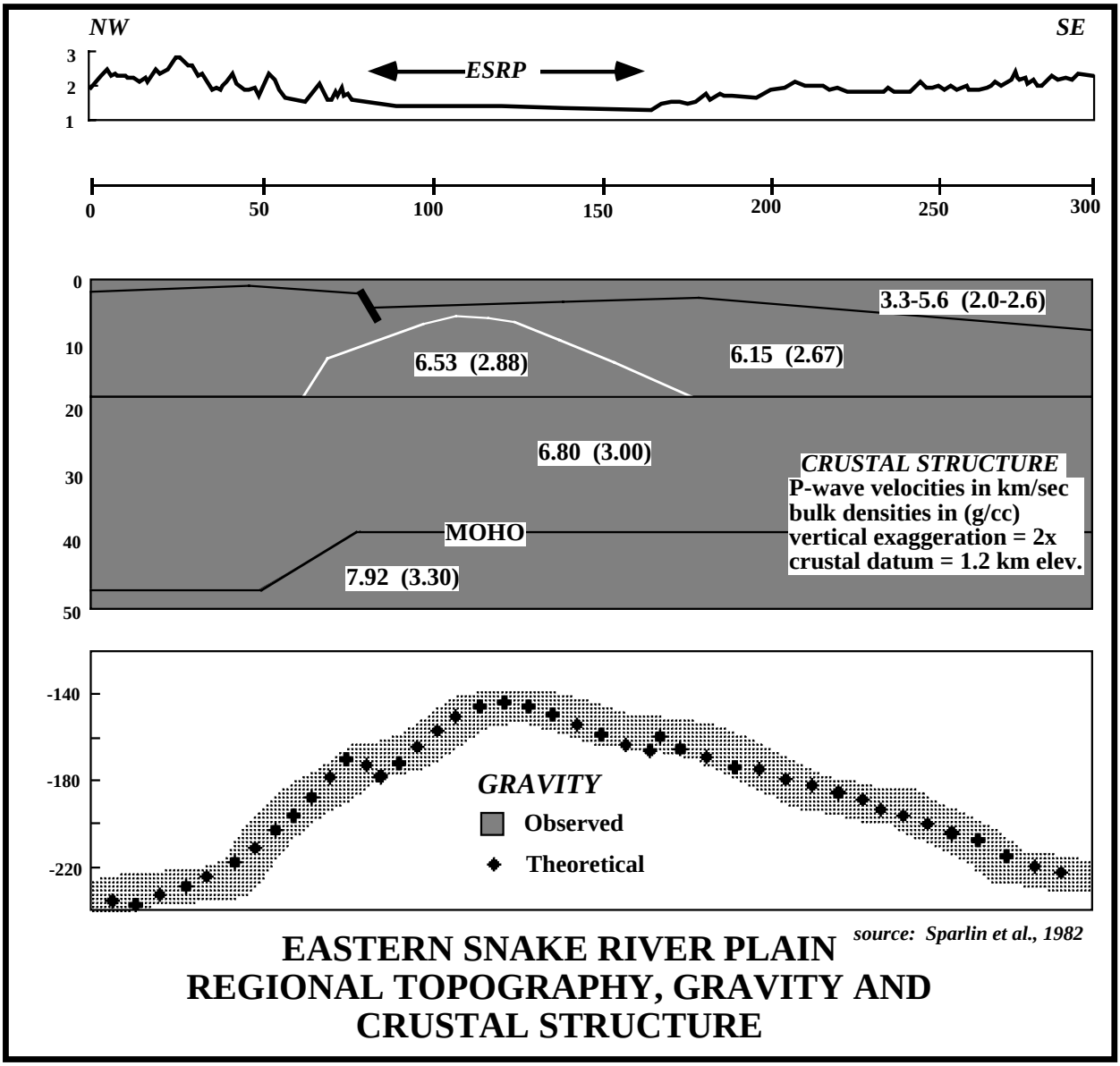

Figure 2.6-8. Topographic Profile, Crustal Structure, and Gravity Profile of the ESRP (modified from Sparlin et al., 1982).

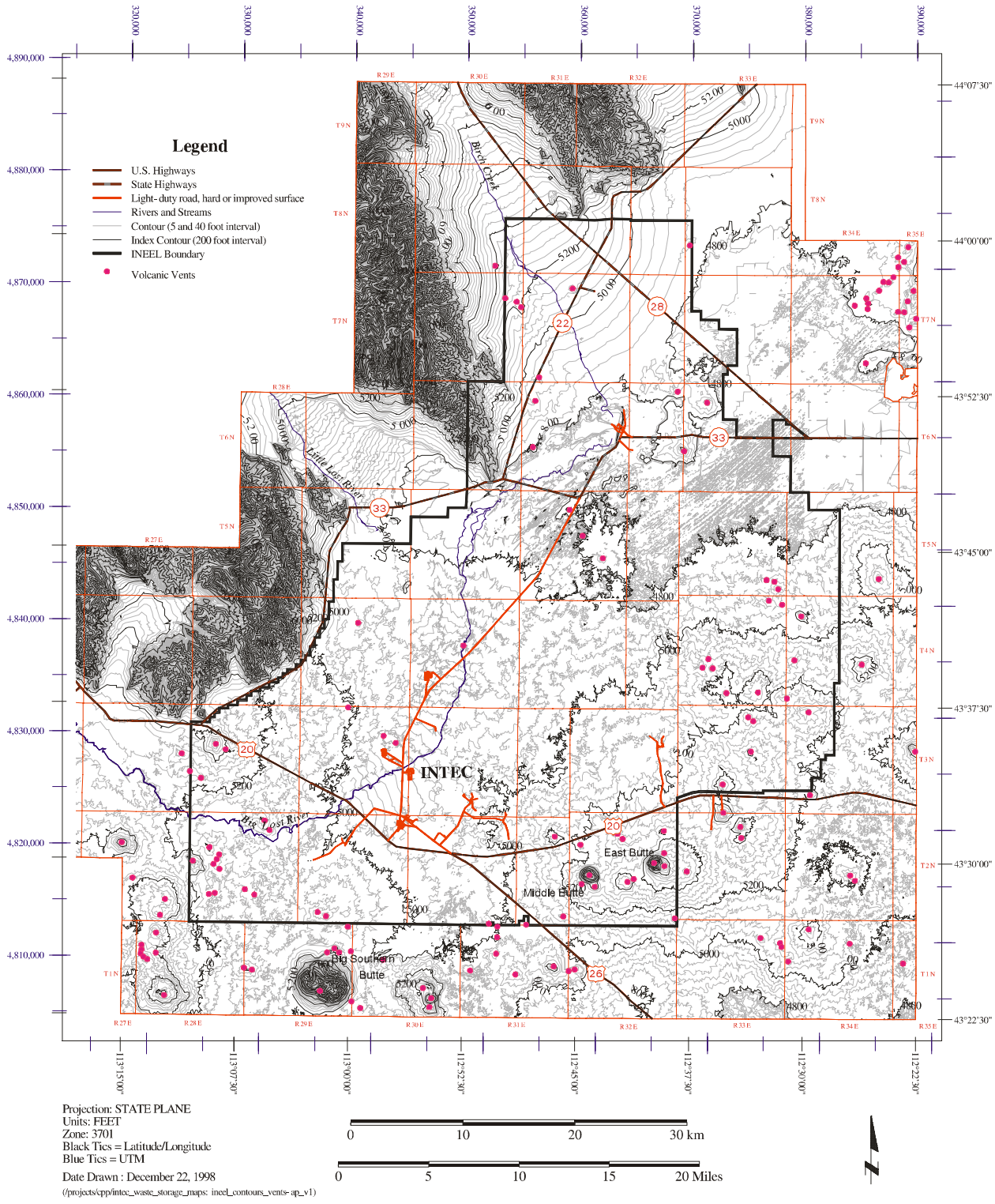

Figure 2.6-9. Topographic Map of the INEEL Area With Volcanic Vents.

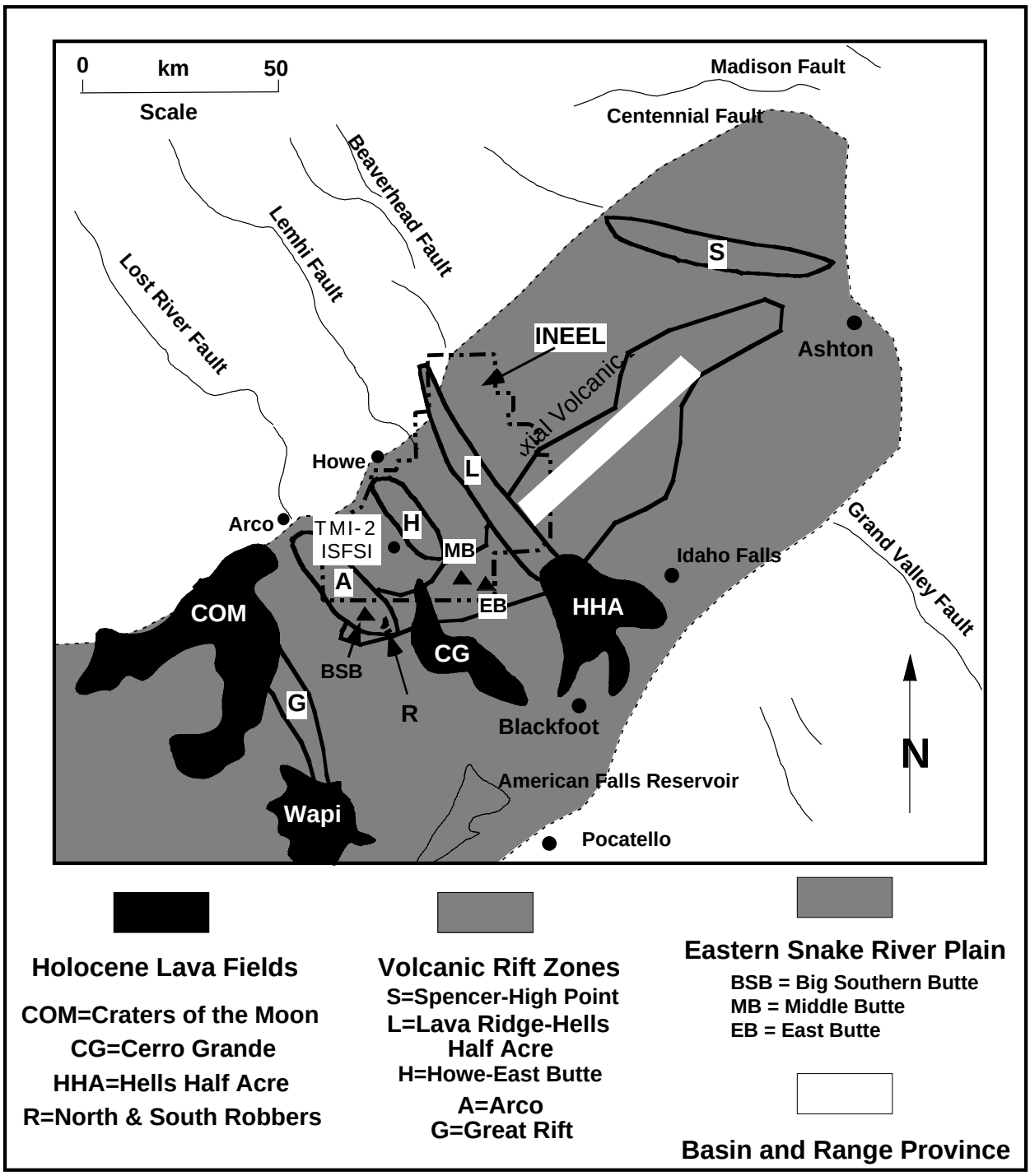

Figure 2.6-10. Map of the ESRP Showing Locations of Volcanic Zones, Holocene Volcanic Fields, the INEL, and the Location of the ISFSI Site.

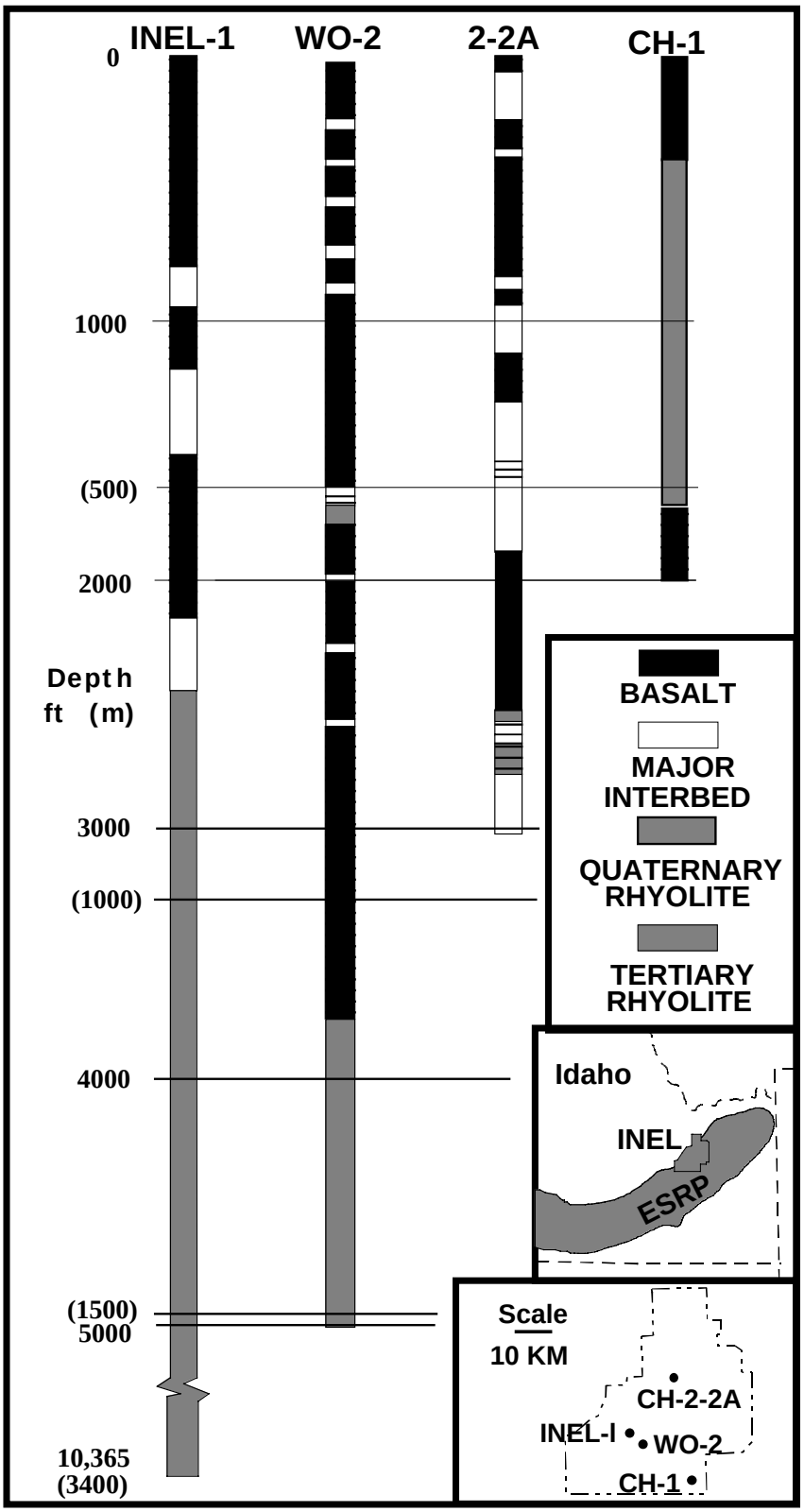

Figure 2.6-11. Lithographic Logs of the Four INEEL Deep Drill Holes

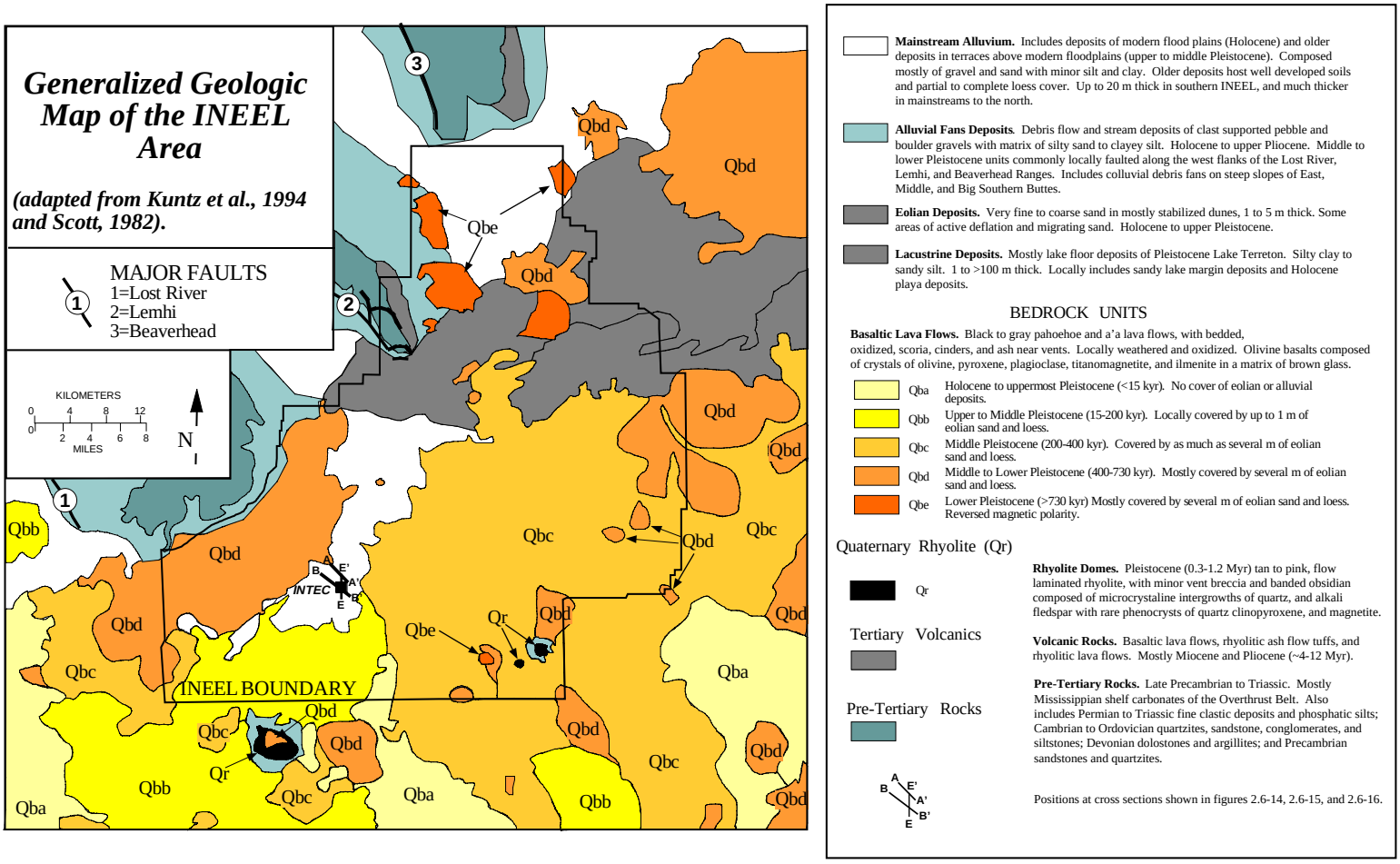

Figure 2.6-12. Geologic Map of the INEEL with INTEC Located

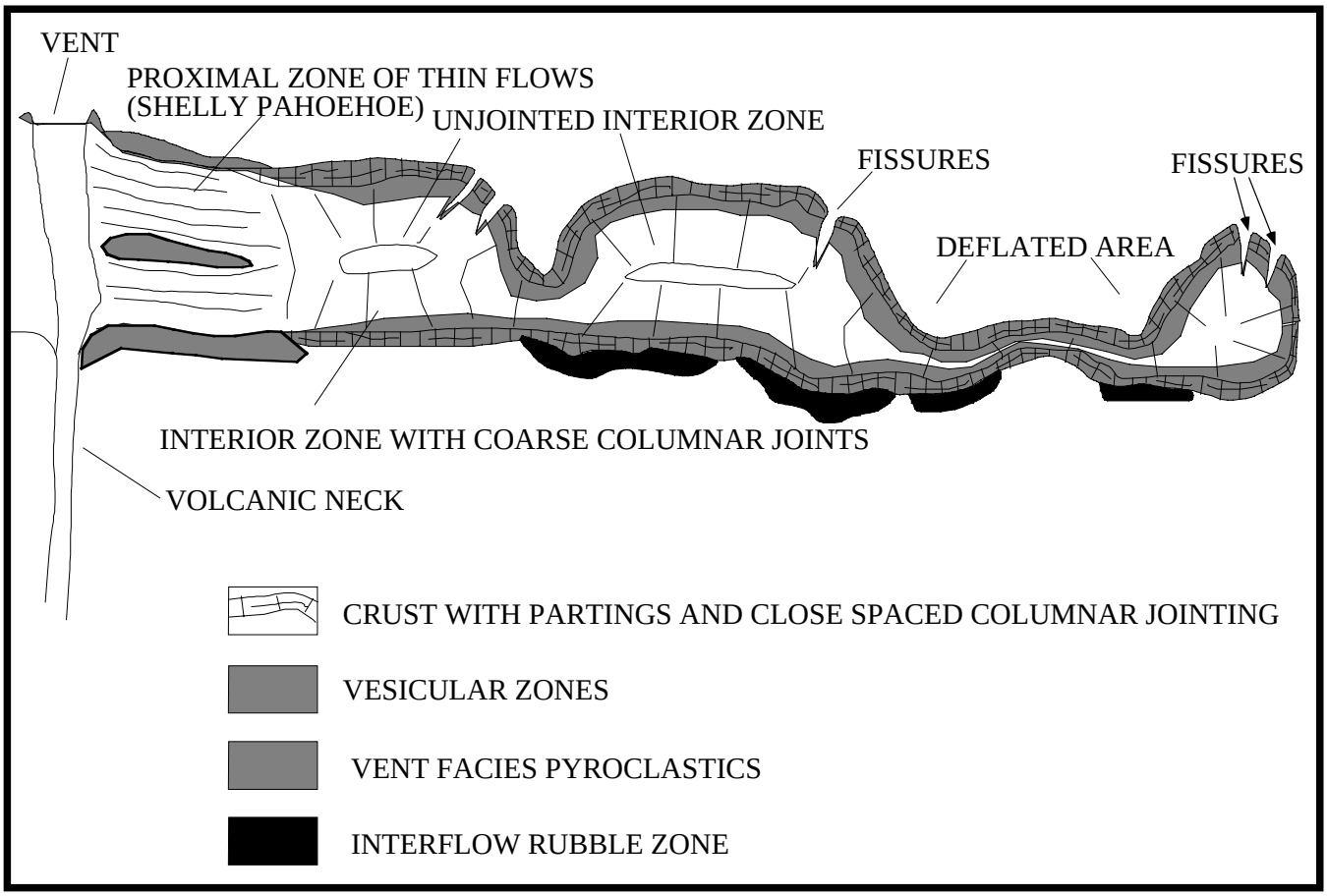

Figure 2.6-13. Idealized Longitudinal Section of an ESRP Basalt Lava Flow.

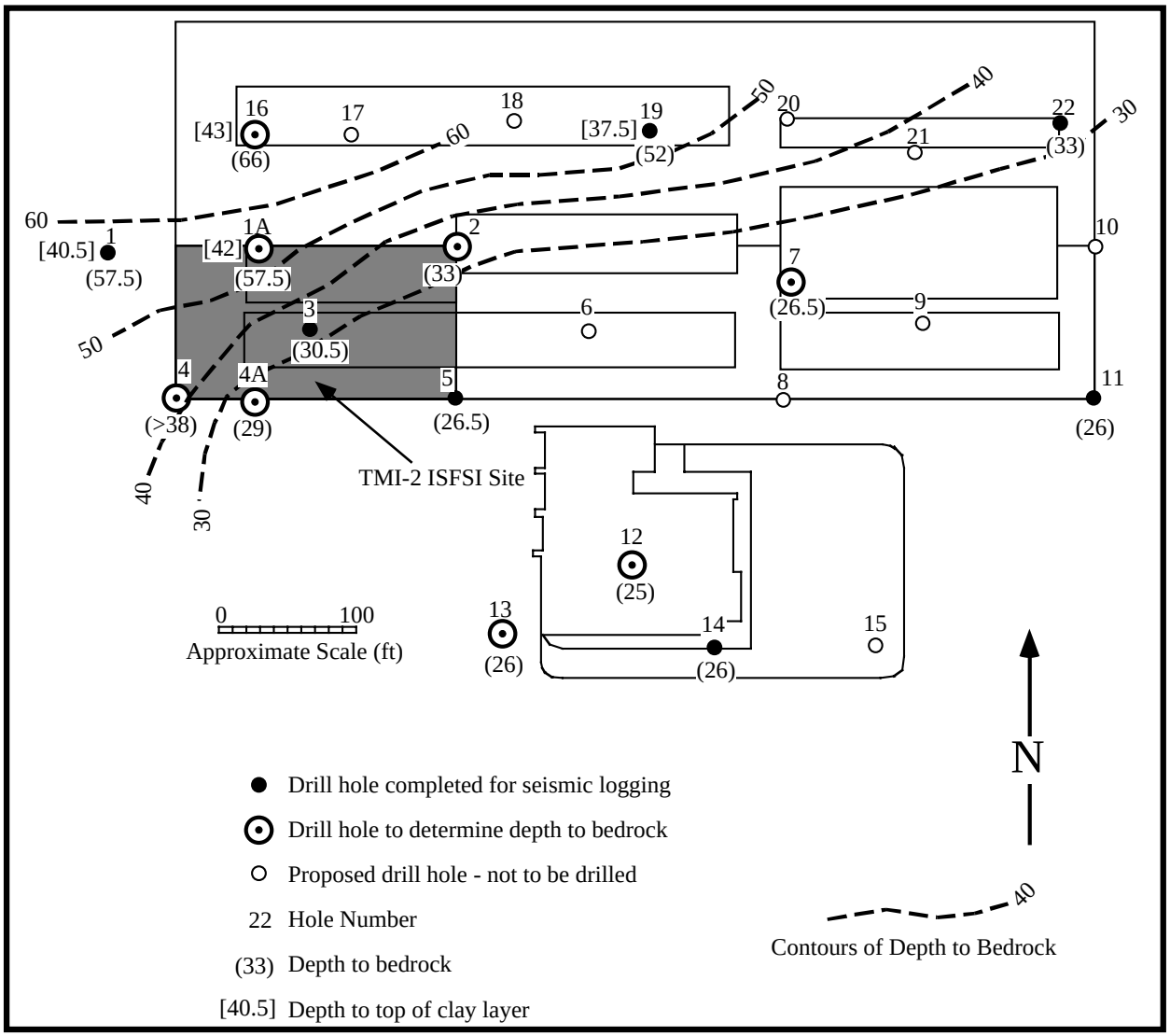

Figure 2.6-14. Drill Hole Locations and Elevation Contours on the Bedrock Surface at the TMI-2 ISFSI site.

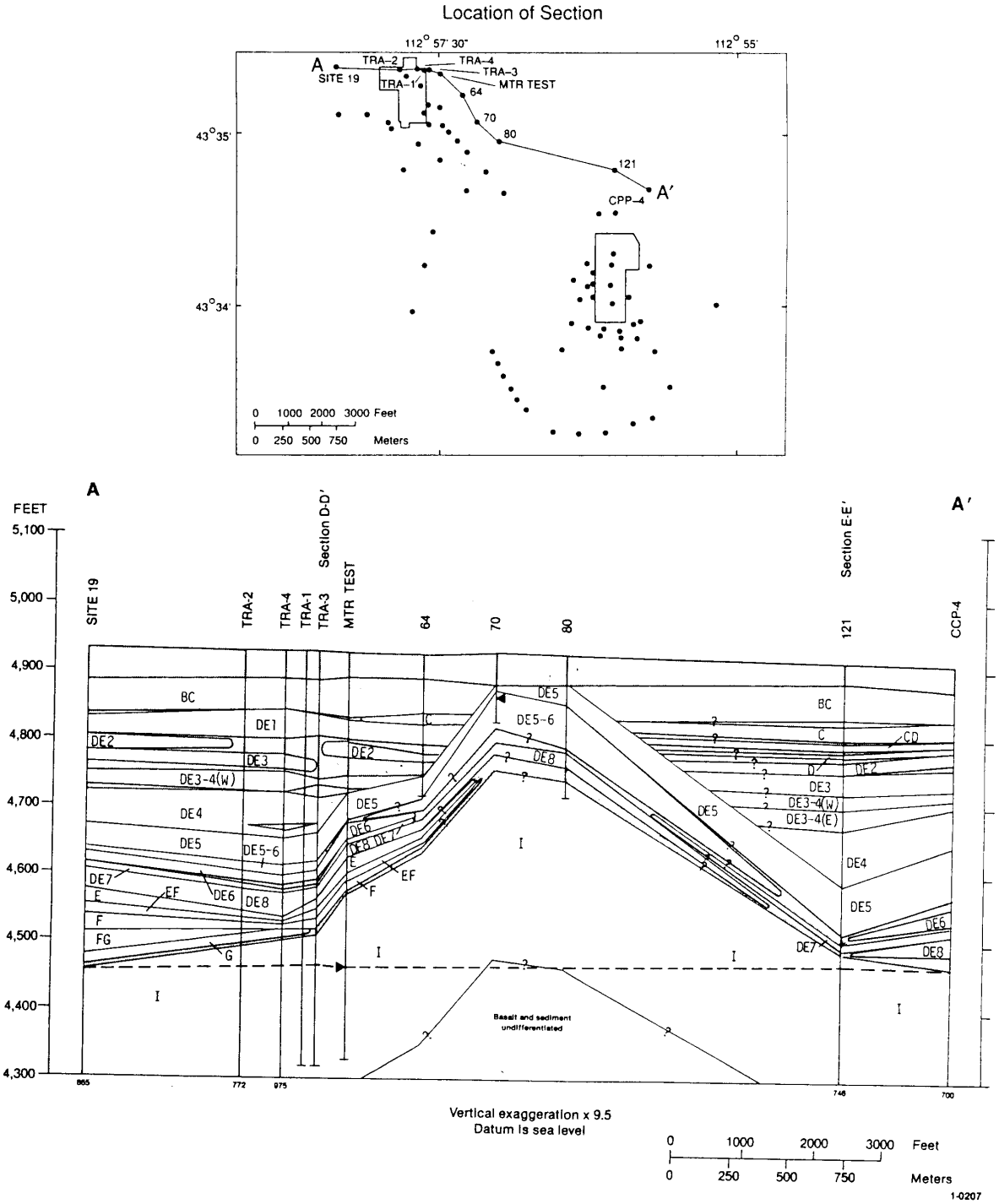

Figure 2.6-15. Geologic Cross Section Through the INTEC-TRA Area, Showing Anderson's (1991) Interpreted Dome**.**

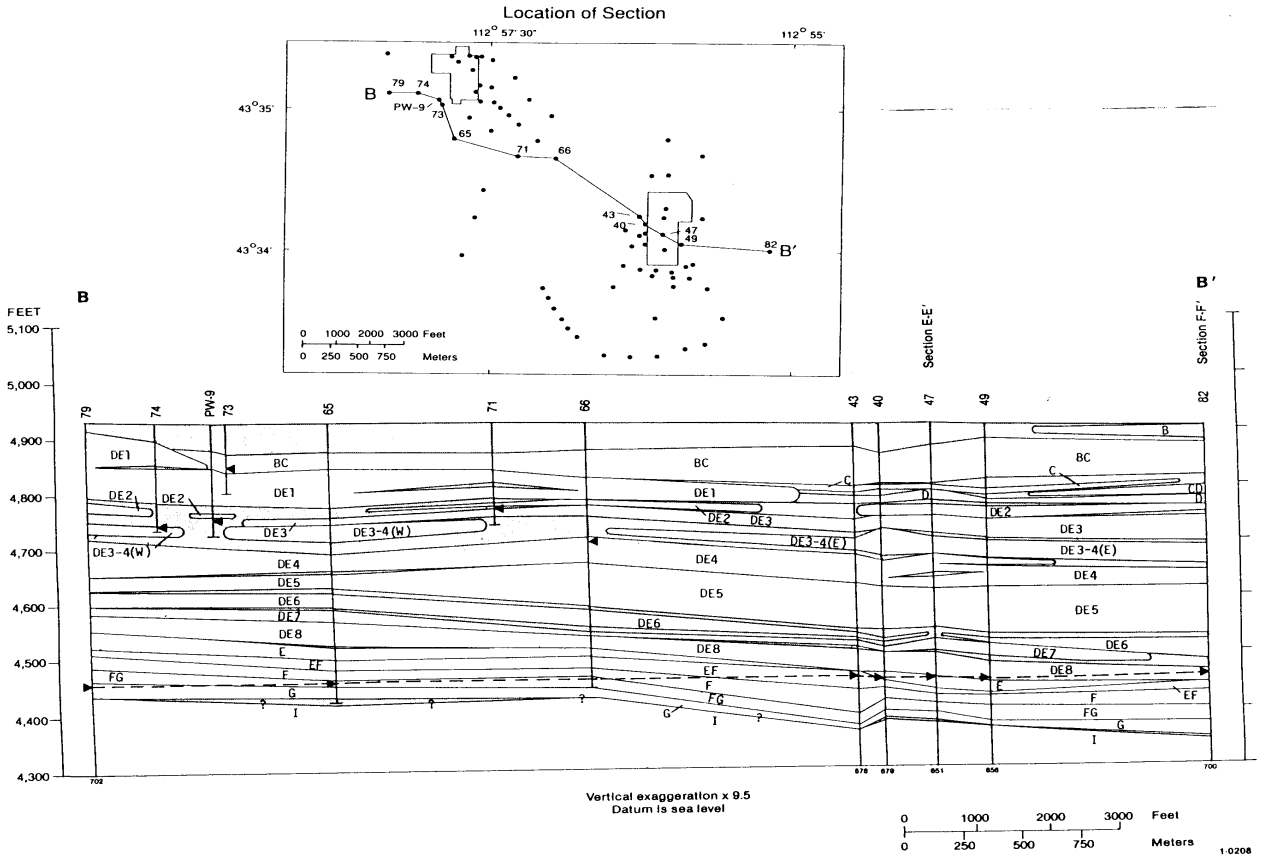

Figure 2.6-16. East-West Geologic Cross-Section Through the INTEC-TRA Area (Anderson, 1991)

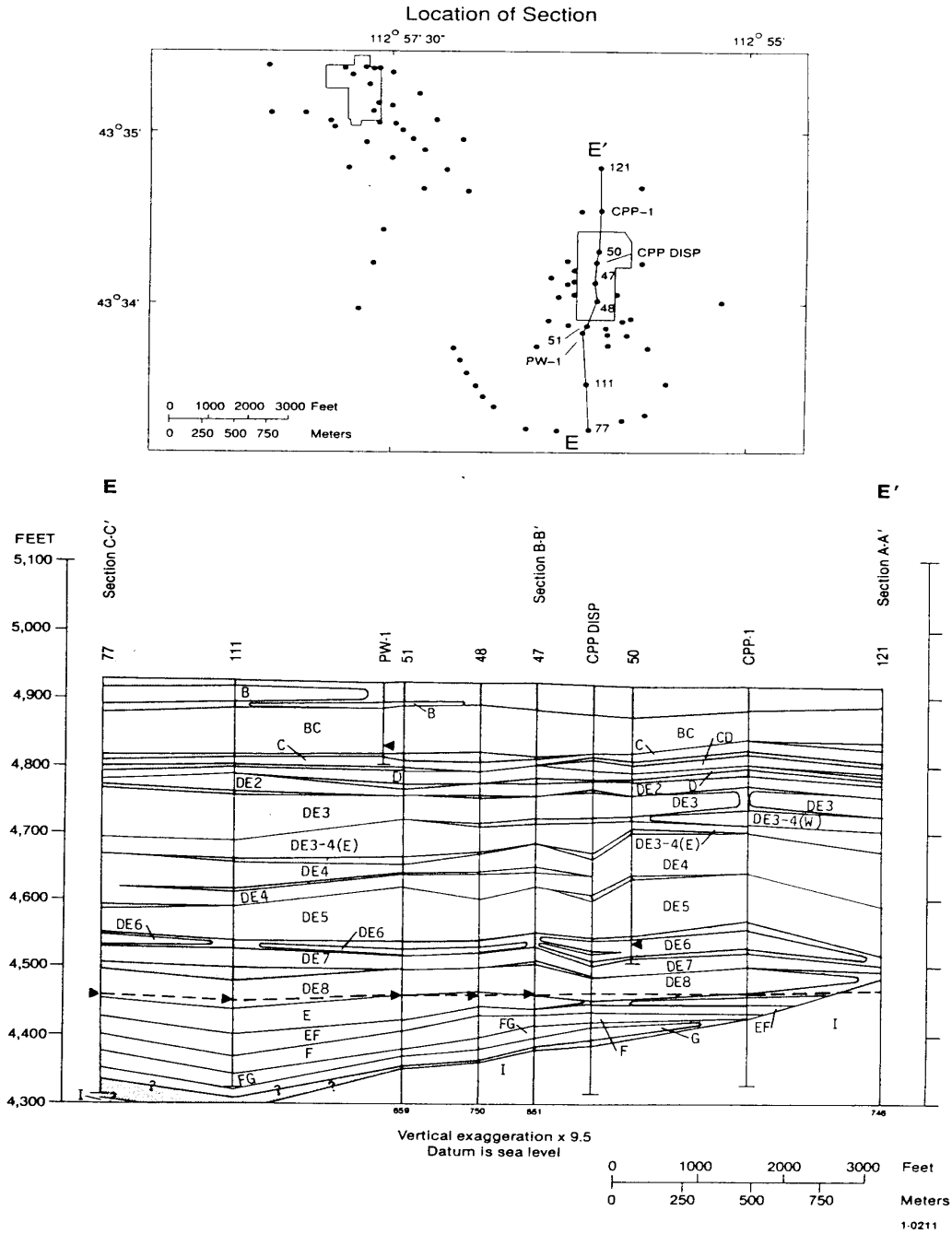

Figure 2.6-17. North-South Geologic Cross Section Through the INTEC-TRA Area **(**Anderson, 1991**).**

Faults, Volcanic Zones and Historic Earthquakes in the INEEL Region

Shaded Relief Map

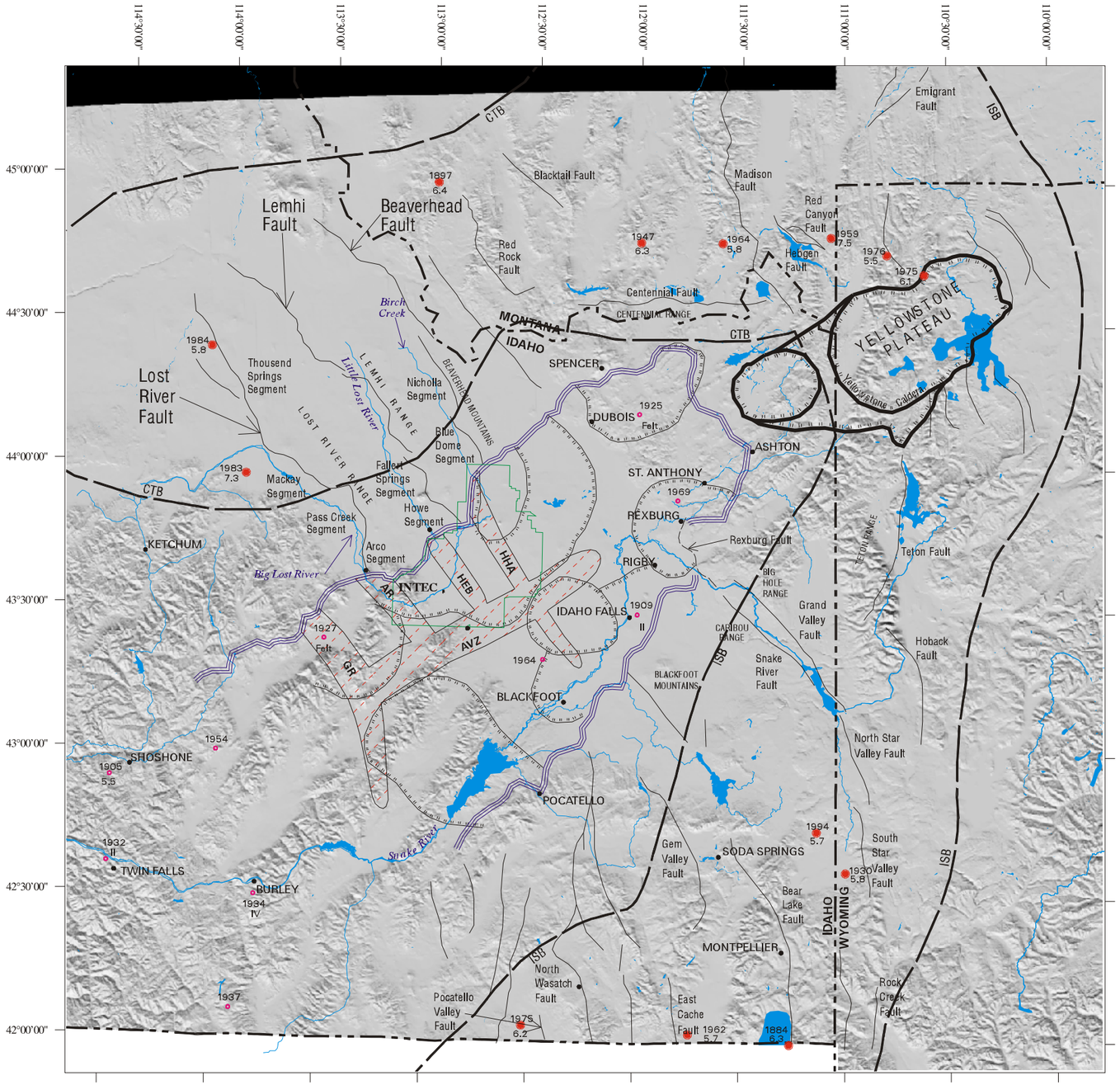

LEGEND

- Rivers
- INEEL Boundary
- State Boundaries
- Faults
- Possible Faults
- Seismic Belts
- Mapped Calderas
- Calderas
- Eastern Snake River Plain Boundary
- Lakes
- Volcanic Zones
- Cities
- Historic Earthquakes of Magnitude > 5.5 Outside the ESRP Boundary
- Historic Earthquakes That Have Been Located Within the ESRP Boundary

Seismic Belts

CTB - Continental Tectonic Belt
ISB - Intermountain Seismic Belt

Volcanic Zones

GR - Great Rift VRZ*
AR - Arco VRZ*
HEB - Howe- East Butte VRZ*
HHA - Lava Ridge - Hells Half Acre VRZ*
AVZ - Axial Volcanic Zone
* VRZ = Volcanic Rift Zone

AREA COVERED BY MAP

0 20 40 60 80 100 km
0 20 40 60 80 Miles

Date Drawn : December 23, 1998

(projects/ineel/fault_maps: faults_hist_earthquakes_greyshd- bl_v1)

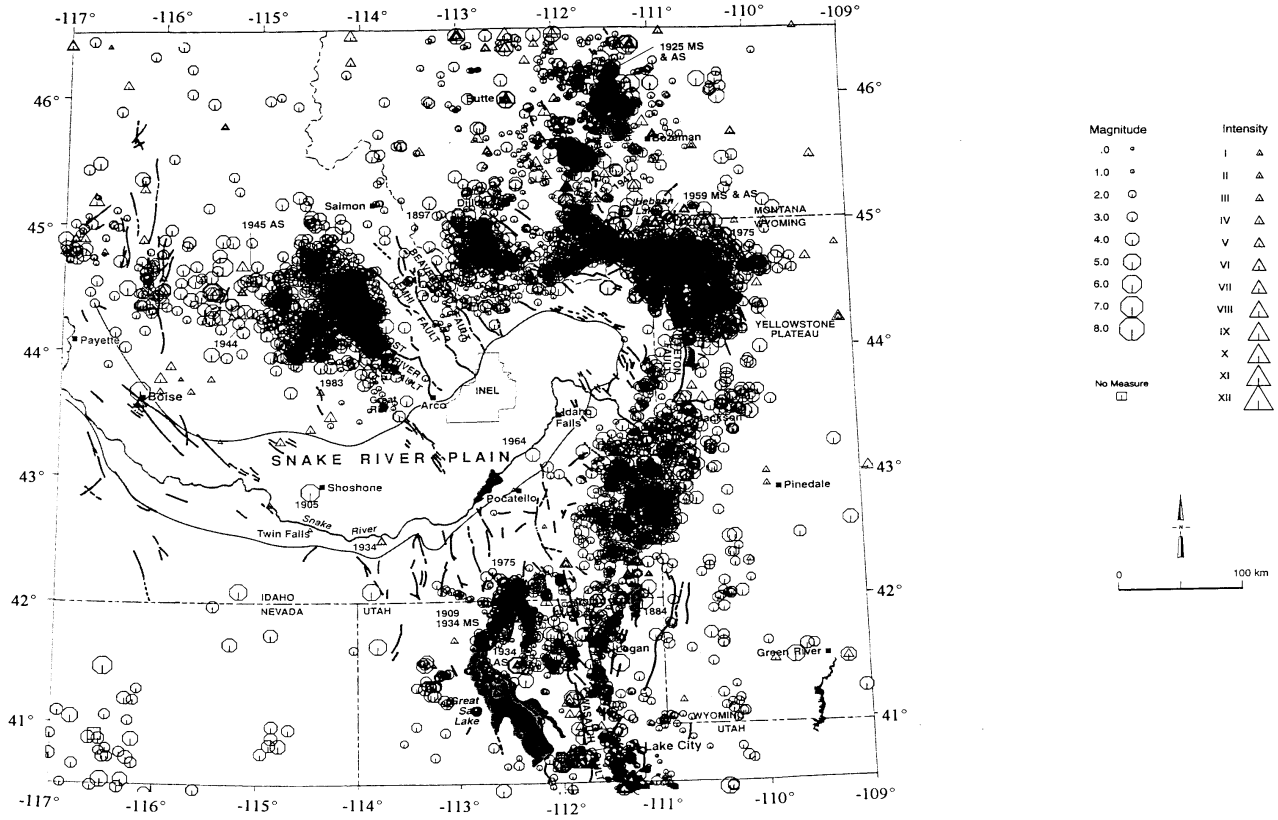

Figure 2.6-20. Seismicity Map Showing the ESRP in Relation to the Intermountain Seismic Belt and the Centennial Tectonic Belt (form Woodward-Clyde Federal Services, 1996a)

Earthquake Epicenters in the INEEL Region 1850 - 1995

Shaded Relief Map

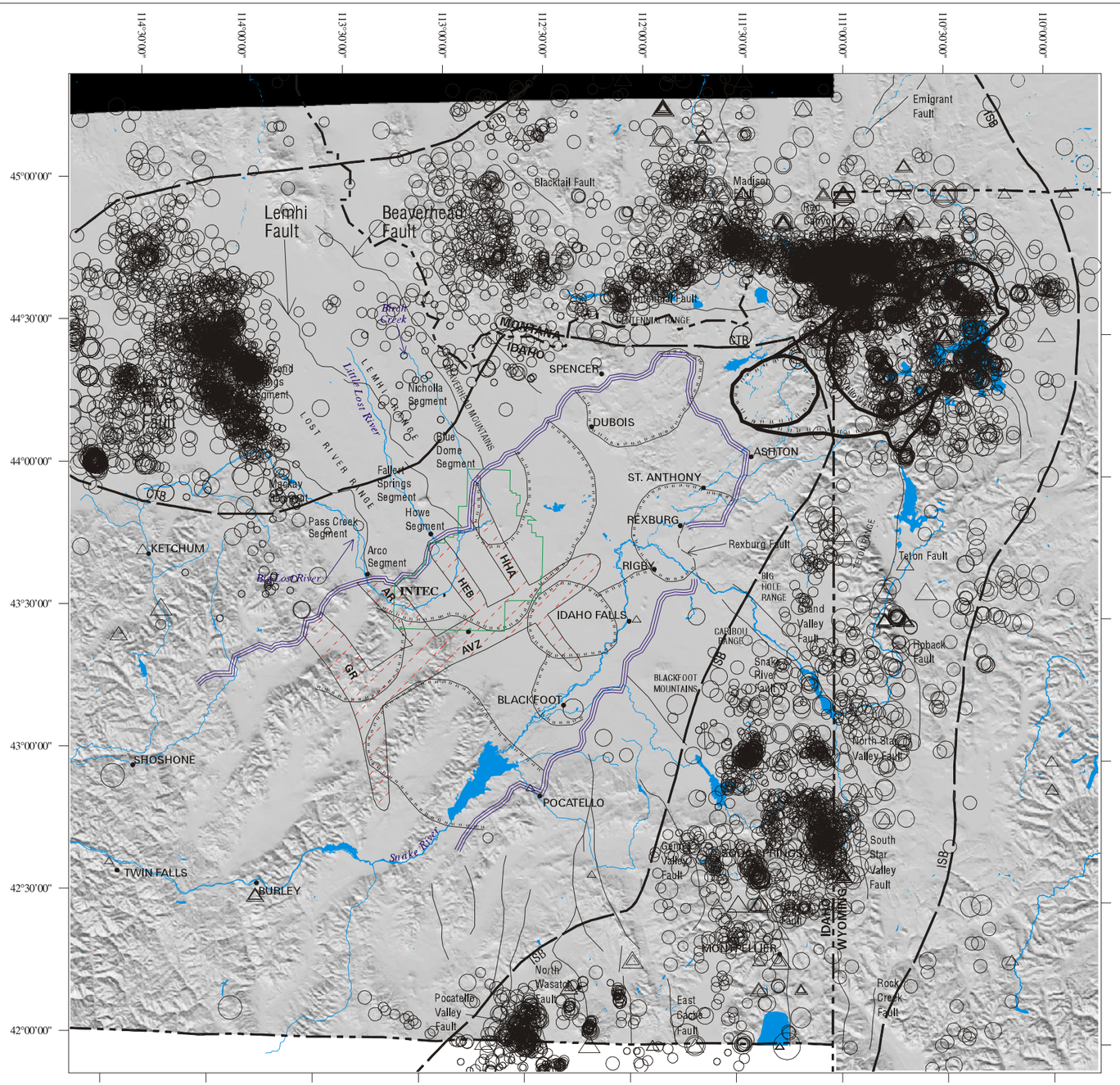

LEGEND

- Rivers
- INEEL Boundary
- State Boundaries
- Faults
- Possible Faults
- Seismic Belts
- Mapped Calderas
- Calderas
- Eastern Snake River Plain Boundary
- Lakes
- Volcanic Zones
- Cities

Intensity	Magnitude
I	< 1
II	1 - 2
III	2 - 3
IV	3 - 4
V	4 - 5
VI	5 - 6
	6 - 7
	> 7

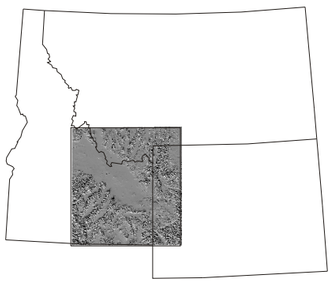

AREA COVERED BY MAP

0 20 40 60 80 100 km

0 20 40 60 80 Miles

Date Drawn : December 23, 1998

(projects/ineel/fault_maps: faults_all_earthquakes_greyshd- bl_v1)

Map of INEEL Seismic Network Stations and Epicenters of Earthquakes Located in a 100 Mile Radius of the Center of the INEEL, 1972 - 1995

Shaded Relief Map

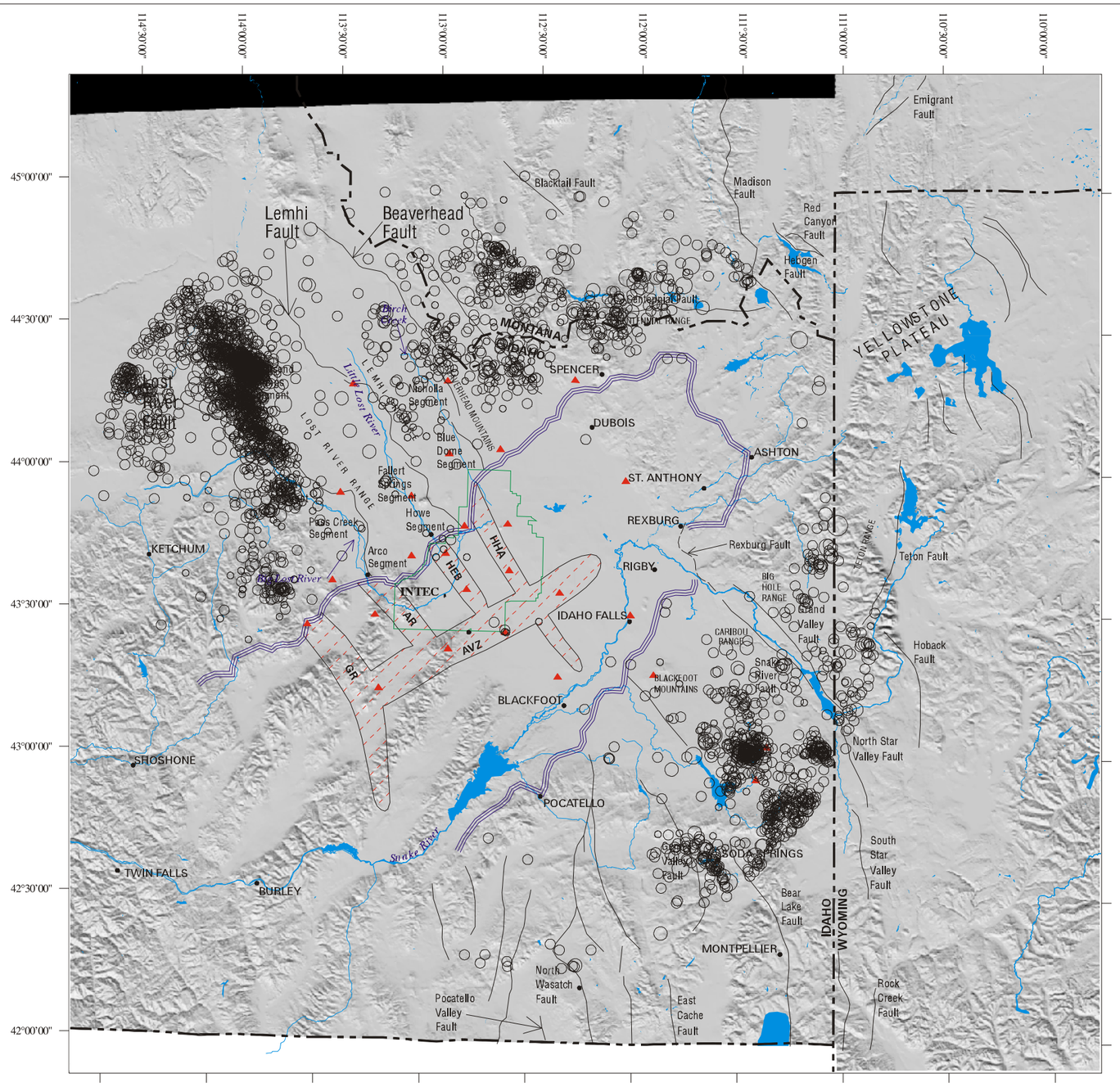

LEGEND

- Rivers
- INEEL Boundary
- State Boundaries
- Faults
- Possible Faults
- Eastern Snake River Plain Boundary
- Lakes
- Volcanic Zones
- Cities
- INEEL Seismic Stations

Magnitude

- < 1
- 1 - 2
- 2 - 3
- 3 - 4
- 4 - 5
- 5 - 6
- 6 - 7
- > 7

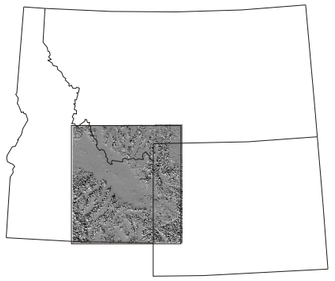

AREA COVERED BY MAP

0 20 40 60 80 100 km

0 20 40 60 80 Miles

Date Drawn : December 23, 1998

(projects/ineel/fault_maps: faults_seismic_stations_greyshd- bl_v1)

Seismic Source Zones in the INEEL Region

Shaded Relief Map

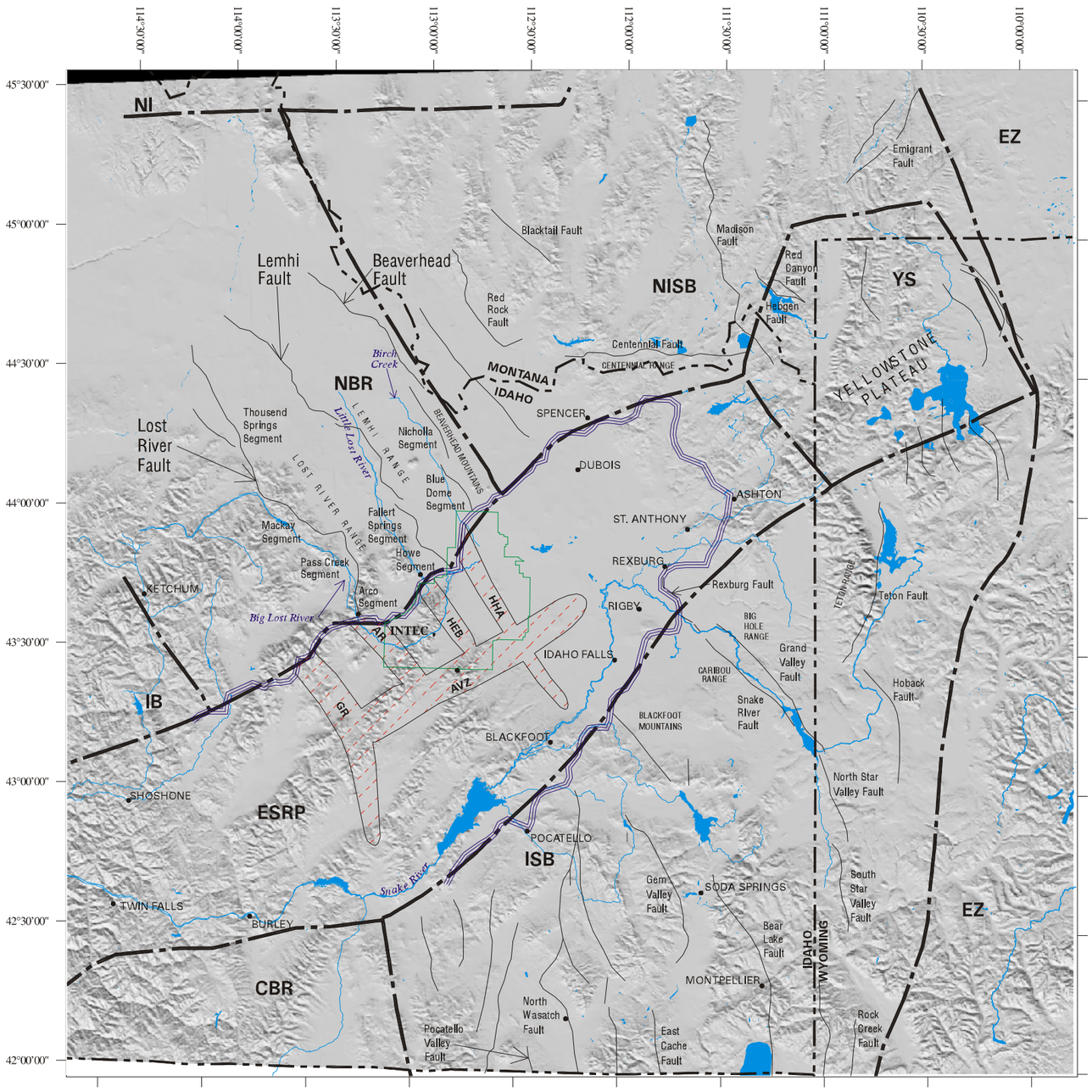

LEGEND

- Rivers
- INEEL Boundary
- State Boundaries
- Faults
- Possible Faults
- Source Zone Boundaries
- Eastern Snake River Plain Boundary
- Lakes
- Volcanic Zones
- Cities

Regional Source Zones

ESRP	-	Eastern Snake River Plain
ISB	-	Central Intermountain Seismic Belt
NISB	-	Norther Inermountain Seismic Belt
NBR	-	Northern Basin and Range
CBR	-	Central Basin and Range
IB	-	Idaho Batholith
YS	-	Yellowstone
NI	-	Northern Idaho
EZ	-	Eastern Zone

AREA COVERED BY MAP

0 20 40 60 80 100 km

0 20 40 60 80 Miles

Date Drawn : December 23, 1998

(projects/ineel/fault_maps: faults_source_zones_greyshd- bl_v1)

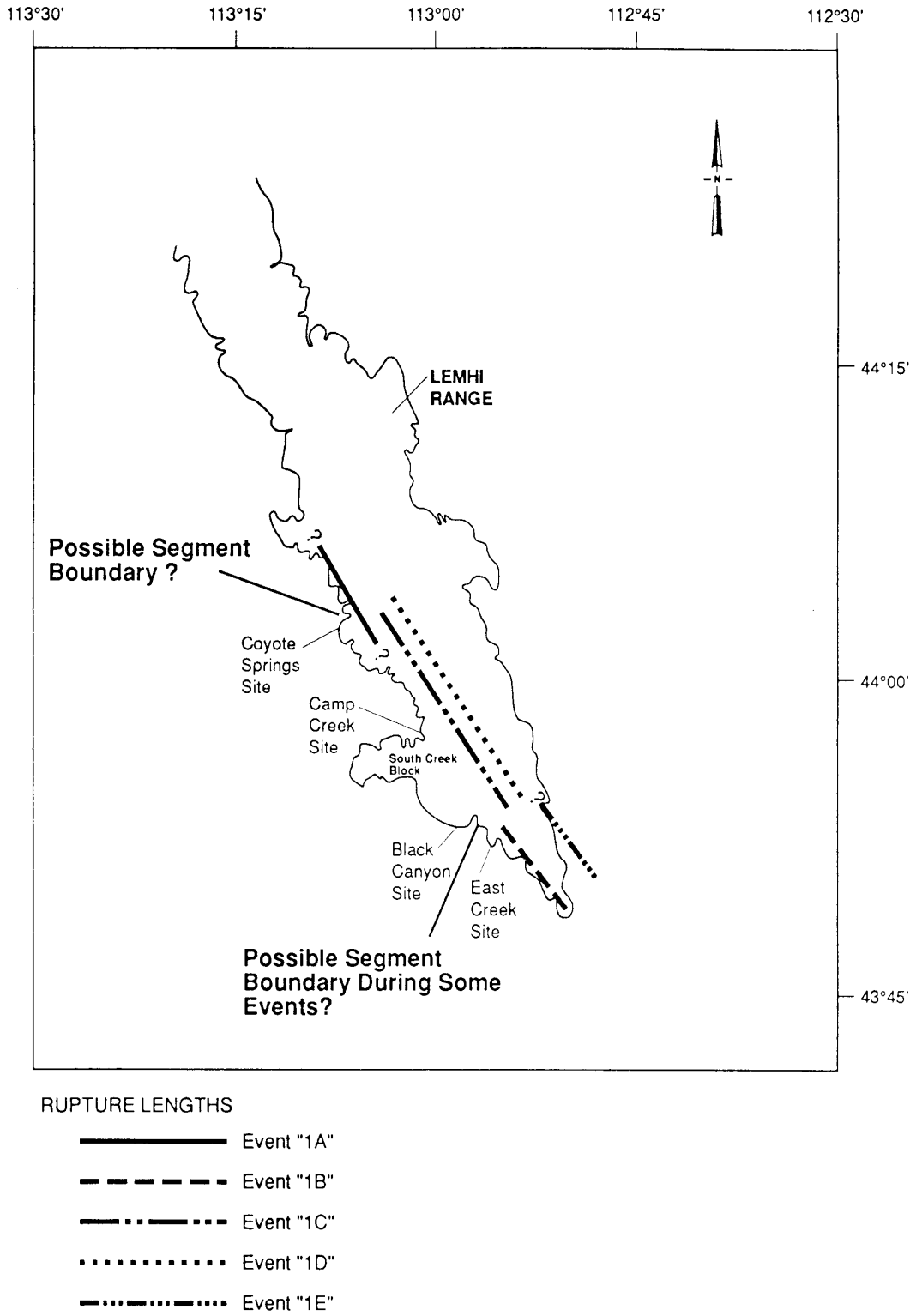

Figure 2.6-24. Possible Rupture Scenerios for Southern Lemhi Fault.

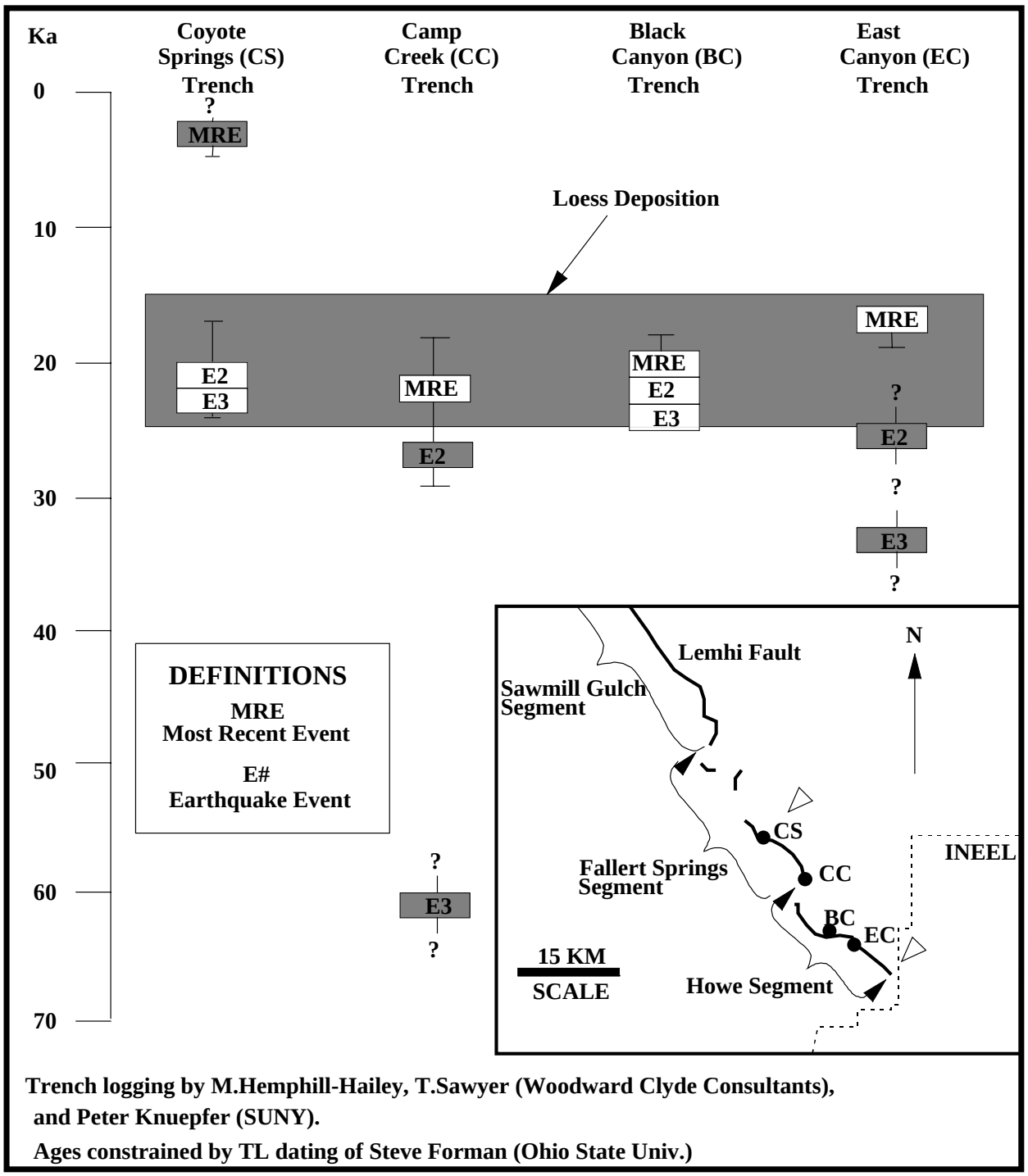

Figure 2.6-25. Summary of Paleoseismic Results for the Lemhi Fault (four trenches).

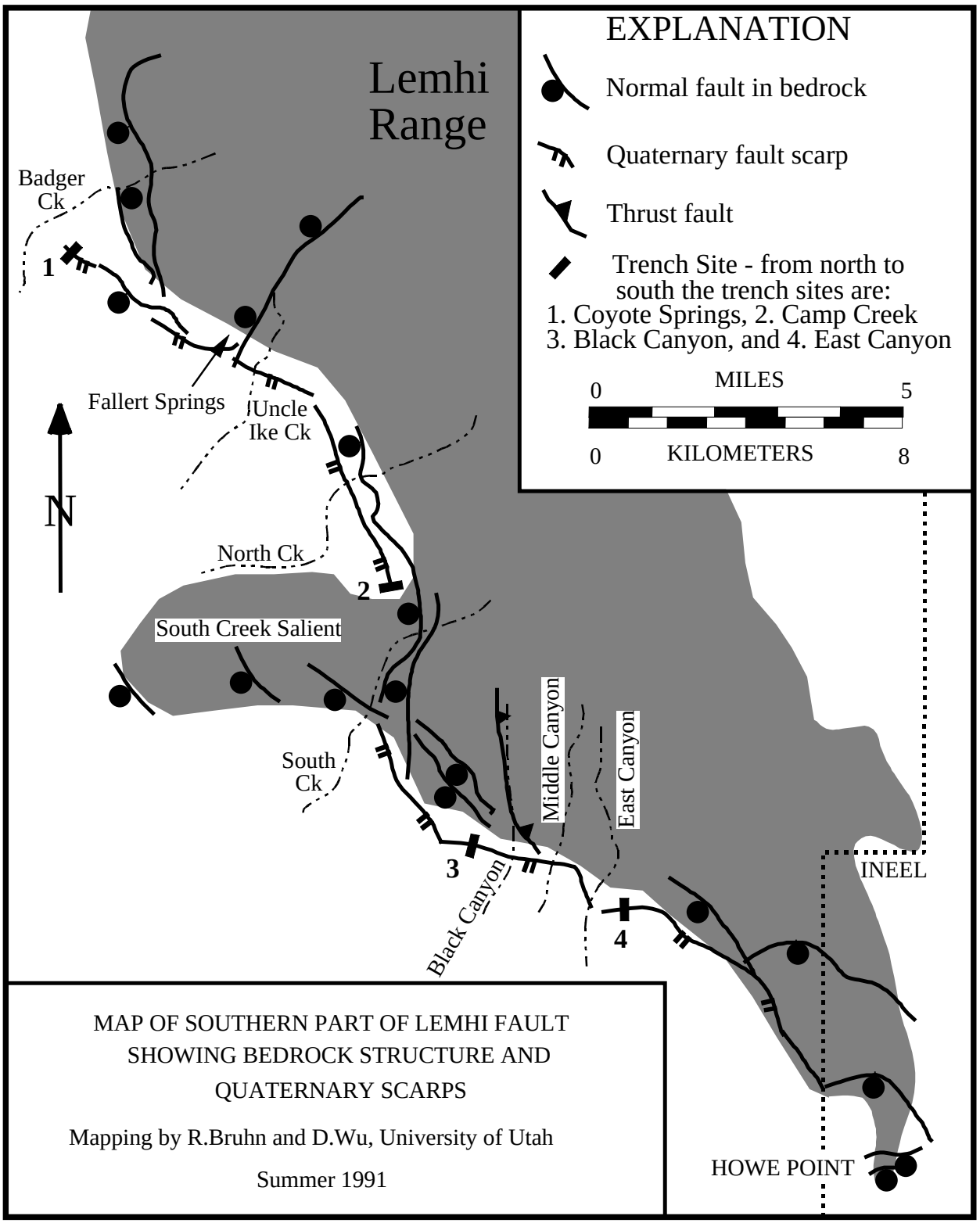

Figure 2.6-26. Bedrock Features of the Southern Lemhi Fault

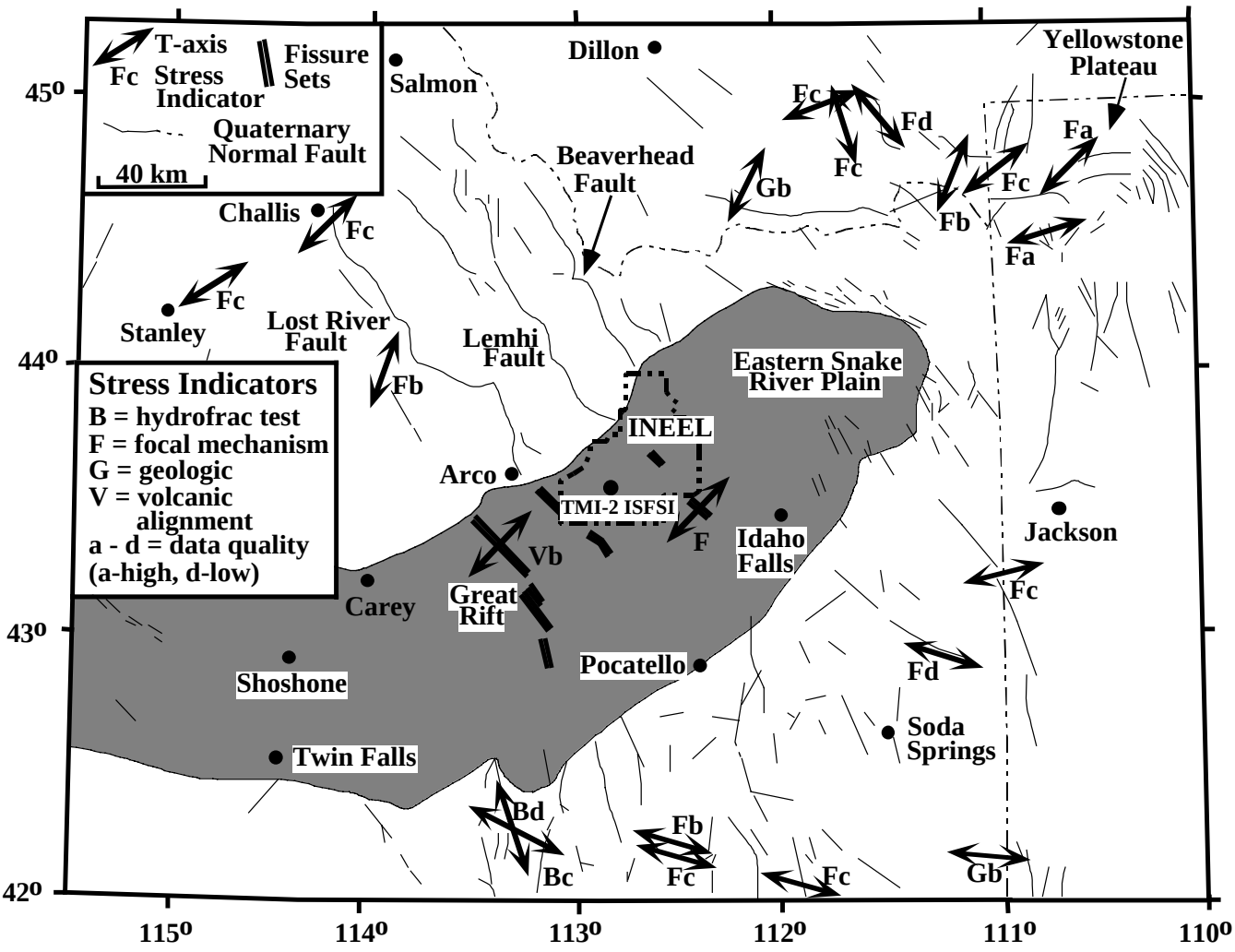

Figure 2.6-27. Map Showing Minimum Principle Stress Orientations in Southern Idaho and Yellowstone

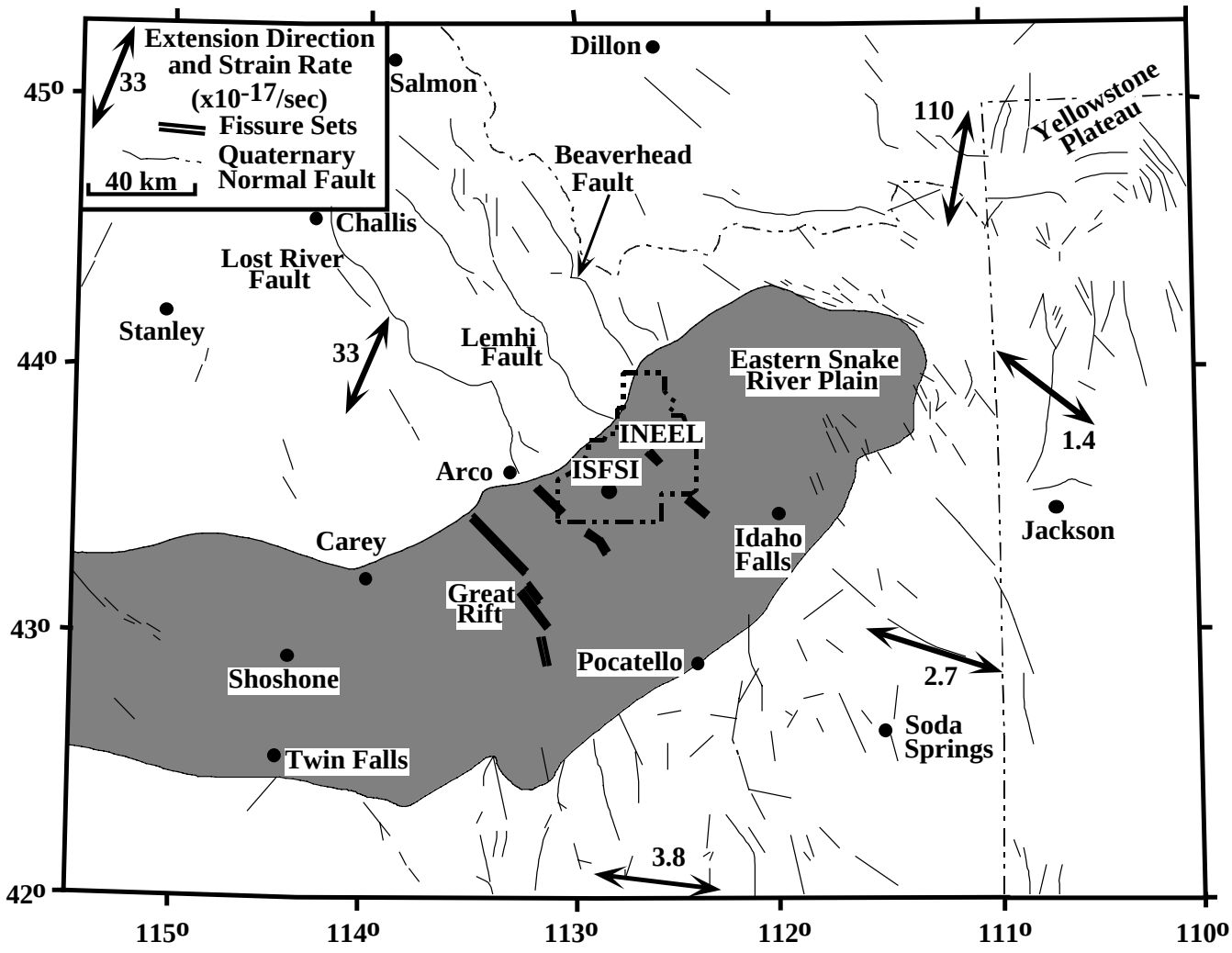

Figure 2.6-28. Strain Rate Map of Southern Idaho and Western Wyoming

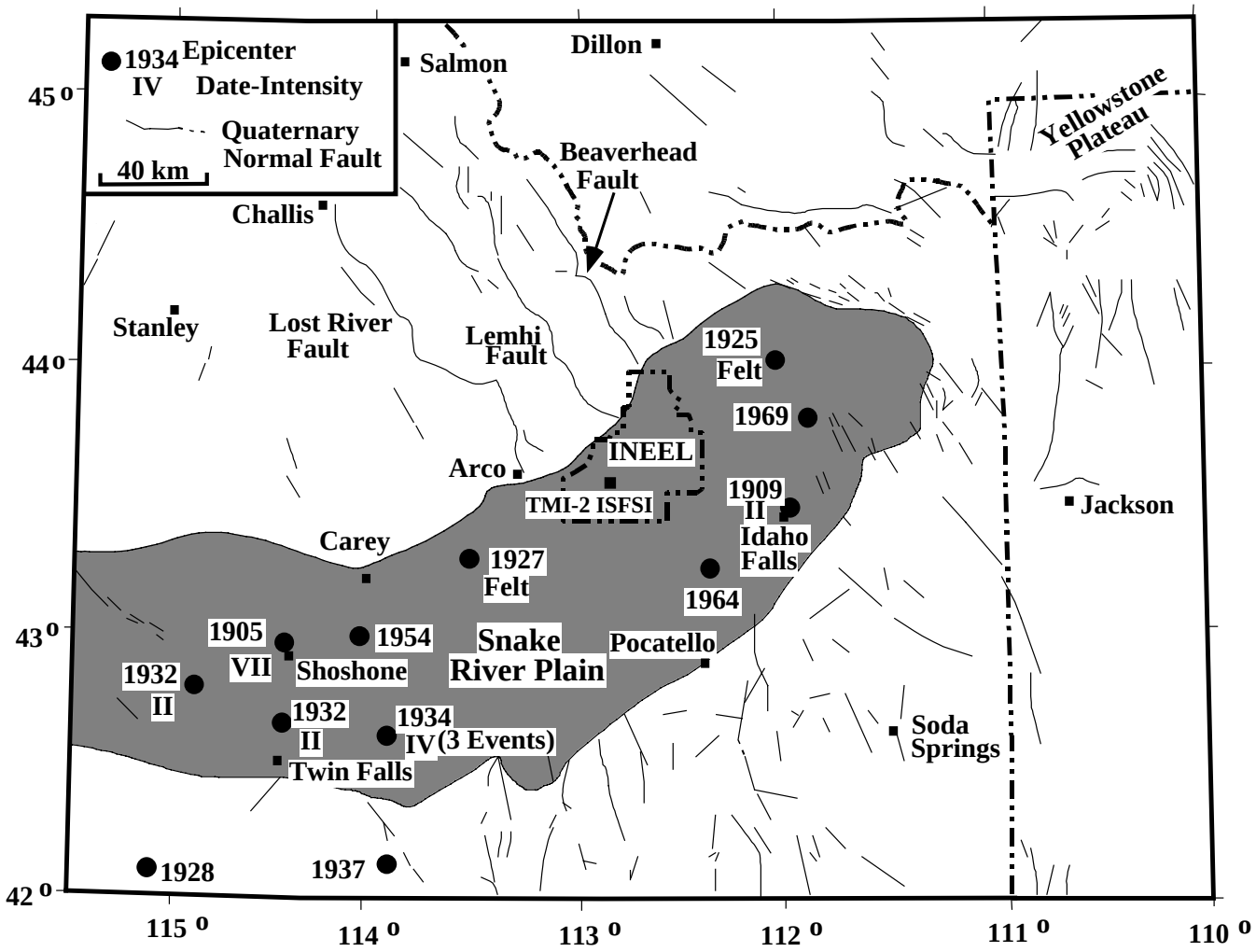

Figure 2.6-29. Location of Historic Earthquakes Reported for the ESRP.

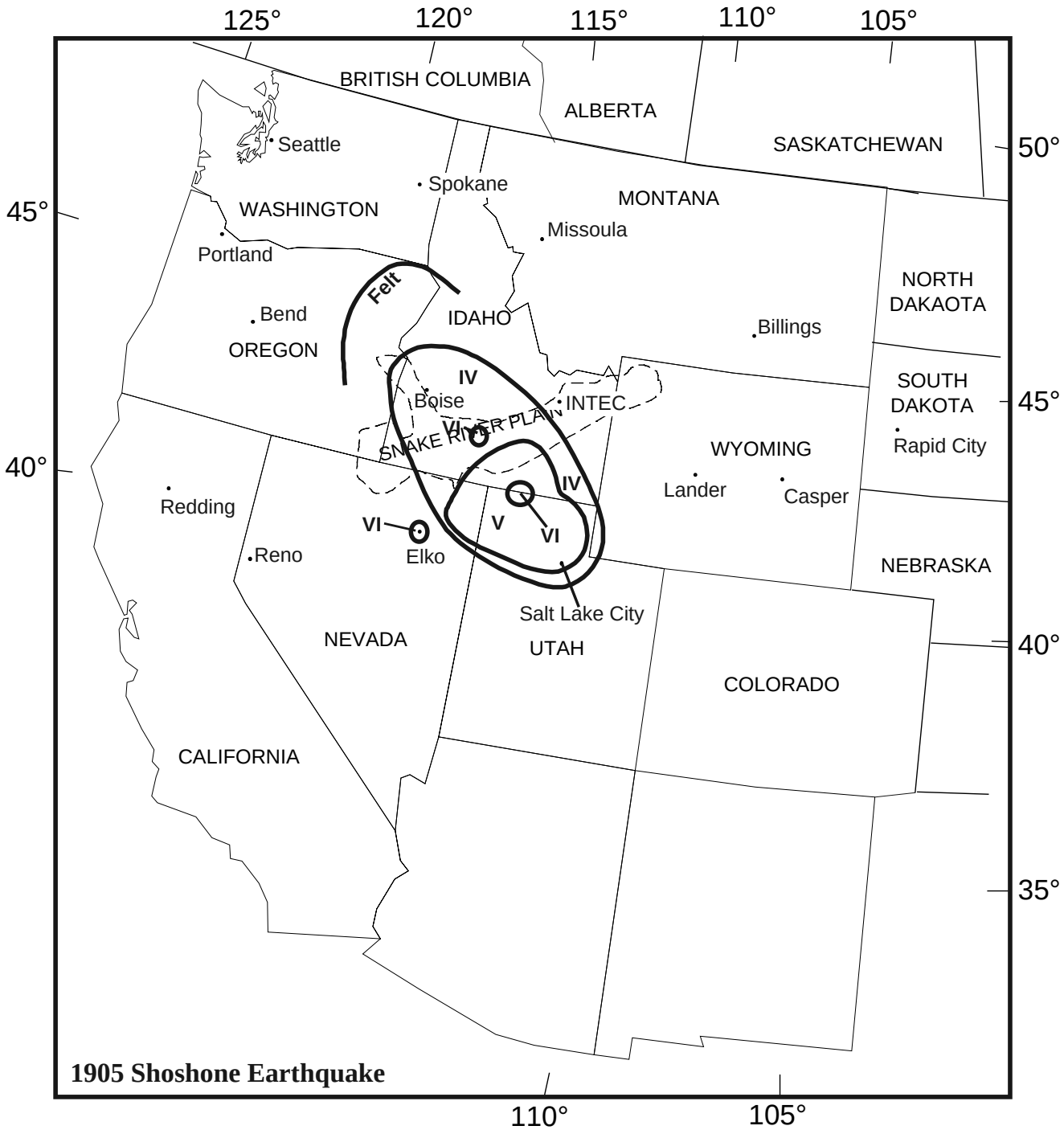

Figure 2.6-30. Isoseismal Map for the 1905 Shoshone Earthquake.

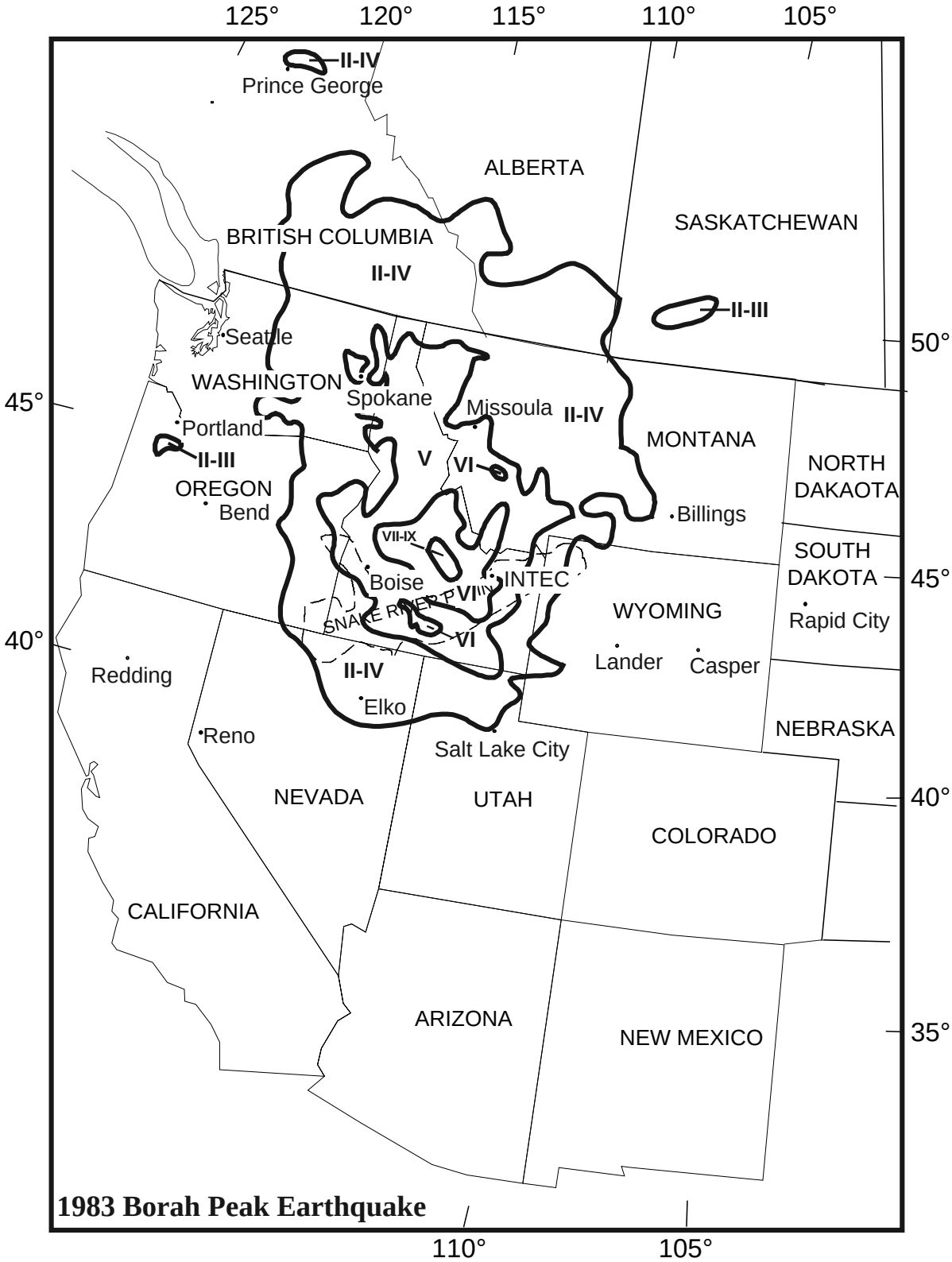

Figure 2.6-31. Isoseismal map for the 1983 Borah Peak Earthquake.

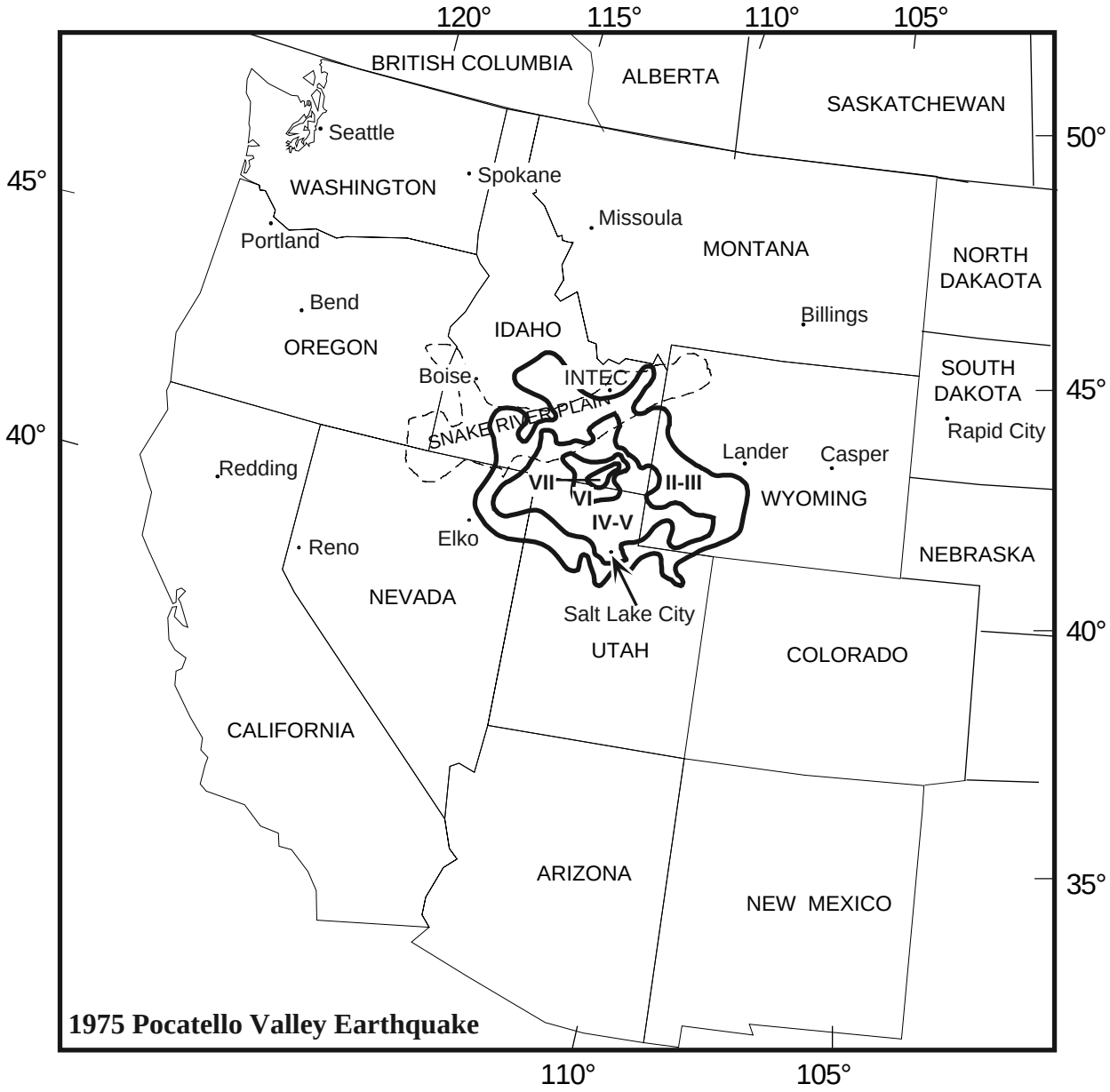

Figure 2.6-32. Isoseismal Map for the 1975 Pocatello Valley Earthquake.

Figure 2.6-33. Isoseismal Map for the 1959 Hebgen Lake Earthquake.

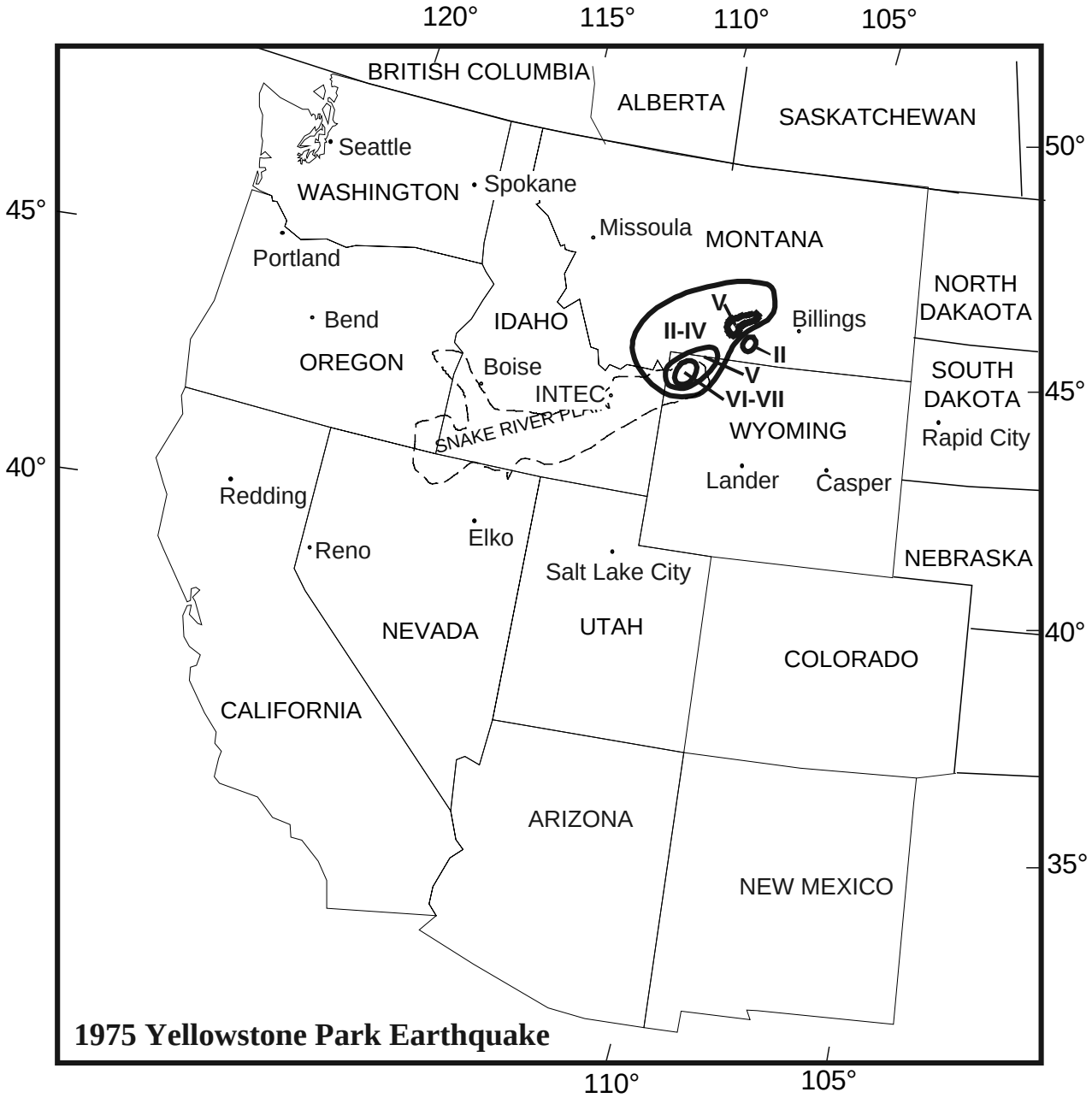

Figure 2.6-34. Isoseismal Map for the 1975 Yellowstone Park Earthquake.

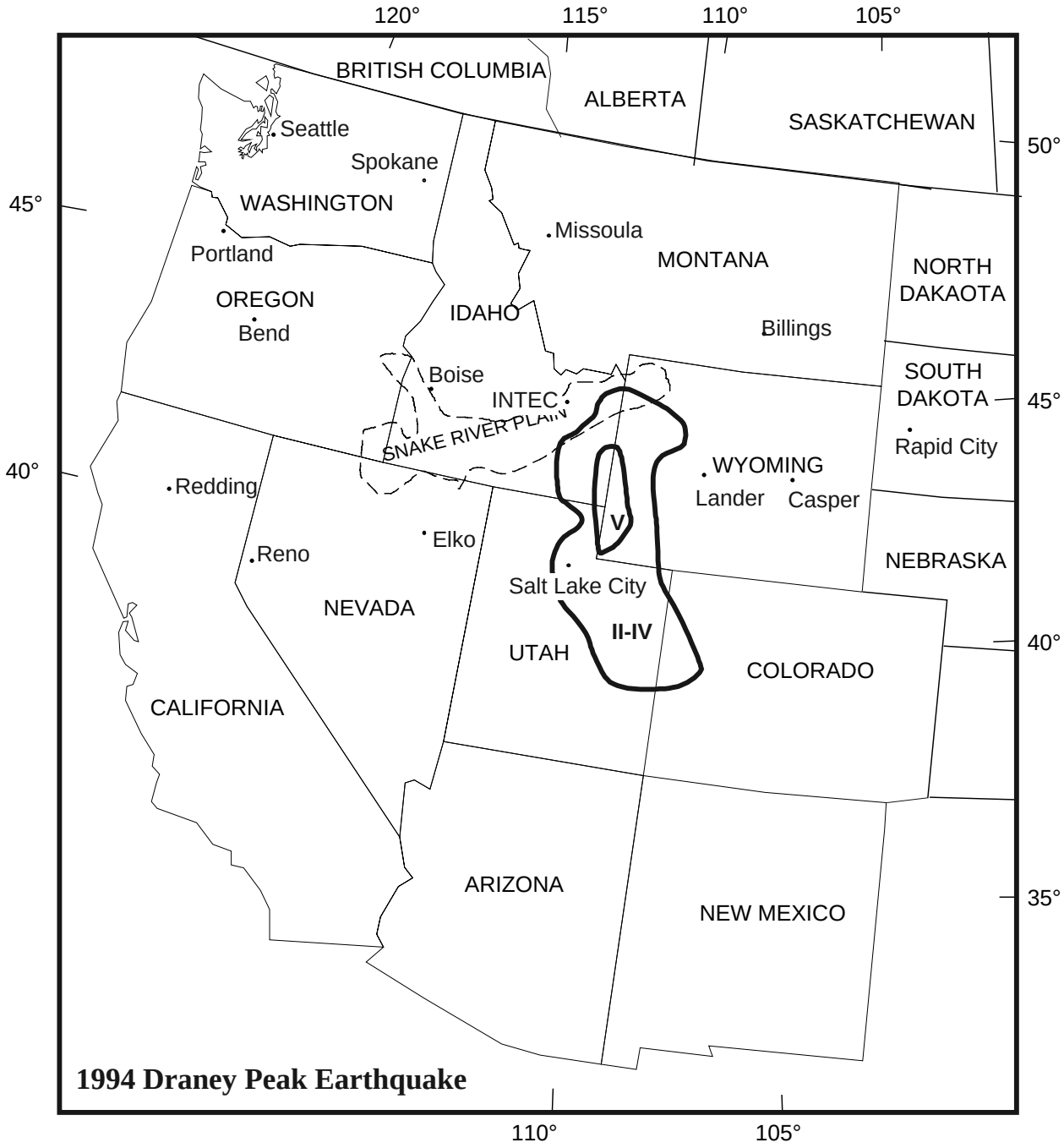

Figure 2.6-35. Isoseismal Map for the 1994 Draney Peak Earthquake.

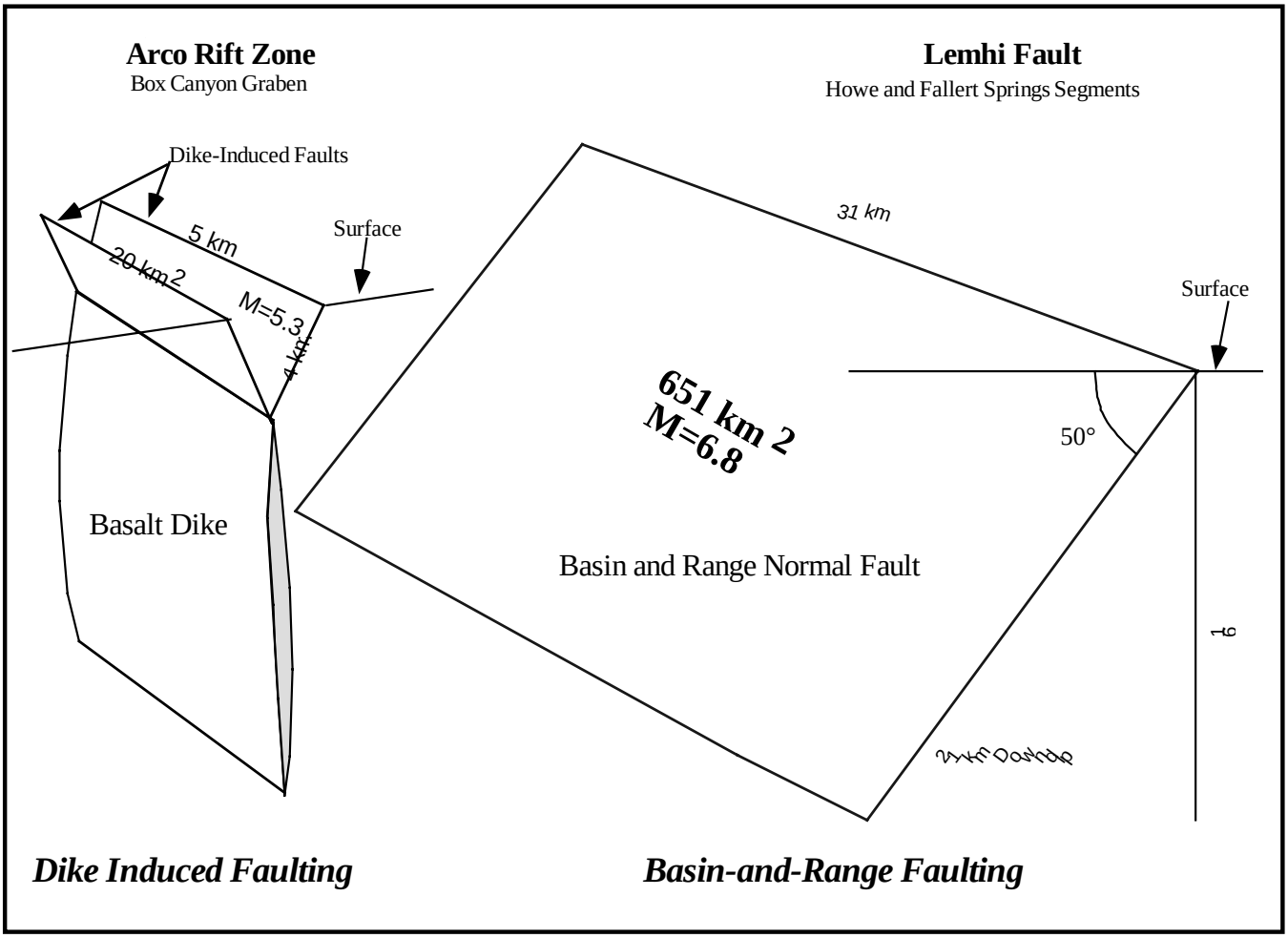

Figure 2.6-36. Comparison of surface area of the Howe segment of the Lemhi fault to the surface area of dike-induced normal faults.

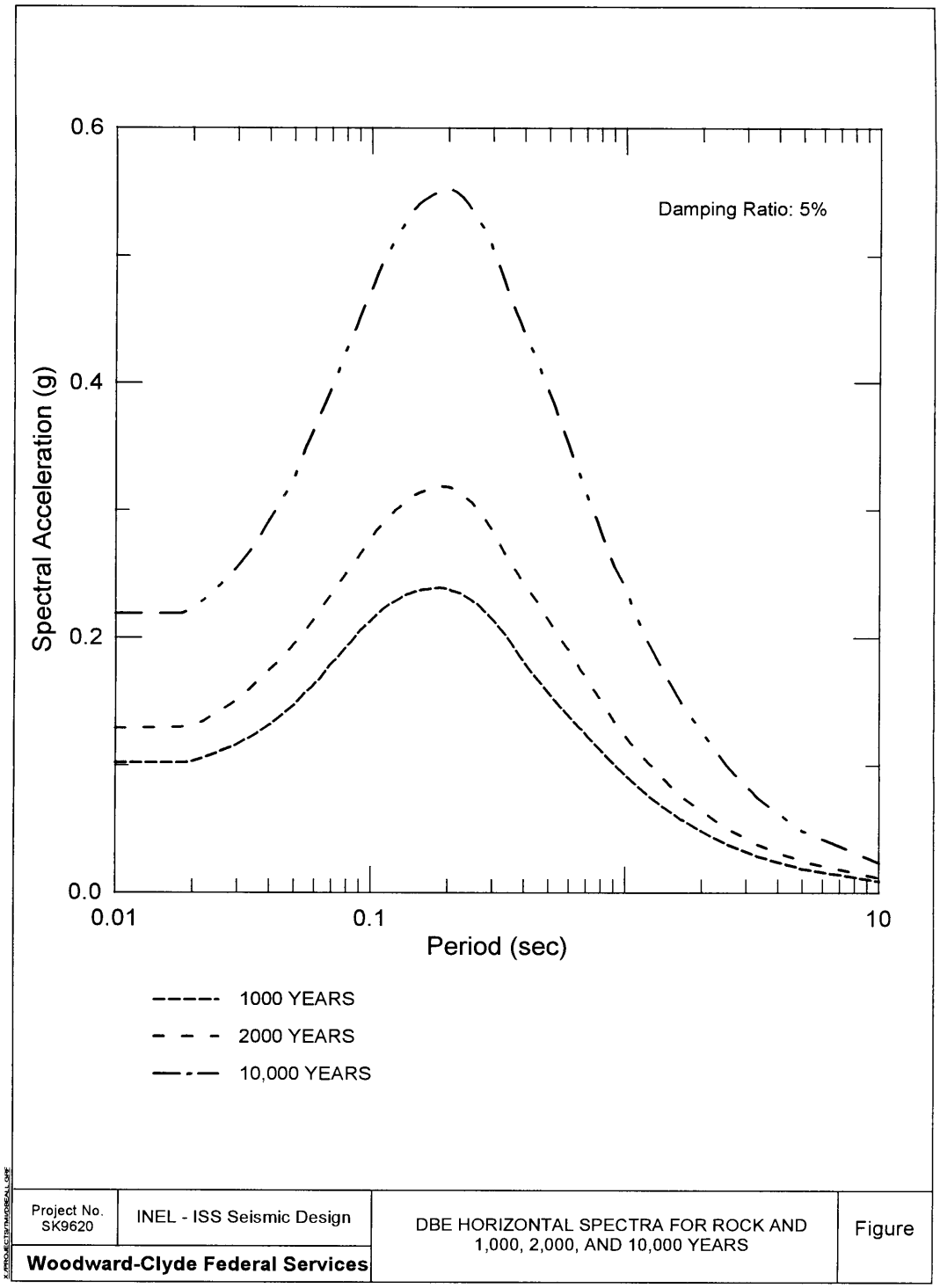

Figure 2.6-37. Smoothed DBE horizontal spectra for rock (5% damped) at 10,000, 2,000, and 1,000 year return periods.

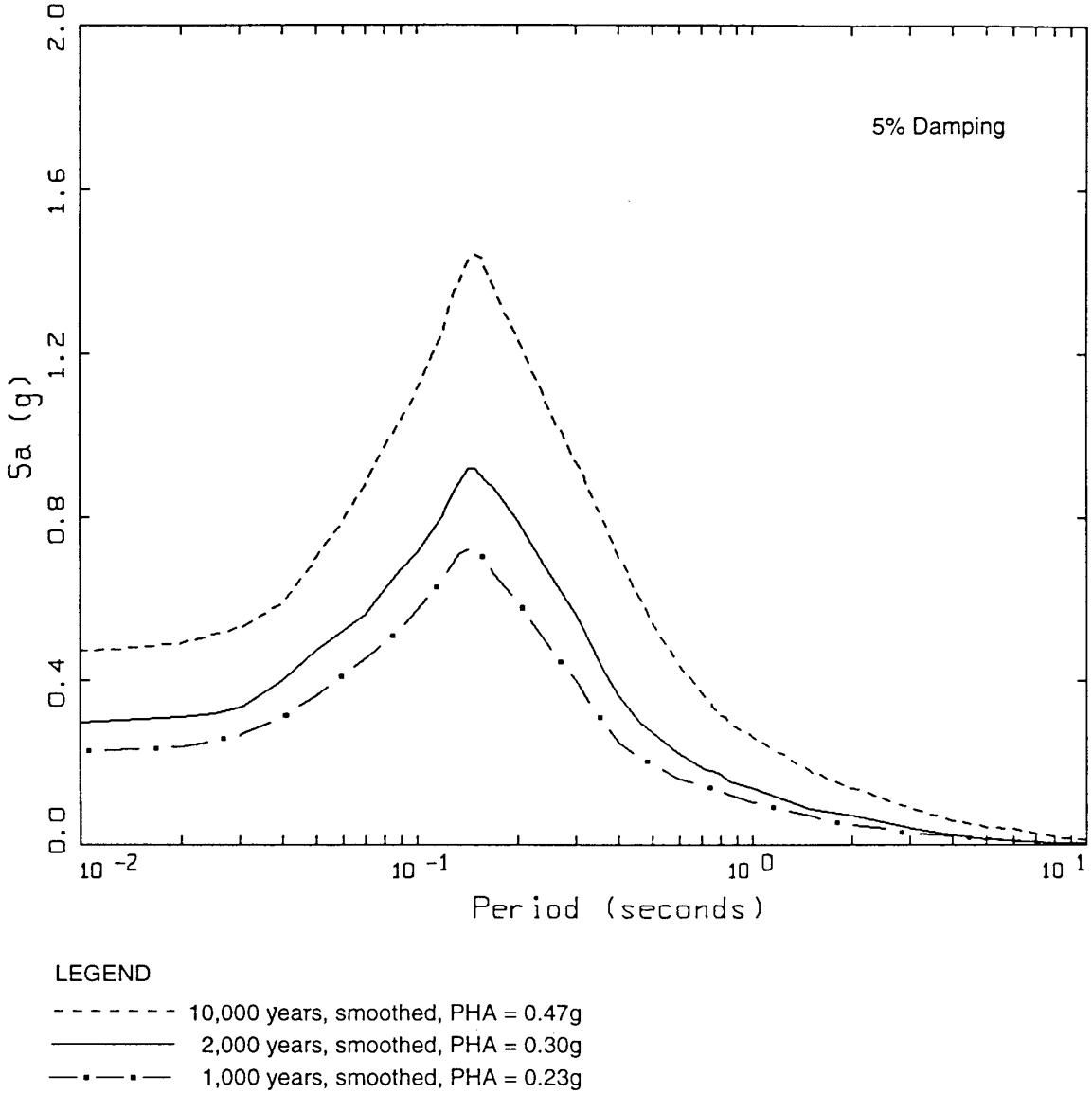

Figure 2.6-38. Smoothed DBE horizontal spectra for soil (5% damped) at 10,000, 2,000, and 1,000 year return periods.

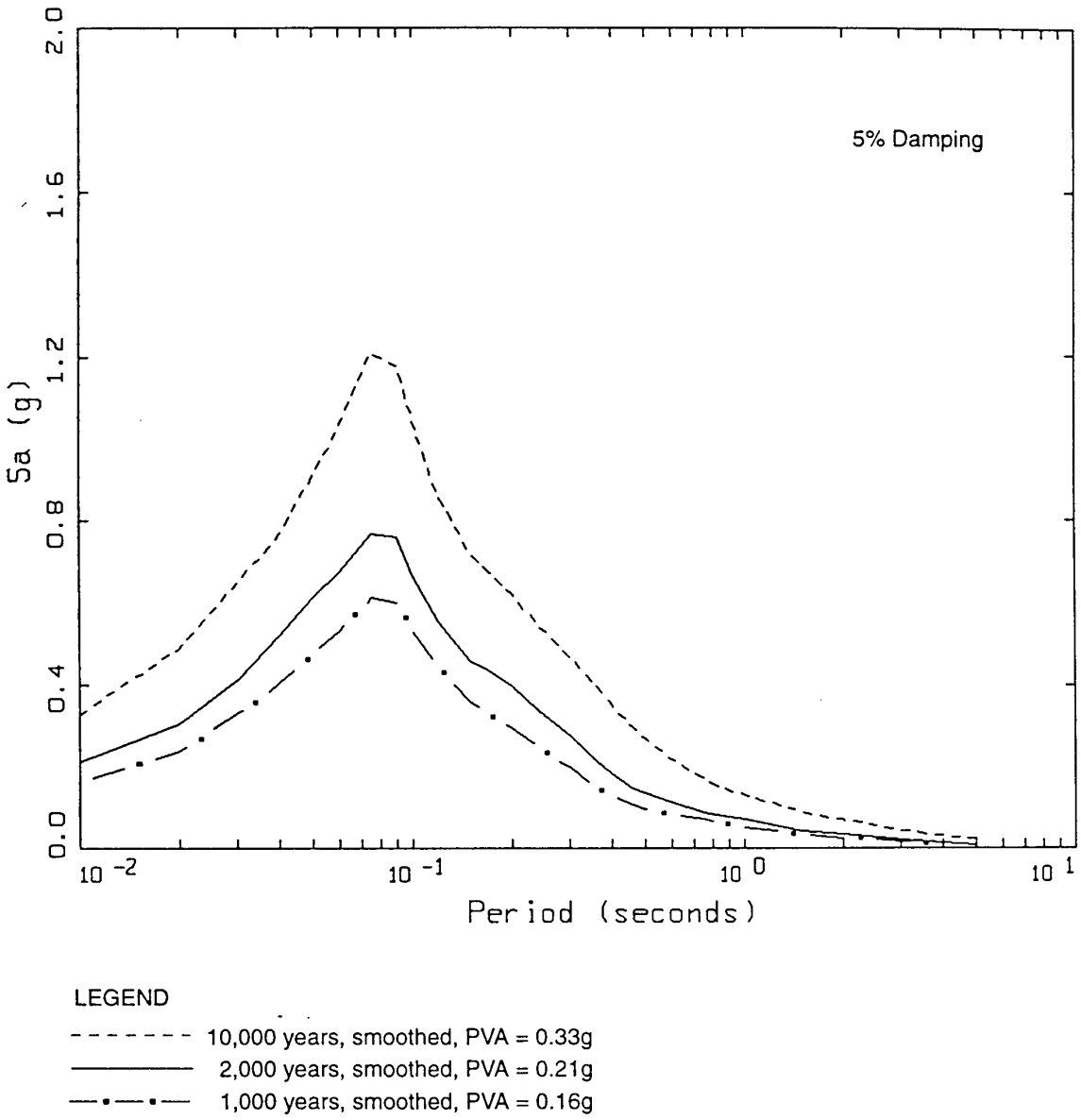

Figure 2.6-39. DBE vertical spectra for soil (5% damped) at 10,000, 2,000, and 1,000 year return periods.

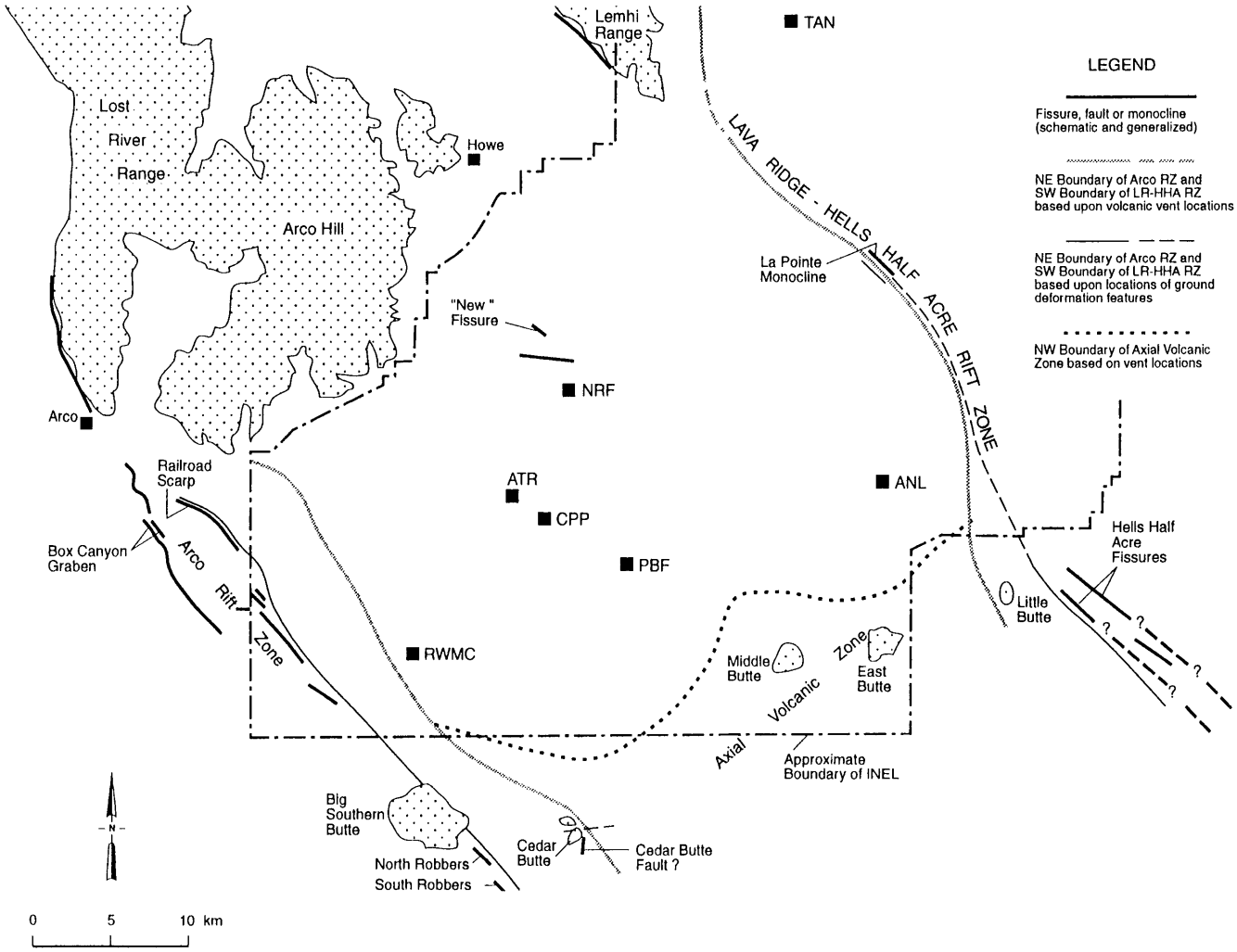

Figure 2.6-40. Map of INEEL showing locations of volcanic rift zones, axial volcanic zone, and fissures north of NRF.

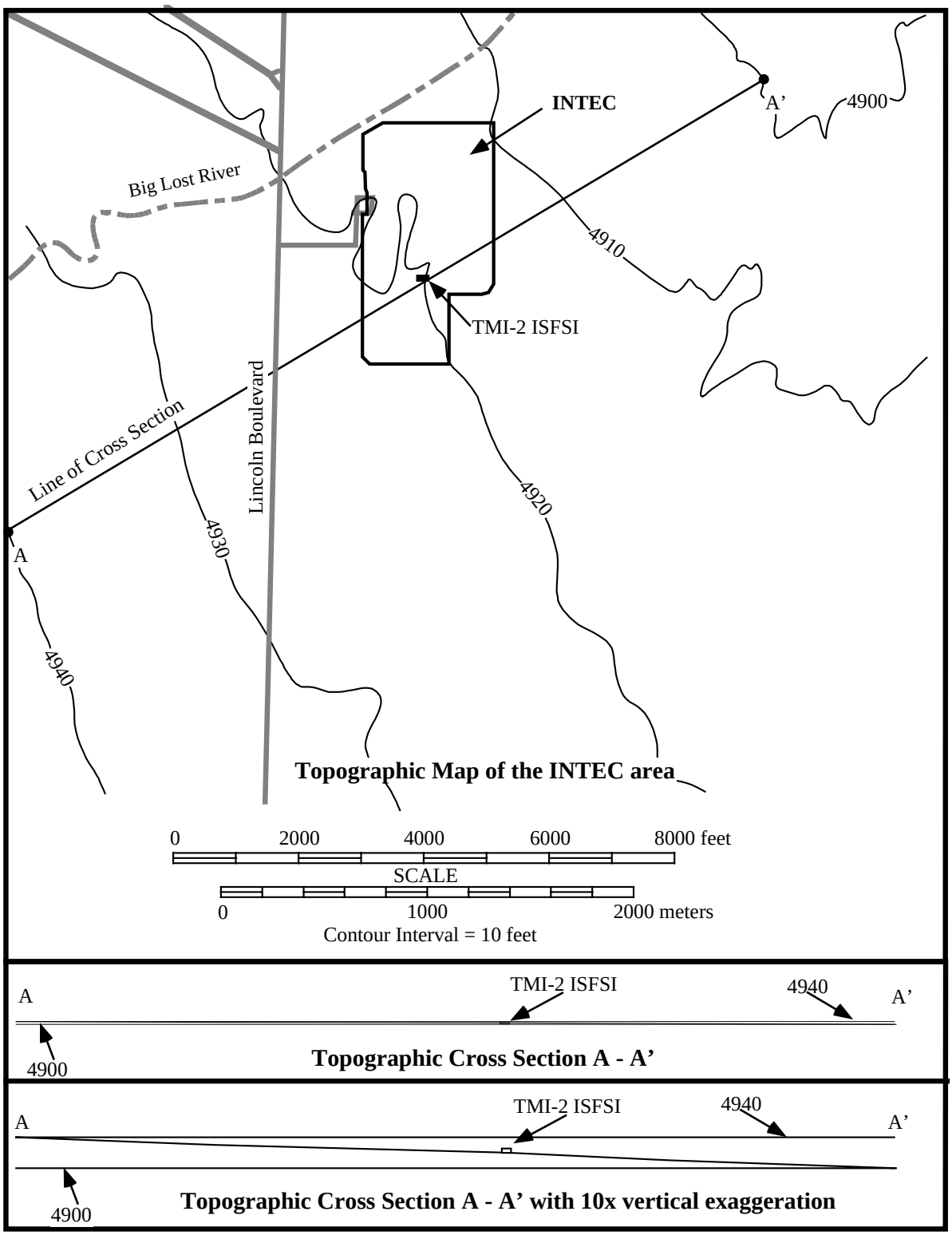

Figure 2.6-41. Topographic Map of the INTEC Area and Cross Sections Showing the Low Relief of the Area.

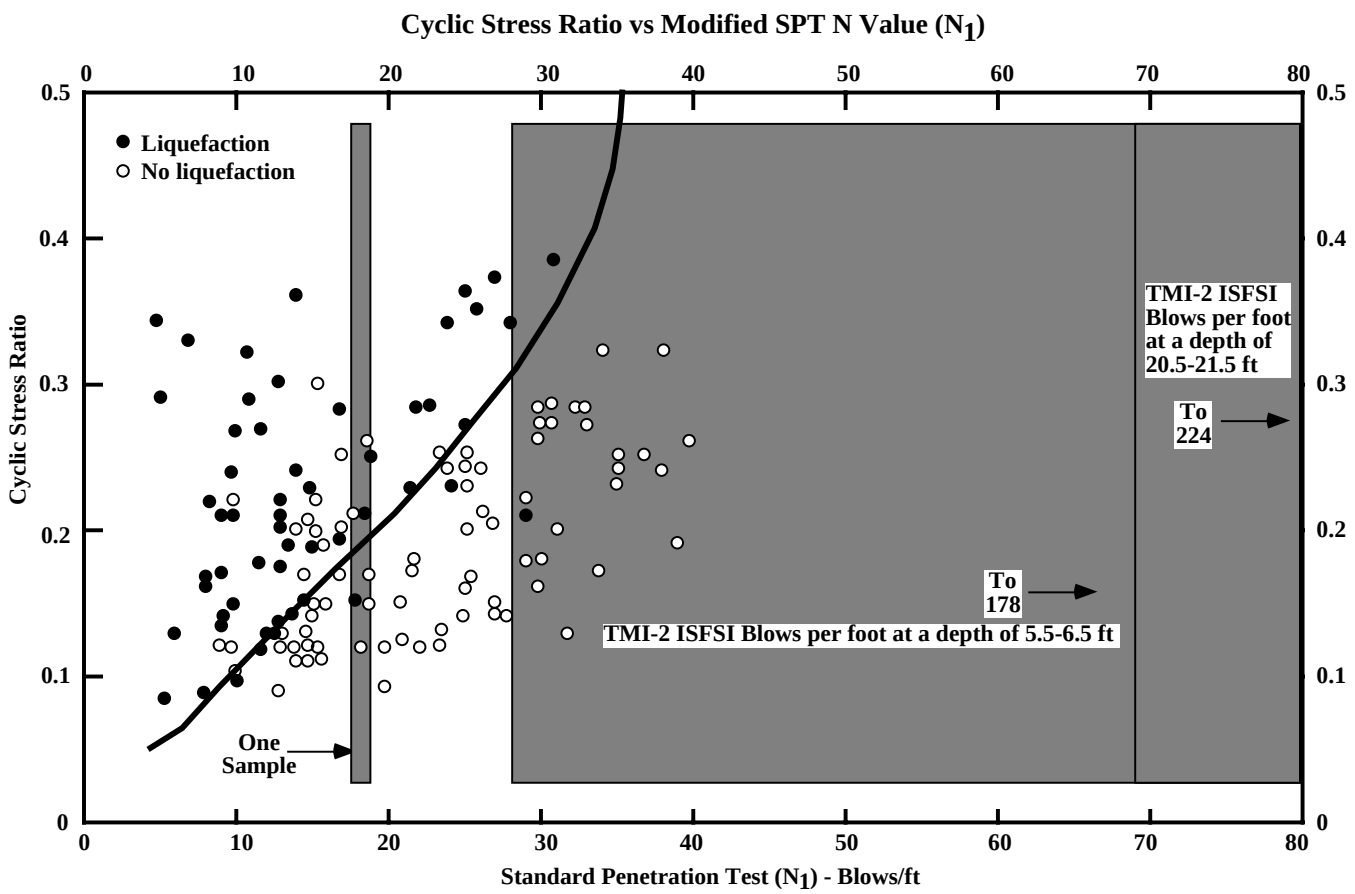

Figure 2.6-42. Plot of Standard Penetration Test Blowcounts for TMI-2 ISFSI soils compared to SPT vs Cyclic Stress Ratios from Kayen (1992) and Seed et al. (1983).

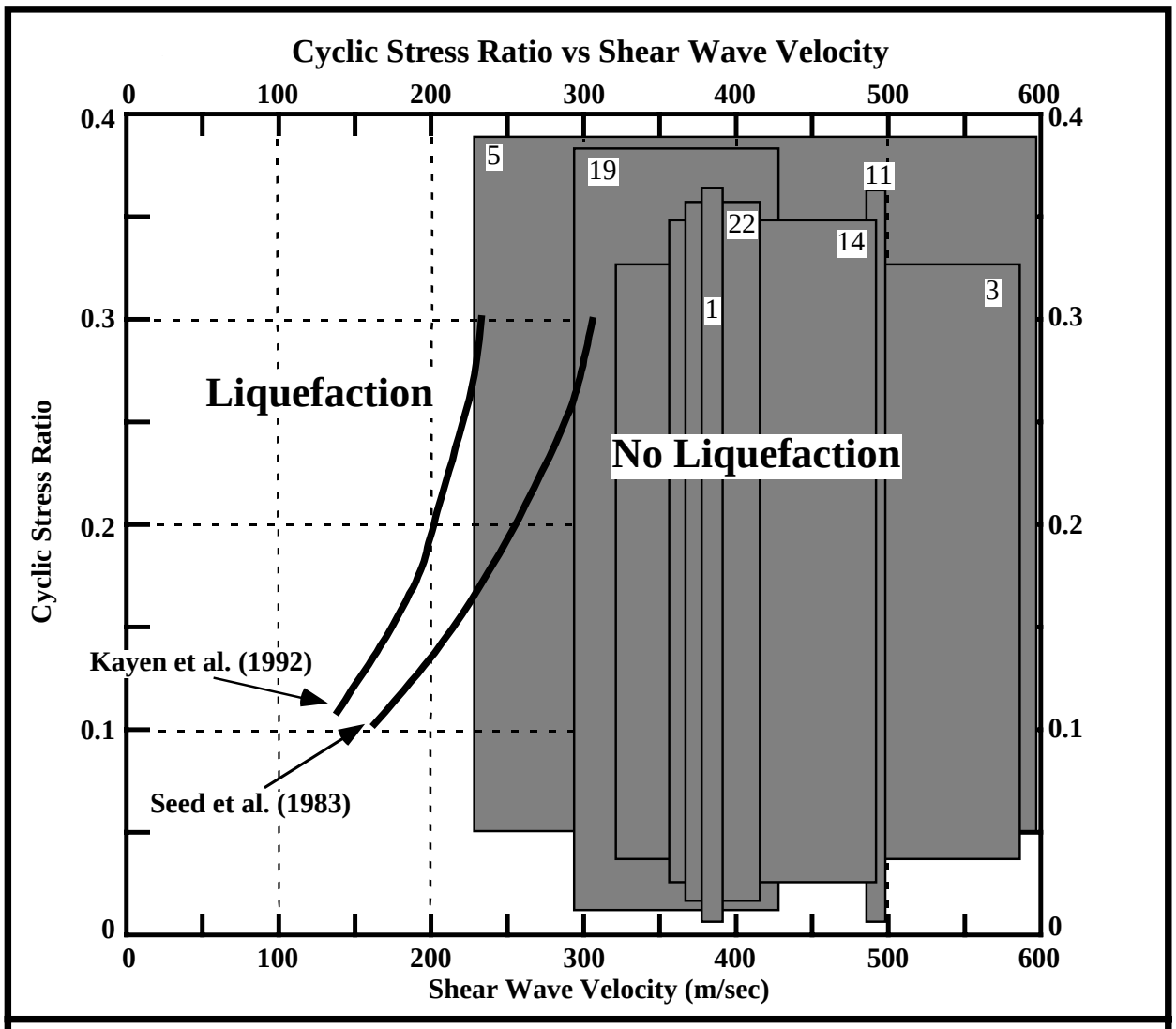

Pattterned boxes show range of shear wave velocities for 7 boreholes at the ISFSI site at INTEC. The 7 boreholes penetrated the entire thickness of the surficial sediment at INTEC (25 to 66 feet). Box numbers correspond to borehole numbers shown in Figure 2.6-14.

Figure 2.6-43. Plot of Shear-wave Velocities of TMI-2 ISFSI Surficial Sediments Compared to Shear-wave Velocity vs. Cyclic Stress Ratio of Kayen (1992) and Seed et al. (1983).

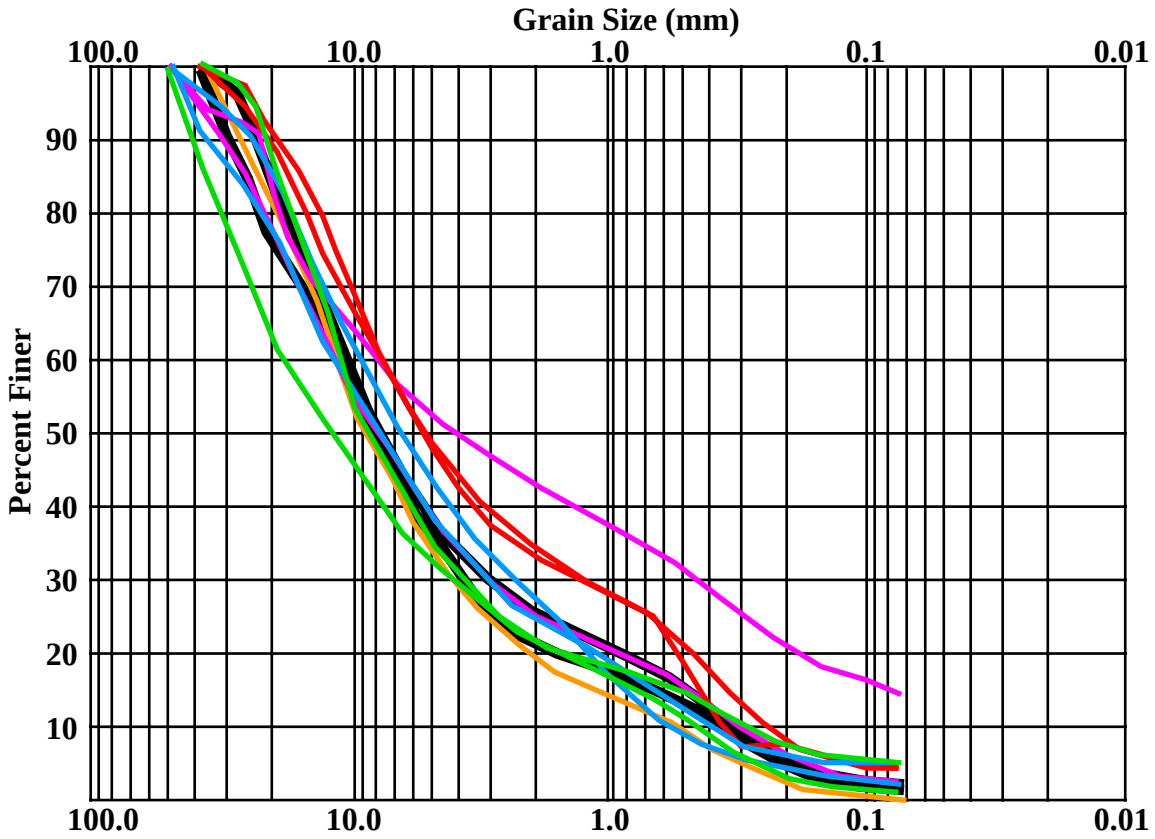

BH number and Footage	% Gravel	%Sand	%Silt and Clay
BH-1 (5-6.5')	62.3	34.7	3.0
BH-1A (5'-6.5')	63.4	34.7	1.9
BH-2 (5-6.5')	67.5	32.2	0.3
BH-3 (10-12.5')	61.8	35.1	3.1
BH-3 (28.5-30.5')	47.9	36.6	15.5
BH-4 (5-6.5')	52.2	43.1	4.7
BH-4A (5-6.5')	50.5	46.8	2.7
BH-5 (5-6.5')	57.1	40.1	2.8
BH-5 (20-21.5')	61.7	33.1	5.2
BH-19 (5-6.5')	68.1	30.4	1.5
BH-19 (20-21.5')	65.2	29.5	5.3

Figure 2.6-44. Plots of gradation (grain size) Analyses of TMI-2 ISFSI Surficial Sediments. See Figure 2.6-14 for borehole locations and Figure 2.6-45 for borehole lithologic logs.

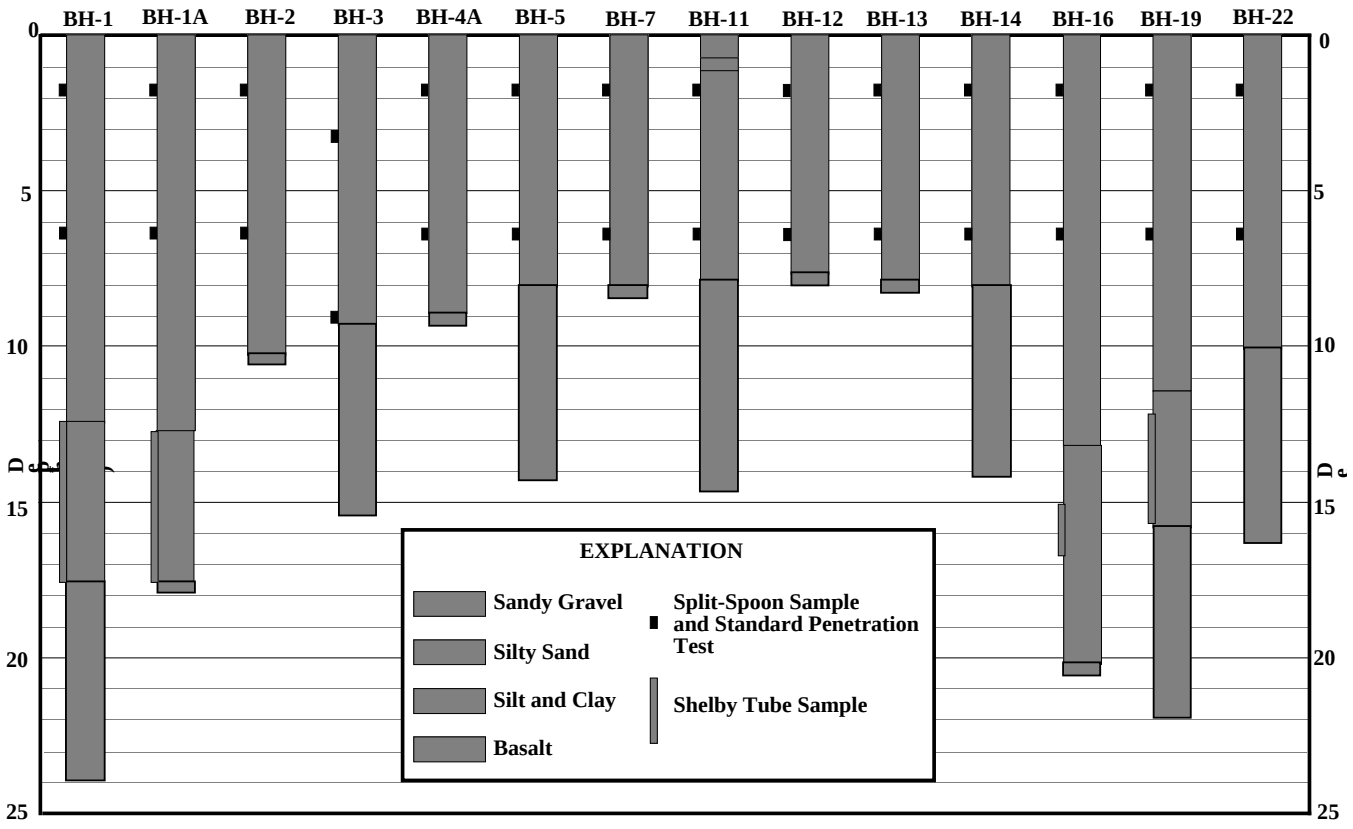

Figure 2.5-45. Lithologic Logs of TMI-2 ISFSI Boreholes. See Figure 2.6-14 for Borehole Locations.

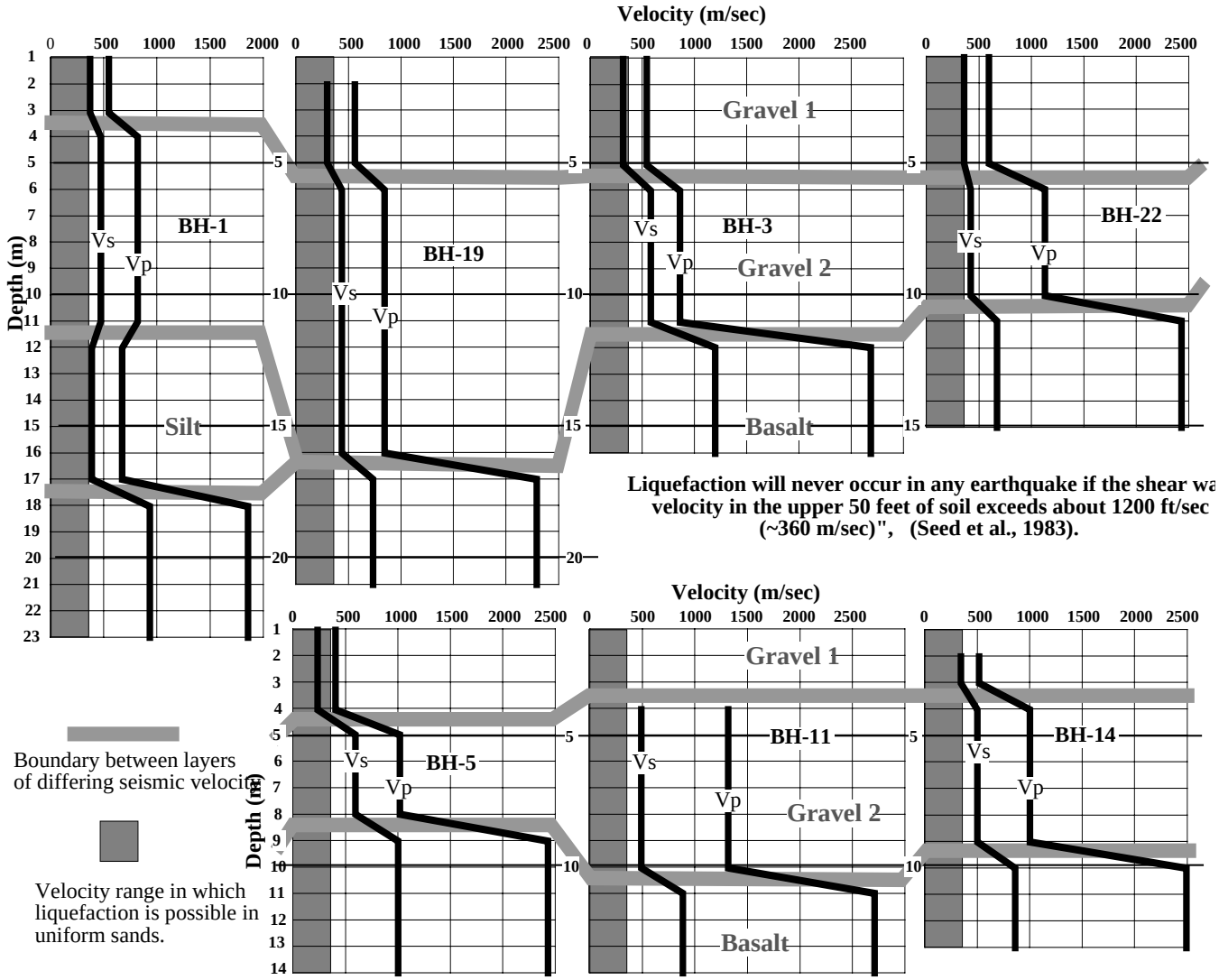

Figure 2.6-46. Surficial Sediment Seismic Velocity Profiles from TMI-2 ISFSI Boreholes. Boreholes Are Arranged from Northwest to Southeast, from Deep (>15 m) to Shallow (8-10 m) Bedrock. See Figure 2.6-14 for Borehole Locations.

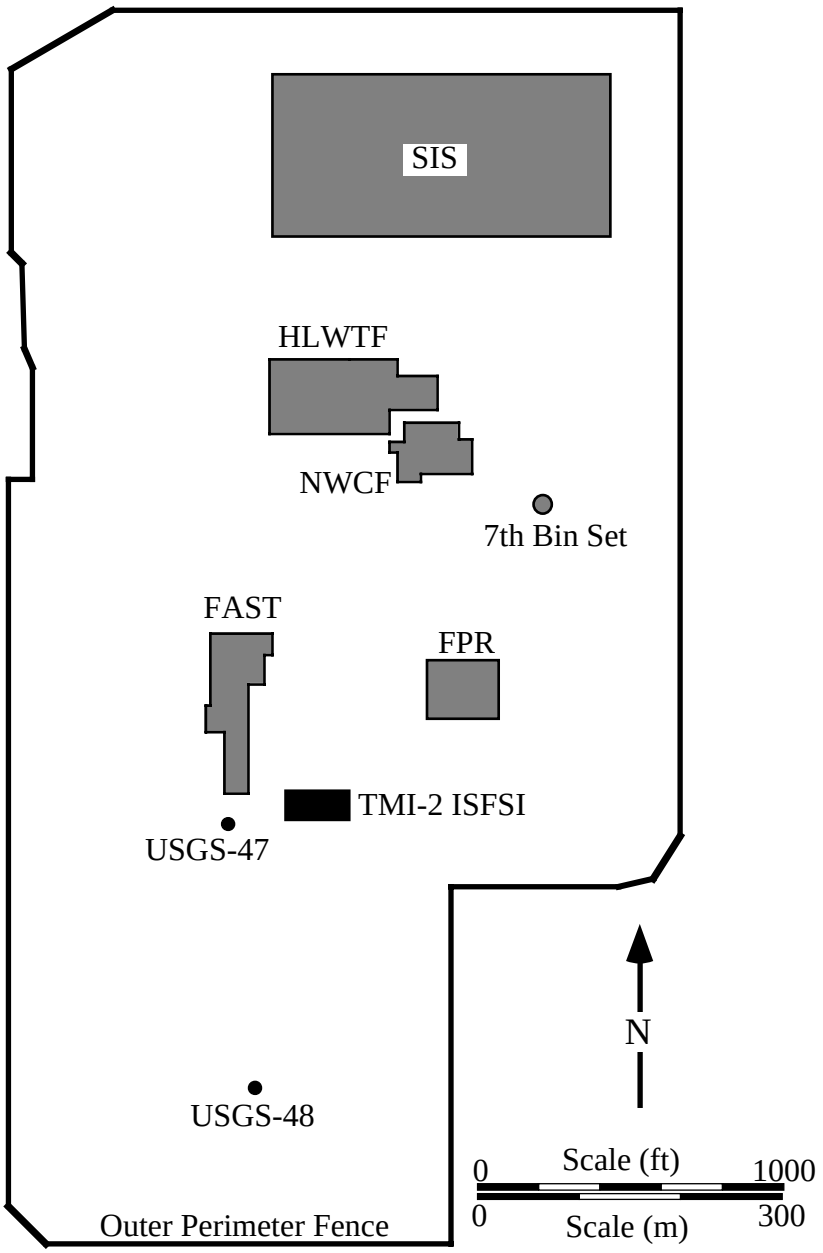

Figure 2.6-47. Map Showing Location of the TMI-2 ISFSI in Relation to Previous Geotechnical Investigations at INTEC. See Table 2.6-13 for Geotechnical Data.

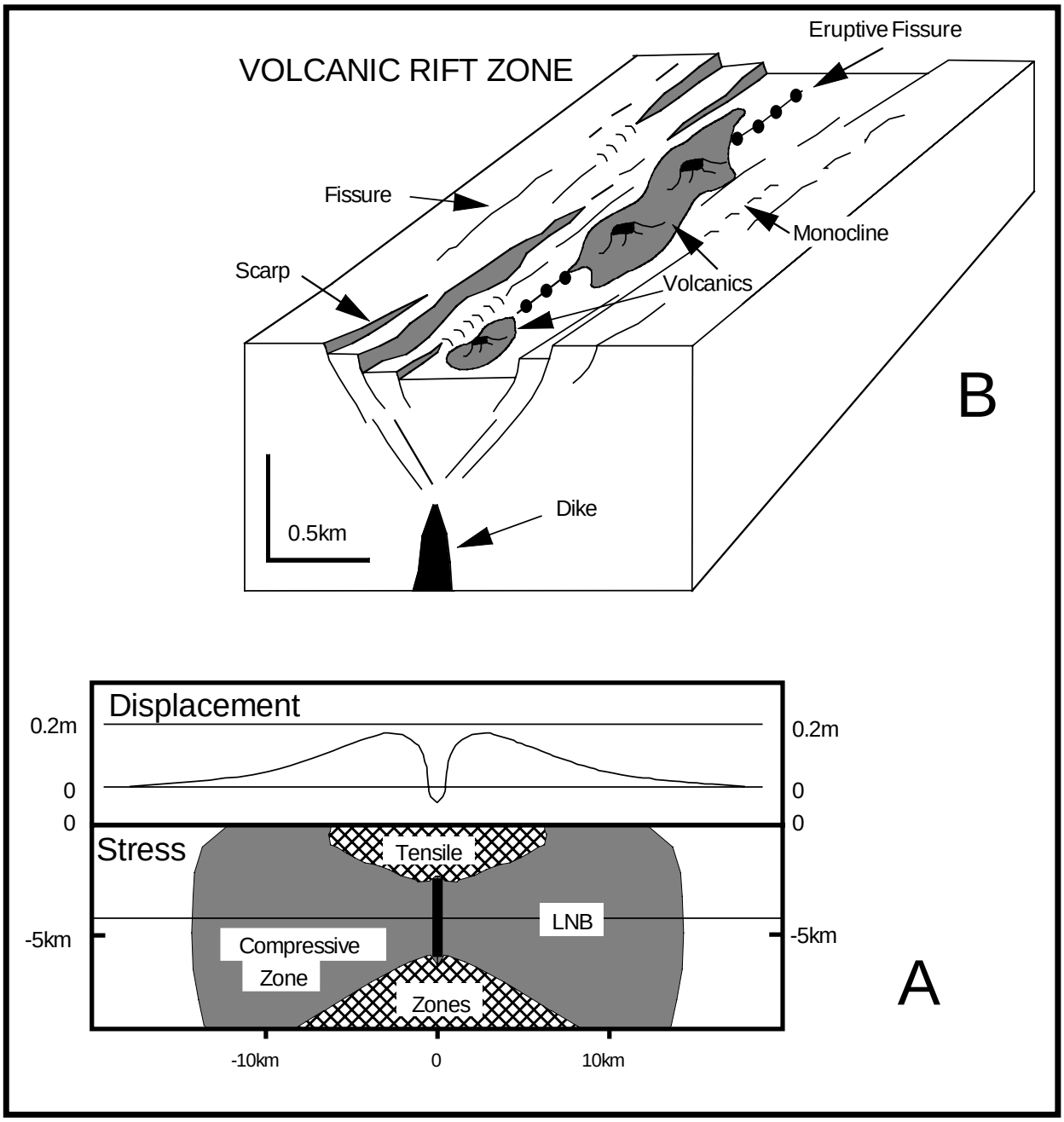

Figure 2.6-48. Diagram Showing, (A) Stress Field and Displacement Caused by Intrusion of a Dike at Shallow Depth in the Crust, and (B) Volcanic Rift Zone Structures Formed Above Shallow Dikes.

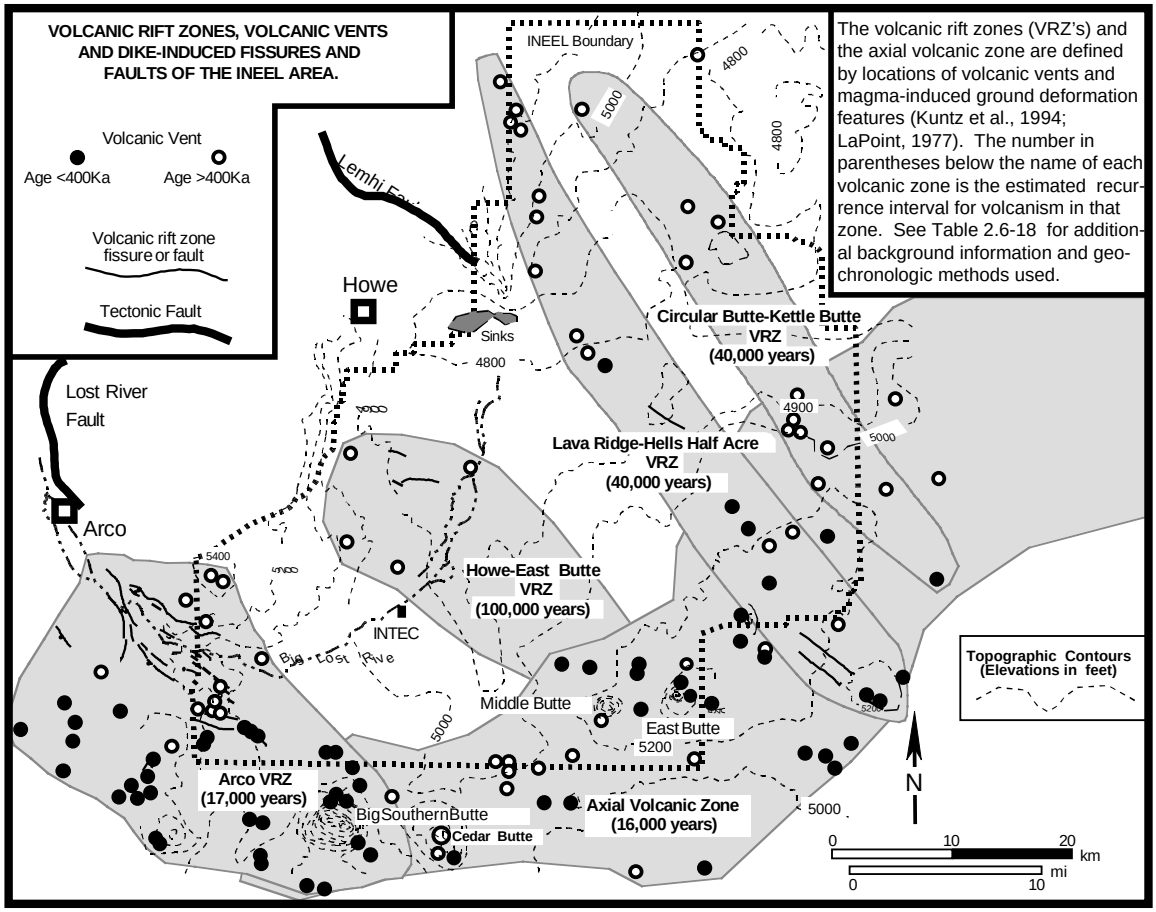

Figure 2.6-49. Map of Volcanic Vents and Volcanic Zones With Estimated Recurrence Intervals.

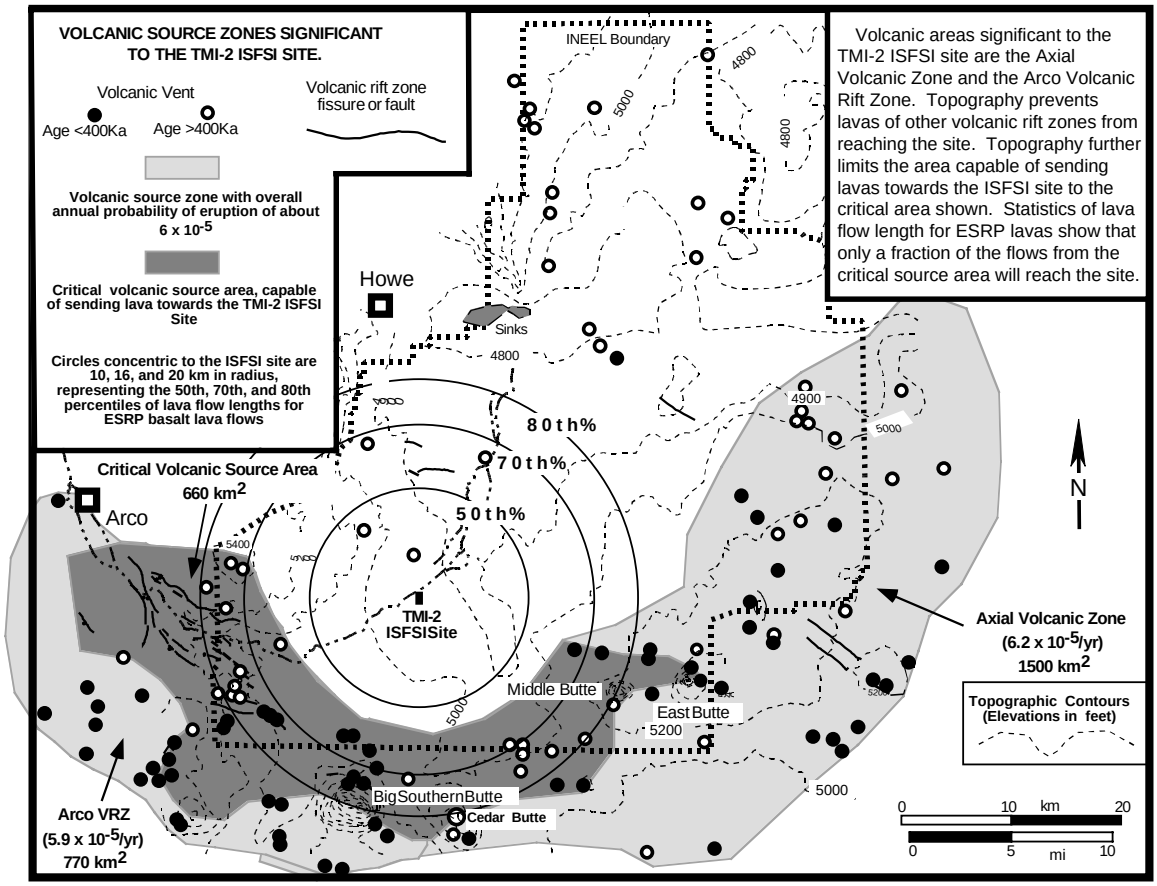

Figure 2.6-50. Map showing Parameters Important for Estimation of Lava Flow Inundation Probability at the TMI-2 ISFSI Site.

2.11 References for Tables and Figures

Anders, M.H., J.W. Geissman, L.A. Piety, and J.T. Sullivan (1989) "Parabolic distribution of circumeastern Snake River Plain seismicity and latest Quaternary faulting: Migratory pattern and association with the Yellowstone Hotspot;" *Journal of Geophysical Research*, v.94, no.B2, p.1589-1621.

Anderson, S.R. (1991). "Stratigraphy of the unsaturated zone and uppermost part of the Snake River Plain aquifer at the Idaho Chemical Processing Plant and Test Reactors Area, Idaho National Engineering Laboratory, Idaho," *U.S. Geol. Surv. Water Resources Invest. Report* 91-4010, 71 p.

Anderson, S.R. and B.D. Lewis (1989). "Stratigraphy of the unsaturated zone at the Radioactive Waste Management Complex, Idaho National Engineering Laboratory, Idaho," *U.S. Geol. Surv. Water Resources Invest. Report* 89-4065, 54 p.

Arabasz W.J., W.D. Richins, and C.J. Langer (1979). "The Pocatello Valley (Idaho-Utah border) earthquake sequence of March to April 1975," in *Earthquake Studies in Utah 1850 to 1978*, W.J. Arabasz, R.B. Smith, and W.D. Richins, editors, University of Utah Special Publication, p. 339-374.

Armstrong, R. L., W. P. Leeman, and H. E. Malde (1975). "Quaternary and Neogene volcanic rocks of the Snake River Plain, Idaho", *American Journal of Science* 275, 225-251.

Bache, T.C., D.G. Lambert and T.G. Barker (1980). "A source model for the March 28, 1975, Pocatello Valley earthquake from time-domain modeling of teleseismic P waves," *Bull. Seis. Soc. Am.*, v. 70, p. 405-418.

Baltzer, E. M., P. L. K. Knuefer, and M. J. Turko (1989). "Late Quaternary slip events along the central Lemhi fault, Idaho (Abstract)," *Geol. Soc. Am. Abstr. Progr.*, v. 21, no. 5, p. 53.

Barberi, F., A. Bertagnini, and P. Landi, (1990), *Mt. Etna, The 1989 Eruption*, Gianini, Pisa.

Bennett, C.M. (1990). *Streamflow losses and ground-water level changes along the Big Lost River at the Idaho National Engineering Laboratory, Idaho*, U.S. Geol. Surv. Water-Resources Invest. Rept. 90-4067.

Bonaccorosco, A., and P. M. Davis, (1993), Dislocation Modelling of the 1989 Dike Intrusion into the Flank of Mount Etna, Sicily, Journal of Geophysical Research, v.98, p. 4261-4268.

Brandsdottir, B. and P Einarsson (1979) " Seismic activity asociated with the September 2977 deflagration of the Krafla central volcano in northeastern Iceland," Journal of Volcanology and Geothermal Reaseach, v. 6, p. 197-212

Bruhn, R.L, Wu, D., and Lee, J-J (1992) *Final Report on the structure of the southern Lemhi and Arco fault zone, Idaho*; EG&G Idaho, Inc., Informal Report EGG-NPR-10680, 6 plates, 26 p.

Byrd, J.O., D. Giessman, J. William, and R.B. Smith (1988). " Seismotectonics of the Teton fault and possible relationship to the Yellowstone Hotspot," *EOS Transactions, Am. Geophys. Union* v. 69, no. 44, p. 1419.

Champion, D.E., M.A. Lanphere, and M.A. Kuntz (1988). " Evidence for a new geomagnetic reversal from lava flows in Idaho: Discussion of short polarity reversals in the Brunhes and Late Matuyama polarity chrons," *J. Geophys. Res*., v. 93, p. 11,667-11,680.

Cook, K. L. and R. K. Nye (1979). *Effects of the Pocatello Valley (Idaho-Utah border) earthquake of March 28, 1975 (UTC)*, Earthquake Studies in Utah 1850 to 1978, W. J. Arabasz, R. B. Smith, and W. D. Richins, editors, p. 445-457.

Crone, A.J., M.N. Machette, M.G. Bonilla, J.J. Lienkaemper, K.L. Pierce, W.E. Scott, and R.C. Bucknam (1987) " Surface faulting accompanying the Borah Peak earthquake and segmentation of the Lost River fault, central Idaho;" *Bulletin Seismological Society of America*, v.77, no.3, p.739-770.

Dames and Moore (1976) *Soils/foundation investigation, New Waste Calcining Facility, INEL, for the Energy Research and Development Administration*, prepared for Fluor Engineers and Constructors, Inc., Los Angeles.

Dames and Moore (1977) *Report of Foundation Investigation, Flourinal and Fuel Storage Facilities*, Chemical Processing Plant, Idaho Falls, Idaho.

Dewey, J. W. (1987). *Instrumental seismicity of central Idaho*, Bulletin of the Seismological Society of America, v. 77, no. 3, p. 819-836.

Dewey, J.W., W.H. Dillinger, J. Taggart, and S.T. Algermissen (1973). " A technique for seismic zoning: Analysis of earthquake locations and mechanisms in northern Utah, Wyoming, Idaho, and Montana," in *Contributions to seismic zoning*, S.T. Harding, editor, NOAA Technical Rept. ERL 267-ESL 30, p. 541-575.

Doherty, D.J. (1979a) *Drilling data from exploration well 1, NE 1/4, sec.22, T.2N., R. 32E., Bingham County, Idaho*; U.S. Geological Survey Open-file Report 79-1225, 1 sheet.

Doherty, D.J. (1979b) *Drilling data from exploration well 2-2A, NW 1/4, sec.15, T.5N., R.31E., Idaho National Engineering Laboratory, Butte County, Idaho*; U.S. Geological Survey Open-file Report 79-851, 1 sheet.

Doherty, D.J., L.A. Morgan, and M.A. Kuntz (1979) *Preliminary geologic interpretation and lithologic log of the exploratory geothermal test well (INEL-1), Idaho National Engineering Laboratory, eastern Snake River Plain, Idaho*; U.S. Geological Survey Open-file Rep. 79-1248, 10p.

Doser, D. I. (1984). *Source parameters and faulting processes of the August 1959 Hebgen Lake, Montana, earthquake sequence*, Ph.D. Thesis, Univ. of Utah, Salt Lake City, Utah, 165p.

Doser, D. I. (1985a). "The 1983 Borah Peak, Idaho and 1959 Hebgen Lake, Montana earthquakes: Models for normal fault earthquakes in the Intermountain seismic belt;" *in Proceedings of Conference XXVIII on the Borah Peak, Idaho Earthquake*, U. S. Geol, Surv., Open-File Rept. 85-290, p. 368-384.

Doser, D. I. (1989a). "Source parameters of Montana earthquakes (1925-1964) and tectonic deformation in the northern Intermountain Seismic Belt;" *Bulletin of the Seismological Society of America*, v.79, No. 1, p.31-50.

Doser, D. I. (1989b). "Extensional tectonics in northern Utah-southern Idaho, U.S.A., and the 1934 Hansel Valley sequence," *Physics of the Earth and Planetary Interiors*, v. 54, p. 12-134.

Doser, D.I. (1985b). "Source parameters and faulting processes of the 1959 Hebgen Lake, Montana, earthquake sequence," *Journal of Geophysical Research*, v. 90, no. B6, p. 4537-4555.

Doser, D.I. and R.B. Smith (1985). "Source parameters of the 28 October 1983 Borah Peak, Idaho earthquake from body wave analysis," *Bull. Seis. Soc. Am.* 75, 1041-1051.

Doser, D.I. and R.B. Smith (1989). "An assessment of source parameters of earthquakes in the Cordillera of the western United States," *Bull. Seis. Soc. Am.* v. 79, p. 1383-1409.

EG&G Geosciences Unit (1984a*) Report of the geotechnical investigation for the 7th Bin Set at the Chemical Processing Plant, INEL*.

EG&G Geosciences Unit (1984b) *Report of the geotechnical investigation for the Fuel Procesing Restoration Project at the Chemical Processing Plant, INEL.*

Engdahl, E.R. and W.A. Rinehart (1988) "Seismicity map of North America, Continent-scale Map-004," *Decade of North American Geology*, Geological Society of America, Scale 1:5,000,000, 4 sheets.

Eppley, R.A. and W.K. Cloud (1961). *United States earthquakes 1959*, U.S. Coast and Geodetic Survey, 115 p.

Ferrucci, F., and D. Petane, (1993), Seismic Activity Accompanying the Uotbreak of the 1991-1993 Eruption of Mt. Etna (Italy), Journal opf Volcanology and Geothermal Research, v.57, p. 125-135.

Gilbert, J. D., D. Ostenaa, and C. Wood (1983). *Seismotectonic study for Jackson Lake dam and reservoir, Minidoka Project, Idaho-Wyoming* (unpubl.), Boise, Idaho and Denver, Colorado, U. S. Bureau of Reclamation, Pacific Northwest Regional Office and Engineering and Research Center, Seismotectonic Report 83-8, 123 p.

Golder Associates (1992a) *New Production Reactor Site Characterization, Volume I: Volcanic Zones Mapping Report, Volume II: Regional Geomorphic Study, and Volume III: NPR Site Geologic Report*; EG&G Informal Report EGG-NPR-10625.

Golder Associates (1992b) *High level waste tank farm replacement project geotechnical investigation*; Report prepared for Westinghouse Idaho Nuclear Company under contract C90-132739.

Hackett, W. R. and L. A. Morgan (1988). "Explosive basaltic and rhyolitic volcanism of the eastern Snake River Plain, Idaho," in P.K. Link and W.R. Hackett, editors, *Guidebook to the Geology of Central and Southern Idaho*, Idaho Geological Survey, Bulletin 27, 283-301.

Hackett, W. R. and R.P. Smith (1992). "Quaternary volcanism, tectonics, and sedimentation in the Idaho National Engineering Laboratory area," *in* J.K. Wilson editor, *Field Guide to Geologic Excursions in Utah and Adjacent Areas of Nevada, Idaho, and Wyoming*, Utah Geological Survey, Miscellaneous Publlication 92-3, p. 1-17.

Haller, K. M. (1988). *Segmentation of the Lemhi and Beaverhead faults, east-central Idaho, and Red Rock fault, southwest Montana, during the late Quaternary*, M.S. Thesis, University of Colorado, 141 p.

Hayden, K.P. (1992) *Geology and petrology of the Cedar Butte eruptive center, eastern Snake River Plain, Idaho*; Masters thesis, Idaho State University, Pocatello.

Jackson, S. M. and J. E. Zollweg (1988). *Seismic studies of an earthquake sequence in the White Cloud Peaks, Idaho* (Abstract), Seismological Research Letters, v.59, no.1, January-March, p.6.

Jackson, S. M., J. E. Zollweg, and C. J. Langer (1991a) *1984 Devil Canyon sequence near Challis, Idaho: Structural complexity near the north end of the Borah Peak aftershock zone*; Seismological Research Letters, v.62, p.51.

Johnson, P. P. (1981). *Geology of the Red Rock fault and adjacent Red Rock Valley, Beaverhead County, Montana*, M.S. Thesis, University of Montana, Missoula, Montana, 73 p.

Knuepfer, P. L. K. (1989). *Late Quaternary segmentation and recurrence, southern Lemhi fault, Idaho*; report written to R. P. Smith, EG&G Idaho Inc., Idaho Falls, Idaho.

Koslow, K.N. and D.H. Van Haaften, (1986), *Flood Routing Analysis for a Failure of Mackay Dam*, EGG-EP-7184, EG&G Idaho Inc., Idaho Falls, ID.

Kuntz, M. A. (1978). *Geology of the Arco-Big Southern Butte area, eastern Snake River Plain, and potential volcanic hazards to the Radioactive Waste Management Complex and other waste storage and reactor facilities at the Idaho National Engineering Laboratory, Idaho*, U. S. Geol. Surv. Open-File Report 78-691, 70 p.

Kuntz, M. A., B. Skipp, M.A. Lanphere, W. E. Scott, K.L. Pierce, G.B., Dalrymple, D.E. Champion, G.F. Embree, W.R. Page, L.A. Morgan, R.P. Smith, W.R. Hackett, and D.W. Rodgers (1994) *Geologic map of the Idaho National Engineering Laboratory and adjoining areas, eastern Idaho*; U.S. Geolological Survey Miscellaneous Investigations Map I-2330, 1:100,000 scale.

Kuntz, M. A., D. E. Champion, E. C. Spiker, and R. H. Lefebvre (1986). "Contrasting magma types and steady-state, volume-predictable, basaltic volcanism along the Great Rift, Idaho;" *Geological Society of America Bulletin*, v. 97, p. 579-594.

Kuntz, M. A., D. E. Champion, R. H. Lefebvre, and H. R. Covington (1988) *Geologic map of the Craters of the Moon, Kings Bowl, Wapi lava fields and the Great Rift volcanic rift zone, south-central Idaho*; U. S. Geological Survey Miscellaneous Investigations Series Map I-1632, scale 1:100,000.

Link, P.K., Skipp, B., Hait, M.H., Janecke, S.U., and Burton, B.R. (1988) *Structural and stratigraphic transect of south-central Idaho: A field guide to the Lost River, White Knob, Pioneer, Boulder, and Smoky Mountains*; Idaho Geological Survey Bulletin 27, p.5-42.

Machette, M.N., S.F. Personius, and A.R. Nelson (1992). *Paleoseismology of the Wasatch fault zone: A summary of recent investigations, interpretations, and conclusions, in Assessments of regional earthquake hazards and risk along the Wasatch Front, Utah*, P.L. Gori and W.W. Hays, editors, U.S. Geol. Surv. Professional Paper 1500, p. A1-A71.

Malde, H. E. (1987). "Quaternary faulting near Arco and Howe, Idaho," *Bull. Seis. Soc. Am*., v. 77, no. 3, p. 847-867.

Malde, H.E. (1991) "Quaternary geology and structural history of the Snake River Plain, Idaho and Oregon;" in Morrison, R.B., editor, *Quaternary non-glacial geology, conterminous United States*; Boulder Colorado, Geological Society of America, The Geology of North America, v.K-2, p.251-281.

Mastin, L. G. and D. D. Pollard (1988). "Surface deformation and shallow dike intrusion processes at Inyo Craters, Long Valley, California," *J. Geophy. Res*., v. 93, p. 13,221-13,235.

McCalpin, J.P., L.A. Piety, and M.H. Anders (1990). *Part 1. Latest Quaternary faulting and structural evolution of Star Valley, Wyoming, in Geologic field tours of western Wyoming and parts of adjacent Idaho, Montana, and Utah*, S. Roberts, editor, Geol. Surv. Wyoming Public Information Circular No. 29, p. 5-14.

Morgan, L.A. (1988). *Explosive rhyolitic volcanism of the eastern Snake River Plain* (unpublished, Ph.D. Thesis), Manoa, University of Hawaii, 191 p.

Nace, R.L., Voegely, P.T., Jones, J.R., and Deutsch, S. (1975) *Generalized geologic framework of the National Reactor Testing Station, Idaho*; U.S. Geological Survey Professional Paper 725-B, 49p.

Nava, S.J., W.J. Arabasz, and J.C. Pechmann (1994). "The M5.9 Draney Peak, Idaho earthquake of February 3, 1994: A preliminary report, Fault Line Forum, Utah Earthquake Advisory Board," *Utah Geological Survey*, v. 10, no. 1, p. 5-7.

Northern Engineering and Testing (1987) *Report of Geotechnical Investigation for the Special Isotope Separation Facility, Idaho Chemical Processing Plant, Idaho National Engineering Laboratory;* Prepared for M-K Ferguson Company.

Oaks, S.D. (1992*) Historical seismicity investigation for the November 11, 1905 earthquake*; EG&G Informal Report EGG-GEO-10203, 106p.

Pierce, K. L. (1985). *Quaternary history of faulting on the Arco segment of the Lost River fault, central Idaho, in Proceedings of Conference XXVIII on the Borah Peak, Idaho Earthquake*, U. S. Geol, Surv., Open-File Rept. 85-290, p. 195-206.

Pierce, K. L. (1988). *Field guides to the Quaternary geology of central Idaho: Part E. History of Quaternary faulting and scarp degradation studies, southern Lost River Valley, Guidebook to the Geology of Central and Southern Idaho,* Idaho Geol. Surv. Bull., 27, p. 233-240.

Pierce, K.L. and Morgan, L.A. (1992) "The track of the Yellowstone hot spot: Volcanism, faulting, and uplift," in P.K. Link et al., editors, *Regional Geology of Eastern Idaho and Western Wyoming*: Geological Society of America Memoir 179, 1-54.

Piety, L. A., C. K. Wood, J. D. Gilbert, J. T. Sullivan, and M. H. Anders (1986). *Seismotectonic study for Palisades Dam and Reservoir, Palisades Project*: U. S. Bureau of Reclamation, Engineering Research Center, Seismotectonic Division, Denver, Colorado, and Pacific Northwest Region Geology Branch, Boise Idaho, Seismotectonic Report 86-3, 198 pp.

Pitt, A.M., Weaver, C.S., and Spence, W. (1979) "The Yellowstone Park earthquake of June 30, 1975," *Bulletin of the Seismological Society of America*, 69, 187-205.

Pollard, D. D., T. T. Delany, W. A. Duffield, E. T. Endo, A. T. Okamura, (1983), "Surface Deformation in Volcanic Rift Zones," Technophysics, v.94, p. 541-584.

Richins, W.D. (1979). "Earthquake data for the Utah region, 1850 to 1978," in Arabasz, W.J., Smith, R.B. and Richins, W.D., editors, *Earthquake studies in Utah 1850 to 1978*, University of Utah, p. 57-251.

Rubin, A. M. (1992). "Dike-induced faulting and graben subsidence in volcanic rift zones," *J. Geophys. Res*. v. 97, p. 1839-1858.

Ryan, M. P. (1987) "Neutral buoyancy and the mechanical evolution of magmatic systems," in *Magmatic Processes: Physiochemical Principles*, The Geochemical Society Special Publication No. 1, B.O. Mysen, editor, p. 259-287.

Schneider, N. P. (1985) *Morphology of the Madison Range fault scarp, southwest Montana: implications for fault history and segmentation*; M. S. Thesis, Miami University, Oxford, Ohio, 131 p.

Schwartz, D. P. (1988) "Geologic characterization of seismic sources: moving into the 1990's," *Earthquake Engineering and Soil Dynamics II Proceedings*, ASCE meeting in Park City, Utah, June, 42 p.

Scott, W. E. (1982). *Surficial Geologic Map of the Eastern Snake River Plain and Adjacent Areas, Idaho and Wyoming*; U. S. Geological Survey Miscellaneous Investigation Map I-1372, scale 1:250,000.

Scott, W. E., K. L. Pierce, and M. H. Hait, Jr (1985) "Quaternary tectonic setting of the 1983 Borah Peak earthquake, central Idaho;" *Bulletin of the Seismological Society of America*, v.75, no.4, p.1053-1066.

Shenon, P. J. (1936). "The Utah earthquake of March 12, 1934 (extracts from unpublished report)," *in* Neumann, F., *United States Earthquakes*, 1934, U. S. Coast and Geodetic Survey, Serial 593, 43-48.

Slemmons, D.B. A.E. Jones, and J.I. Gimlett (1965) "Catalog of Nevada earthquakes, 1852-1960," *Bull. Seis. Soc. Am.* v. 55, p. 519-565.

Smith, R. B., W. D. Richins, and D. I. Doser (1985). "The 1983 Borah Peak, Idaho earthquake: Regional seismicity, kinematics of faulting, and tectonic mechanism," in *Proceedings of Conference XXVIII on the Borah Peak, Idaho Earthquake*, U. S. Geological Survey Open-File Report 85-290, p. 236-263.

Smith, R. P., W. R. Hackett, and D. W. Rogers (1989). "Geological Aspects of seismic hazards assessments at the INEL, Southeastern Idaho," in *Proceedings of the second DOE Natural Hazards Mitigation Conference, Knoxville, Tennessee*, 282-289.

Smith, R.B., J.O. Byrd, D.D. Susong, A.G. Sylvester, R.L. Bruhn, and J.W. Geissman (1990) *Three year progress report: An evaluation of earthquake hazards of the Grand Teton National Park emphasizing the Teton fault*; Unpublished, University of Utah, Salt Lake City, Utah, 149 p.

Sparlin, M. A., L. W. Braile, and R. B. Smith (1982). "Crustal Structure of the Eastern Snake River Plain Determined from Ray Trace Modeling of Seismic Refraction Data," *Journal of Geophysical Research*, v. 87, no. B4, p. 2619-2633.

Stickney, M. C. and M. J. Bartholomew (1987). "Seismicity and late Quaternary faulting of the northern Basin and Range province, Montana and Idaho," *Bull. Seis. Soc. Am*. v. 77, 1602-1625.

Stover, C. W. (1985). "The Borah Peak, Idaho earthquake of October 28, 1983 - Isoseismal map and intensity distribution," *Earthquake Spectra*, 2, No. 1, 11-21.

Stover, C. W., G. E. Reagor, and S. T. Algermissen (1986*). Seismicity map of the state of Idaho*, U. S. Geological Survey Map MF1857.

Susong, D.D., R.B. Smith, and R.L. Bruhn (1987). "Quaternary faulting and segmentation of the Teton fault zone, Grand Teton National Park, Wyoming," *EOS Transactions*, Am. Geophys. Union, v. 68, p. 1452.

Swan, F. H. III, D. P. Schwartz, and L. S. Cluff (1980). "Recurrence of moderate to large magnitude earthquakes produced by surface faulting on the Wasatch fault zone," *Utah, Bull. Seis. Soc. Am.*, v. 70, p. 1438-1462.

Turko, J. M. (1988). *Quaternary Segmentation History of the Lemhi Fault, Idaho*, M.S. Thesis, State University of New York at Bringhamton.

U.S. Geological Survey (1972) *Geologic map of Yellowstone National Park*, U.S. Geol. Surv. Misc. Geologic Invest. Map I-711, scale 1:125,000.

U.S. Geological Survey (1994). *Preliminary determination of epicenters, monthly listing*, U.S. Department of Interior, National Earthquake Information Center, February.

Wells, D.L. and Coppersmith, K.J. (1994) "New empirical relationships among magnitude, rupture length, rupture area, and surface displacement," *Bulletin of the Seismological Society of America*, v.84, p.974-1002.

Westaway, R. and R. B. Smith (1989). "Source parameters of the Cache Valley (Logan), Utah earthquake of 30 August 1962," *Bull. Seis. Soc. Am.*, v. 79, no. 5, p. 1410-1425.

Wood, H.O. and F. Neumman (1931). *Modified Mercalli intensity scale of 1931*, Seismologica Society of America Bulletin, v.52, no.4, p.163-180.

Woodward-Clyde Consultants (1992a). *Earthquake strong ground motion evaluations for the proposed New Production Reactor at the Idaho National Engineering Laboratory, Volume I: Deterministic Evaluation and Volume II: Probabilistic Evaluation*, EG&G Idaho, Inc. Informal Report EGG-GEO-10304.

Woodward-Clyde Consultants (1992b). *Paleoseismic investigations of the southern Lemhi Fault, Idaho*, EG&G Idaho, Inc., Informal Report EGG-GEO-10178, 32 p.

Woodward-Clyde Federal Services (1996a) *Site Specific Probabilistic Seismic Hazard Analysis for the INEL*, Final Report, Lockheed Idaho Technologies Company, Technical Report INEL-95/0536, two volumes.